



HAL
open science

Caractérisation de la réactivité de surface de matériaux d'électrode positive riches en nickel pour batteries Li-ion

Angelica Laurita

► To cite this version:

Angelica Laurita. Caractérisation de la réactivité de surface de matériaux d'électrode positive riches en nickel pour batteries Li-ion. Matériaux. Nantes Université, 2022. Français. NNT : 2022NANU4025 . tel-03783581

HAL Id: tel-03783581

<https://theses.hal.science/tel-03783581>

Submitted on 22 Sep 2022

HAL is a multi-disciplinary open access archive for the deposit and dissemination of scientific research documents, whether they are published or not. The documents may come from teaching and research institutions in France or abroad, or from public or private research centers.

L'archive ouverte pluridisciplinaire **HAL**, est destinée au dépôt et à la diffusion de documents scientifiques de niveau recherche, publiés ou non, émanant des établissements d'enseignement et de recherche français ou étrangers, des laboratoires publics ou privés.

THESE DE DOCTORAT DE

NANTES UNIVERSITE

ECOLE DOCTORALE N° 596

Matière, Molécules, Matériaux

Spécialité : Sciences des Matériaux

Par

Angelica LAURITA

Characterisation of the surface reactivity of Ni-rich positive electrode materials for Li-ion batteries

Thèse présentée et soutenue à Nantes, le 15 juin 2022

Unité de recherche : CNRS, UMR 6502, Institut des Matériaux de Nantes Jean Rouxel (IMN)

Rapporteurs avant soutenance :

Laurence CROGUENNEC
Gianluigi BOTTON

Directrice de Recherche, Université de Bordeaux, CNRS-ICMCB, Bordeaux
Professeur, McMaster University, Hamilton, Canada

Composition du Jury :

Président : Christel GERVAIS

Professeure, Sorbonne Université, LCMCP, Paris

Examineurs : Odile STEPHAN

Professeure, Université Paris-Saclay, LPS, Paris

Christel GERVAIS

Professeure, Sorbonne Université, LCMCP, Paris

Jérémie AUVERGNIOT

Open Innovation Manager, UMICORE, Grenoble

Dir. de thèse : Philippe MOREAU

Professeur, Nantes Université, CNRS-IMN, Nantes

Co-dir. de thèse : Nicolas DUPRE

Chargé de Recherche, Nantes Université, CNRS-IMN, Nantes

Co-enc. de thèse : Dominique GUYOMARD

Dir. de Recherche Emérite, Nantes Université, CNRS-IMN, Nantes

Invité :

Liang ZHU

Head of Technology Development Team, UMICORE, Olen, Belgique

Acknowledgments

It took me some time before starting writing these lines. This white page is even more difficult to fill than the first of the manuscript, just under the title “Chapter 1”. How to resume in some words all the support so many people have given to me during these years? How to acknowledge every colleague, friend, roommate I had the pleasure to share this journey with, without being too long and emotional? The task still seems to me to be extremely hard, but I will try my best to be short and effective since this manuscript is already long enough.

Let me start by thanking Umicore for funding this project, and in particular Liang, Jérémie and Pierre-Etienne for accompanying me. Similarly, my acknowledgements to Florent Boucher for welcoming me at the Institut des Matériaux de Nantes Jean Rouxel, I spent three beautiful years in this lab.

I would like to thank sincerely all the members of the jury that had the tough burden to evaluate my work: Pr. Christel Gervais, Dr. Laurence Croguennec, Pr. Gianluigi Botton, Pr. Odile Stephan, Dr. Jérémie Auvergniot and Dr. Liang Zhu. I really enjoyed the enriching discussion we had together and I will hardly forget your kind words. I want to thank particularly Laurence and Gianluigi for having taken the time to carefully read and review this manuscript, making precious remarks and comments.

Relationships between PhD students and supervisors are not always easy, but personally, I had the chance to have excellent guides for this 3 years trip: Philippe, “le chef”, not the easiest to approach at first, he always deserved my sincerest respect; Nicolas, half boss half friend, the best teacher of French expressions; Dominique, wise, smiling and calm, always ready to discuss and listen.

My relationship with Philippe was for sure the one that helped my growing the most, making me question myself to find the best way to work together. During these years,

it has been a real pleasure to build with him a wonderful team, improving day after day, sharing opinions, coffees, laughs, science and pizzas. Thank you for being always there, available to discuss scientific and personal matters despite the overwhelming quantity of things you had to do, you have been a great boss.

Nicolas has shown me himself from day 1, the first person to ask me to have lunch with him and other colleagues, discrete but always kind and ready to welcome new people. He made me laugh on terrible days, always having the good words to say, he made me work when I was too lazy to, and he made me learn something new every day. Thank you for your terrible jokes, the crosswords you let me do, our brainstorming, the beers, the explanations and answers to my never-ending questions, the conferences, your advices on the colours and the style of my figures, and for your "ouai mais il faut". Working with you was a real, sincere pleasure.

Despite the time I spent with Dominique was relatively short, he surely has been a huge support for me. Exactly like Pierre-Etienne, who also left the project quite early, these two people continued being present and available to discuss with me and answer my questions. I had beautiful discussions with both of them, that allowed me growing personally and professionally, and for this I truly thank them.

One of my greatest acknowledgments is certainly to address to the technical support of the IMN. In particular, I want to thank "les gars du CMC", Eric and les NicolasS, who trained me, helped me and supported me during these years. Their assistance was so precious, just as their coffee, and their smiles and jokes fresh air during the days spent at the microscope.

It will be impossible for me to name all the colleagues that were by my side during this PhD, they are way too many. I decided to mention some of them only, hoping this will not arise hard feelings from the others: Lou, Lucas and Julio, who I began (and finished) this journey with, were the first true friends I made in Nantes. I shared with each one of them incredible moments, from the office decoration and girls' nights with

Acknowledgments

Lou, to the weekends spent writing and eating “joue de boeuf” and burgers on the melodies of Mac Miller with Lucas. Impossible not to mention Stéven and Elodie, who opened up showing me their best and worst sides (Stéven playing tarots sort of bad side), becoming family to me. I want to thank these five people as well as all the other colleagues and friends I had the pleasure to meet, for allowing me to feel home even so far from Italy.

At last, thanks to Justine and Guillaume for being the most wonderful people in my life and for tolerating me every single day, and to my sisters and my parents for accepting and loving me as I am.

Abstract

The electrification of vehicles is currently based on the use of lithium-ion batteries using lamellar oxides of nickel, manganese and cobalt (NMC) as positive electrode materials. At the industrial level, the production of nickel-rich materials is now the main focus in order to satisfy the need for longer range battery performances demanded by consumers. However, these materials are affected by strong outgassing during battery cycling. Several studies have been conducted to define the main factors contributing to this outgassing and to find the best solutions to reduce it. The majority of this research, though, focuses exclusively on observing the materials during cycling.

To address the necessity of a systematic characterisation of Ni rich NMC in its initial state, the surfaces of several industrial samples were observed using different analytical techniques. ^7Li MAS-NMR, XPS, STEM-EELS and SEM-FIB were used to obtain a thorough description of the materials and their surfaces. The limitations and complementarities of each technique are discussed and the results obtained compared and exploited in a synergistic way. It was thus possible to describe in detail the surface of the material in its initial state at the nanometric scale and to evaluate the influence of the storage conditions, as well as the electrode preparation steps. The procedure thus defined could then be used to analyse the surface of materials from different synthesis methods.

Résumé Long en Français

Notre monde est en train de changer progressivement à cause du réchauffement climatique et notre mode de vie doit s'adapter afin de diminuer les émissions de GES responsables du changement du climat. Étant donné qu'une quantité importante de CO₂ est produite chaque année par le secteur des transports, les gouvernements, les fabricants de VE et les milieux académiques consacrent de nombreux efforts pour assurer une transition mondiale vers une mobilité verte. C'est dans ce contexte que s'inscrit la recherche sur les batteries Li ion - actuellement le meilleur choix pour l'électrification des véhicules - et sur les nouveaux matériaux de batterie plus performants.

C'est pour cette raison que la recherche se concentre aujourd'hui sur les matériaux de cathodes lamellaires riches en Ni, qui présentent non seulement des capacités spécifiques plus élevées, mais aussi moins de problèmes sociaux et gouvernementaux dus à l'extraction du cobalt, qui est encore présent en trop grandes quantités dans de nombreux composés utilisés.

Cependant, les composés riches en Ni tels que le Li(Ni_{0.8}Mn_{0.1}Co_{0.1})O₂ (ou NMC811), sont connus pour être particulièrement instables thermodynamiquement. Leur fabrication au niveau industriel est un problème majeur car ils nécessitent un chauffage à l'oxygène dispendieux et un soin particulier lors du packaging. Leur stabilité pendant le cyclage est problématique et affectée par des phénomènes de production de gaz qui influencent leurs performances électrochimiques et, surtout, leur fiabilité. Cette composition de métaux de transition est l'une des plus étudiées dans la littérature et constitue le cœur de cette thèse. Malgré l'existence de ce grand nombre d'études, seules quelques-unes d'entre elles se concentrent sur la corrélation possible entre le phénomène de production de gaz et l'état de la surface du matériau

avant le cyclage, car il est généralement estimé que les matériaux à l'état initial sont *parfaits*.

Fournir le meilleur matériau aux fabricants de batteries est bien sûr essentiel dans la chaîne de production puisque les matériaux définissent non seulement l'énergie et la puissance théoriques maximales du système électrochimique, mais induisent également des choix d'additifs et de formulations pour tenter d'atteindre cette performance théorique. Cette volonté fait partie des ambitions de la société Umicore au sein de sa division Rechargeable Battery Materials. Avec plus d'une batterie sur cinq fabriquée qui intègre la technologie d'Umicore, l'entreprise est l'un des leaders du marché. La caractérisation au plus haut niveau de ses produits est clairement un incontournable compte tenu des investissements importants dans de nouvelles usines de production. Le financement de cette thèse s'inscrit dans cette démarche mondiale et justifie que tous les échantillons analysés dans ce travail aient été exclusivement fournis par notre partenaire industriel.

Afin de faire avancer la compréhension de la réactivité de surface des matériaux de cathode et donc le développement de nouveaux matériaux fonctionnalisés pour les applications en batterie, il est essentiel de caractériser le plus précisément possible les matériaux avant leur cyclage. Cependant, nous soulignerons dans le premier chapitre de ce manuscrit le manque de précision dans la littérature existante concernant les surfaces de NMC à l'état initial.

Cette thèse a permis de caractériser de manière approfondie la réactivité de surface d'échantillons industriels en utilisant une approche multi-analytique et en se concentrant sur des matériaux ayant toujours le même historique afin d'obtenir des informations comparables.

En particulier, cette thèse s'est attachée à :

- a) Exploiter les techniques avancées de STEM-EELS, STEM-EDX, SEM-FIB, ^7Li MAS-NMR et XPS pour l'analyse des échantillons d'NMC811, avec un intérêt

particulier pour la surface, et la combinaison de ces techniques de manière optimale pour obtenir des informations complètes et avec une haute confiance statistique;

- b) Caractériser la poudre à l'état initial telle qu'elle arrive de chez le producteur et déterminer les corrélations possibles entre les modifications à la fois du bulk et de la surface ;
- c) Étudier l'influence du stockage à court terme dans des conditions contrôlées de faible humidité sur la surface des NMC et sur la quantité d'espèces lithiées en surface, qui a été soigneusement quantifiée ;
- d) Déterminer les effets des procédés de préparation des électrodes en analysant à la fois les encres et les électrodes finales ;
- e) Analyser les surfaces de matériaux synthétisés en faisant varier plusieurs paramètres et déterminer comment les différences observées peuvent affecter le dégagement gazeux dans des cellules complètes.

Dans la première partie des résultats de ce manuscrit, nous observons en effet comment la surface de la poudre est différente du bulk directement après sa réception, et comment les changements observés pourraient être dus à la réactivité très élevée du matériau face à l'humidité extrêmement faible des salles sèches industrielles qui sont considérées comme conventionnelles pour une production et un stockage fiables. En particulier, un excès de manganèse ainsi que du nickel dans un état plus réduit sont trouvés à la surface des particules primaires de matériau. Parallèlement, les espèces lithiées diamagnétiques telles que Li_2O , Li_2SO_4 , LiOH et Li_2CO_3 contenues dans la couche de contamination native sont identifiées et quantifiées. Il est démontré que les propriétés de la surface du matériau actif et de la couche de contamination native sont exacerbées, voire alimentées, lors d'un stockage à court terme dans les conditions de faible humidité étudiées, en présence ou non de CO_2 .

L'importance de ces espèces lithiées est particulièrement évidente lors de l'analyse des encres séchées et des électrodes. En effet, il est démontré qu'une extraction

supplémentaire de lithium, alimentant la couche de surface, se produit pendant la préparation de l'encre. Dans ce contexte, il est suggéré que la quantité de Li_2O puisse être corrélée à la formation de LiF pendant la préparation de l'encre, entraînant la dégradation du liant PVdF. De même, on suggère que cette même réaction se produit pendant le cyclage, produisant le LiOH qui pourrait être responsable de la production de gaz observée. Contrairement à ce qui est souvent supposé dans la littérature, nous montrons ici que le Li_2CO_3 n'a pas d'influence significative sur le dégagement gazeux.

Des études de synthèses à différentes températures de calcination montrent comment ce paramètre peut influencer la formation d'espèces lithiées en surface. Même si une corrélation directe avec la quantité de LiOH formée n'est pas identifiée ici, nous montrons comment une température plus élevée entraîne l'extraction d'une plus petite quantité de lithium et la formation de plus faibles quantités de Li_2O .

De plus, l'atmosphère de calcination et le mélange Li/TM utilisés pour la synthèse exercent une influence synergique à la fois sur l'ordre cationique dans le bulk et sur la spéciation et la quantification des espèces lithiées en surface. Une corrélation claire entre ces paramètres de synthèse et l'enrichissement en Mn précédemment observé n'a cependant pas été trouvée lors de l'étude pilote concluant cette thèse même si la combinaison d'un mélange Li/TM élevé et d'une calcination dans l'air synthétique conduit à un changement drastique des caractéristiques de surface.

Ces résultats ont été obtenus en combinant judicieusement plusieurs techniques de caractérisation, permettant l'observation du matériau à différentes échelles, jusqu'au niveau sub-nanométrique. Nous montrons tout au long de ce travail comment l'utilisation synergique de STEM-EELS, STEM-EDX, MAS-NMR et XPS peut donner des résultats fiables et aider à dépasser les limites de chaque technique prise individuellement. Des acquisitions exploitant le couplage de la reconstruction 3D par SEM-FIB et de la cartographie EDX sont également reportées ici, suggérant cette approche comme un moyen possible de confirmer le mécanisme de réaction de formation du LiF .

Table of Contents

Abstract	i
Résumé Long en Français	iii
Table of Contents	vii
General Introduction	1
Chapter 1: General and Scientific Context	5
Part 1. Climate change and its impact on the advent of sustainable energy	7
1.1. Global warming and GHG emissions: how is our world changing?	7
1.2. Governments actions to face climate change	10
1.2.1. Focus on France.....	12
1.3. Implication of EV manufacturers	13
1.4. Battery 2030+: a European joint effort.....	15
1.5. Drawbacks of Li-ion batteries	16
1.5.1. Social and governance problems of Co extraction.....	18
Part 2. Li-ion batteries	21
Part 3. Positive electrode materials	25
3.1. LiCoO ₂	26
3.2. LiMnO ₂	26
3.3. LiNiO ₂	27
3.4. NMC.....	28

3.4.1. Generalities on NMC materials	29
3.4.2. Cycling behaviour	34
3.4.2.1. After cycling characterisation.....	37
3.4.3. Storage conditions	40
3.4.3.1. Humidity	40
3.4.3.2. Temperature.....	43
3.4.3.3. Electrolyte.....	44
3.4.4. Gassing	45
3.4.5. Possible solutions.....	48
3.4.6. Surface characterisation	54
Part 4. Conclusions and research aim	57
References.....	59
Chapter 2: Characterisation Techniques	71
Part 1. Transmission Electron Microscopy	73
1.1. Basic principles and instrument description.....	73
1.2. Spectroscopies in a TEM	75
1.2.1. Energy-Dispersive X-ray Spectroscopy (EDX)	76
1.2.1.1. Instrument configuration and technique limitations.....	76
1.2.1.2. Acquisition and data treatment parameters	78
1.2.1.3. Profile extraction	80
1.2.2. Electron Energy Loss Spectroscopy (EELS)	81
1.2.2.1. Instrument configuration.....	83
1.2.2.2. Validation of PCA and MLLS results.....	86

1.2.2.3. Data processing for elemental quantification	88
1.3. Experimental conditions	91
Part 2. Focused Ion Beam	93
2.1. Instrument configuration.....	93
2.2. TEM lamellas preparation	94
2.2.1. Pt protection layer deposition.....	95
2.2.2. Lift-out and attachment on the TEM grid	96
2.2.3. Lamella thinning.....	98
2.3. Acquisition of 3D volumes	100
2.3.1. Experimental set-up and sample preparation.....	101
2.3.2. Data treatment.....	103
2.3.3. 3D-FIB-EDX coupling.....	104
2.4. Experimental conditions	107
Part 3. Solid State Magic Angle Spinning Nuclear Magnetic Resonance	109
3.1. Theoretical principles	109
3.2. Quantification method	115
3.3. Technique limitations and possible solutions.....	116
Part 4. X-rays Photoelectron Spectroscopy (XPS)	121
4.1. Theoretical principles	121
4.2. Experimental conditions	123
4.3. Technique limitations and possible solutions.....	124
4.3.1. Depth analysis and spot size.....	124
4.3.2. Degradation issues	125
4.3.3. Difficulties in data processing	127

4.4. Compounds quantification: how to exploit XPS data to obtain speciation information.....	128
Part 5. Conclusions	131
References	133
Chapter 3: Characterisation of NMC811 surface before cycling	135
Part 1. Influence of storage conditions	137
1.1. Introduction	138
1.2. Experimental section	142
1.2.1. Pristine samples	142
1.2.2. Electron Energy Loss Spectroscopy (EELS).....	142
1.2.3. NMR spectroscopy	144
1.2.4. XPS Analysis.....	145
1.3. Results and discussion	146
1.3.1. Nanometric characterization of the pristine material	147
1.3.2. Analysis of the native contamination layer	149
1.3.3. Nanometric quantification at the primary particle surface.....	158
1.3.4. Influence of storage conditions.....	162
1.4. Conclusion	167
References	169
Supporting information for	173
A. Second Derivative Method for elemental quantification of transition metals 173	
B. XPS reference spectra and data fit	178
References	179

Part 2. Influence of the electrode preparation steps	181
2.1. Contamination layer	181
2.2. A focus on LiF.....	186
2.3. Calendering step	193
Part 3. Conclusions	199
References	201
Chapter 4: Influence of synthesis conditions on NMC811 surface	203
Part 1. Influence of the firing temperature	205
1.1. Samples description.....	205
1.2. Gassing evaluation.....	209
1.2.1. Room temperature cycling	211
1.2.2. High temperature cycling.....	213
Part 2. Influence of Li/TM blend and firing atmosphere	217
2.1. Bulk characterisation	217
2.2. Surface characterisation	221
Part 3. Conclusions	227
References	229
General Conclusion and Future Work	231

General Introduction

The global warming, due to the high greenhouse gases (GHG) emissions coming from human activity, has been affecting the Earth system for more than a century now, having a huge impact on our planet. An increasing number of extreme weather events is registered every year, the oceans are warming up putting at risk the oceanic ecosystem, and glaciers are melting. The responsibility of inverting this tendency relies on each individual and we all have to adapt our way of living to transit towards a more sustainable world.

Since a significant part of the GHG are emitted by the transportation sector, governments, industrials and academic researchers are putting a great effort in improving the quality of electric vehicles. In particular, performance of Li-ion batteries –the main actor in the electrification of vehicles– in terms of energy density (Wh/kg or Wh/L) are to be enhanced to respond to the consumer demand for long driving-range means of transportation. For this reason, the research is nowadays focusing on Ni-rich layered cathode materials, presenting not only higher specific capacities, but also lower social and governance problems due to the extraction of cobalt, which is still present in too large amounts in many utilised compounds.

However, Ni-rich compounds such as the $\text{Li}(\text{Ni}_{0.8}\text{Mn}_{0.1}\text{Co}_{0.1})\text{O}_2$ (or NMC811), are known to be particularly unstable thermodynamically. Their preparation at industrial level is a major issue as they require expensive oxygen furnaces and special care during packaging. Their stability during cycling is problematic and affected by gassing issues influencing electrochemical performance and most importantly security. This composition of transition metals is one of the most studied in literature and is the core of this PhD. Despite the existence of this large number of studies, only a few among them focus on the possible correlation between the gassing phenomenon and the state of the material surface before cycling, assuming that pristine materials are *perfect*. Since

performance decreases with cycling, it is quite understandable to look for reasons of failure after electrochemical testing. Nevertheless, what if the gassing issues were already engraved in the pristine material? What if the reasons were deeply hidden at a scale only attainable with the best techniques and protocols? What if the materials were already modified right from production plant? It is the principal objective of this PhD thesis to try and answer these questions on industrial samples of interest.

Delivering the best material to battery manufacturers is of course essential in the production chain since materials not only define the maximum theoretical energy and power of the electrochemical system, but also induce choices of additives and formulations to try and reach this theoretical performance. This is the aim of the Umicore company in its Rechargeable Battery Materials business unit. With over 1 out of 5 batteries ever made containing Umicore's technology, the company is one of the leaders on the market. The optimal characterisation of products is clearly a must considering the substantial investments in new production plants. Funding this PhD was part of this worldwide initiative and justifies that all samples analysed in this work were exclusively provided by our industrial partner.

NMC materials are becoming more and more complex due to the diversification in chemistry, the mass production constrains and the importance of their extreme surface on gassing phenomenon. Solely high-end techniques now allow pinpointing the relevant characteristics of these advanced materials. Techniques (and associated competences) all present at the Institut des Matériaux de Nantes Jean Rouxel. Due to the complexity of the matter, a single high-level technique or even multiple but disconnected techniques are insufficient. This PhD demonstrates the need of combining multiple techniques, pushing them to their here-required extreme limit. As a matter of fact, STEM-EELS (Electron Energy Loss Spectroscopy), XPS (X-ray Photoelectron Spectroscopy) and MAS-NMR (Magic Angle Spinning Nuclear Magnetic Resonance) will be used in combination in all the chapters of the thesis.

This manuscript is divided in four chapters, describing and discussing the work that was carried out during these years. Each chapter is divided into two or more parts having a common topic, but focusing on different aspects of it.

Chapter 1 aims to put this work in a global context and in a more scientific one. After analysing the possible impact of climate changes affecting our world on the advent of sustainable energy, the focus will be shifted to Li-ions batteries, providing some theoretical basis that are going to be useful while reading the rest of the manuscript. The largest part of this chapter will be dedicated to a review of the most relevant, recent and cited publications about NMC811, aiming at pointing out the principal features of these materials and the most important lacks in the existing literature.

The characterisation techniques exploited throughout this work will be then introduced in Chapter 2. The scope of this chapter will be not only to give some theoretical basis of each technique, but also to investigate their limits and present the principle approaches we used to overcome these limitations. A large number of pages will be concentrated on these themes, as they represent a significant part of the work conducted during these years. In particular, in addition to the already mentioned coupling between different techniques, we will show in this chapter how a relative quantification of oxygen and transition metals can be obtained by STEM-EELS even in materials containing elements with overlapping edges, commonly tricky to analyse. We will also talk about degradation, not only under electronic beam, which is often taken into account in electron microscopy studies, but also due to the less energetic X-ray, typically ignored when dealing with XPS measurements.

The last two chapters gather the results obtained during the investigation of the effect of short-term storage in low-humidity conditions, electrode preparation steps and synthesis parameters on the surface of NMC811. The first part of Chapter 3 consists in a full paper written in the frame of this thesis and evidences the importance of an extended characterisation of materials surfaces before cycling. In the following part,

we will instead focus on the possible reactions occurring during the electrode preparations, suggesting a new PVdF degradation path.

Chapter 4 puts the basis for a possible correlation between the gassing behaviour and the state of the material surface just after synthesis. Some possible reactions concerning gas production will be proposed here, always taking into account the considerations resulting from the previous chapter. In addition, the influence of the firing temperature and atmosphere and of the Li/TM ratio blend used for the synthesis will be put in relation with lithium extraction from the material, surface composition and bulk structure of NMC811.

As expected for a PhD thesis relying on high-end techniques, if the instruments had been willing, some additional data could have been obtained. However, I tried to privilege statistically relevant acquisitions, often not evidenced in literature, over plethoric material characterisations, always with an eye on the coupling between them. I hope the reading through the manuscript will be evidence of this, and that the journey at the nanosurface of the Ni-rich materials will be enlightening.

Chapter 1

General and Scientific Context

This chapter aims to insert this work in a complete context, taking into account not only the scientific background, but also a more global one. Therefore, the first part will focus on the climate changes that are affecting our world to give the reader a clear picture of the actual status of our planet and of the importance of a sustainable transition. The development of lithium-ion batteries, which will be introduced in the second part of this chapter, is situated in this context. Despite the importance of scientific advancements in this field to significantly decrease the impact of road transportation on the greenhouse gases (GHG) emissions, it is essential to keep in mind that individual and collective efforts towards energetic sobriety still are the best and only option to slow down climate change. The choice of dedicating such a large number of lines to this subject arises from the desire of finding a contact point between our scientific work — often very specific, theoretical, almost a niche product — and our everyday lives and the more generic issues affecting our world.

To get back to science, a literature review about layered cathode materials for automotive applications will then be the main topic of the third part of this chapter. This part will focus in particular on Ni-rich materials belonging to the NMC family (with general formula $\text{Li}(\text{Ni}_x\text{Mn}_y\text{Co}_{1-x-y})\text{O}_2$) since they are the materials this entire work is about. Considering the incredibly large number of publications concerning this topic and the impossibility to cite all of them, only the most relevant, cited and recent works will be presented. The principal lacks of the existing literature will be pointed out in the last section of this chapter, with particular focus on the surface characterisation of pristine materials; this will be followed by the motivation and the objectives of this thesis.

Part 1. Climate change and its impact on the advent of sustainable energy

How many times have we heard talking about climate change, global warming and greenhouse gas emissions (GHG) over the last few years? These subjects are already on everyone's lips, from children to governments, and are having a great impact on our everyday life. Nevertheless, some confusion is still present in our conversations and people are often not aware of what is really going on. However, with the right tools and notions explained in an easy-to-understand way, everybody should be conscious of the impact single individuals' actions can have on the future course of climate.

The aim of this first part is to give a clear and wide picture of the changes that are affecting our world, with unambiguous information and numbers, and to show how climate change is having a great impact on the advent of sustainable energy at a worldwide scale thanks to governments, industries and academic researchers. Similarly, the impact of lithium-ion batteries for electric vehicles on the transition towards a more sustainable world will be also taken into account.

1.1. Global warming and GHG emissions: how is our world changing?

The Earth system is undergoing a long-term heating due to human activities named global warming for more than a Century now. The data collected by National Oceanic and Atmospheric Administration and relayed in the World Meteorological Organisation's report about the state of global climate in 2021 are represented in Figure 1.1 and give an indication of the temperature increase over the last century from the 1880-1900 period.¹ The growth of coal consumption and air pollution due to the Industrial Revolutions of the 19th century had an enormous impact on the world temperature, that never stopped increasing since, except for the periods affected by economic crisis especially after the first and the second World Wars. In the last years, temperatures have reached the 1.1-1.2°C increase from the 1880-1900 period and this

value is expected to cross the global warming level of 1.5°C in the next decade if serious actions are not taken.^{1,2}

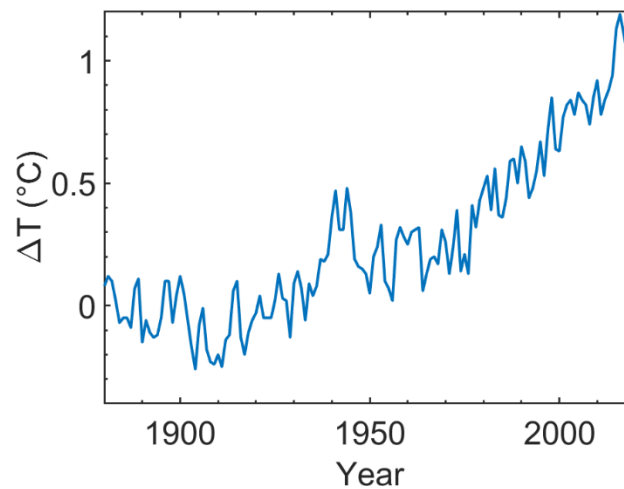


Figure 1.1. Global temperature rise recorded by the National Oceanic and Atmospheric Administration (NOAA) with respect to the average temperature between years 1880 and 1900.¹

The global warming is already having and will have a huge impact on our lives and on the planet we are living on. Together with the fires in Canada due to the extremely high temperatures of July 2021, this summer was characterised by rain—instead of snow— falling for the first time on Summit Station (3216 m) in Greenland on August 14th and temperatures remained above freezing for almost 9 hours. Glaciers are melting and sea level increases (+20 cm in 2022), due to the intensification of the water cycle, causing coastal flooding and erosion.² Oceans warming rates showed a very strong increase in the past two decades and oceans temperatures are expected to continue rising in the future. This, as well as the acidification of oceanic waters due to the absorption of the atmospheric CO_2 , affects —and will continue to affect— the ocean ecosystems and people relying on them. Moreover, extreme weather bringing to natural disasters and climate events such as storms, cyclones and hurricanes are often hitting large parts of Africa, Asia and Latin America making it difficult for the population and ecosystems to recover from repeated weather shocks.^{1,2}

This situation is going to get worse if temperatures keep on increasing as expected, so the question we have to ask ourselves in front of this scenario is: how can we make

things better? How can our actions change the future course of climate? The Intergovernmental Panel on Climate Change (IPCC) report states clearly that greenhouse gas (GHG) emissions from human activities are responsible for the 1.1°C temperature increase of the last century. It is therefore essential to lower the GHG emissions and to know where exactly those GHG are coming from in order to modify our actions and behaviours towards a more sustainable future.

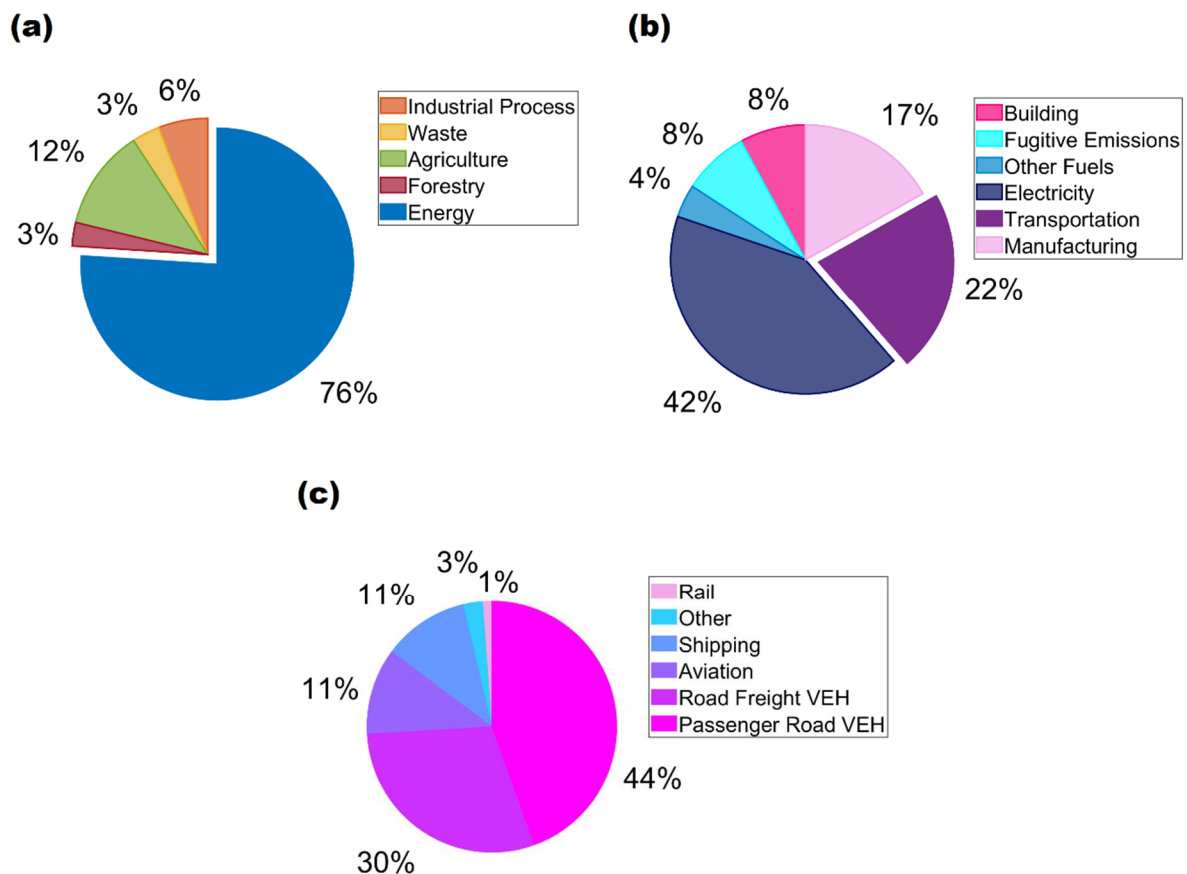


Figure 1.2. Global Greenhouse Gases (GHG) emissions percentages in all sectors (a), energy sector only (b) and transportation sector (c). Data for (a) and (b) were collected by the World Resources Institute (WRI), while data in (c) were reported by the International Energy Agency (IEA).^{3,4}

The Climate Data Explorer from the World Resources Institute (WRI) is a new online data platform that is very useful to have insights on national and global progress of climate change. Data gathered by the Climate Analysis Indicators Tools (CAIT) about the global GHG emissions in 2018 are represented in Figure 1.2a. The 76% of GHG emissions at a world scale are coming from energy and this number is even higher (96%) when looking at the CO₂ only, meaning the main driver of climate change.³

Figure 1.2b represents the distribution of global GHG emissions in the energy sector. Since the amount of emitted CO₂ corresponds to almost the totality of the energy GHG emissions, these numbers are very similar to those recorded for CO₂ only ($\pm 1\%$). Transportation (aviation, shipping or road transports) is responsible for the 22% of the GHG emissions of the energy sector as also pointed out in the Paris Declaration on Electro-Mobility and Climate Change written during the 21st Conference of Parties (COP21) of 2015 and this number is expected to rise by 20% in 2015-2030 and by 50% by 2050 unless major actions are endeavoured to limit CO₂ emissions.^{3,5} It is worth noticing how the road transportation was responsible for 77% of CO₂ emissions in 2018 (data from the International Energy Agency in Figure 1.2), explaining the need for the development of electric vehicles which will be the focus of next sections.⁶

1.2. Governments actions to face climate change

In 2015 —meaning 7 years ago— climate change was already an important matter, so important that for the first time, 195 countries signed a binding agreement at the Paris Climate Change Conference, specifying goals and making commitments for immediate actions to take for a transition towards low-carbon economy. More specifically, in the so-called Paris Agreement, a 5 year-cycle of climate actions was announced to limit global warming to 1.5°C compared to pre-industrial levels. Among the different discussion topics proposed during the conference, such as forests, agriculture, building and others, a collective call to action on electro-mobility was presented.⁵ In this context, the United Nations agreed on the necessity for at least 20% of all the road vehicles to be electric by 2030.

Despite that, the five-year period 2015-2019 following the Paris Agreement saw an acceleration in global warming, with temperatures exceeding of 0.2°C the previous five-year period, as stated in the WMO Global Change report, meaning that the world was set for a global temperature rise of more than 1.5°C. A continued increase in carbon dioxide emissions and other GHGs was recorded during this period, together with a further acidification and warming of oceans —2018 had the warmest ocean

temperature ever recorded. Moreover, only 30% of the countries was aiming to obtain net zero targets — meaning same amount of carbon emission and removal — in 2019.^{1,2}

For these reasons, at the 26th United Nations Conference on Climate Change in Glasgow (COP26) the parties agreed through the Glasgow Climate Pact on the need for an accelerate action on climate change, to keep the 1.5°C target alive and finalise the elements of the Paris Agreement. After the COP26, 90% of the world set net zero targets and imposed the totality of all new vehicles to be zero-emissions by 2050.^{7,8}

This new wave of commitments brought new policies to promote electric vehicles deployment all over the world. Just before signing the Glasgow Pact, the European Union was launching its “Fit for 55%” measures that aim to support Europe’s climate policy framework and to put the EU on track for a 55% reduction in carbon emissions by 2030, and net-zero emissions by 2050.⁹ This ambition necessitates improvements in different fields: from the housing sector, where the goal is to achieve the 32% of renewable energy, to the forestry and land-use for which EU puts an effort in planting a considerable number of trees, to again a system of taxation on CO₂ emissions and company pollutions. Furthermore, EU stated that a push to green mobility is essential in accomplishing the zero-emission target. In this context, 1 million charging points have to be installed around Europe by 2025 and 3 millions by 2030, a percentage of sustainable fuel supply is meant to be used for aircrafts and zero petrol and diesel vehicles should be driven in 2035.

It is worth noticing however, that electricity production accounts for 42% of global GHG emissions (Figure 1.2b) and since its demand will increase with the expected transition to electric vehicles, it is important to move towards a more sustainable energy mix. While in Europe more than half of the energy production comes from “renewable” sources (among which the highest contributions come from nuclear energy —almost 30%— and hydroenergy —11%), other countries are in fact still struggling to move apart from coal and oil. In China, e.g., the 70% of the produced

energy comes from coal, and this number is still rising due to the increasing energy demand.

Even if the governments implication in the climate framework is growing in the last few years, the zero net emissions target everybody is always talking about is still far, and major actions still have to be taken in order to slow down climate change.

1.2.1. Focus on France

Following the world's commitments in terms of sustainable mobility, the Loi des Mobilités (LOM) was approved in late 2019 in France as a support to the already existing Loi de la Transition Ecologique pour la Croissance Verte (LTECV) of 2015. The principal goal of these laws is to improve the everyday mobility, by increasing investments in infrastructures, proposing alternative solutions such as car-sharing or bicycles and adapting transports regulation.¹⁰ Moreover, through these tools, the French government decided to have a stronger engagement in the development of the electric mobility with the intent of stopping the sales of fossil fuel vehicles by 2040.

The accomplishment of a lower environmental impact of transports —representing the 38% of CO₂ emissions in 2018 in France— was pursued by focusing on the following points:

- Lowering of the emissions of vehicles;
- Increasing of the installation of recharging points;
- Development of biogas fuels;
- Encouragement of the use of bicycles;
- Reliance on industries by imposing low emissions vehicles in the renewal of their fleet.

However, in order to promote the fast diffusion of electric vehicles, some drawbacks have to be overcome; among them, it is important to mention the cost. The price of an electric powered Clio by Renault was in fact 13000 € higher than a diesel and 16500 € higher than a petrol one in 2018. For this reason, the French government, in addition

to the previously mentioned measures, endorsed the establishment of a taxes and bonus system in order to promote the purchase of electric vehicles.¹⁰

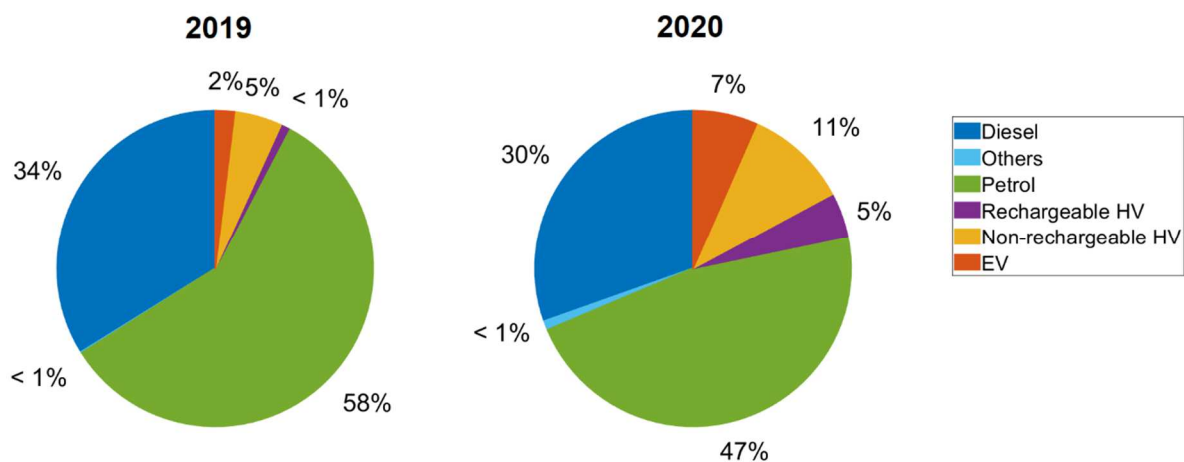


Figure 1.3 Percentages of registered vehicles in France in 2019 and 2020 as a function of the supply mode. Data was gathered by the Service des Données et Études Statistiques (SDES).¹¹

The first fruits of these new governmental actions are already visible in 2020, as shown in the data, collected by SDES (Service des Données et Études Statistiques) and published by the French Ecologic Transition Ministry, represented in Figure 1.3.¹¹ The percentage of registered petrol and diesel cars decreased by almost 11% and 4% respectively in 2020 compared to 2019. Simultaneously, the amount of sold electric and hybrid vehicles —rechargeable and not— more than doubled over the same period.

The recent measures implemented by the French government in terms of electric mobility during the last few years seem thence to have found some audience among citizens, even if a large number of fossil-fuel powered cars are still circulating.

1.3. Implication of EV manufacturers

The demand for electric and hybrid vehicles all over the world for the last few years implies the need for a huge effort in their production. As a consequence, EV manufacturers announced the construction of several new gigafactories—factories producing batteries at a very large scale— in order to meet the necessity of the huge number of batteries needed for the electrification of new vehicles. Elon Musk, CEO and product architect of Tesla, Inc., declared during the Tesla Battery Day 2020 that

the production of 10 TWh/year for 5 years is required to transition the global fleet of vehicles to electric. If we consider that there are 1.446 billion cars in the world in 2022 and that an average battery size for cars accounts for 30 kWh, it is easy to calculate that 43 TWh are needed to power the worldwide fleet.

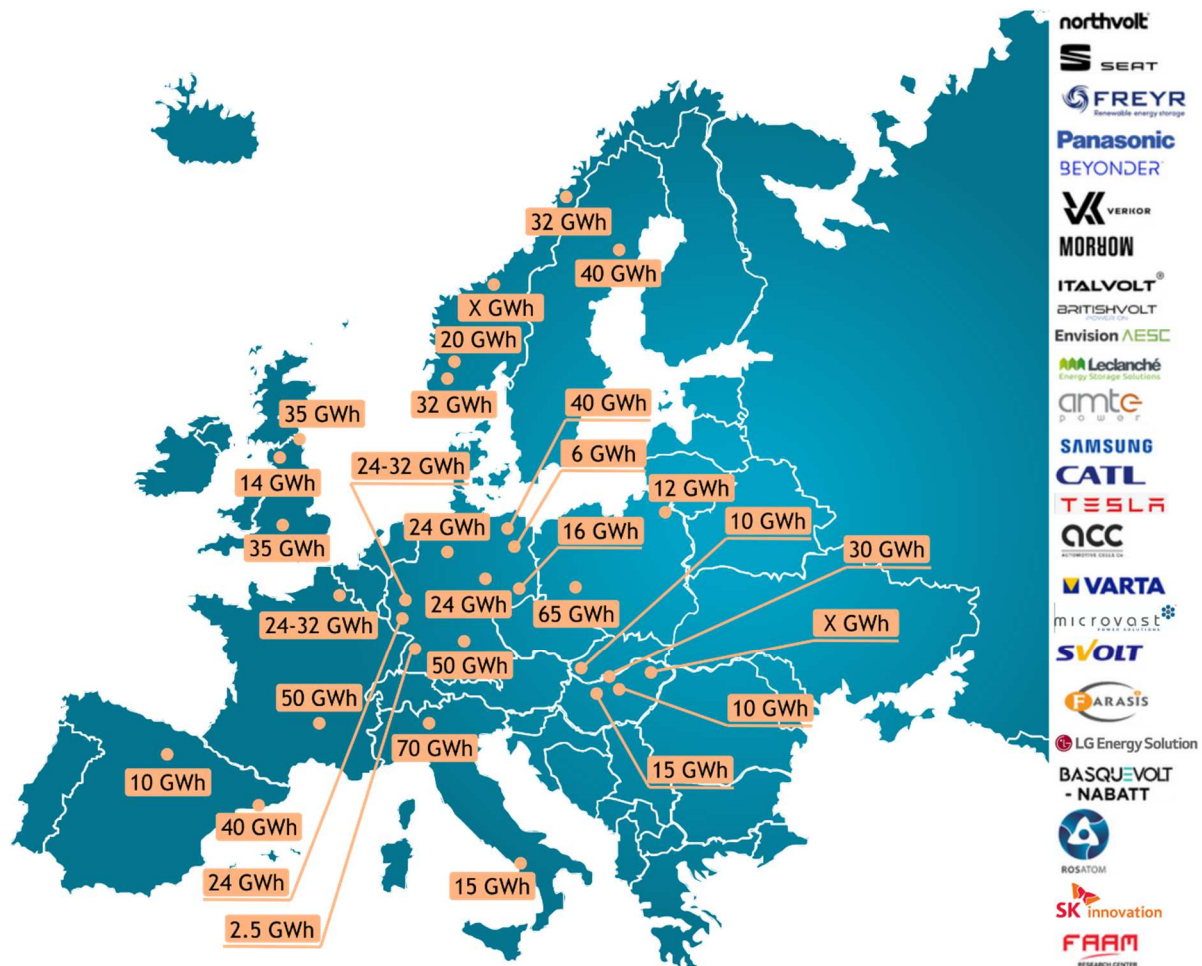


Figure 1.4. Schematic representation of gigafactories in Europe. Predicted annual productions at full regime are reported.

Since one gigafactory production is roughly 0.015 TW/y at the moment, the construction of new ones is essential to cover the automobile manufacturers needs in terms of batteries for EV. Together with large OEMs such as Tesla, Mercedes-Benz and Volkswagen, several other companies (Northvolt, Parasonic, Samsung and others) announced the construction of new gigafactories in Europe in the near future (Figure 1.4), for a total production predicted to be of 600 GWh/y at full regime.

Moreover, in order to accelerate the transition to sustainable energy, together with a larger production, it is EV fabricators' responsibility to produce more affordable vehicles accessible to all. As a matter of fact, the cost per kWh is not decreasing fast enough to allow the worldwide diffusion of long and middle range electric vehicles, which are still considered as a luxury product nowadays. New cheaper processes, materials and designs have to be probed for batteries conception, though maintaining quite high performances. Research at all levels is thence still essential to improve battery performance, lower costs and allow the crucial transition of the world to renewable and sustainable energy.

The necessity of a huge batteries production often results in collaborations with companies that are leaders in clean mobility materials, as in the case of the partnership between Volkswagen and Umicore announced in December 2021. The technology, innovation and industrial knowhow coming from years of research and development provided by materials producers, in fact, provide a strong framework for this sort of joint ventures.

1.4. Battery 2030+: a European joint effort

Funded by the European Commission in the framework of the European energy and climate policies over the last few years, Battery 2030+ aims to provide scientific and technological basis for the batteries of the future by gathering the contributions of governments, industrials and research institutes.

Six research and innovations projects coordinated by Denmark, Belgium, Finland, France, Spain and Germany, together with one coordination and support action directed by Uppsala University in Sweden, constitute the Battery 2030+ initiative. From the study of interfaces, to the batteries recycling passing through the integration of smart functionalities, Battery 2030+ is a large-scale and long-term research initiative that intends to allow European industries to produce competitive high-performance and climate-neutral products. Unlike the SET-Plan⁷ of 2006, which focuses mainly on

the transport sector, the Battery 2030+ initiative proposes actions for a wider range of applications.¹²

The importance of projects like Battery 2030+ is growing together with the need towards a more sustainable future. In fact, some drawbacks still affect Li-ion batteries and research at all levels is the most powerful tool to overcome them and to provide a safe, green and performant alternative to the technologies we have been using for too long time now and that are contributing to harm the planet we are living on.

1.5. Drawbacks of Li-ion batteries

Among the different energy storage technologies, Li-ion batteries (LIBs) represent the best choice for the electrification of vehicles, as it will be explained later on in this chapter. However, the increasing demand in this type of devices recently arose concerns about material exhaustion, in addition to environmental, social and governance issues already noted. As a matter of fact, LIBs, and in particular cathode materials, contain a high amount of critical metals such as Li, Co and Ni. Despite the difficulty in estimating lithium demand and supply due to the large number of parameters to be taken into account, Murdock et al. affirm in their review about the sustainability of cathode materials for LIBs that all recent works agree that lithium supply will be sufficient to meet the increasing demand in the short or mid-term only.¹³

Together with the availability of resources, another major issue is represented by the supply risk. When looking at Europe, for instance, almost the totality of the lithium for European batteries is imported from abroad. In fact, more than a half of the worldwide lithium is extracted in Australia (55%), followed by Chile (23%), China (10%) and Argentina (8%). With the global commercial block due to the Covid19 pandemic, the need of more secure “in house” supply became even more undeniable. Together with supply security, this would lead to a simpler logistic, lower cost and transport emissions.

On the other hand, the reinforcement of supply chains with a more diverse stream of lithium will not reduce the risks related to mining; quite the opposite, mining areas will increase together with social, ecological and environmental concerns associated with it. Actually, the opening of new mines is often linked with forced relocation of locals living in those territories who cannot return after the closing of the mine because of the lower land quality, soil erosion and land instability due to extensive mining. Mining areas already cover about 50 million km² of the terrestrial crust, 82% of which is for the extraction of critical materials for clean energy production; 14% of protected areas is within these territories and this number, together with the threats to biodiversity associated with it, will increase by increasing mining.¹³

Moreover, it should be kept in mind that the cost of lithium is fluctuating significantly, as well as that of cobalt (cf. Section 1.5.1) as the demand for lithium-ion batteries is growing together with the identification of new lithium resources owing to continuing exploration. As a matter of fact, the price of battery-grade lithium carbonate increased from 8000 \$/ton in 2020 to 17000 \$/ton in 2021 —meaning + 112%—, after two years with prices going down overall. It has to be noticed that the known world reserves also increased over the same period from 14 million tons to 22 million tons of Li₂CO₃, together with the amount of Li used for batteries (56% in 2018 vs 74% in 2021).¹⁴ If we consider that about 8 kg of pure Li are needed for one EV battery, one can easily calculate that the world reserves presently known are sufficient to convert approximately 520 million cars to electric, meaning half of the present amount of vehicles in the world.

In order to overcome the limited availability of lithium on Earth and problems related to its extraction, recent researches have focused on *post-lithium* technologies, such as Na-ion, K-ion and Mg-ion batteries. Indeed, the ionic radius and the redox potential of these ions are not very different from those of lithium, as summarised in Table 1.1. For this reason, such ions can be inserted/deinserted reversibly in some materials with a mechanism very similar (but not always identical) to that of LIBs. At the same time,

their abundance and their easier extraction make them a viable alternative to lithium-based systems. Nevertheless, progresses on these topics are still too slow and LIBs remain the best alternative in terms of electrochemical performance for high energy density and portable applications.

Table 1.1. Properties of principal ions for Li-ion batteries.

M^{z+}	E^0 (V <i>vs.</i> SHE)	g/mol e^-	Ionic radius (Å)
Li ⁺	−3.04	6.94	0.68
Na ⁺	−2.71	22.99	1.02
K ⁺	−2.93	39.10	2.27
Mg ²⁺	−2.37	12.15	0.74

The present consumption and production model appears thence to be not bearable in the long-term. One possible solution could be LIBs recycling that is, on the other hand, still struggling to overcome a certain amount of problems as well explained in a recent review by Neumann et al.¹⁵ Despite efforts already made by different groups, in fact, the variety of LIBs materials and technologies still represents a major challenge in the design of a universal and flexible recycling process. Moreover, cathode materials only are currently subject to recycling, making the idea of a completely circular economy not achievable. In addition, elevated cost and GHG production involved in recycling operations make this process not particularly interesting for industrial application yet. Nevertheless, research in this domain is significantly increasing as it is one of the major challenges of the last few years and a suitable recycling process is likely to be found in the near future.¹⁵

1.5.1. Social and governance problems of Co extraction

Cobalt is the metal currently used in LIBs that poses the biggest runout concern and the huge demand related to its use in portable devices and vehicles applications (see Part 3) makes its price incredibly high (46k U.S. \$ per ton in late 2021, meaning +46%

compared to 2020) and its market often volatile, a major issue for materials manufacturers.¹⁴

Co extraction is geographically concentrated in the Democratic Republic of Congo (DRC), a country affected by profound political instability and it was recently related to a large number of social issues, such as gender discrimination, child labour and public health consequences.

The exploitation of women, often performing the most exhausting and yet poorly paid jobs, and children –23% of which is exploited and physically, physiologically and sexually abused in Co mines— within DRC has been known for a while now and has arisen increasing consciousness towards responsible sourcing.¹³ Umicore, for example, was the first company in the world to introduce a Sustainable Procurement Framework in 2004. This document aims to minimize risks of human rights abuses and unethical mining and business practices. Umicore cobalt's supply is also exempted from any artisanal or small-scale mining source, which represent a significant part of Co extracted in DRC.¹⁶ However, the ban of such sources could cause unintended harmful consequences, since Co mining often represents the only income for a big part of the local population and the only way to escape poverty, mining being often more remunerative than agriculture. On the other hand, regulations and controls like Umicore's are essential to assure ethical and low health impact Co sourcing. Long-lasting term health issues due to an improper waste disposal were in fact found to affect populations occupying areas near Co mines. High cobalt levels in blood and urines causing potential heart, lung and thyroid complications were recorded as well as the presence of heavy metals in water systems and food.¹³

Thanks to the increasing consciousness about Co extraction drawbacks, the research in the battery field is putting more and more effort to obtain new performant materials with low Co content, as it will be explained in the third part of this Chapter.

Part 2. Li-ion batteries

The commercialisation of lithium-ion batteries (LIBs) started at the beginning of the 90^{ies} and has been growing since then at an increasing pace.

LIBs belong to the family of accumulators, i.e., rechargeable energy storage devices able to reversibly convert chemical energy into electric one, and thus able to store electric energy provided by an external source and to give it back on demand. More specifically, such devices, also called secondary batteries, are based on a reversible chemical reaction, which occurs spontaneously during the discharge, and which can be reversed during the charge of the battery by applying a current in the opposite direction. By contrast, the so-called primary batteries cannot be recharged and their useful life ends once the reactants are consumed during the discharge process.

LIBs were born as a solution to a safety problem observed in the preceding Li-metal batteries. In fact, in Li-metal batteries, lithium was used directly as the negative electrode material, and during the charge process, its electrodeposition occurred with the growth of metal dendrites which eventually crossed over the separator and contacted with the positive electrode, leading to shortcuts and often explosion hazards.¹⁷ To avoid this security issue, lithium metal is replaced by a different negative electrode material able to reversibly insert/deinsert lithium. In this material lithium ions are exploited as positive charges in the so called rocking chair system described by Goodenough and Whittingham in 1981, on which LIBs are based.¹⁸ In LIBs, in fact, during the discharge lithium cations are simultaneously deinserted from the negative electrode and inserted in the positive one. Therefore, while the average concentration of lithium in the electrolyte remains constant during the whole process, lithium ions constantly flow from the negative to the positive electrode, accompanied by the flow of electrons in an external circuit needed for the oxidation and the reduction of the electrode materials. During charge, the flow of electrons and lithium ions is reversed (Figure 1.5).

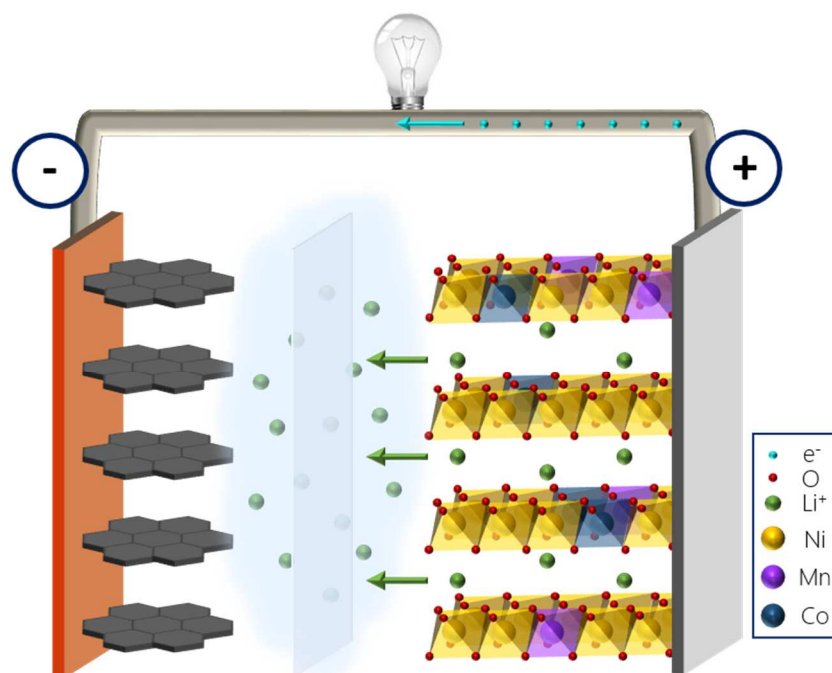


Figure 1.5. Schematic representation of a Li-ion battery having graphene at the negative electrode and NMC811 at the positive one.

Lithium-based batteries have better storage ability than other battery technologies thanks to the low self-discharge rate and the absence of the so-called memory effect, which affects other types of batteries. In nickel-cadmium batteries, for example, a shallow discharge makes the battery "remember" the final discharge conditions, and a voltage drop occurs once the discharge capacity reaches the reminded value during following cycles.

In terms of applications, these characteristics make LIBs the best choice for application in portable devices as well as in electric vehicles.

Even if lithium metal is highly reactive, in fact, it is widely used in batteries because it is the most electro-positive (-3.04 V vs SHE) and because of its lightness; these characteristics make LIBs the best technology in terms of both volumetric and gravimetric energy density.

The energy density represents the amount of electric energy deliverable by a battery per unit of volume or weight and it is expressed in $\text{W}\cdot\text{h}\cdot\text{L}^{-1}$ or $\text{W}\cdot\text{h}\cdot\text{kg}^{-1}$:

$$E = \frac{C \cdot V}{m} \quad (1.1)$$

where V is the potential in Volt, m is the mass in kg and C is the nominal capacity in mA·h, i.e., the amount of electricity which the battery is able to deliver in fixed discharge conditions of time and current:

$$C = \int_0^t i(t) dt = i \cdot t \quad (1.2)$$

Similarly, the specific theoretical capacity can be defined as the amount of charge delivered per unit weight of active electrode material, and it is thus expressed in $A \cdot h \cdot g^{-1}$.

When testing a battery, a current is usually imposed as far as the voltage of the battery stays in a given potential window, as well as a cycling rate (or C-rate), meaning the rate of insertion of lithium ions in the active material. A rate of C/n corresponds to the time (n in hours) needed to deliver the full capacity of the battery. The use of higher C-rates generally implies a lower amount of secondary unwanted reactions since a faster cycle allows to spend less time at critical potentials. As a matter of fact, a stability window of potential exists for both the electrode materials and the electrolyte and it corresponds to the difference between the HOMO (Highest Occupied Molecular Orbital) and LUMO (Lowest Occupied Molecular Orbital) orbitals of the considered compound. The stability windows of the different components of a LIB are schematised in Figure 1.6. In particular, when the electrochemical potential of the positive material (μ_+) is higher than the HOMO of the electrolyte, the latter is oxidised and a passivation layer consisting of electrolyte's degradation products is formed at the surface of the positive electrode (Cathode Electrolyte Interphase or CEI). These conditions usually exist at the end of the charge, when working potentials are particularly elevated. Similarly, a SEI (Solid Electrolyte Interphase) is formed at low potentials at the negative electrode surface. If SEI is well defined —and actually the main reason why a LIB works—, the CEI concept is not well scientifically established.

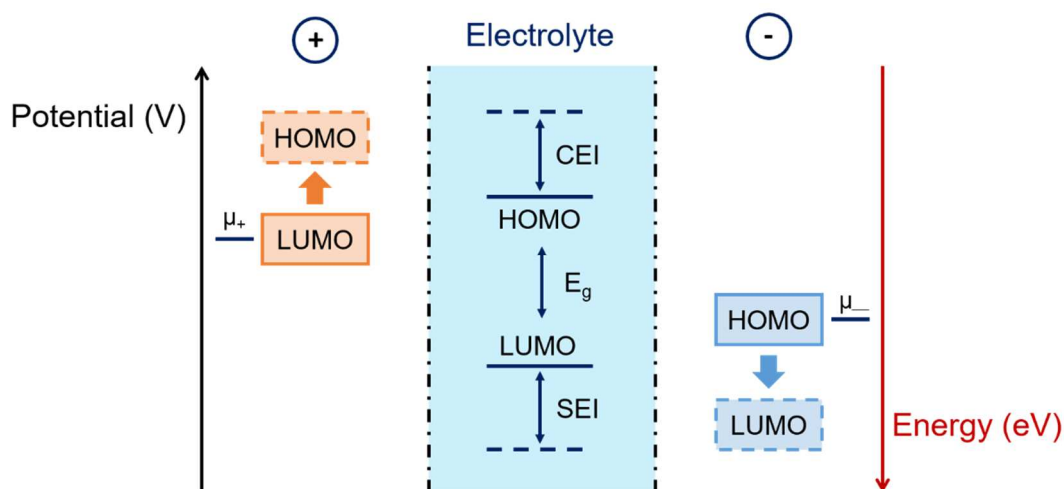


Figure 1.6. Schematic representation of the energy and potential levels of all the components of a Li-ion battery.

It is worth mentioning here that a specific potential can be imposed when testing a battery; the current passing into the circuit will thence be dependent on the electrons needed to reach the thermodynamic equilibrium at the considered material surface. In this way, it is possible to force the degradation reactions occurring at too high (for positive electrode materials) or too low (for negative electrode materials) potentials. For NMC materials, for example, high potentials (4.5-4.8 V vs Li^+/Li) are often applied to analyse gasses produced when the material is outside its stability window (cf. Section 3.4).

Part 3. Positive electrode materials

Since Li^+ ions are shuttling alternatively between the positive and the negative electrode, both active electrode materials (AM) in LIBs must be able to reversibly host lithium cations. A large variety of solids has such properties and has been tested for this application in the last three decades, and many research groups are still investigating new compounds to find out the best compromise between all the properties (capacity, working potential, cycle life, security, etc.).

Negative electrode materials can be divided into three different groups depending on the reaction mechanism with Li^+ : conversion, alloy and insertion type materials. Even if both conversion- and alloy-type materials can reach very high nominal capacities, their main drawback is the really high volume expansion (up to 200% for alloy-type materials) resulting from the strong structural modifications occurring during the reaction with lithium ions.¹⁷ For this reason, intercalation-type materials e.g. the graphite or $\text{Li}_4\text{Ti}_5\text{O}_{12}$ are now dominating the LIBs market; since Li^+ ions are inserted inside the electrode lattice without modifying it, in fact, the volume expansion is limited.

While negative electrode materials can react electrochemically with Li^+ via different reaction mechanisms almost all positive electrode materials work through the insertion mechanism.

During the discharge, the positive electrode (often inaccurately called “cathode”, definition that works only during the discharge process) is reduced and lithium ions can be inserted inside its lattice. A distinction can be made between low voltage materials such as, e.g., vanadium oxides and titanium disulfide, with working potentials in the 2-3.2 V vs Li^+/Li range, and the nowadays more common high voltage materials. High voltage cathode materials can be classified in three different groups depending on whether the structure of the solids allows lithium diffusion via 3D, 2D or 1D channel systems:

- Layered lithium-transition metal oxides (e.g., LiCoO_2);
- Lithium metal oxides with a spinel structure (e.g., V_2O_5);
- Lithiated polyanionic materials (e.g., LiFePO_4).

Since the main topic of this manuscript is NMC materials, belonging to the first category, the principal properties of the most relevant layered lithium-transition metal oxides only will be the main focus of next sections of this chapter.

3.1. LiCoO_2

Historically, the first cathode material used in LIBs was LiCoO_2 belonging to the family of the layered lithium-transition metal oxides (with general formula $\text{Li}_{(1-x)}\text{MO}_2$, with $\text{M}=\text{Co}, \text{Ni}$ etc.). Lithium cobalt oxide (LCO) has a rock salt fcc structure with alternate ordered (111) layers of Li^+ and Co^{3+} cations. The diffusion of Li^+ in LCO occurs with a 2D process in the Li-containing planes. During the charge process, Co^{3+} is oxidized to Co^{4+} while Li^+ ions are extracted from the structure. The theoretical capacity of LCO is 274 mAh/g, corresponding to the extraction of all the lithium; however, since this material undergoes irreversible structural changes if more than 0.5 Li^+ are extracted, its practical capacity decreases to 137 mAh/g. In fact, the delithiated form of LCO forming beyond 4.45 V vs Li^+/Li is not able to insert Li^+ anymore and becomes thermally instable.^{19,20}

Despite the environmental and social problems related to Co extraction (cf. 1.5.1), LCO is still the most largely used cathode material in nowadays LIBs for portable applications thanks to its outstanding performances. Actually, LCO is a great example to show that we need continuous material development even though LCO is more than 40years old.

3.2. LiMnO_2

Belonging to the same family, the cheapest and most environmentally benign alternative to cobalt layered oxide is represented by LiMnO_2 (LMO). Despite its high theoretical capacity (285 mAh/g), this material appears to be thermodynamically

instable at high temperature, inducing the need of exploring alternative synthesis methods such as ion exchange or hydrothermal synthesis.¹⁹

As a consequence to its instability, this material tends to convert to LiMn_2O_4 both upon overheating and long-time cycling. Actually, the spinel LiMn_2O_4 itself has been considered as a potential cathode material, before being ruled out due to its capacity fade principally caused by Mn^{2+} dissolution in the electrolyte via the disproportionation of Mn^{3+} ($2 \text{Mn}^{3+} \rightarrow \text{Mn}^{4+} + \text{Mn}^{2+}$).²¹ Substituting part of the Mn with Ni, it was possible to obtain the so-called “high voltage spinel”, able to cycle up to 4.7 V vs Li^+/Li against the 4.1 V vs Li^+/Li upper cut-off voltage of LiMn_2O_4 .

Similarly, partially Ni-substituted derivatives of LiMnO_2 such as the layered $\text{LiNi}_{0.5}\text{Mn}_{0.5}\text{O}_2$ were also widely studied by many groups in order to overcome problems due to the structural instability of LMO during cycling.²²⁻²⁶

3.3. LiNiO₂

Considered as a cathode material for LiBs in the 80^{ies}, LiNiO_2 (LNO) has recently raised new interest since it allows overcoming problems due to Co extraction while maintaining a relatively high theoretical capacity ($\approx 275 \text{ mAh/g}$). Actually, you can notice that all the transition metals layered oxides are characterised by similar theoretical capacities. The main interest of LNO is therefore the higher voltage that can be attained with respect to LCO, allowing a better practical capacity.

However, stoichiometric LNO is particularly difficult to synthesise due to the similar ionic radius of Ni^{2+} and Li^+ (0.76 Å and 0.69 Å respectively) resulting in high cation mixing. Ni^{2+} ions tend in fact to migrate in Li^+ sites impeding their diffusion both during synthesis —leading to non-stoichiometric LNO— and cycling —promoting the transformation to a cubic electrochemically inactive phase at high voltage.^{27,28}

Along the review about Ni-rich NMC reported in the next Section, it will be interesting to notice how the principal drawbacks and advantages of the three materials just presented are often reflected in the behaviour of NMC materials as well.

3.4. NMC

Most positive electrode materials currently produced by the industry belong to the NMC family, described as layered oxides with general formula $\text{Li}(\text{Ni}_x\text{Mn}_y\text{Co}_{1-x-y})\text{O}_2$ with properties that depend on the relative amount of the different transition metals.²⁹

In particular, in order to achieve a higher capacity and thence higher energy density, the research has been heading towards high Ni-content NMCs for some years now.^{29,32} Moreover, this approach allows lowering the Co content, reducing the cost in the material production, its toxicity and the humanitarian issues related to Co mining already mentioned in Section 1.5.1. Nevertheless, by increasing the Ni content, the material thermodynamic instability increases as well as the gas evolution upon electrochemical cycling, phenomenon of which the comprehension becomes an essential safety challenge at the industrial level (cf. Section 3.4.4).³³

Considering the extremely wide literature about NMCs, we decided to focus particularly on NMC811 properties in next sections. Different compositions will only be mentioned here as a comparison to explain and comment some behaviours of the Ni-rich phase.

Actually, a large number of studies were conducted on Ni-rich NMCs too in order to understand the gassing and instability issues during cycling and to elucidate both their origins and consequences. Different gases in various amounts are released during the electrochemical cycling depending on the battery state of charge.³³ As already mentioned, the SEI formation in NMC-graphite full-cells at low potential, often resulting in the release of H_2 , C_2H_4 and CO . Moreover, CO_2 , CO and O_2 , forming at the interface between active material and electrolyte at the end of the first charge, were demonstrated to be released from the cathode material. Among these gases, the quantity of released oxygen was proposed to be dependent on the material composition. In particular, theoretical calculations showed a decrease in the Ni—O energy bonding upon increase of the Ni oxidation state.³⁴ The oxygen release mechanism is thus logically exacerbated in the richest Ni-rich NMC due to the overall

increase of Ni oxidation state with Ni concentration, in order to balance the total charge.

In addition, both high voltage reactions with the electrolyte and the degradation of surface impurities like Li_2CO_3 were proposed by several groups as a possible reason for the release of CO and CO_2 .³⁵⁻³⁷

As a consequence, it is clear that the nature of the active material surface, which often depends on synthesis and storage conditions, leads to different reactivities towards the electrolyte. Since it is the seed for later evolution in cycling, the pristine surface of the NMC material is thus of utmost importance. However, despite the large number of publications on Ni-rich NMCs, only a few studies precisely describing the pristine material can be found in the literature.^{38,39}

It also has to be kept in mind, that the last few years saw the fast development of gradient composition Ni-Rich NMCs, where surface compositions are purposely tailored to differ from that in the bulk, with tremendous positive consequences on the cycling behaviour.⁴⁰ The previous considerations are all the more important now and the actual state of the surface just after synthesis needs thus to be determined precisely.

The aim of this section is to summarize and review the above mentioned characteristics of NMCs to give the reader the tools to place this study among the already existing huge scientific production. After providing some generalities about NMC materials in their different compositions, the cycling and gassing behaviours as well as the effect of storage conditions will be analysed, with particular focus on NMC811. This section will then be concluded by a review about the new technologies being developed in these last years, such as coated and doped materials and NMCs with gradient compositions.

3.4.1. Generalities on NMC materials

The largest part of EV was powered by batteries based on $\text{Li}(\text{Ni}_{1/3}\text{Mn}_{1/3}\text{Co}_{1/3})\text{O}_2$ (NMC111) cathode material in 2012. However, the low energy density provided by

this material together with the demand for always more performant vehicles, pushed the market towards materials with higher specific capacities. Since nickel is the main active redox species (Ni^{2+} to Ni^{4+}) in NMC, by increasing its content, higher discharge capacities can be easily achieved. Moreover, this would allow to lower the total amount of Co and thence limit all the issues related to its extraction and purchase already mentioned in Section 1.5.1. These reasons brought industries to focus on the development of NMCs with a higher Ni content for automotive applications, making this technology widely spread and produced by all the battery manufacturers nowadays. In Figure 1.7, the specific capacity of the first cycle at 0.1 C (20 mA/g) and 25°C as well as the capacity retention after 100 cycles at 0.5 C (100 mA/g) and 55°C of different NMCs synthesised by Noh et al. are reported as function of the Ni content.³¹

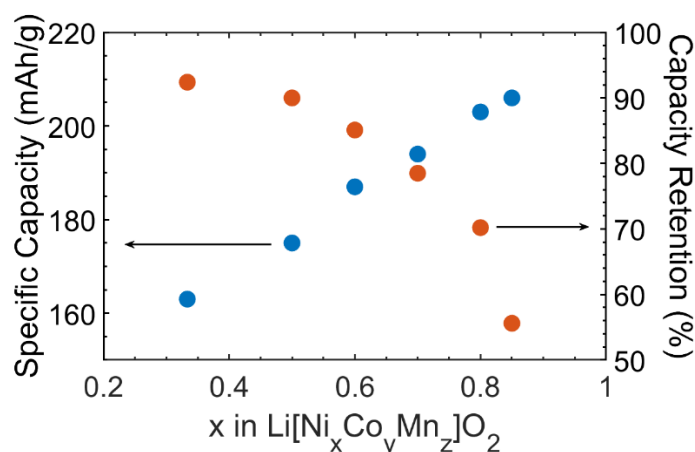


Figure 1.7. Specific capacity (blue points) and capacity retention (red points) for the principal NMC compositions as reported by Noh et al.³¹

It has to be mentioned that in the last few years, Co-free Mn-Ni layered oxides was often taken into account at a laboratory scale as a possible alternative to the Ni-rich composition presently used.^{28,41,42} In particular, Clemente et al. recently obtained Co-free overlithiated layered oxide (LRLO) with a limited nickel content (not reported in Figure 1.7) providing an experimental specific capacity of 230 mAh g⁻¹ at C/10 for almost 200 cycles.⁴²

Other than affecting electrochemical properties, which will be the focus of Section 3.4.2, NMC composition – and in particular Ni content – can have an influence on the morphological and structural characteristics too.

Nickel cobalt manganese oxides usually show spherical secondary particles with an average diameter around 10 μm , as the ones represented in Figure 1.8a. Such a spherical morphology is not reported by Steiner et al. though, showing smaller and irregular secondary particles instead, evidencing the influence of the synthesis method already on the microstructure.⁴³ Each secondary particle is thence composed of an agglomerate of single crystals named primary particles (Figure 1.8b and c) of different sizes depending on the nickel content. As Noh et al. pointed out, in fact, while the morphology of the secondary particles does not depend on the nickel content, the primary particles size can vary between 1.8 μm for low nickel contents and 0.2 μm for nickel-rich compositions.³¹ The importance of these primary particles was presented by Teichert et al. – among others – in their paper about the advantages of single crystal particles in NMC622 electrochemical performance compared to the classical polycrystalline morphology; these beneficial properties were though not found for NMC811.⁴⁴

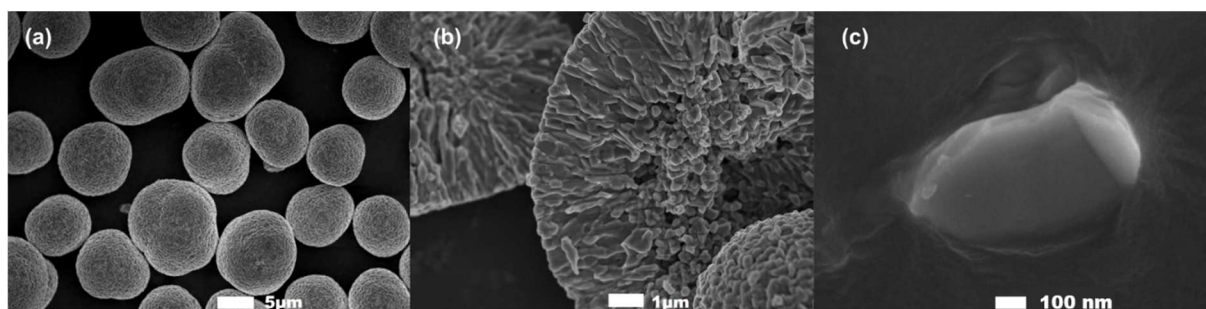


Figure 1.8. SEM image of the hierarchical microstructure of NMC, from micrometre agglomerates (a) composed of crystallites of few tens of nanometres (b) to primary particles (c).

From a structural point of view, NMC materials are organised in a layered structure based on a hexagonal $\alpha\text{-NaFeO}_2$ cell with an R-3m space group. Here, the octahedral sites of a Face Centered Cubic network of oxygen are occupied by lithium and transition metals in an ordered way. Thence if one describes the cubic structure using

a hexagonal cell, it corresponds to the stacking of MO_2 layers built up with edge-sharing MO_6 octahedra in between which Li is located. Thus, the structure can be described as a superposition of Li, M and O layers as shown in Figure 1.9. The c parameter describing the thickness of both the LiO_6 and TMO_6 slabs was found to decrease with increasing Ni content. The TM–O bond length in fact decreases when the Ni is in a higher oxidation state, as for Ni-rich compositions.

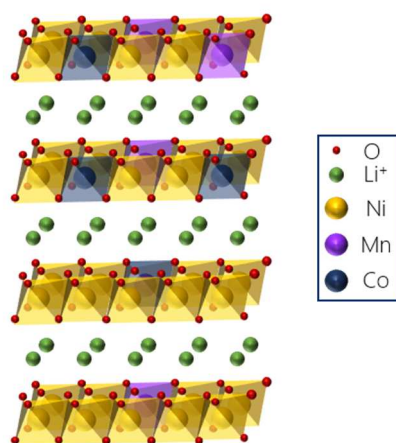


Figure 1.9. Representation of the crystallographic structure of NMC811.

Since nickel and lithium cations have similar ionic radius (0.76 \AA for Li^+ , 0.69 \AA for Ni^{2+} , 0.56 \AA for Ni^{3+} and 0.48 \AA for Ni^{4+}), nickel can however occupy lithium sites in Ni-rich NMC, as Li^+ occupies transition metal layers in Li-rich compositions.^{31,45,46,47} Nickel ions in lithium layers could lead to decreasing discharge capacities and hindrance of Li^+ ionic diffusivity, leading to poor electrochemical performance. Actually, Q. Lin et al. recently proposed the migration of nickel ions into lithium diffusion channels as the cause of the structural transformation to the rock salt structure during cycling –and thus of the material continuous performance decay– that will be discussed in the following Section.⁴⁵ Cation intermixing is a very discussed and controversial topic. While the majority of research groups often stated that a higher Ni concentration in the material results in a higher cation mixing, Lee et al. gave a new insight on this

phenomenon focusing on the study of NMC compositions with a constant Co amount.⁴⁸ Co^{3+} ions are in fact known to strongly stabilize layered structures reducing cation disorder even when in very small quantities. Rietveld refinements of the high-resolution powder diffraction patterns acquired by this group showed that the amount of Ni^{2+} in Li layers decreases from 4.71% in NMC523 to 1.81% in NMC721. This behaviour can be explained by keeping in mind that a higher average Ni oxidation state is needed in Ni-rich materials in order to compensate the charge, 2.4+, 2.67+ and 2.86+ in NMC532, NMC622 and NMC712 according to Lee et al. An increasing Ni content entails thence a lower Ni^{2+} amount – meaning the one with the most similar ionic radius compared to Li^+ – amount, resulting in less Ni ions in the Li interslabs. On the other hand, one should keep in mind that even the richest Ni-rich NMC analysed by this group has a lower Ni content than the typically studied Ni-rich composition (NMC811).

The electronic structure of Ni-rich NMC is even more complicated to be experimentally defined than the crystalline structure since it is challenging to obtain nickel absolute oxidation states due to the lack of clean references for Ni^{3+} and Ni^{4+} with a similar crystal symmetry.⁴⁹ An unambiguous description of the electronic structure is thus not always achievable, especially in the characterisation of the material during and after cycling. Moreover, the exact lithium amount is difficult to evaluate and an excess of lithium often has to be added in the synthesis mix to obtain the wanted composition. Electronic state calculations based on the hypothesis that $\text{Li}/\text{TM} = 1$ could thence induce false results. As just mentioned, nickel is expected to have an oxidation state near Ni^{3+} according to the typical charge compensation in pristine NMC. On the other hand, as evidenced by Steiner et al. the manganese has an oxidation state of Mn^{4+} and the cobalt is Co^{3+} during all the cycles.⁴³ These same conclusions were drawn by Dixit et al. by analysing density of states, bond covalency, magnetic structure and molecular orbital diagrams of different NMC compositions before and during cycling .

In summary, a proper characterisation of NMCs appears quite challenging to be obtained. Even if theoretical calculations can often help to analyse some characteristics, when observing real samples, it is easy to find different –or even contradictory– results.

3.4.2. Cycling behaviour

During the charging process, Li ions are extracted from the layered structure and nickel is oxidised. TM ions can occupy vacant Li sites in order to stabilise the material structure, causing a lattice distortion and the growth of a spinel phase on the particle surface.⁵⁰ Nickel ions, in particular, having an ionic radius similar to that of lithium ions can easily migrate to the lithium layers. This was largely demonstrated by both atomic-resolution STEM-HAADF and electron diffraction experiments and simulations.^{31,45,50} During the subsequent discharge, lithium ions should return to their original positions, but the presence of transition metals prevents them from occupying the previous sites. This could be one possible explanation for the increasing irreversible capacity and the consequent deterioration of the cyclability, typical of nickel-rich NMCs.

Figure 1.10a represents a typical incremental capacity curve as a function of voltage for the first cycle for an industrial NMC811 by Umicore. For an easier interpretation of these data a typical pattern of the differential capacity vs cell voltage for a Li/NMC811 cell that can be found in the literature is reported in Figure 1.10b.⁵¹ Comparing these cycles to those obtained for other NMC composition –with a lower amount of Ni– it is possible to notice that similar cycles are obtained up to 3.9 V vs Li⁺/Li; after that, NMC811 deviates significantly from the other materials behaviour.³³ A first broad small peak, in fact, appears in NMC811 around 4.0 V vs Li⁺/Li, followed by another large narrower anodic peak at 4.2 V vs Li⁺/Li. Actually, these peaks had already been associated to a monoclinic to hexagonal (M→H2) and hexagonal to hexagonal (H2→H3) phase transition respectively by Ohzuku et al. for LiNiO₂.⁵² For this reason,

it is well agreed that this very same interpretation can be used for NMC811 electrochemical cycles too.³³

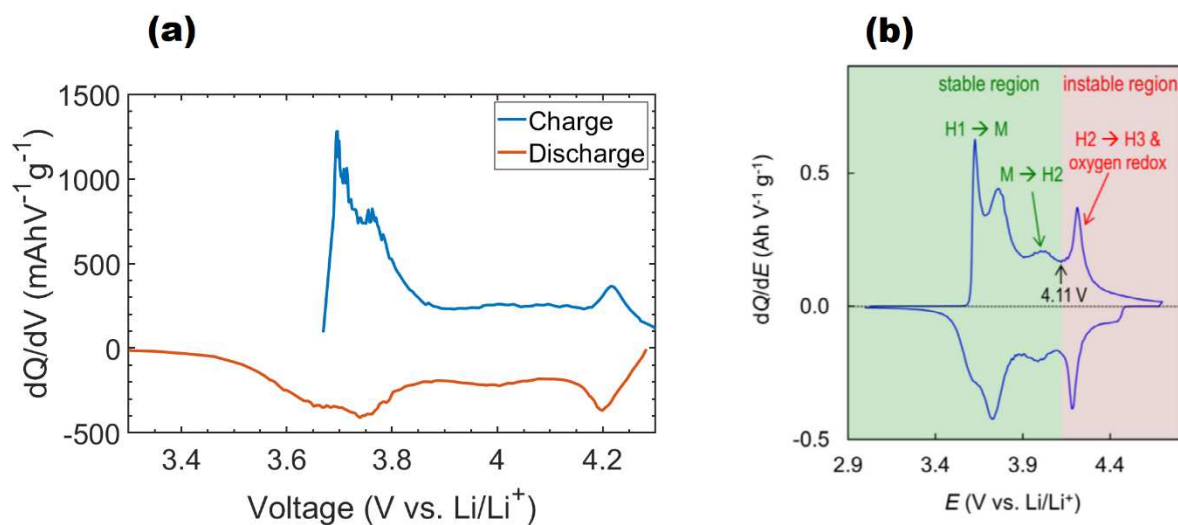


Figure 1.10. Incremental capacity curve as a function of voltage for the first cycle for an industrial NMC811 synthesised by Umicore (a) and for one reported in the literature (b).⁵¹

By decreasing the amount of lithium in the structure, the H2 phase transforms into another hexagonal phase (H3) in a biphasic process. This last structure is characterised by shorter interlayer distances and thus a smaller c parameter than the previous H2.⁵³ In the case of LiNiO₂, this phenomenon was explained as a consequence of the presence of the large amount of Ni⁴⁺ produced during the charge at high potential. This cation having a smaller ionic radius, can give shorter interlayer distances. This shrinkage was not observed though for Li_(1-x)Ni_(1+x)O₂ samples containing a larger amount of nickel compared to the stoichiometric LiNiO₂. In this case, in fact, substitutive nickel in the lithium layer could disturb the layer shrinkage.⁵⁴

In the paper from Jung et al. it appears that peaks similar to those observed for NMC811 at 4.0 and 4.2 V vs Li⁺/Li, can be found at higher potentials (4.1 and 4.6 V vs graphene respectively) in low-nickel formulations as well (NMC111 and NMC622). Since no H2→H3 transitions had never been reported for these materials to the best of our knowledge, the exact origin of these peaks is still not sure. Despite this, Jung et al. reported that a stable cycling was only possible when the cut-off potential

was below the onset of the very last peak at 4.6 V vs graphene and they proposed the H2→H3 transition as the main cause of the electrochemical performance decay due to the significant reduction of the unit cell upon this phase transition.^{31,53}

On the other hand, other authors frequently associated the discharge capacity fade and the increasing polarisation during cycling with a surface phase transition to the electrochemically inactive rock-salt structure.^{43,45,49,55} In particular, Q. Lin et al. proposed a continuous performance degradation due to Ni migration along the lithium ion diffusion channels during the whole cycling, leading to this same phase transition.

Moreover, once Ni ions arrive at the material surface, they can dissolve in the electrolyte resulting in capacity fading and a nickel concentration gradient in the cycled sample.²⁵ A similar behaviour of transition metals was actually observed by F. Lin et al., who demonstrated the existence of an oxidation state gradient along the NMC particles, together with a transition from an R-3m to a Fm-3m structure at the surface. In addition, since they observed this same structural change in the NMC particles that were only exposed to electrolytic solution without applying a potential, they could conclude that electrode-electrolyte interaction too can have an influence on the formation of the rock-salt structure.⁴⁹

Even if the collapse of the c-axes due to the phase transition occurring at high voltage is generally accepted as the principal cause of the low cyclability of Ni-rich NMC, Lee et al. dissociated the two phenomena. As a matter of fact, they demonstrated that the LiO₆ interslab thickness — the one responsible for Li⁺ movement — is even larger in the fully delithiated state than in the beginning of the charge. The c-axes collapse was thence associated with a shorter TMO₆ interslab thickness only, not impacting the Li⁺ diffusion channels. This could be explained by considering that high-valence Ni ions — as the ones present in the charged material — form shorter bonds with the oxygen (Figure 1.11). Similarly, the calculation results of Dixit et al. showed an increasing covalency (and so lower ionicity) in the Ni—O bond for high Ni oxidation states.

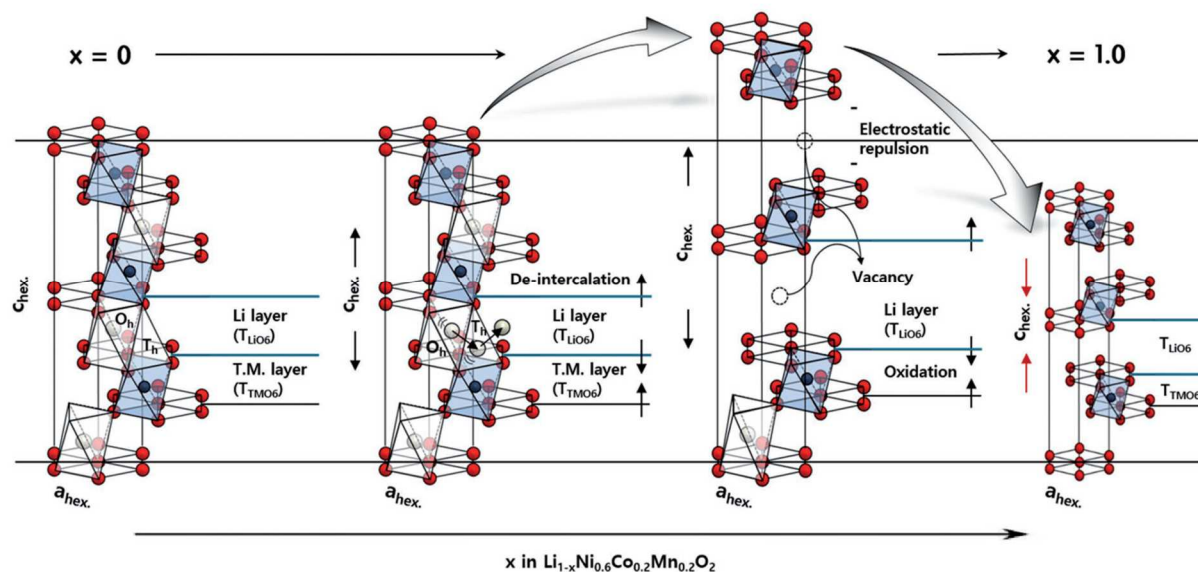


Figure 1.11. Structural transformations of an NMC622 upon electrochemical cycling. Figure adapted from the literature.⁴⁸

It is thus clear that a structure change takes place on Ni-rich NMC surface during cycling deteriorating the cell performance, even if the exact origin of this transition is not well defined yet. Moreover, the oxidation state of transition metals as well as their role in the structural stability of the material have not been completely explained.

3.4.2.1. After cycling characterisation

The just mentioned structural changes during cycling were largely demonstrated to occur thanks to STEM-HAADF and electron diffraction experiments on cycled materials (Figure 1.12a).

Moreover, the behaviour of the crystal structure changes can also be denoted by the oxidation state of the transition metals in the charged material, particularly the nickel and the oxygen ones: as nickel moves from a layered structure into a rock-salt structure it is reduced to the Ni^{2+} oxidation state. The element-specific nature of soft XAS, along with its varying probing depth by tuning the detection mode was indeed used by Steiner et al. to probe electronic structure of the material at the surface and in the bulk.⁴³ In particular, the integrated area of the pre-edge TM 3d-O 2p peak is higher in the bulk (analysed in the Fluorescence yield mode) than in the surface (analysed in the

Total Electron Yield mode). Similarly, the ratio of the L₂/L₃ nickel peaks is consistently smaller in TEY than in FY for all the states of charge.

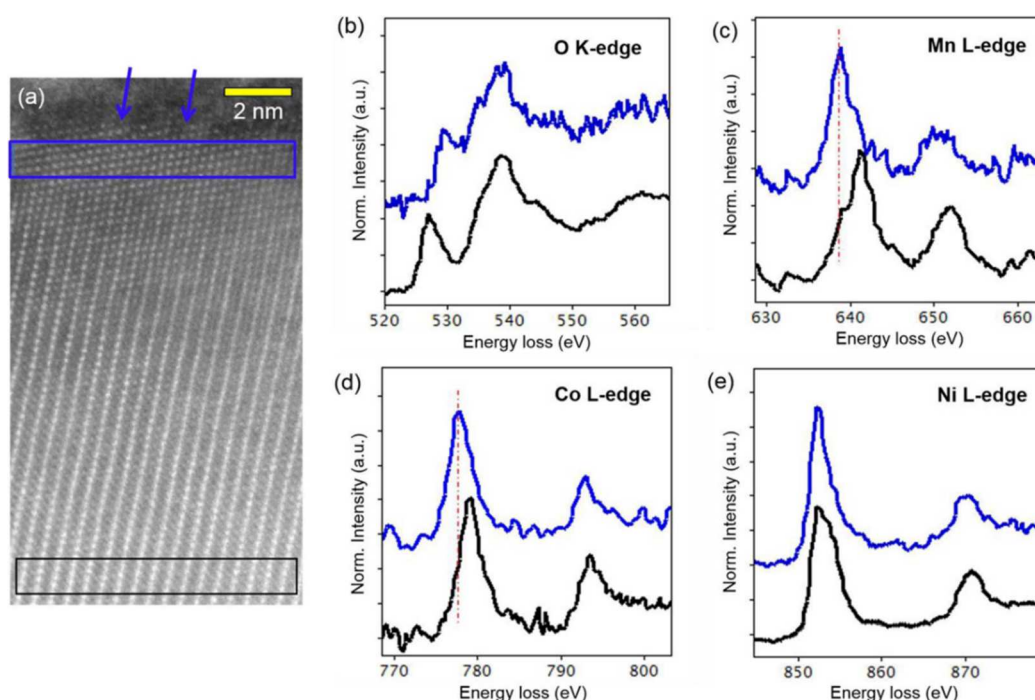


Figure 1.12. STEM-HAADF image of an NMC811 particle after 83 cycles with upper cut-off potential of 4.3 V (a) and corresponding EEL Spectra at O K-edge, Mn L-edge, Co L-edge and Ni L-edge (b, c, d and e).⁵⁶

These observations are consistent with the hypothesis that the surface reconstruction from a layered structure to a mixed rock-salt/spinel structure only occurs at the surface, probably as a result of a reorganisation after the possible dissolution of the transition metals at the surface in the organic electrolyte already mentioned.^{43,49,50,57} Nickel reduction at the surface and thus the larger Ni²⁺ concentration was also confirmed by EELS by several authors. Similarly, it was reported a higher TM 3d–O 2p hybridisation showed by the increasing intensity of the first peak on oxygen K-edge (Figure 1.12b).^{45,49,50,56} On the contrary, J. D. Steiner et al. reported no obvious shift in the EELS L-edges for all three TMs as the probing goes deeper into the bulk from the surface after one cycle.⁴³

From a morphological point of view, it was largely demonstrated that NMC secondary particles present significant intragranular cracks on the surface after long cycling.^{45,57,58}

This is clearly due to the repeated anisotropic contraction and expansion of each primary particle during the phase transitions occurring during the electrochemical cycles.

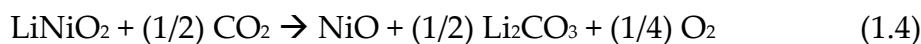
The cracks formation is expected to result in a loss of grain-to-grain connectivity among primary particles and it could open up new penetration paths for the electrolyte to react with fresh NMC surfaces. This was thus largely associated to the decay of the electrochemical performance since the structural degradation of the material to form an impedance-increasing rock-salt layer could be due to the contact with the electrolyte solution.^{43,49,50,57,58} Moreover, the higher concentration of high-valence Ni in Ni-rich compositions would thence bring to a more rapid degradation of the internal exposed surface, since Ni⁴⁺ is known to be more reactive and tends to lead to NiO like phase more easily.

It is also interesting to notice that the group of Yang-Kook Sun and co-workers focused on the impact of different depth of discharge (DOD) in the cracking behaviour of Ni-rich NCA. Their results show how the application of an upper DOD of 60% — meaning cycling in the 3.76-4.3 V vs Li⁺/Li range— has the most detrimental effect giving the poorest capacity retention upon 100 cycles. Without completely discharging the material to 2.7 V vs Li⁺/Li, the anisotropic strain produced by the H2-H3 phase transition is not fully relieved and microcracks persist in the discharged state allowing the electrolyte to penetrate inside the secondary particles. The same high-nickel NCA will thence have higher energy density and capacity retention when cycled in the full discharge range (2.7-4.3 V vs Li⁺/Li), highlighting the importance of a full discharge. In the same way, the best capacity retention is obtained by cycling the material in a lower 60% DOD range: the formation of cracks is reduced —but the energy density is poorer— thanks to the low charge voltage (4.0 V vs Li⁺/Li) and the discharge at 2.7 V vs Li⁺/Li allows the relief of the strain produced by the phase transition avoiding the infiltration of the electrolyte.

In conclusion, the huge number of studies about the structural degradation mechanism of Ni-rich NMCs during cycling always highlighted the noxious effect of the high voltage phase transition, with slightly different results often depending on the applied cycling conditions.

3.4.3. Storage conditions

Ni-rich NMCs are known to be particularly sensitive to moisture and humid storage conditions. As a matter of fact, it was largely demonstrated how such storage can induce the formation of surface lithium compounds and the surface phase transformation to a NiO-rock-salt type structure, both resulting in lower electrochemical performances. In particular, residual lithium compounds such as LiOH, Li₂CO₃, Li₂O, Li₂O₂ and LiHCO₃ are inevitably formed at the Ni-rich cathode surface both during synthesis and upon storage, according to the proposed reactions, that will be shown to be oversimplified and discussed in the following Section:⁵⁹



Subsequently, LiOH can react with CO₂ to become Li₂CO₃:



The impact of storage conditions on the formation of such species and on the electrochemical performance of exposed materials were thence largely studied in the literature since it is a problem seriously affecting Ni-rich layered oxides.

3.4.3.1. Humidity

In order to clarify the phenomena occurring at the surface of Ni-rich NMCs, it has to be mentioned that Faenza et al. proved that CO₂ alone does not cause the degradation

of high-nickel layered oxides. The thermogram of a sample stored in a pure CO₂ bag (< 10 ppm H₂O) is in fact very similar to the pristine one, differing only slightly in the mass lost during the 150°C isotherm, corresponding to H₂O. Therefore, the presence of water results to be a prerequisite to the formation of Li₂CO₃ making Equation 1.4 not plausible.⁶⁰ Moreover, Shkrob et al. only hypothesised the Li⁺/H⁺ exchange of Equation 1.3, but actual proofs have not been provided yet.⁵⁹

In order to investigate the possible reactions with water, the effect of washing was largely investigated demonstrating it to decrease the amount of lithium residuals at the surface of the AM. For this reason, it was often proposed as a possible solution to increase the cyclability of the material. However, Lee et al. recently studied the influence of the water-washing process on the stability of the surface structure of Li(Ni_{0.88}Mn_{0.066}Co_{0.054})O₂ and evidenced how, together with the Li₂CO₃ decrease, the water washing seems to decrease the surface stability of Ni-rich NMC, making it more vulnerable to side reactions with the electrolyte during cycling. This results in facilitating the formation of an insulating NiO-like phase in the washed material compared to the bare one: a reconstructed layer of more than 20 nm is formed in the water washed material after 200 cycles while the rock-salt phase accounts for only 4-8 nm in the bare NMC.⁶¹

Similarly, many are the groups studying the effect of storage in high humidity conditions on the contamination layer composition and on the electrochemical cycling behaviour after exposure, while the influence of ambient or low humidity storage was scarcely explored. In this context, it has to be mentioned that Jung et al. investigated the formation of surface impurities on NMC111 and NMC811 after one-year ambient storage. An increase of carbonate species by a factor 5 at the surface of NMC811 was reported, while the surface and electrochemical performances of NMC111 remained unchanged, demonstrating once again the higher reactivity of high-Ni compositions. It is interesting to notice how this group proposed here the formation of basic nickel carbonate at the NMC811 surface as the major and most critical contaminant for the

first time.⁶² Although, one should keep in mind that extra care must be taken in interpreting XPS spectra — here used to prove the presence of nickel carbonates — since the fast decomposition of the contamination layer upon X-rays exposition could induce false results, as it will be discussed in Chapter 2.

The impact of ambient storage on electrochemical performances of NMC811 was also efficiently investigated by Busà et al., who exposed electrodes for 28 days in ambient atmosphere showing lower initial discharge capacity and capacity retention in all the stored samples compared to fresh ones. The loss of surface lithium from the AM to form Li_2CO_3 and LiOH species was identified as the cause of the lower first cycle discharge capacity, together with the inferior ionic and electronic conductivity of the newly formed contamination layer. On the other hand, the fast capacity fade was related to the most severe cracking due to the accumulated moisture and formed species.⁶³

However, when discussing these topics, it is important to take into consideration that residual lithium species can also have an impact on the cathode slurry instability and particularly on the degradation of PVdF often used as binder, as recently highlighted in the Perspective of Manthiram's group.⁶⁴ This topic will not be covered in this first Chapter, but it is important to mention it for the discussion about electrode manufacturing that the reader will find in the second part of Chapter 3. Moreover, it is interesting to notice how the authors evidenced here the importance of developing reliable methods and techniques for measuring residual lithium content, which is one of the principal challenges of this PhD work. Actually, the absence of a universally accepted method for the analysis of lithated compounds formed during storage in humid conditions makes it difficult to compare results between different studies and groups. In addition, it is important to highlight here how all the above mentioned studies investigate the effect of long-term exposure, without ever considering the possibility of a much faster reactivity to humidity of the Ni-rich NMC surface.

3.4.3.2. Temperature

Together with instabilities associated with cycling and moisture exposure, high-nickel layered oxides were largely demonstrated to have poor thermal stability, often leading to gassing phenomena and phase transitions. Even if a deep analysis of the NMC thermal behaviour is out of scope in this manuscript, some important studies have to be mentioned to show once again how the composition of layered oxides can impact the stability of the material.

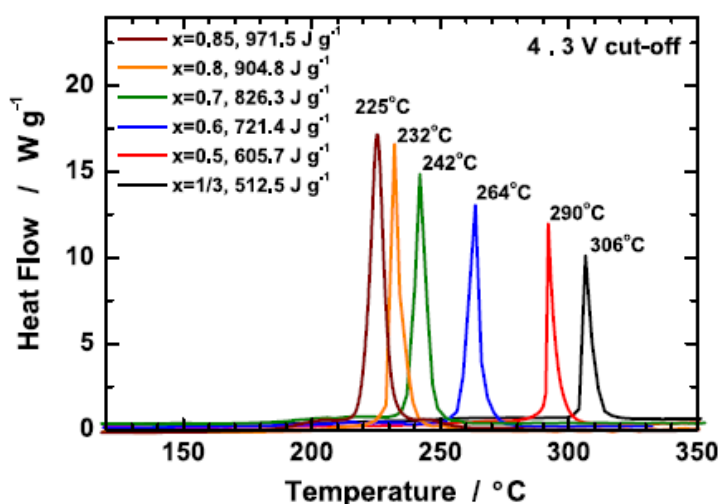


Figure 1.13. Differential Scanning Calorimetry (DSC) curves of $\text{Li}(\text{Ni}_x\text{Mn}_y\text{Co}_{1-x-y})\text{O}_2$ with $x = 1/3$ (black), 0.5 (red), 0.6 (blue), 0.7 (green), 0.8 (orange) and 0.85 (brown) charged at 4.3 V.³¹

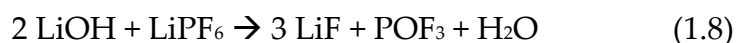
The principal tools typically employed to study such an instability are thermal analysis such as Thermal Gravimetric Analysis (TGA) and Differential Scanning Calorimetry (DSC). H. J. Noh et al., for example, reported the study of the thermal behaviour as a function of the de-lithiated material composition. They showed here how the exothermic event associated with the degradation of the NMC leading to the NiO phase takes place at lower temperatures and with higher heat generation as the nickel amount in the material increases (Figure 1.13). Similarly, TGA results showed three distinct features accompanied by increasing weight loss for increasing nickel content. The three events were attributed by the authors to the oxygen release associated with the already mentioned phase transitions from the layered (R-3m) to the rock-salt (Fm3m) through the spinel structure (Fd-3m). The total amount of released oxygen

increases thence from 18.4% for $\text{Li}_{0.27}(\text{Ni}_{1/3}\text{Mn}_{1/3}\text{Co}_{1/3})\text{O}_2$ to 51.7% for $\text{Li}_{0.21}(\text{Ni}_{0.85}\text{Mn}_{0.075}\text{Co}_{0.075})\text{O}_2$ together with the instability of the considered delithiated phases.³¹ It has to be mentioned that such thermal behaviours were already explained likewise in 2006 by Belharouak et al. Thanks to the XRD diagrams of the samples recovered at different temperatures during the TGA experiments, they could prove how the phase transitions can be affected by the temperature.⁵⁵

3.4.3.3. Electrolyte

Among the different degradation mechanisms affecting NMCs, it is worth to mention the effect of the electrolyte, already briefly discussed in Section 3.4.2. In particular, the dissolution of transition metals ions in the electrolyte appears to be an inevitable process known to increase at high temperature and high operating voltages. Little quantities of water are in fact typically present in organic solvents for electrolytes and lead to the decomposition of the electrolyte Li salts (LiPF_6 or LiClO_4) in acid byproducts such as HF or HClO_4 , that are known to corrode the cathode material provoking the dissolution of TM ions. Moreover, since transition metals are more soluble in the electrolyte in lower oxidation states, the dissolution might also occur during cycling as a result of the formation of low valence ions due to the oxygen loss caused by the already discussed phase transition. This results in the degradation of the capacity due to the loss of Li ions insertion sites.⁶⁵

Moreover, the reaction of the previously mentioned residual lithium compounds with the electrolyte was proposed to be at the origin of CO_2 production during cycling (c.f. Section 3.4.4) as described by the following reactions:⁶⁶



3.4.4. Gassing

Since one of the principal application for NMC active materials is in the electrification of vehicles, the security is one of the most important requirements that has to be demonstrated to allow the commercialisation of the battery.²⁹ One of the principal security issues of NMC comes from the tendency of such materials to produce high quantities of gas during electrochemical cycles.

The gas evolution of different NMC formulations and similar layered oxides was followed by different research groups through in situ mass spectrometry techniques such as differential/operando electrochemical mass spectrometry (DEMS/OEMS).⁶⁷⁻⁷² These are in fact invaluable tools that allow the real-time quantification of volatile products while the potential is monitored. While it is largely accepted that the O₂ evolution is from irreversible charge compensation by the oxygen lattice from delithiation at high voltage, the source of CO and CO₂ is still under debate and different hypothesis have been proposed.

As already mentioned in the introduction to this Section, calculations demonstrated that the quantity of released oxygen is supposed to be dependent on the Ni amount in the material, since the Ni—O energy bonding decreases upon increase of the Ni oxidation state.³⁴ As a matter of fact, Ni oxidation state increases with Ni concentration and thence the oxygen release mechanism is logically exacerbated in the richest Ni-rich NMC. The energy levels of Ni⁴⁺ formed during cycling are indeed closer to oxygen energy levels than Ni²⁺ ones, yielding an overall increase of the covalency of the M—O bonding within the NMC active material. This trend was supported experimentally by Dixit et al.³⁴ as they showed that Ni⁴⁺—O bonding is more covalent, thus destabilizing the ionic network and resulting in the release of O₂ together with a reduction of Ni to its more stable state (Ni²⁺).

On the other hand, it has to be noted that R. Jung et al. tested three different NMC composition (NMC111, NMC622 and NMC811) and they found very similar results about gas release, differing only slightly in the onset voltage and in the quantity of

released oxygen in the first four electrochemical cycles.³³ A positive relationship between the nickel amount and the released gases was thus not proposed by this group.

However, by looking at the reported DEMS/OEMS data for NMC811, one can distinguish two regions: CO₂ and CO begin to evolve at around 3.8 V vs Li⁺/Li and are sustained until the high voltage regime of around 4.3 V vs Li⁺/Li; here a sudden onset of O₂ evolution is reported as well as an increasing amount of CO and CO₂. Since there are several sources of C and O in a lithium-ion battery, it is important to divide each contribution in order to understand the origin of gas evolution. For example, any conductive carbon contribution was excluded by Jung et al. by performing DEMS on electrodes prepared with ¹³C-labeled carbon instead of the conventional one.³³ Since the presence of ¹³CO and ¹³CO₂ was not recorded, authors concluded that CO and CO₂ could only generate from the electrolyte solvent (ethylene carbonate) chemical decomposition or electro-oxidation, proposing the same reaction as the one proposed by H. Tsukasaki et al.⁷³



From these studies, it resulted that the largest amount of CO/CO₂ only evolved once the evolution of O₂ was observed (Figure 1.14). The amount CO and CO₂ released at the very beginning of the first cycle was instead attributed by the group to the CEI formation (CO) and carbonate impurities oxidation (CO₂). Moreover, the amount of released oxygen was found to be largest in the first cycle and to decrease in the subsequent cycles; this brought to the conclusion that the oxygen is only released from the surface-near regions and so it is faster in the first cycle and slower in subsequent cycles due to the more difficult diffusion from the bulk through the material.

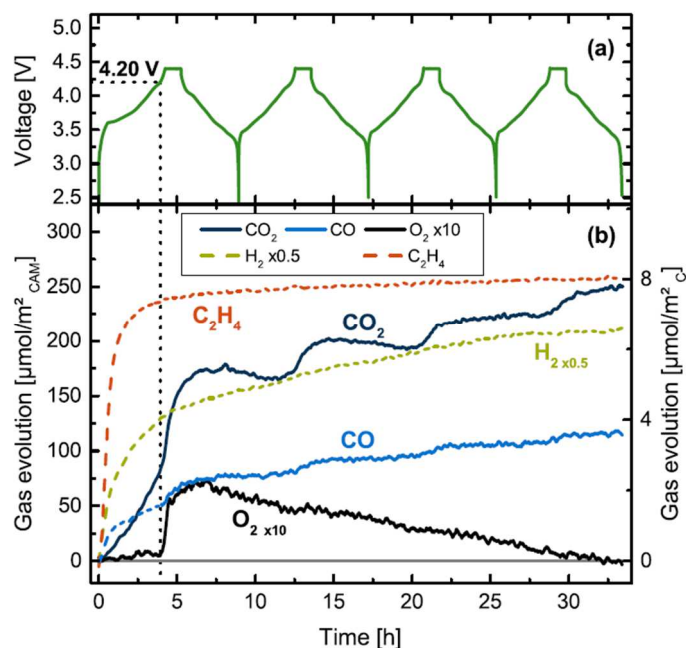


Figure 1.14. (a) Cell voltage vs. time of a NMC811-Graphite cell over four charge/discharge cycles at 0.2 C and 25°C between 2.6 and 4.4 V. (b) Evolution of CO₂ (dark blue), H₂ (green), C₂H₄ (orange), CO (blue), and O₂ (black, 10-fold magnified) as a function of time. Solid lines indicate the gases stemming from the NMC electrode and dashed lines from the graphite electrode; gas concentrations are referenced to the NMC BET area (left y-axis) and to the sum of graphite and conductive carbon BET area (right x-axis).³³

It has to be noted that in the majority of DEMS/OEMS studies, the carbonate electrolyte decomposition was once again claimed to be the main source of high voltage CO/CO₂ evolution. In this context, many different mechanisms were proposed. The NMC surface, and nickel in particular, could act as a catalyst by lowering the onset potential of the electrochemical oxidation of the electrolyte without taking part into the reaction, as proposed by different groups.^{40,41,43} Alternatively, the released active oxygen could react with the electrolyte to produce CO/CO₂ both at low and high potential or in the high voltage region only as suggested by H. Tsukasaki et al and Jung et al. respectively.^{33,73} In this context, it has to be mentioned that Ni-rich materials have a lower LUMO energy level –and so higher LUMO potential– compared to other active materials. In other words, when looking to Figure 1.6 the electrochemical potential of the positive material is closer to the electrolyte HOMO and thence to the potential window in which the CEI is formed.

Another possible conclusion was later advanced by Sara E. Renfrew and Bryan D. McCloskey. In particular, they proposed the degradation of Li_2CO_3 at the NMC surface as the main source of the majority of the CO/CO_2 evolution during the first charge. As a matter of fact, it was possible to distinguish the contributions of the electrolyte and of the active material by enriching the NMC surface in ^{18}O . Through an accurate carbonate titration with H_2SO_4 coupled with DEMS measurements of the so-evolved CO_2 , it was then possible to determine the isotopic enrichment of the surface carbonate and to compare it with the ^{18}O enrichment of the released gases during the electrochemical cycle. In this way, they were able to attribute the whole CO/CO_2 production of the first charge to the Li_2CO_3 degradation and to prove that all the oxygen evolution comes from the surface NMC lattice instead. Moreover, reducing the amount of Li_2CO_3 at the NMC surface by chemical treatment with a mild acid, they found, together with the expected reduction in the amount of evolved CO_2/CO , the absence of released oxygen.³⁷

Because of the large number of possible explanations for the gassing phenomenon, a universally accepted description of the reactions bringing to this gas generation has still to be found.

3.4.5. Possible solutions

Different strategies were proposed by many groups in order to achieve better electrochemical and structural stability and hinder the gas generation during cycling. Together with novel synthesis methods and microstructural modifications, chemical modifications of NMC materials and surfaces consisting either in element doping, surface coating or gradient composition surface engineering were often identified as the most promising solutions to NMC issues.

Element doping is, for instance, an effective way to decrease Li/Ni disorder, improve the material structural stability and lower the possibility of intergranular cracks in secondary particles. Actually, it was demonstrated that “pillar ions” can strengthen the bulk forming stronger bonds with the oxygen and that cations with a larger ionic

radius than Li^+ can increase the expansion of Li^+ diffusion channels improving the material electrochemistry. In particular, Chen et al. studied the effects of Ca doping on the NMC811, demonstrating that the use of low-valence ions with larger ionic radius (0.1 nm) than Ni^{2+} (0.069 nm) can reduce the Li/Ni disorder and improve the lithium ions diffusion coefficient. In this way, the group could obtain higher capacity retentions and better rate capabilities. Moreover, the authors demonstrated here how an efficient doping is possible by using dopant quantities up to 6%; higher Ca^{2+} amounts showed instead lower electrochemical performance (Figure 1.15).⁷⁴ Similarly, K. Min et al. investigated the effect of Al and Mg doping on the formation of oxygen vacancies and cation disordering on Ni-rich NMC by *ab-initio* simulation. As Ca^{2+} doping, Mg was demonstrated to prevent the Li/Ni exchange and to provide a better structural stability. The Mg-doped structure, in fact, exhibits the lowest changes in the lattice parameters over cycling. On the other hand, the Al-doping showed to improve oxygen stability, decreasing the amount of oxygen vacancies.⁷⁵

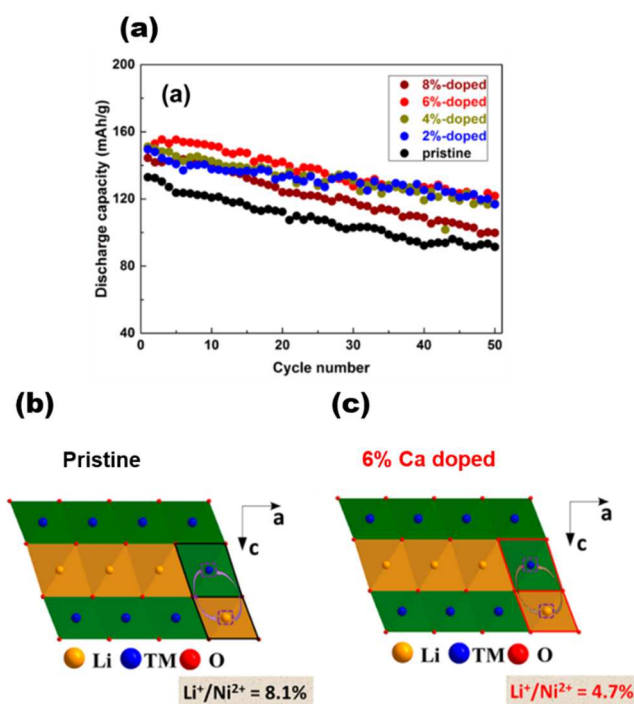


Figure 1.15. Effect of Ca^{2+} doping on the electrochemical properties (a) and on the NMC811 structure (b and c).

F. Schipper et al. studied instead the impact of high charge-state dopants. They demonstrated here that NMC622 doped with Zr^{4+} shows better structural and electrochemical properties. Zr^{4+} can in fact destabilise the Ni tetrahedral sites and reduce the concentration of Jahn-Teller active Ni^{3+} ions. The layered structure is thus stabilised and the phase transformation upon Li^+ de-intercalation inhibited.⁷⁶

Recently, the addition of elemental sulphur as a cathode additive was studied as well, in order to decrease the oxygen evolution at high potential and remove the alkaline Li residual compounds from the NMC811 surface. During the synthesis process, the elemental sulphur can reduce the transition metal ions to rock-salt phase, resulting in a MO barrier that can protect the inner active material from parasitic reactions with the electrolyte. The so formed $Li_2S_2O_3$ can then react with the surface lithium impurities during the first charge forming the electrochemically stable Li_2SO_4 .⁷⁷ A summary of the principal dopants tested for Ni-rich NMCs found in the literature and adapted from the review by Jiang et al. is reported in Table 1.2.

Table 1.2. List of the principal dopants for Ni-rich NMC materials found in the literature. The formula of the doped material is given as well as cycling parameters and properties.

Dopant	Material	Cut-off voltage (V vs Li ⁺ /Li)	1 st cycle specific capacity (mAh/g)	Capacity retention (%)	Ref
Na ⁺ and Al ³⁺	Li(Ni _{0.88} Mn _{0.04} Co _{0.08})O ₂	2.8–4.35	215	84% after 50 cycles	78
Ca ²⁺	Li(Ni _{0.8} Mn _{0.1} Co _{0.1})O ₂	3.0–4.3	150 ^a	81.1% after 50 cycles	74
Mg ²⁺	Li(Ni _{0.83} Mn _{0.05} Co _{0.12})O ₂	2.8–4.5	200	87.2% after 200 cycles	79
Sr ²⁺	Li(Ni _{0.8} Mn _{0.1} Co _{0.1})O ₂	2.7–4.3	202	98.5% after 150 cycles	80
Al ³⁺	Li(Ni _{0.8} Mn _{0.05} Co _{0.15})O ₂	2.8–4.35	208	98% after 100 cycles	81
B ³⁺	Li(Ni _{0.92} Mn _{0.04} Co _{0.04})O ₂	2.5–4.4	221	78% after 100 cycles	82
Ga ³⁺	Li(Ni _{0.8} Mn _{0.1} Co _{0.1})O ₂	2.8–4.3	203	91.2% after 100 cycles	83
Zr ⁴⁺	Li(Ni _{0.6} Mn _{0.2} Co _{0.2})O ₂	2.8–4.3	163 ^b	96% after 50 cycles	76
Ti ⁴⁺	Li(Ni _{0.9} Co _{0.1})O ₂	2.8–4.3	205	97.96% after 100 cycles	84
Ta ⁵⁺	Li(Ni _{0.6} Mn _{0.2} Co _{0.2})O ₂	3.0–4.5	197	79.2% after 100 cycles	85
Nb ⁵⁺	Li(Ni _{0.8} Mn _{0.1} Co _{0.1})O ₂	3.0–4.3	210	97% after 100 cycles	86
P ⁵⁺	Li(Ni _{0.92} Mn _{0.04} Co _{0.04})O ₂	2.5–4.4	221	72% after 100 cycles	82
Mo ⁶⁺	Li(Ni _{0.8} Mn _{0.1} Co _{0.1})O ₂	2.75–4.3	216	92.4% after 100 cycles	87

^a Cycled at 0.2 C

^b Cycled at 0.15 C

Dopant	Material	Cut-off voltage (V vs Li ⁺ /Li)	1 st cycle specific capacity (mAh/g)	Capacity retention (%)	Ref
W ⁶⁺	Li(Ni _{0.9} Mn _{0.05} Co _{0.05})O ₂	2.7–4.3	235	96% after 100 cycles	88
F ⁻	Li(Ni _{0.8} Mn _{0.15} Co _{0.05})O ₂	2.7–4.3	216	95.6% after 100 cycles	89
Br ⁻	Li(Ni _{0.815} Co _{0.15} Al _{0.035})O ₂	2.8–4.3	196	73.7% after 100 cycles	90

It is interesting to notice how some anions like F⁻ and Br⁻ can be used as well to substitute O²⁻ and form stronger chemical bonds with transition metal ions, resulting in a more stable structure.^{89,90}

An alternative solution to element doping is the surface coating, which allows to separate the bulk materials from the electrolyte solutions, reducing the electrode surface reactivity and the resulting parasitic reactions. Coating has already been largely studied as one of the best solutions to improve the stability and cyclability of NMC materials. Depending on the composition, coating materials can be divided into two different categories: non-conductive with high stability, and ionic conductive materials with high Li⁺ conductivity. Metal oxides such as alumina, CaO, SiO₂ and ZrO₂ were demonstrated to prevent the material degradation by the electrolyte. On the other hand, lithium salts like Li₂SiO₃, Li₃PO₄, LiF, and conductive organic materials (polyimide, polyaniline etc.) allow to overcome the poor lithium-ion diffusion.^{91,92,92–101} If the reader is interested to go further into surface modification of layered oxides, I suggest to immerse him/herself into the recent review arisen from the collaboration between different American laboratories that presents a very complete summary of all the strategies that has been used to mitigate surface instability.¹⁰²

Moreover, it is worth mentioning that multiple studies are recently investigating concentration gradient strategies often consisting in core-shell structures or full

concentration gradients. In both cases, two different compositions and/or structures are integrated on the same secondary particle in order to provide both high capacity and stability at the same time. Typically, a Ni-rich layered component is located in the bulk of the particles, while a Mn-rich layered or spinel phase is in the outer part.^{103,104} Figure 1.15 represents two concentration-gradient Ni-rich NMCs synthesised by K. Amine's group:

NC-NM82 (with composition $0.5(\text{LiNi}_{0.8}\text{Co}_{0.2})_{\text{bulk}} 0.5(\text{LiNi}_{0.8}\text{Mn}_{0.2})_{\text{surface}}$) and NM-NC82 (with composition $0.5(\text{LiNi}_{0.8}\text{Mn}_{0.2})_{\text{bulk}} 0.5(\text{LiNi}_{0.8}\text{Co}_{0.2})_{\text{surface}}$). The material presenting the Co-rich surface was found to present negligible morphology damage and improved stability of the H2-H3 phase transition upon extended cycling (Figure 1.16). On the contrary, the Mn-rich surface appeared stiffer and NM-NC82 showed severe particle cracking along with lower cycling stability. This study significantly draws attention to the importance of Co/Mn composition in structural and morphological stability.

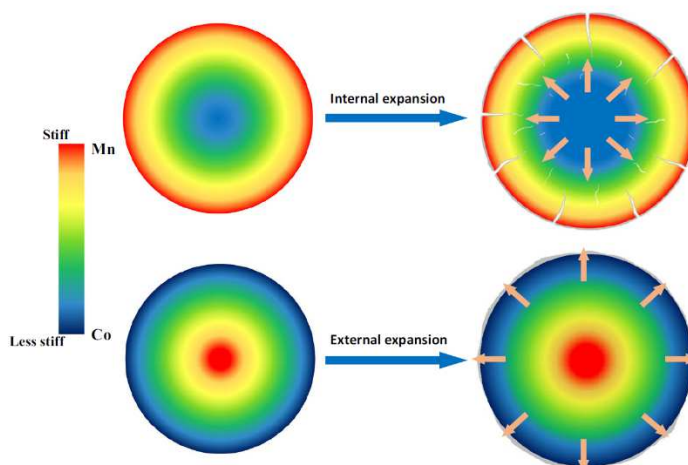


Figure 1.16. Schematic representation of NMC secondary particles with a concentration gradient architecture leading to a Mn-rich surface (in red) or a Co-rich surface (in blue) and of their mechanical stability.¹⁰⁵

With the emergence of such technologies, having a precise characterisation of the surface that we intend to functionalise is more and more important. It is in fact essential to have a clear picture of actual state of the pristine surface in order to better understand the effects of potential modifications.

3.4.6. Surface characterisation

Despite the incredibly huge number of publications about NMC materials of the last few years, a deep and complete characterisation of the material surface is still missing in the existing literature, although this is an essential topic to explore before functionalising materials as just clarified. As a matter of fact, such an exploration of the initial state of positive electrode active materials, conducted by other groups on other similar transition metal oxides such as LiCoO_2 (LCO),¹⁰⁶ $\text{Li}_{1.2}(\text{Mn}_{0.6}\text{Ni}_{0.2})\text{O}_2$ (LMNO)¹⁰⁷ and Li-Mn rich oxides,^{108,109} always demonstrated a different nature of the surface compared to the bulk of the material. Among these studies about the surface of layered oxides, it is important to mention that a Li-poor and thus Co-rich surface (the electrochemically inactive Co_3O_4 layer) was observed at the surface of LiCoO_2 at the interface with the solid electrolyte.¹¹⁰ In addition, this behaviour was proven to exist also in the case of NCA cathode materials.¹⁰⁶ Similarly, the segregation of Co and Ni along with the nucleation of domains with a spinel structure at the surface of Li-Mn-rich transition metal oxides (LMRTMOs) was reported by both Shukla et al. and Yan et al., at the pristine state.^{108,109} Lastly, a surface Ni segregation was observed in LMNO as well; here the authors suggested that this increase in the Ni concentration at the surface could occur during the synthesis.¹⁰⁷

Similar studies do not exist for NMC materials yet to the best of our knowledge and obtaining clear and universal information about the surface state of Ni-rich layered oxides is still quite difficult. As a matter of fact, when new synthesis methods or material composition are investigated, the characterisation is usually based on bulk techniques such as XRD or XAS in order to demonstrate the attainment of the good crystallographic phase or chemical composition. TEM and EDX are often used to confirm the information obtained with the above-mentioned techniques, looking thence exclusively in the bulk of the particles. Actually, Steiner et al. analysed the surface oxidation state of NMC811 electrodes by soft XAS in TEY mode and observed a nickel reduction at the surface. However, since the electrodes only were analysed

here and not the pristine powder, this Ni²⁺ segregation at the surface was attributed to changes occurring during the electrode preparation, without further investigating the actual state of the powder surface.⁴³ Moreover, it is important to mention that the proposed new materials are always synthesised at a laboratory scale and that the results cannot be reproduced or compared by other research groups since the materials will never be exactly the same. NMC811 is in fact particularly sensitive to synthesis conditions, as it will be demonstrated in Chapter 4, and different results can be found when some parameters are even slightly changed.

Despite the use of surface techniques such as XPS in publications about surface functionalisation by coating, the aim is often here just to prove that the surface is successfully functionalised, without really using these techniques for understanding the original state of the surface. As in the paper by Lee et al. a rough interpretation of XPS results is often given, since a deeper interpretation is usually considered out of scope.¹¹¹

Moreover, when investigating the effect of storage conditions on cycling or gassing behaviour of Ni-rich NMCs, residual lithium compounds are often analysed without verifying possible changes on the surface of the AM, as in the studies by Jung et al.^{33,62,112} In these works electrodes are usually analysed and, since they are generally prepared in ambient atmosphere as is the work of Renfrew et al. the original state of the material surface is not really taken into account, as Ni-rich are sensitive even to small amount of humidity and for short periods of time, as it will be showed later on in this manuscript (cf. Chapter 3). This same issue is encountered when EELS is used to investigate the surface of NMC in papers about degradation mechanisms that focus especially on the characterisation of cycled electrodes.¹¹³

Part 4. Conclusions and research aim

Our world is progressively changing due to global warming and our way of living has to adapt in order to decrease the GHG emissions responsible for the climate change. Since a significant amount of CO₂ is produced every year by the transportation sector, governments, EV manufacturers and academic researchers are putting a great effort to assure a global transition to green mobility. The research on Li-ion batteries – currently the best choice for the electrification of vehicles— and new and performant battery materials is situated in this context.

The layered cathode material NMC811 was the main character of the third part of this chapter, which aimed at summarizing and reviewing the existing scientific production on this compound. The principal aspects of this part can be resumed with the following points:

- A structure change occurs during cycling at high cut-off voltage, deteriorating the cell performance and inducing cracks formation. Even if often observed in the analysed studies, the exact origin of this phase transition has not been well defined yet.
- Residual lithium is often found at the material surface after synthesis, under the form of Li₂CO₃ and LiOH. The importance of developing a reliable method for the measure of such compounds and ease the comparison between different works was highlighted.
- The lithiated compounds were demonstrated to accumulate upon long-term exposure to humid atmosphere and to affect gassing by reacting with the electrolyte and/or as a consequence of electrochemical reduction (for Li₂CO₃). Moreover, LiOH was often identified as the principal responsible for slurry instability and gelification.

To further advance the understanding of the surface reactivity of cathode materials and therefore the development of new functionalised materials for battery

applications, it is essential to properly characterise materials before cycling. However, in the third part of this chapter, we highlighted the lack of a proper understanding of pristine NMC surfaces in the existing literature.

This PhD project aims at deeply characterising the surface reactivity of industrial samples using a multi-analytical approach and focusing on materials always having the same history in order to obtain comparable data.

In particular, it is in our interest to:

- a) Exploit STEM-EELS, STEM-EDX, SEM-FIB, ^7Li MAS-NMR and XPS for the analysis of NMC811 samples, with a particular focus on the surface, and the optimal combination between these techniques to obtain truthful and complete information;
- b) Characterise the pristine powder as it comes from the industrial shelves and determine possible correlations between bulk and surface respective modifications;
- c) Investigate the influence of short-term storage in controlled low-humidity conditions on both the NMC surface and the amount of surface lithiated species, which will be carefully quantified;
- d) Determine the effects of the electrode preparation processes by analysing both slurries and finished electrodes;
- e) Analyse surfaces of materials synthesised by varying multiple parameters and determine how the observed differences could affect gassing in full cells.

References

- (1) Nisbet, E. G.; Manning, M. R.; Dlugokencky, E. J.; Fisher, R. E.; Lowry, D.; Michel, S. E.; Myhre, C. L.; Platt, S. M.; Allen, G.; Bousquet, P.; Brownlow, R.; Cain, M.; France, J. L.; Hermansen, O.; Hossaini, R.; Jones, A. E.; Levin, I.; Manning, A. C.; Myhre, G.; Pyle, J. A.; Vaughn, B. H.; Warwick, N. J.; White, J. W. C. State of Global Climate 2021 - WMO Provisional Report. *Glob. Biogeochem. Cycles* **2019**, *33* (3), 318–342. <https://doi.org/10.1029/2018GB006009>.
- (2) Climate Change 2021: The Physical Science Basis. Contribution of Working Group I to the Sixth Assessment Report of the Intergovernmental Panel on Climate Change; Masson-Delmotte, V., Zhai, P., Pirani, A., Connors, S. L., Péan, C., Berger, S., Caud, N., Chen, Y., Goldfarb, L., Gomis, M. I., Huang, M., Leitzell, K., Lonnoy, E., Matthews, J. B. R., Maycock, T. K., Waterfield, T., Yelekçi, Ö., Yu, R., Zhou, B., Eds.; *Cambridge University Press*, **2021**.
- (3) Climate Watch Historical GHG Emissions. 2021. Washington, DC: World Resources Institute. Available Online at: <https://www.climatewatchdata.org/ghg-emissions>.
- (4) Transport sector CO₂ emissions by mode in the Sustainable Development Scenario, 2000-2030—Charts—Data & Statistics <https://www.iea.org/data-and-statistics/charts/transport-sector-co2-emissions-by-mode-in-the-sustainable-development-scenario-2000-2030> (accessed 2022 -03 -19).
- (5) United Nations. Paris Declaration Electro-Mobility and Climate Change & Call to Action <https://unfccc.int/news/the-paris-declaration-on-electro-mobility-and-climate-change-and-call-to-action>.
- (6) Transport sector CO₂ emissions by mode in the Sustainable Development Scenario, 2000-2030—Charts—Data & Statistics <https://www.iea.org/data-and-statistics/charts/transport-sector-co2-emissions-by-mode-in-the-sustainable-development-scenario-2000-2030> (accessed 2022 -03 -19).
- (7) Transitioning to Zero Emission Cars and Vans: 2035 Delivery Plan. 57.
- (8) HOME - UN Climate Change Conference (COP26) at the SEC – Glasgow 2021 <https://ukcop26.org/> (accessed 2022 -03 -19).
- (9) European Commission, official website https://ec.europa.eu/info/index_en (accessed 2022 -03 -19).
- (10) Légifrance - Publications officielles - Journal officiel - JORF n° 0299 du 26/12/2019 <https://www.legifrance.gouv.fr/download/pdf?id=dFFucSM4dRWHkEQLMHYgb--nam6aCtsgM2LdqyWZyGE=> (accessed 2022 -01 -16).
- (11) Essor des ventes de voitures neuves à motorisations alternatives en 2020 <https://www.statistiques.developpement-durable.gouv.fr/essor-des-ventes-de-voitures-neuves-motorisations-alternatives-en-2020> (accessed 2022 -01 -16).
- (12) Amici, J.; Asinari, P.; Ayerbe, E.; Barboux, P.; Bayle-Guillemaud, P.; Behm, R. J.; Berecibar, M.; Berg, E.; Bhowmik, A.; Bodoardo, S.; Castelli, I. E.; Ceki-

Laskovic, I.; Christensen, R.; Clark, S.; Diehm, R.; Dominko, R.; Fichtner, M.; Franco, A. A.; Grimaud, A.; Guillet, N.; Hahlin, M.; Hartmann, S.; Heiries, V.; Hermansson, K.; Heuer, A.; Jana, S.; Jabbour, L.; Kallo, J.; Latz, A.; Lormann, H.; Løvvik, O. M.; Lyonard, S.; Meeus, M.; Paillard, E.; Perraud, S.; Placke, T.; Punckt, C.; Raccurt, O.; Ruhland, J.; Sheridan, E.; Stein, H.; Tarascon, J.; Trapp, V.; Vegge, T.; Weil, M.; Wenzel, W.; Winter, M.; Wolf, A.; Edström, K. A Roadmap for Transforming Research to Invent the Batteries of the Future Designed within the European Large Scale Research Initiative BATTERY 2030+. *Adv. Energy Mater.* **2022**, 2102785. <https://doi.org/10.1002/aenm.202102785>.

(13) Murdock, B. E.; Toghiani, K. E.; Tapia-Ruiz, N. A Perspective on the Sustainability of Cathode Materials Used in Lithium-Ion Batteries. *Adv. Energy Mater.* **2021**, 11 (39), 2102028. <https://doi.org/10.1002/aenm.202102028>.

(14) Mineral Commodity Summaries 2022. **2022**, 206.

(15) Neumann, J.; Petranikova, M.; Meeus, M.; Gamarra, J. D.; Younesi, R.; Winter, M.; Nowak, S. Recycling of Lithium-Ion Batteries—Current State of the Art, Circular Economy, and Next Generation Recycling. *Adv. Energy Mater.* **2022**, 2102917. <https://doi.org/10.1002/aenm.202102917>.

(16) Sustainable cobalt 1 Umicore
<https://www.umicore.com/sustainability/value-chain-and-society/sustainable-cobalt/> (accessed 2022 -03 -19).

(17) Tarascon, J.-M.; Armand, M. Issues and Challenges Facing Rechargeable Lithium Batteries. *Nature* **2001**, 414 (6861), 359–367. <https://doi.org/10.1038/35104644>.

(18) Mizushima, K.; Jones, P. C.; Wiseman, P. J.; Goodenough, J. B. Li_xCoO_2 ($0 < x < 1$): A New Cathode Material for Batteries of High Energy Density. **1980**, 15 (6), 7. [https://doi.org/10.1016/0025-5408\(80\)90012-4](https://doi.org/10.1016/0025-5408(80)90012-4).

(19) Whittingham, M. S. Lithium Batteries and Cathode Materials. *Chem. Rev.* **2004**, 104 (10), 4271–4302. <https://doi.org/10.1021/cr020731c>.

(20) Lyu, Y.; Wu, X.; Wang, K.; Feng, Z.; Cheng, T.; Liu, Y.; Wang, M.; Chen, R.; Xu, L.; Zhou, J.; Lu, Y.; Guo, B. An Overview on the Advances of LiCoO_2 Cathodes for Lithium-Ion Batteries. *Adv. Energy Mater.* **2021**, 11 (2), 2000982. <https://doi.org/10.1002/aenm.202000982>.

(21) Jiao, F.; Bao, J.; Hill, A. H.; Bruce, P. G. Synthesis of Ordered Mesoporous Li-Mn-O Spinel as a Positive Electrode for Rechargeable Lithium Batteries. *Angew. Chem. Int. Ed.* **2008**, 47 (50), 9711–9716. <https://doi.org/10.1002/anie.200803431>.

(22) Dupré, N.; Martin, J.-F.; Oliveri, J.; Soudan, P.; Guyomard, D.; Yamada, A.; Kanno, R. Aging of the $\text{LiNi}_{1/2}\text{Mn}_{1/2}\text{O}_2$ Positive Electrode Interface in Electrolyte. *J. Electrochem. Soc.* **2009**, 156 (5), C180. <https://doi.org/10.1149/1.3098494>.

(23) Dupré, N.; Martin, J.-F.; Oliveri, J.; Soudan, P.; Yamada, A.; Kanno, R.; Guyomard, D. Relationship between Surface Chemistry and Electrochemical Behavior of $\text{LiNi}_{1/2}\text{Mn}_{1/2}\text{O}_2$ Positive Electrode in a Lithium-Ion Battery. *J. Power Sources* **2011**, 196 (10), 4791–4800. <https://doi.org/10.1016/j.jpowsour.2010.07.049>.

- (24) Cuisinier, M.; Martin, J.-F.; Moreau, P.; Epicier, T.; Kanno, R.; Guyomard, D.; Dupré, N. Quantitative MAS NMR Characterization of the $\text{LiMn}_{1/2}\text{Ni}_{1/2}\text{O}_2$ Electrode/Electrolyte Interphase. *Solid State Nucl. Magn. Reson.* **2012**, *42*, 51–61. <https://doi.org/10.1016/j.ssnmr.2011.09.001>.
- (25) Lee, J.; Dupre, N.; Avdeev, M.; Kang, B. Understanding the Cation Ordering Transition in High-Voltage Spinel $\text{LiNi}_{0.5}\text{Mn}_{1.5}\text{O}_4$ by Doping Li Instead of Ni. *Sci. Rep.* **2017**, *7* (1). <https://doi.org/10.1038/s41598-017-07139-2>.
- (26) Liu, A.; Phattharasupakun, N.; Väli, R.; Ouyang, D.; Dahn, J. R. Tracking the Fate of Excess Li in the Synthesis of Various $\text{Li}_y[\text{Ni}_{1-x}\text{Mn}_x]\text{O}_2$ Positive Electrode Materials under Different Atmospheres. *J. Electrochem. Soc.* **2022**. <https://doi.org/10.1149/1945-7111/ac5483>.
- (27) Kalyani, P.; Kalaiselvi, N. Various Aspects of LiNiO_2 Chemistry: A Review. *Sci. Technol. Adv. Mater.* **2005**, *6* (6), 689–703. <https://doi.org/10.1016/j.stam.2005.06.001>.
- (28) Muralidharan, N.; Self, E. C.; Dixit, M.; Du, Z.; Essehli, R.; Amin, R.; Nanda, J.; Belharouak, I. Next-Generation Cobalt-Free Cathodes – A Prospective Solution to the Battery Industry’s Cobalt Problem. *Adv. Energy Mater.* **2022**, *12* (9), 2103050. <https://doi.org/10.1002/aenm.202103050>.
- (29) Myung, S.-T.; Maglia, F.; Park, K.-J.; Yoon, C. S.; Lamp, P.; Kim, S.-J.; Sun, Y.-K. Nickel-Rich Layered Cathode Materials for Automotive Lithium-Ion Batteries: Achievements and Perspectives. *ACS Energy Lett.* **2017**, *2* (1), 196–223. <https://doi.org/10.1021/acseenergylett.6b00594>.
- (30) Assat, G.; Tarascon, J.-M. Fundamental Understanding and Practical Challenges of Anionic Redox Activity in Li-Ion Batteries. *Nat. Energy* **2018**, *3* (5), 373. <https://doi.org/10.1038/s41560-018-0097-0>.
- (31) Noh, H.-J.; Youn, S.; Yoon, C. S.; Sun, Y.-K. Comparison of the Structural and Electrochemical Properties of Layered $\text{Li}[\text{Ni}_x\text{Co}_y\text{Mn}_z]\text{O}_2$ ($x = 1/3, 0.5, 0.6, 0.7, 0.8$ and 0.85) Cathode Material for Lithium-Ion Batteries. *J. Power Sources* **2013**, *233*, 121–130. <https://doi.org/10.1016/j.jpowsour.2013.01.063>.
- (32) Zhang, S.; Ma, J.; Hu, Z.; Cui, G.; Chen, L. Identifying and Addressing Critical Challenges of High-Voltage Layered Ternary Oxide Cathode Materials. *Chem. Mater.* **2019**, *33*.
- (33) Jung, R.; Metzger, M.; Maglia, F.; Stinner, C.; Gasteiger, H. A. Oxygen Release and Its Effect on the Cycling Stability of $\text{LiNi}_x\text{Mn}_y\text{Co}_z\text{O}_2$ (NMC) Cathode Materials for Li-Ion Batteries. *J. Electrochem. Soc.* **2017**, *164* (7), A1361–A1377. <https://doi.org/10.1149/2.0021707jes>.
- (34) Dixit, M.; Markovsky, B.; Schipper, F.; Aurbach, D.; Major, D. T. Origin of Structural Degradation During Cycling and Low Thermal Stability of Ni-Rich Layered Transition Metal-Based Electrode Materials. *J. Phys. Chem. C* **2017**, *121* (41), 22628–22636. <https://doi.org/10.1021/acs.jpcc.7b06122>.
- (35) Gao, H.; Cai, J.; Xu, G.-L.; Li, L.; Ren, Y.; Meng, X.; Amine, K.; Chen, Z. Surface Modification for Suppressing Interfacial Parasitic Reactions of a Nickel-

Rich Lithium-Ion Cathode. *Chem. Mater.* **2019**, *31* (8), 2723–2730. <https://doi.org/10.1021/acs.chemmater.8b04200>.

(36) Sicklinger, J.; Metzger, M.; Beyer, H.; Pritzl, D.; Gasteiger, H. A. Ambient Storage Derived Surface Contamination of NCM811 and NCM111: Performance Implications and Mitigation Strategies. *J. Electrochem. Soc.* **2019**, *166* (12), A2322–A2335. <https://doi.org/10.1149/2.0011912jes>.

(37) Renfrew, S. E.; McCloskey, B. D. Residual Lithium Carbonate Predominantly Accounts for First Cycle CO₂ and CO Outgassing of Li-Stoichiometric and Li-Rich Layered Transition-Metal Oxides. *J. Am. Chem. Soc.* **2017**, *139* (49), 17853–17860. <https://doi.org/10.1021/jacs.7b08461>.

(38) Zhu, J.; Sharifi-Asl, S.; Garcia, J. C.; Iddir, H. H.; Croy, J. R.; Shahbazian-Yassar, R.; Chen, G. Atomic-Level Understanding of Surface Reconstruction Based on Li[Ni_xMn_yCo_{1-x-y}]O₂ Single-Crystal Studies. *ACS Appl. Energy Mater.* **2020**, *3* (5), 4799–4811. <https://doi.org/10.1021/acsaem.0c00411>.

(39) Han, B.; Key, B.; Lapidus, S. H.; Garcia, J. C.; Iddir, H.; Vaughey, J. T.; Dogan, F. From Coating to Dopant: How the Transition Metal Composition Affects Alumina Coatings on Ni-Rich Cathodes. *ACS Appl. Mater. Interfaces* **2017**, *9* (47), 41291–41302. <https://doi.org/10.1021/acsami.7b13597>.

(40) Sun, Y.-K.; Myung, S.-T.; Park, B.-C.; Prakash, J.; Belharouak, I.; Amine, K. High-Energy Cathode Material for Long-Life and Safe Lithium Batteries. *Nat. Mater.* **2009**, *8* (4), 320–324. <https://doi.org/10.1038/nmat2418>.

(41) Yu, L.; Liu, T.; Amine, R.; Wen, J.; Lu, J.; Amine, K. High Nickel and No Cobalt—The Pursuit of Next-Generation Layered Oxide Cathodes. *ACS Appl. Mater. Interfaces* **2022**, *acsami.1c22091*. <https://doi.org/10.1021/acsami.1c22091>.

(42) Celeste, A.; Tuccillo, M.; Santoni, A.; Reale, P.; Brutti, S.; Silvestri, L. Exploring a Co-Free, Li-Rich Layered Oxide with Low Content of Nickel as a Positive Electrode for Li-Ion Battery. *ACS Appl. Energy Mater.* **2021**, *4* (10), 11290–11297. <https://doi.org/10.1021/acsaem.1c02133>.

(43) Steiner, J. D.; Mu, L.; Walsh, J.; Rahman, M. M.; Zydlewski, B.; Michel, F. M.; Xin, H. L.; Nordlund, D.; Lin, F. Accelerated Evolution of Surface Chemistry Determined by Temperature and Cycling History in Nickel-Rich Layered Cathode Materials. *ACS Appl. Mater. Interfaces* **2018**, *10* (28), 23842–23850. <https://doi.org/10.1021/acsami.8b06399>.

(44) Teichert, P.; Jahnke, H.; Figgemeier, E. Degradation Mechanism of Monocrystalline Ni-Rich Li[Ni_xMn_yCo_z]O₂ (NMC) Active Material in Lithium Ion Batteries. *J. Electrochem. Soc.* **2021**, *168* (9), 090532. <https://doi.org/10.1149/1945-7111/ac239f>.

(45) Lin, Q.; Guan, W.; Meng, J.; Huang, W.; Wei, X.; Zeng, Y.; Li, J.; Zhang, Z. A New Insight into Continuous Performance Decay Mechanism of Ni-Rich Layered Oxide Cathode for High Energy Lithium Ion Batteries. *Nano Energy* **2018**, *54*, 313–321. <https://doi.org/10.1016/j.nanoen.2018.09.066>.

(46) Wei, H.; Tang, L.; Huang, Y.; Wang, Z.; Luo, Y.; He, Z.; Yan, C.; Mao, J.; Dai, K.; Zheng, J. Comprehensive Understanding of Li/Ni Intermixing in Layered

- Transition Metal Oxides. *Mater. Today* **2021**, *51*, 365–392. <https://doi.org/10.1016/j.mattod.2021.09.013>.
- (47) Rozier, P.; Tarascon, J. M. Review—Li-Rich Layered Oxide Cathodes for Next-Generation Li-Ion Batteries: Chances and Challenges. *J. Electrochem. Soc.* **2015**, *162* (14), A2490–A2499. <https://doi.org/10.1149/2.0111514jes>.
- (48) Lee, W.; Muhammad, S.; Kim, T.; Kim, H.; Lee, E.; Jeong, M.; Son, S.; Ryou, J.-H.; Yoon, W.-S. New Insight into Ni-Rich Layered Structure for Next-Generation Li Rechargeable Batteries. *Adv. Energy Mater.* **2018**, *8* (4), 1701788. <https://doi.org/10.1002/aenm.201701788>.
- (49) Lin, F.; Nordlund, D.; Markus, I. M.; Weng, T.-C.; Xin, H. L.; Doeff, M. M. Profiling the Nanoscale Gradient in Stoichiometric Layered Cathode Particles for Lithium-Ion Batteries. *Energy Environ. Sci.* **2014**, *7* (9), 3077–3085. <https://doi.org/10.1039/C4EE01400F>.
- (50) Kim, N. Y.; Yim, T.; Song, J. H.; Yu, J.-S.; Lee, Z. Microstructural Study on Degradation Mechanism of Layered $\text{LiNi}_{0.6}\text{Co}_{0.2}\text{Mn}_{0.2}\text{O}_2$ Cathode Materials by Analytical Transmission Electron Microscopy. *J. Power Sources* **2016**, *307*, 641–648. <https://doi.org/10.1016/j.jpowsour.2016.01.023>.
- (51) Zhang, S. S. Understanding of Performance Degradation of $\text{LiNi}_{0.80}\text{Co}_{0.10}\text{Mn}_{0.10}\text{O}_2$ Cathode Material Operating at High Potentials. *J. Energy Chem.* **2020**, *41*, 135–141. <https://doi.org/10.1016/j.jechem.2019.05.013>.
- (52) Ohzuku, T.; Ueda, A.; Nagayama, M. Electrochemistry and Structural Chemistry of LiNiO_2 ($R\bar{3}m$) for 4 Volt Secondary Lithium Cells. *J. Electrochem. Soc.* **1993**, *140* (7), 1862–1870. <https://doi.org/10.1149/1.2220730>.
- (53) Li, W.; Reimers, J. N.; Dahn, J. R. In Situ X-Ray Diffraction and Electrochemical Studies of $\text{Li}_{1-x}\text{NiO}_2$. *Solid State Ion.* **1993**, *67* (1), 123–130. [https://doi.org/10.1016/0167-2738\(93\)90317-V](https://doi.org/10.1016/0167-2738(93)90317-V).
- (54) Arai, H.; Okada, S.; Ohtsuka, H.; Ichimura, M.; Yamaki, J. Characterization and Cathode Performance of $\text{Li}_{1-x}\text{Ni}_{1+x}\text{O}_2$ Prepared with the Excess Lithium Method. *Solid State Ion.* **1995**, *80* (3), 261–269. [https://doi.org/10.1016/0167-2738\(95\)00144-U](https://doi.org/10.1016/0167-2738(95)00144-U).
- (55) Belharouak, I.; Lu, W.; Vissers, D.; Amine, K. Safety Characteristics of $\text{Li}(\text{Ni}_{0.8}\text{Co}_{0.15}\text{Al}_{0.05})\text{O}_2$ and $\text{Li}(\text{Ni}_{1/3}\text{Co}_{1/3}\text{Mn}_{1/3})\text{O}_2$. *Electrochem. Commun.* **2006**, *8* (2), 329–335. <https://doi.org/10.1016/j.elecom.2005.12.007>.
- (56) Li, J.; Liu, H.; Xia, J.; Cameron, A. R.; Nie, M.; Botton, G. A.; Dahn, J. R. The Impact of Electrolyte Additives and Upper Cut-off Voltage on the Formation of a Rocksalt Surface Layer in $\text{LiNi}_{0.8}\text{Mn}_{0.1}\text{Co}_{0.1}\text{O}_2$ Electrodes. *J. Electrochem. Soc.* **2017**, *164* (4), A655–A665. <https://doi.org/10.1149/2.0651704jes>.
- (57) Li, X.; Colclasure, A. M.; Finegan, D. P.; Ren, D.; Shi, Y.; Feng, X.; Cao, L.; Yang, Y.; Smith, K. Degradation Mechanisms of High Capacity 18650 Cells Containing Si-Graphite Anode and Nickel-Rich NMC Cathode. *Electrochim. Acta* **2019**, *297*, 1109–1120. <https://doi.org/10.1016/j.electacta.2018.11.194>.
- (58) Park, K.-J.; Hwang, J.-Y.; Ryu, H.-H.; Maglia, F.; Kim, S.-J.; Lamp, P.; Yoon, C. S.; Sun, Y.-K. Degradation Mechanism of Ni-Enriched NCA Cathode for

Lithium Batteries: Are Microcracks Really Critical? *ACS Energy Lett.* **2019**, *4* (6), 1394–1400. <https://doi.org/10.1021/acsenergylett.9b00733>.

(59) Shkrob, I. A.; Gilbert, J. A.; Phillips, P. J.; Klie, R.; Haasch, R. T.; Bareño, J.; Abraham, D. P. Chemical Weathering of Layered Ni-Rich Oxide Electrode Materials: Evidence for Cation Exchange. *J. Electrochem. Soc.* **2017**, *164* (7), A1489–A1498. <https://doi.org/10.1149/2.0861707jes>.

(60) Faenza, N. V.; Bruce, L.; Lebens-Higgins, Z. W.; Plitz, I.; Pereira, N.; Piper, L. F. J.; Amatucci, G. G. Editors' Choice—Growth of Ambient Induced Surface Impurity Species on Layered Positive Electrode Materials and Impact on Electrochemical Performance. *J. Electrochem. Soc.* **2017**, *164* (14), A3727–A3741. <https://doi.org/10.1149/2.0921714jes>.

(61) Lee, W.; Lee, S.; Lee, E.; Choi, M.; Thangavel, R.; Lee, Y.; Yoon, W.-S. Destabilization of the Surface Structure of Ni-Rich Layered Materials by Water-Washing Process. *Energy Storage Mater.* **2022**, *44*, 441–451. <https://doi.org/10.1016/j.ensm.2021.11.006>.

(62) Jung, R.; Morasch, R.; Karayaylali, P.; Phillips, K.; Maglia, F.; Stinner, C.; Shao-Horn, Y.; Gasteiger, H. A. Effect of Ambient Storage on the Degradation of Ni-Rich Positive Electrode Materials (NMC811) for Li-Ion Batteries. *J. Electrochem. Soc.* **2018**, *165* (2), A132–A141. <https://doi.org/10.1149/2.0401802jes>.

(63) Busà, C.; Belekoukia, M.; Loveridge, M. J. The Effects of Ambient Storage Conditions on the Structural and Electrochemical Properties of NMC-811 Cathodes for Li-Ion Batteries. *Electrochim. Acta* **2021**, *366*, 137358. <https://doi.org/10.1016/j.electacta.2020.137358>.

(64) Seong, W. M.; Kim, Y.; Manthiram, A. Impact of Residual Lithium on the Adoption of High-Nickel Layered Oxide Cathodes for Lithium-Ion Batteries. *Chem. Mater.* **2020**, <https://doi.org/10.1021/acs.chemmater.0c02808>.

(65) Jiang, M.; Danilov, D. L.; Eichel, R.-A.; Notten, P. H. L. A Review of Degradation Mechanisms and Recent Achievements for Ni-Rich Cathode-Based Li-Ion Batteries. *Adv. Energy Mater.* **2021**, 2103005. <https://doi.org/10.1002/aenm.202103005>.

(66) Park, K.-J.; Choi, M.-J.; Maglia, F.; Kim, S.-J.; Kim, K.-H.; Yoon, C. S.; Sun, Y.-K. High-Capacity Concentration Gradient Li[Ni_{0.865}Co_{0.120}Al_{0.015}]O₂ Cathode for Lithium-Ion Batteries. *Adv. Energy Mater.* **2018**, *8* (19), 1703612. <https://doi.org/10.1002/aenm.201703612>.

(67) Berkes, B. B.; Jozwiuk, A.; Sommer, H.; Brezesinski, T.; Janek, J. Simultaneous Acquisition of Differential Electrochemical Mass Spectrometry and Infrared Spectroscopy Data for in Situ Characterization of Gas Evolution Reactions in Lithium-Ion Batteries. *Electrochem. Commun.* **2015**, *60*, 64–69. <https://doi.org/10.1016/j.elecom.2015.08.002>.

(68) La Mantia, F.; Rosciano, F.; Tran, N.; Novák, P. Direct Evidence of Oxygen Evolution from Li_{1+x}(Ni_{1/3}Mn_{1/3}Co_{1/3})_{1-x}O₂ at High Potentials. *J. Appl. Electrochem.* **2008**, *38* (7), 893–896. <https://doi.org/10.1007/s10800-008-9491-9>.

- (69) Mantia, F. L.; Rosciano, F.; Tran, N.; Novák, P. Quantification of Oxygen Loss from $\text{Li}_{1-x}(\text{Ni}_{1/3}\text{Mn}_{1/3}\text{Co}_{1/3})_{1-x}\text{O}_2$ at High Potentials by Differential Electrochemical Mass Spectrometry. *J. Electrochem. Soc.* **2009**, *156* (11), A823–A827. <https://doi.org/10.1149/1.3205495>.
- (70) Holzapfel, M.; Würsig, A.; Scheifele, W.; Vetter, J.; Novák, P. Oxygen, Hydrogen, Ethylene and CO_2 Development in Lithium-Ion Batteries. *J. Power Sources* **2007**, *174* (2), 1156–1160. <https://doi.org/10.1016/j.jpowsour.2007.06.182>.
- (71) Armstrong, A. R.; Holzapfel, M.; Novák, P.; Johnson, C. S.; Kang, S.-H.; Thackeray, M. M.; Bruce, P. G. Demonstrating Oxygen Loss and Associated Structural Reorganization in the Lithium Battery Cathode $\text{Li}[\text{Ni}_{0.2}\text{Li}_{0.2}\text{Mn}_{0.6}]\text{O}_2$. *J. Am. Chem. Soc.* **2006**, *128* (26), 8694–8698. <https://doi.org/10.1021/ja062027+>.
- (72) Imhof, R.; Novák, P. Oxidative Electrolyte Solvent Degradation in Lithium-Ion Batteries: An In Situ Differential Electrochemical Mass Spectrometry Investigation. *J. Electrochem. Soc.* **1999**, *146* (5), 1702–1706. <https://doi.org/10.1149/1.1391829>.
- (73) Tsukasaki, H.; Fukuda, W.; Morimoto, H.; Arai, T.; Mori, S.; Hayashi, A.; Tatsumisago, M. Thermal Behavior and Microstructures of Cathodes for Liquid Electrolyte-Based Lithium Batteries. *Sci. Rep.* **2018**, *8* (1), 15613. <https://doi.org/10.1038/s41598-018-34017-2>.
- (74) Chen, M.; Zhao, E.; Chen, D.; Wu, M.; Han, S.; Huang, Q.; Yang, L.; Xiao, X.; Hu, Z. Decreasing Li/Ni Disorder and Improving the Electrochemical Performances of Ni-Rich $\text{LiNi}_{0.8}\text{Co}_{0.1}\text{Mn}_{0.1}\text{O}_2$ by Ca Doping. *Inorg. Chem.* **2017**, *56* (14), 8355–8362. <https://doi.org/10.1021/acs.inorgchem.7b01035>.
- (75) Min, K.; Seo, S.-W.; Song, Y. Y.; Lee, H. S.; Cho, E. A First-Principles Study of the Preventive Effects of Al and Mg Doping on the Degradation in $\text{LiNi}_{0.8}\text{Co}_{0.1}\text{Mn}_{0.1}\text{O}_2$ Cathode Materials. *Phys. Chem. Chem. Phys.* **2017**, *19* (3), 1762–1769. <https://doi.org/10.1039/C6CP06270A>.
- (76) Schipper, F.; Dixit, M.; Kovacheva, D.; Talianker, M.; Haik, O.; Grinblat, J.; Erickson, E. M.; Ghanty, C.; Major, D. T.; Markovsky, B.; Aurbach, D. Stabilizing Nickel-Rich Layered Cathode Materials by a High-Charge Cation Doping Strategy: Zirconium-Doped $\text{LiNi}_{0.6}\text{Co}_{0.2}\text{Mn}_{0.2}\text{O}_2$. *J. Mater. Chem. A* **2016**, *4* (41), 16073–16084. <https://doi.org/10.1039/C6TA06740A>.
- (77) Zhang, S. S.; Chen, J.; Wang, C. Elemental Sulfur as a Cathode Additive for Enhanced Rate Capability of Layered Lithium Transition Metal Oxides. *J. Electrochem. Soc.* **2019**, *166* (4), A487–A492. <https://doi.org/10.1149/2.0101904jes>.
- (78) Park, H. G.; Min, K.; Park, K. A Synergistic Effect of Na^+ and Al^{3+} Dual Doping on Electrochemical Performance and Structural Stability of $\text{LiNi}_{0.88}\text{Co}_{0.08}\text{Mn}_{0.04}\text{O}_2$ Cathodes for Li-Ion Batteries. *ACS Appl. Mater. Interfaces* **2022**, *14* (4), 5168–5176. <https://doi.org/10.1021/acsami.1c16042>.
- (79) Lv, Y.; Cheng, X.; Qiang, W.; Huang, B. Improved Electrochemical Performances of Ni-Rich $\text{LiNi}_{0.83}\text{Co}_{0.12}\text{Mn}_{0.05}\text{O}_2$ by Mg-Doping. *J. Power Sources* **2020**, *450*, 227718. <https://doi.org/10.1016/j.jpowsour.2020.227718>.

- (80) Ni, L.; Chen, H.; Deng, W.; Wang, B.; Chen, J.; Mei, Y.; Zou, G.; Hou, H.; Guo, R.; Xie, J.; Ji, X. Atomical Reconstruction and Cationic Reordering for Nickel-Rich Layered Cathodes. *Adv. Energy Mater.* **2022**, 2103757. <https://doi.org/10.1002/aenm.202103757>.
- (81) Jeong, M.; Kim, H.; Lee, W.; Ahn, S.-J.; Lee, E.; Yoon, W.-S. Stabilizing Effects of Al-Doping on Ni-Rich $\text{LiNi}_{0.80}\text{Co}_{0.15}\text{Mn}_{0.05}\text{O}_2$ Cathode for Li Rechargeable Batteries. *J. Power Sources* **2020**, 474, 228592. <https://doi.org/10.1016/j.jpowsour.2020.228592>.
- (82) Jung, C.-H.; Kim, D.-H.; Eum, D.; Kim, K.-H.; Choi, J.; Lee, J.; Kim, H.-H.; Kang, K.; Hong, S.-H. New Insight into Microstructure Engineering of Ni-Rich Layered Oxide Cathode for High Performance Lithium Ion Batteries. *Adv. Funct. Mater.* **2021**, 31 (18), 2010095. <https://doi.org/10.1002/adfm.202010095>.
- (83) Wu, L.; Tang, X.; Chen, X.; Rong, Z.; Dang, W.; Wang, Y.; Li, X.; Huang, L.; Zhang, Y. Improvement of Electrochemical Reversibility of the Ni-Rich Cathode Material by Gallium Doping. *J. Power Sources* **2020**, 445, 227337. <https://doi.org/10.1016/j.jpowsour.2019.227337>.
- (84) Wu, F.; Liu, N.; Chen, L.; Su, Y.; Tan, G.; Bao, L.; Zhang, Q.; Lu, Y.; Wang, J.; Chen, S.; Tan, J. Improving the Reversibility of the H2-H3 Phase Transitions for Layered Ni-Rich Oxide Cathode towards Retarded Structural Transition and Enhanced Cycle Stability. *Nano Energy* **2019**, 59, 50–57. <https://doi.org/10.1016/j.nanoen.2019.02.027>.
- (85) Chu, B.; Liu, S.; You, L.; Liu, D.; Huang, T.; Li, Y.; Yu, A. Enhancing the Cycling Stability of Ni-Rich $\text{LiNi}_{0.6}\text{Co}_{0.2}\text{Mn}_{0.2}\text{O}_2$ Cathode at a High Cutoff Voltage with Ta Doping. *ACS Sustain. Chem. Eng.* **2020**, 8 (8), 3082–3090. <https://doi.org/10.1021/acssuschemeng.9b05560>.
- (86) Levartovsky, Y.; Chakraborty, A.; Kunnikuruvan, S.; Maiti, S.; Grinblat, J.; Talianker, M.; Major, D. T.; Aurbach, D. Enhancement of Structural, Electrochemical, and Thermal Properties of High-Energy Density Ni-Rich $\text{LiNi}_{0.85}\text{Co}_{0.1}\text{Mn}_{0.05}\text{O}_2$ Cathode Materials for Li-Ion Batteries by Niobium Doping. *ACS Appl. Mater. Interfaces* **2021**, 13 (29), 34145–34156. <https://doi.org/10.1021/acsam.1c06839>.
- (87) Su, Y.; Yang, Y.; Chen, L.; Lu, Y.; Bao, L.; Chen, G.; Yang, Z.; Zhang, Q.; Wang, J.; Chen, R.; Chen, S.; Wu, F. Improving the Cycling Stability of Ni-Rich Cathode Materials by Fabricating Surface Rock Salt Phase. *Electrochim. Acta* **2018**, 292, 217–226. <https://doi.org/10.1016/j.electacta.2018.09.158>.
- (88) Park, G.-T.; Ryu, H.-H.; Park, N.-Y.; Yoon, C. S.; Sun, Y.-K. Tungsten Doping for Stabilization of $\text{Li}[\text{Ni}_{0.90}\text{Co}_{0.05}\text{Mn}_{0.05}]\text{O}_2$ Cathode for Li-Ion Battery at High Voltage. *J. Power Sources* **2019**, 442, 227242. <https://doi.org/10.1016/j.jpowsour.2019.227242>.
- (89) Kim, U.-H.; Park, G.-T.; Conlin, P.; Ashburn, N.; Cho, K.; Yu, Y.-S.; Shapiro, D. A.; Maglia, F.; Kim, S.-J.; Lamp, P.; Yoon, C. S.; Sun, Y.-K. Cation Ordered Ni-Rich Layered Cathode for Ultra-Long Battery Life. *Energy Environ. Sci.* **2021**, 14 (3), 1573–1583. <https://doi.org/10.1039/D0EE03774E>.

- (90) He, S.; Wei, A.; Li, W.; Bai, X.; Zhang, L.; Li, X.; He, R.; Yang, L.; Liu, Z. An In-Depth Analysis Detailing the Structural and Electrochemical Properties within Br⁻ Modified LiNi_{0.815}Co_{0.15}A_{0.035}O₂ (NCA) Cathode Material. *Electrochimica Acta* **2019**, *318*, 362–373. <https://doi.org/10.1016/j.electacta.2019.06.061>.
- (91) Nelson, K. J.; Abarbanel, D. W.; Xia, J.; Lu, Z.; Dahn, J. R. Effects of Upper Cutoff Potential on LaPO₄-Coated and Uncoated Li[Ni_{0.42}Mn_{0.42}Co_{0.16}]O₂ /Graphite Pouch Cells. *J. Electrochem. Soc.* **2016**, *163* (2), A272–A280. <https://doi.org/10.1149/2.0691602jes>.
- (92) Laskar, M. R.; Jackson, D. H. K.; Guan, Y.; Xu, S.; Fang, S.; Dreibelbis, M.; Mahanthappa, M. K.; Morgan, D.; Hamers, R. J.; Kuech, T. F. Atomic Layer Deposition of Al₂O₃–Ga₂O₃ Alloy Coatings for Li[Ni_{0.5}Mn_{0.3}Co_{0.2}]O₂ Cathode to Improve Rate Performance in Li-Ion Battery. *ACS Appl. Mater. Interfaces* **2016**, *8* (16), 10572–10580. <https://doi.org/10.1021/acsami.5b11878>.
- (93) Laskar, M. R.; Jackson, D. H. K.; Xu, S.; Hamers, R. J.; Morgan, D.; Kuech, T. F. Atomic Layer Deposited MgO: A Lower Overpotential Coating for Li[Ni_{0.5}Mn_{0.3}Co_{0.2}]O₂ Cathode. *ACS Appl. Mater. Interfaces* **2017**, *9* (12), 11231–11239. <https://doi.org/10.1021/acsami.6b16562>.
- (94) Jackson, D. H. K.; Kuech, T. F. Electrochemical Effects of Annealing on Atomic Layer Deposited Al₂O₃ Coatings on LiNi_{0.5}Mn_{0.3}Co_{0.2}O₂. *J. Power Sources* **2017**, *365*, 61–67. <https://doi.org/10.1016/j.jpowsour.2017.08.076>.
- (95) Liu, S.; Dang, Z.; Liu, D.; Zhang, C.; Huang, T.; Yu, A. Comparative Studies of Zirconium Doping and Coating on LiNi_{0.6}Co_{0.2}Mn_{0.2}O₂ Cathode Material at Elevated Temperatures. *J. Power Sources* **2018**, *396*, 288–296. <https://doi.org/10.1016/j.jpowsour.2018.06.052>.
- (96) Han, B.; Paulauskas, T.; Key, B.; Peebles, C.; Park, J. S.; Klie, R. F.; Vaughey, J. T.; Dogan, F. Understanding the Role of Temperature and Cathode Composition on Interface and Bulk: Optimizing Aluminum Oxide Coatings for Li-Ion Cathodes. *ACS Appl. Mater. Interfaces* **2017**, *9* (17), 14769–14778. <https://doi.org/10.1021/acsami.7b00595>.
- (97) Gao, H.; Zeng, X.; Hu, Y.; Tileli, V.; Li, L.; Ren, Y.; Meng, X.; Maglia, F.; Lamp, P.; Kim, S.-J.; Amine, K.; Chen, Z. Modifying the Surface of a High-Voltage Lithium-Ion Cathode. *ACS Appl. Energy Mater.* **2018**, *1* (5), 2254–2260. <https://doi.org/10.1021/acsaem.8b00323>.
- (98) Woo, S.-U.; Yoon, C. S.; Amine, K.; Belharouak, I.; Sun, Y.-K. Significant Improvement of Electrochemical Performance of AlF₃-Coated Li[Ni_{0.8}Co_{0.1}Mn_{0.1}]O₂ Cathode Materials. *J. Electrochem. Soc.* **2007**, *154* (11), A1005–A1009. <https://doi.org/10.1149/1.2776160>.
- (99) Yuan, H.; Song, W.; Wang, M.; Gu, Y.; Chen, Y. Lithium-Ion Conductive Coating Layer on Nickel Rich Layered Oxide Cathode Material with Improved Electrochemical Properties for Li-Ion Battery. *J. Alloys Compd.* **2019**, *784*, 1311–1322. <https://doi.org/10.1016/j.jallcom.2019.01.072>.
- (100) Hu, W.; Zhang, C.; Jiang, H.; Zheng, M.; Wu, Q.-H.; Dong, Q. Improving the Electrochemistry Performance of Layer LiNi_{0.5}Mn_{0.3}Co_{0.2}O₂ Material at 4.5V

Cutoff Potential Using Lithium Metaborate. *Electrochim. Acta* **2017**, *243*, 105–111. <https://doi.org/10.1016/j.electacta.2017.05.075>.

(101) Wu, Z.; Ji, S.; Liu, T.; Duan, Y.; Xiao, S.; Lin, Y.; Xu, K.; Pan, F. Aligned Li⁺ Tunnels in Core–Shell Li(Ni_xMn_yCo_z)O₂@LiFePO₄ Enhances Its High Voltage Cycling Stability as Li-Ion Battery Cathode. *Nano Lett.* **2016**, *16* (10), 6357–6363. <https://doi.org/10.1021/acs.nanolett.6b02742>.

(102) Kim, J.-M.; Zhang, X.; Zhang, J.-G.; Manthiram, A.; Meng, Y. S.; Xu, W. A Review on the Stability and Surface Modification of Layered Transition-Metal Oxide Cathodes. *Mater. Today* **2021**, *46*, 155–182. <https://doi.org/10.1016/j.mattod.2020.12.017>.

(103) Zhang, J.; Yang, Z.; Gao, R.; Gu, L.; Hu, Z.; Liu, X. Suppressing the Structure Deterioration of Ni-Rich LiNi_{0.8}Co_{0.1}Mn_{0.1}O₂ through Atom-Scale Interfacial Integration of Self-Forming Hierarchical Spinel Layer with Ni Gradient Concentration. *ACS Appl. Mater. Interfaces* **2017**, *9* (35), 29794–29803. <https://doi.org/10.1021/acsami.7b08802>.

(104) Liao, J.-Y.; Manthiram, A. Surface-Modified Concentration-Gradient Ni-Rich Layered Oxide Cathodes for High-Energy Lithium-Ion Batteries. *J. Power Sources* **2015**, *282*, 429–436. <https://doi.org/10.1016/j.jpowsour.2015.02.078>.

(105) Liu, T.; Yu, L.; Lu, J.; Zhou, T.; Huang, X.; Cai, Z.; Dai, A.; Gim, J.; Ren, Y.; Xiao, X.; Holt, M. V.; Chu, Y. S.; Arslan, I.; Wen, J.; Amine, K. Rational Design of Mechanically Robust Ni-Rich Cathode Materials via Concentration Gradient Strategy. *Nat. Commun.* **2021**, *12* (1), 6024. <https://doi.org/10.1038/s41467-021-26290-z>.

(106) Nomura, Y.; Yamamoto, K.; Hirayama, T.; Igaki, E.; Saitoh, K. Visualization of Lithium Transfer Resistance in Secondary Particle Cathodes of Bulk-Type Solid-State Batteries. *ACS Energy Lett.* **2020**, *5* (6), 2098–2105. <https://doi.org/10.1021/acsenergylett.0c00942>.

(107) Gu, M.; Belharouak, I.; Genc, A.; Wang, Z.; Wang, D.; Amine, K.; Gao, F.; Zhou, G.; Thevuthasan, S.; Baer, D. R.; Zhang, J.-G.; Browning, N. D.; Liu, J.; Wang, C. Conflicting Roles of Nickel in Controlling Cathode Performance in Lithium Ion Batteries. *Nano Lett* **2012**, *6*.

(108) Shukla, A. K.; Ramasse, Q. M.; Ophus, C.; Duncan, H.; Hage, F.; Chen, G. Unravelling Structural Ambiguities in Lithium- and Manganese-Rich Transition Metal Oxides. *Nat. Commun.* **2015**, *6* (1), 8711. <https://doi.org/10.1038/ncomms9711>.

(109) Yan, P.; Zheng, J.; Zheng, J.; Wang, Z.; Teng, G.; Kuppen, S.; Xiao, J.; Chen, G.; Pan, F.; Zhang, J.-G.; Wang, C.-M. Ni and Co Segregations on Selective Surface Facets and Rational Design of Layered Lithium Transition-Metal Oxide Cathodes. *Adv. Energy Mater.* **2016**, *6* (9), 1502455. <https://doi.org/10.1002/aenm.201502455>.

(110) Nomura, Y.; Yamamoto, K.; Hirayama, T.; Ohkawa, M.; Igaki, E.; Hojo, N.; Saitoh, K. Quantitative *Operando* Visualization of Electrochemical Reactions and Li Ions in All-Solid-State Batteries by STEM-EELS with Hyperspectral Image

Analyses. *Nano Lett.* **2018**, *18* (9), 5892–5898. <https://doi.org/10.1021/acs.nanolett.8b02587>.

(111) Lee, H. B.; Dinh Hoang, T.; Byeon, Y. S.; Jung, H.; Moon, J.; Park, M.-S. Surface Stabilization of Ni-Rich Layered Cathode Materials via Surface Engineering with LiTaO₃ for Lithium-Ion Batteries. *ACS Appl. Mater. Interfaces* **2022**, *14* (2), 2731–2741. <https://doi.org/10.1021/acsami.1c19443>.

(112) Jung, S.-K.; Gwon, H.; Hong, J.; Park, K.-Y.; Seo, D.-H.; Kim, H.; Hyun, J.; Yang, W.; Kang, K. Understanding the Degradation Mechanisms of LiNi_{0.5}Co_{0.2}Mn_{0.3}O₂ Cathode Material in Lithium Ion Batteries. *Adv. Energy Mater.* **2014**, *4* (1), 1300787. <https://doi.org/10.1002/aenm.201300787>.

(113) Lee, S.; Li, W.; Dolocan, A.; Celio, H.; Park, H.; Warner, J. H.; Manthiram, A. In-Depth Analysis of the Degradation Mechanisms of High-Nickel, Low/No-Cobalt Layered Oxide Cathodes for Lithium-Ion Batteries. *Adv. Energy Mater.* **2021**, *11* (31), 2100858. <https://doi.org/10.1002/aenm.202100858>.

Chapter 2

Characterisation Techniques

The importance of a study conducted on industrial samples in having a clear picture of materials, without any influence of the material synthesis method, was already discussed in Chapter 1. However, advantages from an academy-industry collaboration are on both sides. From an industrial point of view, working together with academic partners provides the possibility to characterise samples using advanced techniques not usually available in the materials development centres. In this context, the biggest asset of the Institut des Matériaux de Nantes Jean Rouxel is the possibility to access instruments –and human competences– allowing an extensive and exhaustive surface characterisation. The presence of MAS-NMR, XPS, TEM and SEM-FIB on-site enables the analysis of materials always having the same history, avoiding problems related to the possibility of further surface reactions during shipping to external laboratories. Moreover, the presence of a single user facilitates the data interpretation and the possible links between results coming from different techniques.

The purpose of this chapter is to introduce the principles of the characterisation techniques used to analyse Umicore materials in this project, in order to give every reader some common basis, essential to seize the principal results of this work. In doing so, limits and difficulties encountered during sample preparation, data acquisition and/or treatment will be presented here giving practical examples from the conducted research, and showing how a multi-analytical approach is the only possible way to overcome these limitations and obtain complete information. At the end of each part, the experimental conditions used for data acquisitions will be briefly summarised to ease their consultation.

Part 1. Transmission Electron Microscopy

Transmission Electron Microscopy (TEM) is a high resolution imaging and spectroscopy technique indispensable for chemical, structural and morphological characterisations at a nanometric scale, essential when macroscopic properties are controlled by nanometric defects or interfaces. TEM is based on the interaction between a high energy electron beam and a solid (or liquid in some conditions) specimen to obtain a high resolution image. Secondary signals can then be exploited to obtain information about the composition, atomic bindings and electronic structure down to the nanometric level.

A probe corrected Themis-Z G3 by Thermo Fisher equipped with a Schottky X-FEG gun and a monochromator purchased as a part of the CIMEN (Centre Interdisciplinaire de Microscopie de Nantes) action was used for all the acquisitions that will be presented in this manuscript.

The aim of this first part is to provide a brief description of the instrument, then focusing more on spectroscopy methods, the main subject of this study.

1.1. Basic principles and instrument description

Transmission Electron Microscopy being an extremely complex technique, as well as the instrument used for it, we will let Williams and Carter explaining it in detail.¹ This section will be instead very general, with the aim at focusing on aspects more related with this PhD work only. More details about components related to spectroscopy — such as EDX detectors, the monochromator and cameras used for EELS— will be given in Sections 1.2.1.1 and 1.2.2.1.

Figure 2.1a shows the schematic representation of the principal components constituting the transmission electron microscope used for the analysis. For an easier description of the instrument, we can divide its components into three parts: the illumination system, objective lens and sample holder, and imaging system.

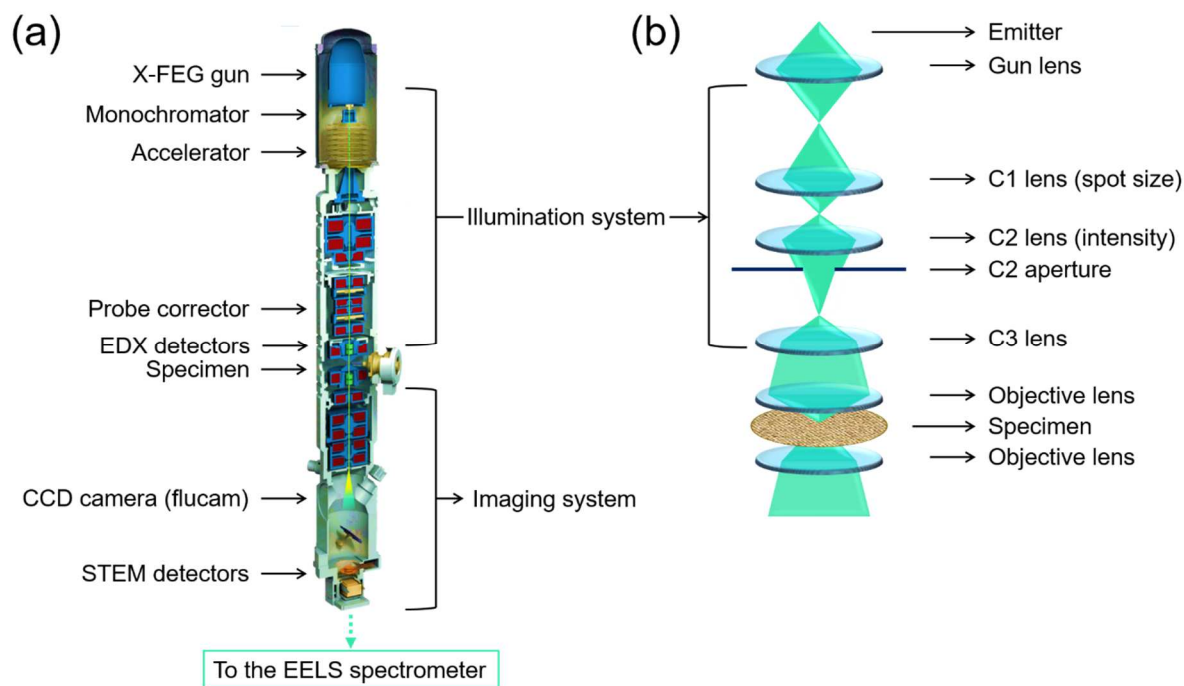


Figure 2.1. Schematic representation of the principal components of the Nant/Themis (Thermo Fisher Scientific S/TEM Themis Z G3), with a focus on its particular illumination system (b) characterised by the presence of three condenser lenses.

The illumination system is constituted by the electron source and condenser lenses, and it has the function of collecting electrons and transferring them from the source to the sample. Electrons are generated by a Field Emission Gun (the X-FEG) consisting in a tungsten tip (the cathode) and an anode that provide the necessary voltage for their extraction from the tip; they are then accelerated to 100 kV or more by a second anode. FEGs are high-brilliance electrons sources providing higher brightness and current density, together with smaller probe size and narrower electron-energy dispersion, when compared to purely thermionic sources. These characteristics make the microscope more suitable for applications needing high spatial and energy resolutions.

The so-generated electrons are then focused on the sample by a system of lenses and apertures. Figure 2.1b represents a typical illumination system in STEM mode. Its role is to focus the beam, obtaining an appropriate current intensity and probe size.

The focused electron beam interacts then with the sample, usually put on a copper grid covered by a carbon membrane. The grid is thence placed in a specimen holder

like the one represented in Figure 2.2. Actually, many holders are available depending on the analysis to be performed (EDX, tomography etc.) and the specifics of the sample to be analysed (sensible to electron beam or not). The peculiarity of the sample holder in Figure 2.2 (the one used for all the observations in this work) is the possibility to retract the tip containing the grid and to close it inside the sample holder, maintaining a controlled atmosphere. The small joint provides in fact the complete airtightness preventing air-sensitive samples from reacting with ambient atmosphere. Once inside the microscope, the sample holder can be opened again to allow for the interaction between the specimen and the electron beam. Images and diffraction patterns are thence created as a consequence of all the beam-specimen interactions that take place here.



Figure 2.2. Airtight TEM sample holder.

Transmitted electrons pass through another system of lenses, the imaging system, which role is to focus the image coming from the lower-objective lens on a viewing screen or computer via a detector, a charge-coupled device (CCD) or a TV camera depending on the imaging mode (TEM or STEM). Different electron detectors are available for imaging in STEM mode and it is the user's role to choose the suitable one for the acquisition, according to the information to be collected.

1.2. Spectroscopies in a TEM

As briefly mentioned in the introduction to this part, secondary signals coming from the electrons-specimen interactions can be exploited by different spectroscopy techniques to obtain more information about the sample than its morphology or

structure. Interactions used in Energy-Dispersive X-ray spectroscopy (EDX) and EELS are schematised in Figure 2.3 and will be explained in the following sections.

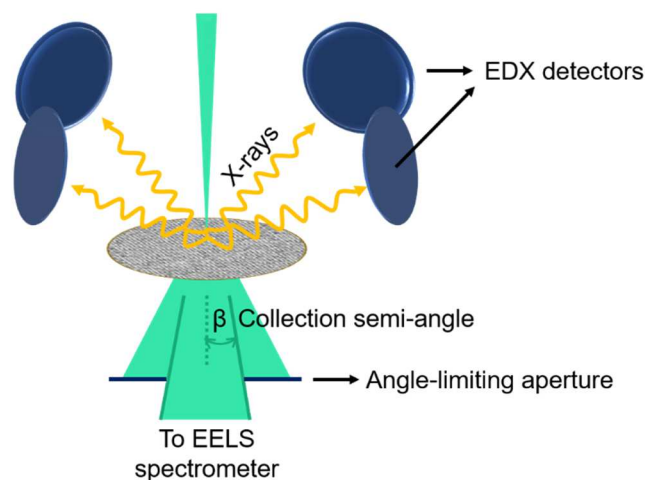


Figure 2.3. Schematic representation of interactions exploited by EDX and EEL Spectroscopy in a TEM.

1.2.1. Energy-Dispersive X-ray Spectroscopy (EDX)

When an atom is exposed to X-rays, electrons can be expelled from inner orbitals because of the high energy of the incident radiation. These electrons create core holes in the excited atom, which can decay either by Auger emission or by X-ray emission. The latter is a phenomenon that occurs when a secondary electron decays to fill the core hole by emitting an X-ray photon. The emitted radiation has an element-characteristic energy equal to the difference in energy between the two orbitals involved in the electronic transition. Since each atom has orbitals with a characteristic energy, by measuring the energy of the emitted photon it is possible to identify the kind of emitting atom. Furthermore, by measuring the intensity of each emission, it is possible to determine the relative quantity of the emitting element.

1.2.1.1. Instrument configuration and technique limitations

The specific configuration of the used Themis Z consists in four EDX detectors situated upon the sample holder (Figure 2.3), allowing the best possible collection of X-rays. In a typical example on a TEM lamella (Figure 2.4), the analysed area is usually situated near the thick copper grid and some detectors are therefore shaded, inducing false

results. Moreover, the possibility of selecting only some detectors during the data analysis in Velox (the program used for the EDX spectra acquisition and treatment) allows excluding detectors having low signal and focus on real data only.

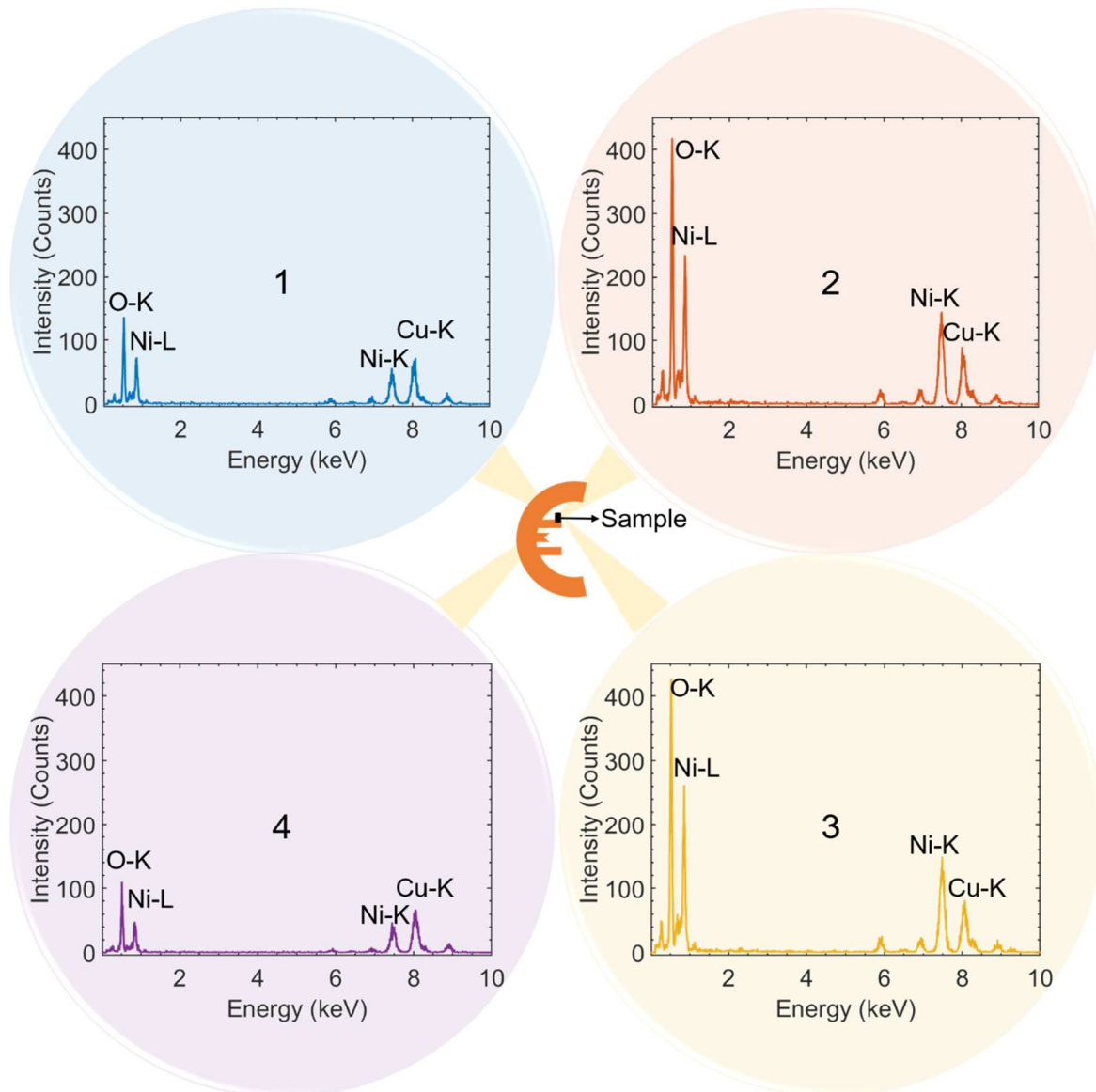


Figure 2.4. Contribution from each EDX detector (from 1 to 4) during the analysis of a typical TEM lamella prepared by FIB. The copper grid (in orange), together with the sample (in black), are represented in the middle of the image; their orientation is the one suggested by the analysis of the spectra of each detector.

Figure 2.4 displays the spectra corresponding to each detector in an acquisition performed on a TEM lamella prepared by FIB. Spectra from detectors 1 and 4 are quite different from those recorded by detectors 2 and 3, with very low signals for O (0.6 keV) and TMs (from 5.9 to 7.5 keV), but a quite intense signal (of the same intensity

as in spectra 2 and 3) from Cu (around 8 keV). This is an eloquent example of how X-ray can be reabsorbed and interact with anything around the observed particles. As a matter of fact, the analysis of these spectra shows how the Cu grid is situated on the side of detectors 1 and 4 as schematised in Figure 2.4. It is thence always essential to examine spectra of each detector before drawing any conclusion about the atomic composition of a sample. The Cu percentage fraction in the averaged spectrum from all the detectors of Figure 2.5 is e.g. 13%; this value decreases down to 10% when selecting detectors 2 and 3 only since Cu accounts for 25% in spectra 1 and 4.

Moreover, the material itself, as mentioned earlier, can also reabsorb X-rays. Particularly, high energy emitted X-rays can be reabsorbed by elements having lower energy that seem thence to be present in higher quantities. This phenomenon is called self-absorption of X-rays and is very common when working with thick samples. Even using a classic TEM grid and not the one for TEM lamellas, self-reabsorption phenomena are present and they have to be dealt with. In particular, the signal intensity is a function of the escape depth, hence the thickness of the sample. If we consider now a typical primary particle of NMC, X-rays reabsorption will be stronger in the bulk (up to 100 nm thickness) and lower at the surface (some tens of nm). Even if it is possible —and mandatory to analyse properly EDX data— to correct this reabsorption phenomenon effects on the raw data, it can be tricky to do it appropriately both in the bulk and at the surface of the particle. Actually, Velox allows giving information about the thickness and the density of the analysed material in order to provide a good reabsorption correction, but it does not take into account the possibility of samples having heterogeneous thicknesses. The responsibility of obtaining accurate data relies thence on the operator during both acquisition and data interpretation.

1.2.1.2. Acquisition and data treatment parameters

The choice of the particle morphology and orientation is very important in this context in order to avoid samples that are too heterogeneous in terms of thickness at the

surface. Primary particles with an abrupt surface will have a thickness that is more similar in both the bulk and at the surface and will thence be more suitable to EDX analysis. Figure 2.5 represents an NMC primary particle with very different surfaces: the one in the blue inset will thence be a better candidate for the acquisition of EDX spectra than the one highlighted by the orange rectangle.

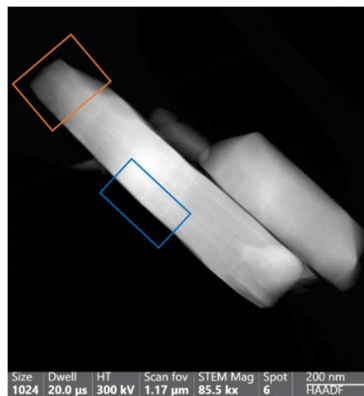


Figure 2.5. STEM image of a suitable (in blue) and unsuitable (in orange) surface for EDX analysis.

In addition, operating conditions have to be decided carefully, paying particular attention on the choice of the accelerating voltage. As already said, reabsorption strongly depends on the escape depth of X-rays. When working with SEM-EDX, this phenomenon will be higher with increasing accelerating voltage since electrons can penetrate deeper in the material due to their higher energy, having a larger electron-matter interaction volume. However, this is not particularly relevant in the case of TEM measurements, since the specimen is usually much thinner. When deciding between working at 300 and 80 kV, the lower voltage seems to be the better choice since there are more electron-matter interactions at lower energy, leading to higher signal. On the other hand, this is accompanied by other drawbacks such as the increasing probability of having radiolysis damages, resulting in the permanent breakage of chemical bonds and a change in the atomic or molecular structure when working with insulators materials.

In order to limit radiation damages (knock-on damages at 300 kV) as much as possible without losing signal, we decided to work at 80 kV accelerating voltage and 60 pA of

current. Dwell time – meaning the time the beam spends on each pixel – of 10 $\mu\text{s}/\text{px}$ and a large number of scans (at least 100) were used during acquisitions. To obtain precise information about the very surface of the primary particles, the pixel size was chosen to be around 0.3 nm.

However, even after choosing the best possible particles and acquisition conditions, the operator continues playing an essential role during data treatment and interpretation. As already mentioned, it is possible correcting the X-rays self-absorption during data treatment, but this could be particularly tricky to do for both the bulk and the surface of the primary particles due to their different thickness. Moreover, since the oxygen K α emission energy (0.5 keV) is much lower than that for transition metals (from 5.9 keV to 7.5 keV), the absorption correction affects more the oxygen percentage determination. When interpreting quantification results, the operator should thence take this phenomenon into consideration and knowing that the quantification of light elements could not be as precise as expected. The atomic quantification of O by STEM-EDX that will be presented in next chapters for NMC has thence to be interpreted very carefully.

1.2.1.3. Profile extraction

STEM-EDX results are often presented by showing Spectrum Images colour mix without really analysing and understanding the corresponding spectra. In this way, it is not possible to properly take into account the errors related to spectra fits. Similarly, it is essential to pay particular attention when showing intensity profiles to evidence changes in the composition. In order to obtain representative data, it is often necessary to sum several pixels in the perpendicular direction with respect to the drawn profile, as shown in Figure 2.6a. Two different profiles can be obtained in this way: the intensity profile and the spectrum profile. In the first case, the spectra corresponding to each pixel are used for the quantification and then averaged. By extracting the profile, it is instead possible to obtain another set of data in which all the perpendicular spectra are averaged before performing the quantification. In this second way, the total

error on the percentage amounts will be lower since the fitted spectra have a better signal/noise ratio, leading to a more precise quantification. The difference between these two methods is not always clearly visible, but in some cases, the use of one or the other can have a huge impact on the final quantification. Figure 2.6b represents the intensity profile coming from the first method in dashed coloured lines, and the spectrum profile obtained after extraction in straight lines. When comparing these atomic percentages with the theoretical composition of NMC811 indicated by dashed black lines in Figure 2.6b (66.7% of O, 26.7% of Ni and 3.3% of Mn and Co), it becomes clear that the profile extraction gives the most reliable results.

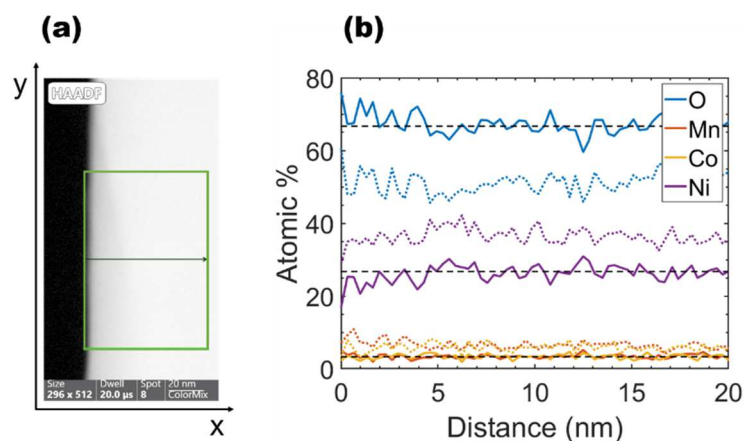


Figure 2.6. EDX Spectrum Image (a); the area from which EDX spectra were extracted is highlighted in green (a). The intensity profile is represented by dashed coloured lines in (b) and it is compared with the spectrum profile in straight coloured lines in (b). The expected bulk composition is indicated by black dashed lines.

1.2.2. Electron Energy Loss Spectroscopy (EELS)

The basic principle of Electron Energy Loss Spectroscopy (EELS) will be here briefly introduced by using the schematic view of Bohr's atom representation, but a more complex understanding can be obtained considering band diagram.²

An electron beam can interact with a solid specimen undergoing elastic or inelastic scattering. In the first case, electrons interact with the nucleus (in yellow in Figure 2.7) and are deflected with typical scattering angles θ_e between 10 and 100 mrad for a 100 kV electron beam. Such a phenomenon is not accompanied by a transfer of energy

for small θ_e . In a crystalline solid, the interference between elastic scattered electrons waves give rise to sharp peaks at angle characteristics of the atomic structure; this is called diffraction.

On the other hand, inelastic scattering occurs when the electron beam interacts with atomic electrons (as the one in orange in Figure 2.7). Inner-shell electrons have stronger interactions with the electron beam, leading to higher scattering angles θ_i of about 10 mrad. Inelastic scattering due to interactions with outer-shell electrons is instead characterised by lower θ_i typically of 1-2 mrad. Upon this interaction, the atomic electron absorbs a certain amount of energy (ΔE) from the electrons beam —necessary to pass to a Bohr orbit of higher quantum number. Primary electrons loose thence the same amount of energy and are scattered in an inelastic way. By measuring the electron beam energy after interaction with the specimen (E), it is thence possible to obtain information about element composition, since each element absorbs a characteristic amount of energy. Similarly, information about crystallographic and energy band structures can be obtained by focusing on the analysis of the fine structures. This is the phenomenon exploited in EELS, in which the number of electrons of the transmitted electron beam is measured as a function of their decrease in kinetic energy.

In an Electron Energy Loss spectrum, electrons transmitted without suffering a measurable energy loss are accounted in the so-called zero loss peak (or “elastic” peak). This represents elastic scattered electrons, those that excite phonon modes for which the energy loss is lower than the energy resolution of the instrument, and the unscattered ones. Electrons that underwent inelastic scattering due to outer-shell electrons will be found in the 4-40 eV region, while electrons scattered by inner-shell electrons are characterised by higher energies and signals having features of edges instead of peaks. On the other hand, sharper peaks can be found at the ionisation threshold, with energy loss similar to the corresponding atomic shell.

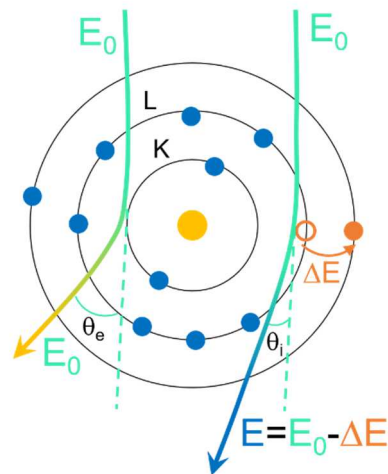


Figure 2.8. Interactions exploited by EEL Spectroscopy explained using Bohr's atom representation. The nucleus is in yellow, the atomic electrons in blue and the electrons beam in light green. Elastic scattering with the nucleus is schematised by the yellow arrow, whilst inelastic scattering with atomic electrons by the blue one. The excited atomic electron resulting from this interaction is in orange.

1.2.2.1. Instrument configuration

The Themis-Z used in this work is one of the first microscopes in Europe equipped with a configuration combining a very high-resolution energy filter (Gatan GIF Quantum 966 ERS) with a direct electron detection camera (Gatan K2 Summit) in addition to the classical CCD camera. This camera technology greatly improves the energy resolution and the signal to noise ratio of the electron energy loss spectra compared to the CCD camera (US1000). It becomes then possible to characterize samples very sensitive to the electron beam by EELS. As a matter of fact, a traditional electron microscopy camera resolution is limited by the scattering of electrons and photons in the scintillator or fibre optics, or by the inherent limitations of lens coupling. Thus, each electron event is delocalized from the point at which the electron enters the camera, into a cloud of light at the sensor. On the other hand, Direct Detection cameras receive the incoming electrons directly onto the sensor, eliminating the need for scintillators and fiber optics or lenses and greatly reducing the electrons spread. Furthermore, the K2 Summit camera has unique sensitivity and Detective Quantum Efficiency (DQE), the most important feature to judge a high-resolution EM camera, allowing very fast –and although high quality– acquisitions. The principal

characteristics of the K2 Summit Camera are listed in Table 2.1, as reported by Gatan Inc.³

Table 2.1. Principal specifics of the K2 Summit Camera, as reported by Gatan Inc.³

Feature	Value
Sensor active area	19.2 mm × 18.6 mm
Sensor size	3840 px × 3712 px
Readout modes	Conventional Counting Counting Super-Resolution
DQE performance (at 300 kV)	> 0.85 (peak) > 0.50 at 0.5 of physical Nyquist
Physical pixel size	5 μm
Sensor readout	400 full fps
Transfer speed to computer	40 full fps
Image display	100 full fps

On the other hand, the US1000 camera allows the acquisition of spectra in dual-EELS mode, meaning the acquisition of both low- and high-loss spectra at the same time. This feature is particularly interesting to obtain information both on the thickness (analysis of the low-loss) and on the oxidation state (analysis of the fine structure of high-loss edges). The use of such configuration was extremely useful for validating the results obtained from the analysis of high-loss edges by Principal Components Analysis (PCA) and Multiple Linear Least Square (MLLS) fitting (c.f. Section 1.2.2.2).

The K2 system was instead used for the acquisition of high-resolution spectra of high-loss edges. In particular, it was often coupled with an excited monochromator to obtain the best possible energy resolution. The monochromator is an electron-optical system that acts as a lens with a strength approximately proportional to its excitation.

Specifically, the monochromator used here is a Single Wien Filter consisting in a Wien Filter and an energy-selecting slit. While the Wien Filter analyses the energy of the electrons by dispersing them (Figure 2.8a), the slit mechanically chooses a portion of the dispersed electrons (Figure 2.8b). In this way, the energy spread of incident electrons is significantly reduced to less than 100 meV.

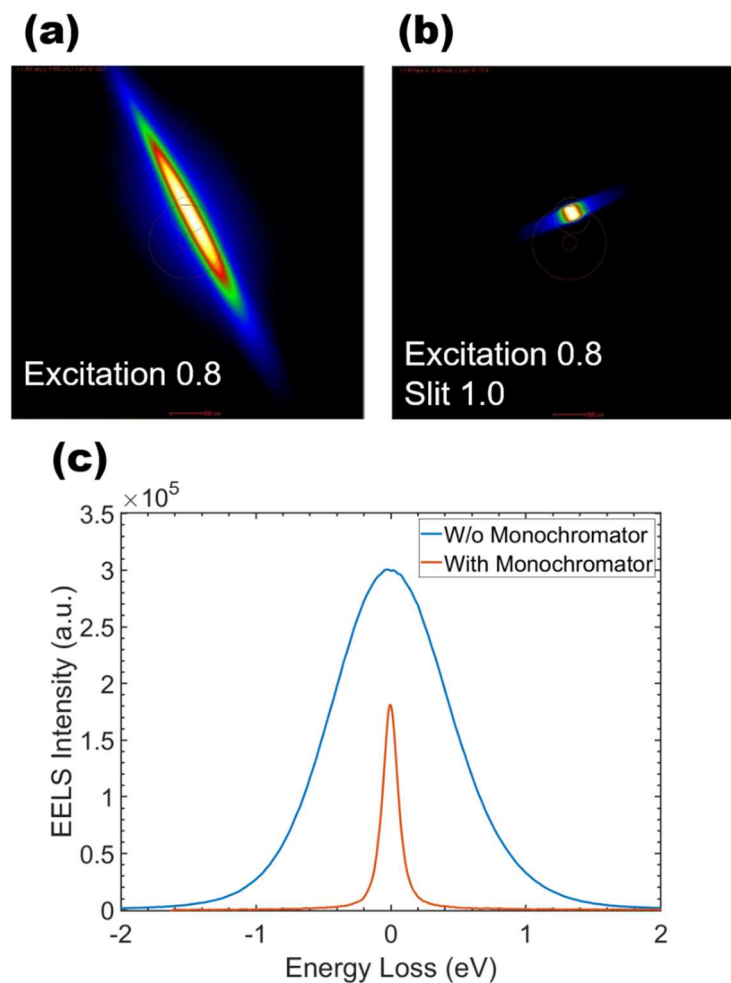


Figure 2.8. Electron beam with the monochromator excited at 0.8 V without (a) and with the slit inserted (b). The zero-loss peak with (orange) and without (blue) an excited monochromator is reported in (c) to show the improvement in energy resolution.

However, while increasing significantly the energy resolution (Figure 2.8c), the use of an excited monochromator makes the acquisition on EEL Spectra more complicated. As a matter of fact, the electron beam can be often unstable. Even slight shifts of the beam could imply a complete loss of the intensity, due to the small size of the slit. For this reason, long acquisitions are preferred to be avoided when working in this

configuration. Moreover, the correction of beam aberrations can become particularly tricky due to the small size of the electron beam on the fluorescent screen. All the apertures have to be removed when off-axial coma has to be corrected, slowing down the rhythm of the acquisitions. A perfect alignment of the microscope is indeed essential to obtain high-quality results in this configuration.

1.2.2.2. Validation of PCA and MLLS results

Since the electron beam passes through the sample before arriving on the camera, it is essential to distinguish surface contribution from bulk ones. As a matter of fact, the upper and the lower surfaces could have an influence on spectra found in the bulk. It will be shown in Chapter 3 how nickel is reduced in the first 5 nm of the surface. In order to properly define the pure bulk spectrum — thus without the influence of the reduced surface— it is essential to do some simple calculations, that will allow validating the results.

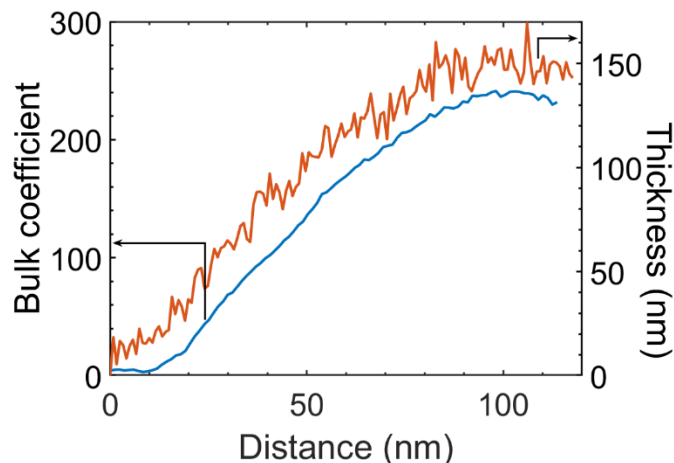


Figure 2.9. Evolution of bulk MLLS fit coefficients (in blue) and thickness (in orange) as a function of the distance from the beginning of the surface.

In particular, both low- and high-loss spectra were acquired using the US1000 camera in dual-EELS mode. The zero loss peak was used to obtain the thickness map of the sample. The high loss spectrum was fitted by MLLS, taking one reference at the very surface — to be sure to avoid any influence of the bulk— and one reference in the bulk. It was thus possible to plot the bulk fit coefficients and the thickness as a function of

the distance from the surface, showing that they follow the exact same trend (Figure 2.9).

It is thence possible to write the following system, in which two experimental spectra at different thicknesses ($S_{10\text{ nm}}$ and $S_{150\text{ nm}}$) are defined as the sum of a pure surface spectrum and a pure bulk spectrum (S_{surf} and S_{bulk}), both multiplied for a coefficient (the previously found fit coefficients):

$$\begin{cases} S_{10\text{ nm}} = a \cdot S_{\text{surf}} + b \cdot S_{\text{bulk}} \\ S_{150\text{ nm}} = c \cdot S_{\text{surf}} + d \cdot S_{\text{bulk}} \end{cases} \quad (2.1)$$

By solving this system, it is possible to find the equation representing the pure bulk spectrum as a function of the two reference spectra used for the fit:

$$\begin{cases} S_{\text{surf}} = \frac{S_{10\text{ nm}}}{92} \\ S_{\text{bulk}} = \frac{1}{136} \cdot \left(S_{150\text{ nm}} - \frac{3}{46} \cdot S_{10\text{ nm}} \right) \end{cases} \quad (2.2)$$

It results that in the bulk spectrum at 150 nm thickness taken as a reference ($S_{150\text{ nm}}$), there is the 6.5% of the surface spectrum ($S_{10\text{ nm}}$). It is thus possible to calculate the pure bulk spectrum and to compare it with the experimental one (Figure 2.10), demonstrating that the two spectra do not present significant differences. Actually, 6.5% of 150 nm (the bulk thickness) is 9.75 nm. Dividing this value by two —because there is a surface above and one under the bulk— we find that the pure surface accounts for around 5nm, which is the thickness of the pure reduced surface initially found by both PCA and MLLS fitting, as it will be shown later (c.f. Chapter 3).

In conclusion, the information found by MLLS fitting are in line with these calculations. We were therefore able to demonstrate that the influence of the surface spectra on the bulk can be ignored since they represent only a minor percentage of the total spectrum. Consequently, results coming from MLLS fits that will be reported in the next chapter can be considered truthful.

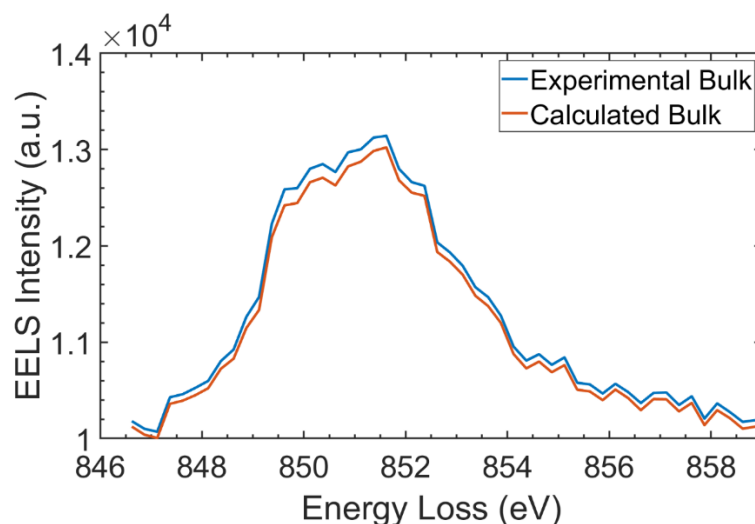


Figure 2.10. Ni L₃-edge experimental bulk spectrum (in blue) and calculated one (in orange) using equation 2.2.

1.2.2.3. Data processing for elemental quantification

Even when working in the best possible conditions, it can sometimes be difficult to obtain enough and reliable signals for elements in low amounts and with edges at higher energy. This is the case for Mn and Co in NMC811. Due to the intense background coming from the increasing sample thickness moving from the surface to the bulk, these signals can often be lost and not properly analysed. This sort of issue related to low EELS intensity can be avoided in the first place by averaging multiple pixels in the y vertical direction before analysing data, just as it was done for EDX data (c.f. Section 1.2.1.3). Binning data brings to a better signal/noise ratio at the surface and in the bulk and allows a proper data analysis that does not provide local information, but averaged and statistically pertinent ones. It is thence of great importance to properly choose an appropriate surface to collect EEL spectra on, since an indented one would bring errors due to the sum of pixels containing information and others with noise only. Figure 2.11 represents an example of unsuitable surface for this type of analysis.

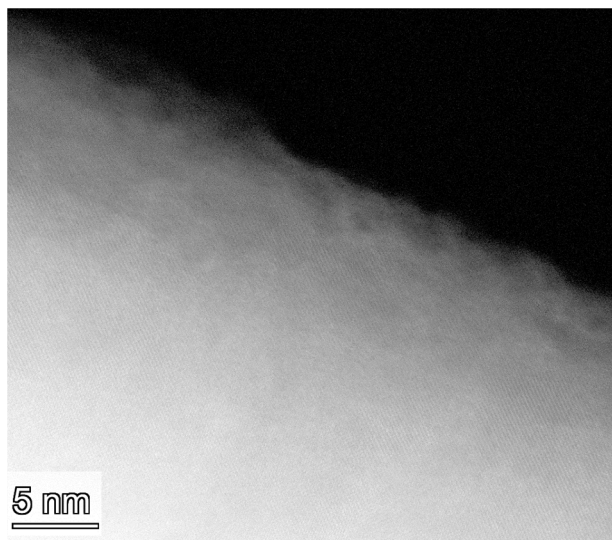


Figure 2.11. Example of an unsuitable surface for EELS analysis.

Furthermore, the background removal – usually essential to do a proper elemental quantification – can be tricky and unreliable when working with edges very close in energy to each other, as Co-L (around 770 eV) and Ni-L edges (around 840 eV) are. The method of second derivatives used throughout this work exploits the fact that such background extraction is no longer necessary.⁴ Moreover, it allows overcoming the problem of overlapping edges and obtaining more important signals for elements in low amounts. This approach consists in calculating the second derivative of spectra contained in each pixel – after binning in the y direction.

In order to proceed to the elemental relative quantification, the Multiple Linear Least Square (MLLS) fitting was then performed on this new dataset. Two reference spectra for each edge (one taken in the bulk, far from the surface, and one corresponding to noise only) were extracted directly from the SI and implemented in the MLLS fitting routine of DM (Figure 2.12).⁵ The fit ranges for all edges (O-K edge, L_{2,3} edges of TMs), represented in colour in Figure 2.12b, were chosen by taking into account both the extend of EEL signal and the noise appearing in the second derivatives. Since the pre-peak at the oxygen K edge is known to be very sensitive the oxidation state and site environment, it was not included in the fit. Likewise, the ratio of L₃/L₂ edges of TM are known to be sensitive to oxidation states, so fits were performed based on their L₃ edge

only. Slight energy shifts at the L_3 edges have in fact no effect considering the energy resolution we used for the quantification (> 1.0 eV in non-monochromated mode). The method showed a remarkable robustness whatever the analysed particles.

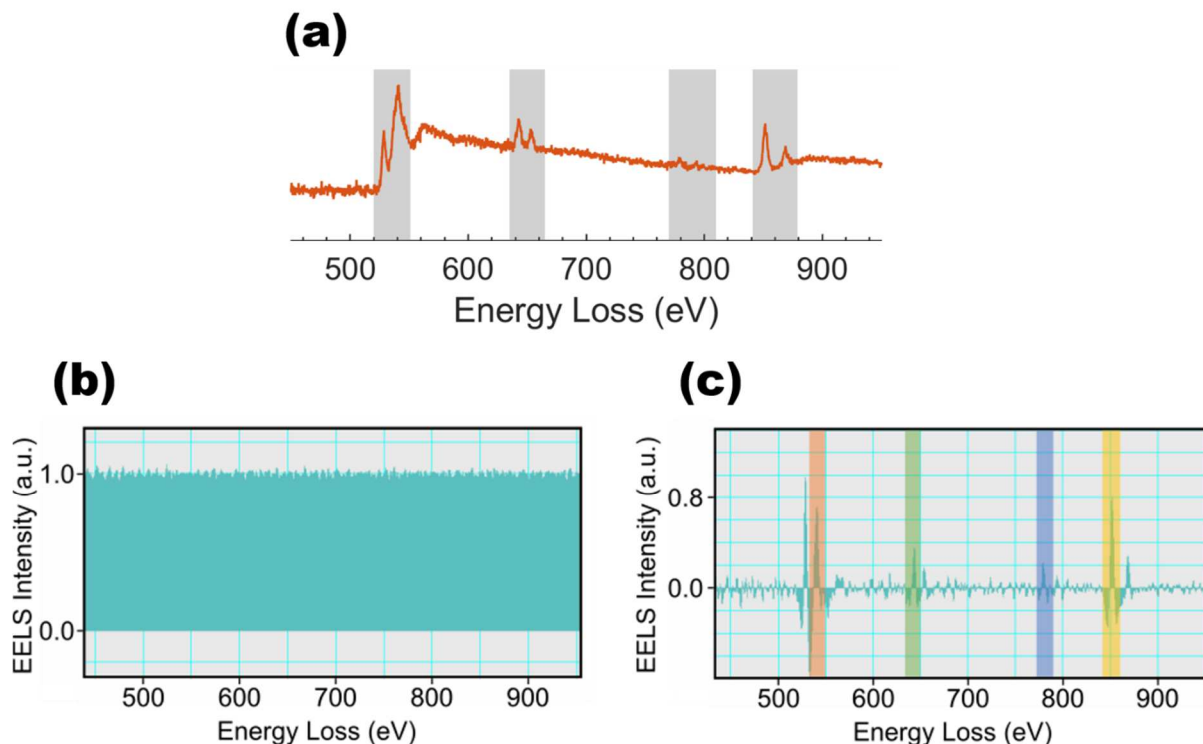


Figure 2.12. A typical EEL Spectra at the surface of NMC811 (a) and reference spectra used for the MLLS fitting for quantification. The noise only reference is represented in (b), while the bulk one in (c). Coloured areas in (c) indicate the energy ranges used for the fit: O K in orange, Mn L_3 in green, Co L_3 in blue and Ni L_3 in yellow.

The fit coefficients obtained for the four MLLS fits (one for each edge) represent the relative contributions of the two reference spectra within each binned pixel. The relative amount of each element can thus be calculated as a function of the distance from the surface. We decided to take Ni as reference since its signal is less prone to be influenced by noise. Ratio values in the bulk (far from the surface) are set to the expected nominal values (1/8 for Co and Mn and 2.5 for O).

A more detailed description of this method will be given in the Supporting Information of the article reported in Chapter 3.

1.3. Experimental conditions

Experimental conditions for STEM-EDX and STEM-EELS acquisitions are reported in Table 2.2.

Table 2.2. Principal experimental parameters used for EDX and STEM-EELS analyses.

Parameter	STEM-EDX	STEM-EELS	STEM-EELS
		Mono on	Mono off
Accelerating Voltage (kV)	80	300	300
Current (pA)	60	50	60
Dispersion	10 eV/ch	0.25 eV/ch.	0.25 eV/ch.
Pixel size (nm)	0.3	0.5-1.0	0.3
Approximate probe size (nm)	0.15	0.10	0.10
Dwell time (ms)	0.01	20	20
Number of scans	>100	10	10
Data treatment	Velox	Digital Micrograph	Digital Micrograph
Convergence semi-angle (mrad)	29.1	25.8	29.1
Collection semi-angle (mrad)	---	19.0	34.1

Part 2. Focused Ion Beam

Scanning Electron Microscopes (SEM) can be associated with an ionic column, which allows extending significantly the application field of such devices. The focused ion beam (FIB) is usually employed for deposition of matter and for milling of the specimen. The coupling with electron imaging can be exploited not only for the 3D analysis (c.f. Section 2.2) of the sample morphology, but also to prepare thin specimens for TEM characterization (TEM lamellas, c.f. Section 2.1). Moreover, the SEM-FIB from Zeiss used for this work is equipped with an EDX detector, which allows the analysis of the composition of internal volumes.

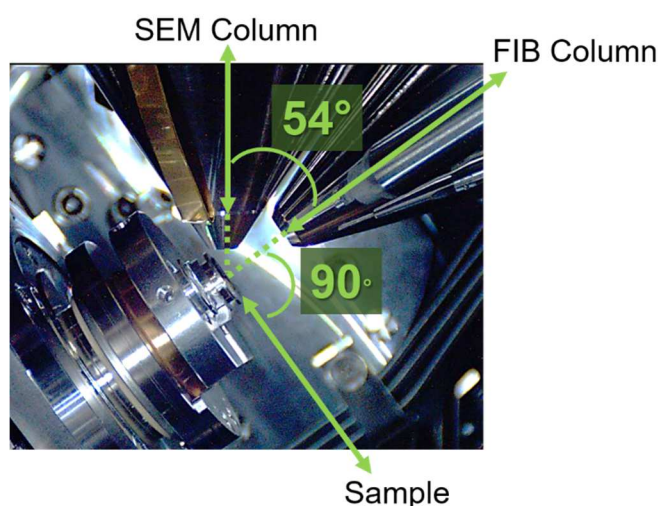


Figure 2.13. SEM-FIB instrument configuration.

2.1. Instrument configuration

The FIB column, positioned at 54° with respect to the SEM column, accelerates gallium ions. The sample has to be tilted by 54° to be perpendicular to the ionic column (see Figure 2.13). Depending on the applied current, Ga^+ ions can deposit or erode matter: high currents (300 pA to 30 nA) are usually employed to produce high precision cross-sections, while lower currents (50 pA to 300 pA) can be used to deposit matter. We will see in next Sections how Pt and C can be deposited in this way to protect the sample or to ease the automated 3D acquisition process. As a matter of fact, Gas

Injection Systems (GIS) can be inserted in the vacuum chamber to inject Pt or C in their gas state. Ga^+ ions interact thence with the gas leading to the deposition of a solid amorphous Pt or C film.

The electron column, on the other hand, is used to produce images as in a normal SEM, or EDX Spectrum-Images. During the preparation of TEM lamellas, its scope is to help visualizing the progress of the milling steps, giving another point of view on the sample, since the observation with Ga^+ ions (more energetic than electrons) is not always easy due to the fast degradation of the sample under ionic beam. When performing 3D acquisitions, SEM is instead used to obtain the cross-section images that will be then analysed to reconstruct the volume.

In the following sections, we will show how SEM-FIB was used both to prepare TEM samples and to obtain 3D volumes on pristine electrodes throughout this work; the main drawbacks of these methods will be the focus of this discussion, together with some modifications that can be applied to the classical procedure to overcome them. The attempt of coupling 3D-FIB acquisitions with EDX will also be explored, presenting the difficulties we encountered during the implementation of the experimental setup and some possible solutions.

2.2. TEM lamellas preparation

TEM lamellas represent one of the multiple ways to prepare samples for TEM observations and they are particularly useful when working with porous and hard samples and air-sensitive materials. The preparation of TEM specimens from this sort of materials by classical ways e.g. ultramicrotome is in fact not conceivable. For these reasons, TEM lamellas were prepared to observe pristine NMC electrodes. The targeted thickness for a lamella strongly depends on the analysis one wants to perform. Electron diffraction and EDX experiments do not require very thin specimens, while EEL Spectroscopy needs the specimen thickness to be at least inferior to 100 nm. Of course, the thinner the lamella has to be, the most challenging the procedure is.

The different steps of this procedure will be presented here, focusing on the problematic hotspots that could lead to well-identified issues due to these materials nature.

2.2.1. Pt protection layer deposition

Due to the high energy of Ga^+ ions, it is essential to protect the sample surface before proceeding to the milling. For this reason, a Pt protection layer is deposited on the surface of the material.

Actually, due to its Gaussian shape, the ionic beam has not the homogeneous intensity that is needed during milling. The tails of the ionic beam could in fact interact with the sample in a non-perpendicular way, worsening the so-called curtaining effect (giving the vertical stripes visible on the bottom on the lamella in Figure 2.14b). The aim of the Pt protection layer is to “consume” the tail of the ionic beam, allowing a more homogeneous interaction with the sample (Figure 2.14a), even if the curtaining effect cannot be completely avoided due to the high porosity of this specimen.

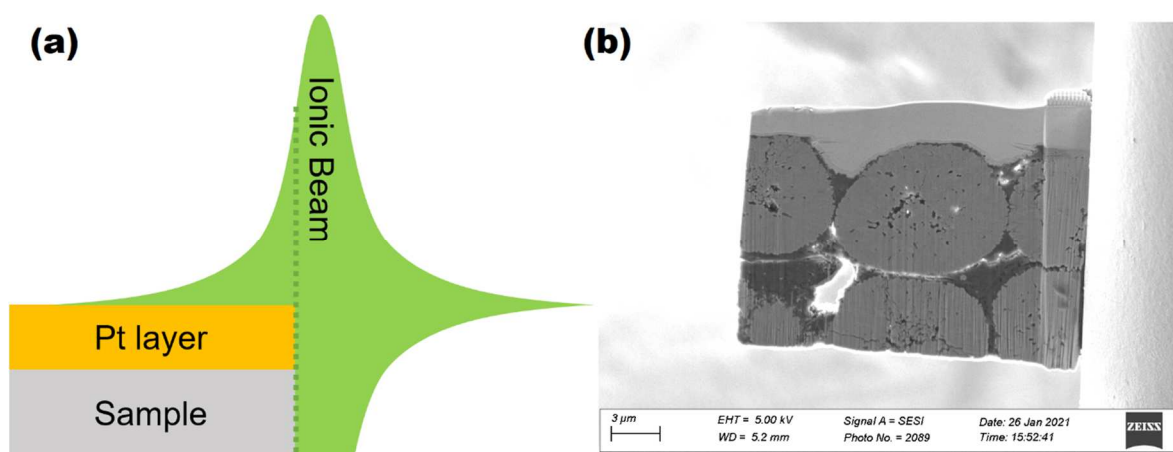


Figure 2.14. Beneficial effect of the protection platinum layer (a) during the preparation of TEM lamellas by FIB and an example of a TEM lamella obtained from an NMC811 electrode before the thinning step (b). The so-called curtaining effect is visible on the bottom of the lamella in (b).

A first very thin Pt layer (around 100 nm) is deposited by the electron beam, before depositing a thicker one (up to 2-3 μm) by the ion beam. Even at low currents, the Ga^+ beam can in fact erode the surface during Pt deposition, making the electronic deposition essential before proceeding with the ionic one.

The ionic current values are chosen as a function of the surface size to be protected. For a rectangle of $5 \times 15 \mu\text{m}$, the current for deposition has to be between 150 and 375 pA, following the rule $a \times b \times 2 < i < a \times b \times 5$. Even if such measures were used for all the tests, we know now that smaller areas should have been taken into account in order to overcome problems related to porosities. Actually, since the mean diameter of a NMC secondary particle is $10 \mu\text{m}$, by considering such big surfaces, the porosities between at least two secondary particles are inevitably included in the lamella. Figure 2.14b shows how a Pt layer of inhomogeneous thickness is obtained in such conditions, bringing to a worse interaction with Ga^+ ions and thence to a less homogeneous beam arriving on the sample.

On the other hand, having a larger surface to analyse significantly improves statistic and the probability of having a zone thin enough to be analysed by EELS. The choice of the area to be observed is particularly difficult in this type of analysis, since the user has no information on what is hidden into the bulk of the material (a bigger particle, some binder only, a big porosity etc.). It is thence essential to find the best compromise between the feasibility of the procedure and the results that can be obtained from it when deciding the lamella size.

2.2.2. Lift-out and attachment on the TEM grid

The classical lift-out procedure consists in the milling of two rough cross sections at high current (30 nA) on each side of the Pt layer (Figure 2.15). It is important to subsequently clean the so-obtained surfaces at lower current (700 pA) to have the two sides as parallel as possible. The size of the cross-sections is directly related to the depth of the milling and thence to the final height of the lamella. Once again, a deeper cross-section —and so a higher lamella— will give more information, affecting though significantly the stability of the lamella itself. All the preparations along this work were done aiming at around $10 \mu\text{m}$ height. Looking back now, with the acquired expertise, we can safely say that such big lamellas were not necessary and that it should have

been better to focus on smaller areas given the difficulty of handling NMC materials during lamellas preparation.

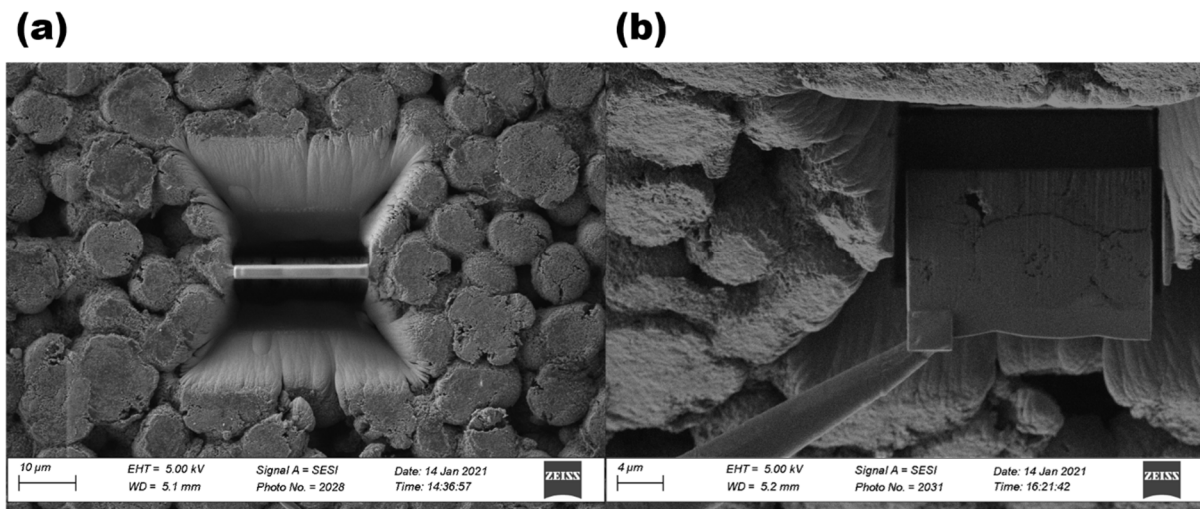


Figure 2.15. TEM lamella lift-out step seen by FIB (a) and by SEM (b).

Once the lamella is cut off from the rest of the material, it can be lifted-out with the help of the “nanomanipulator” (visible in the left bottom corner for Figure 2.15) and attached to the TEM grid. The attachment can be done in two different ways: with the attachments points either on the bottom right and bottom left corner, or on one side only. These two approaches are schematised in Figure 2.16a.

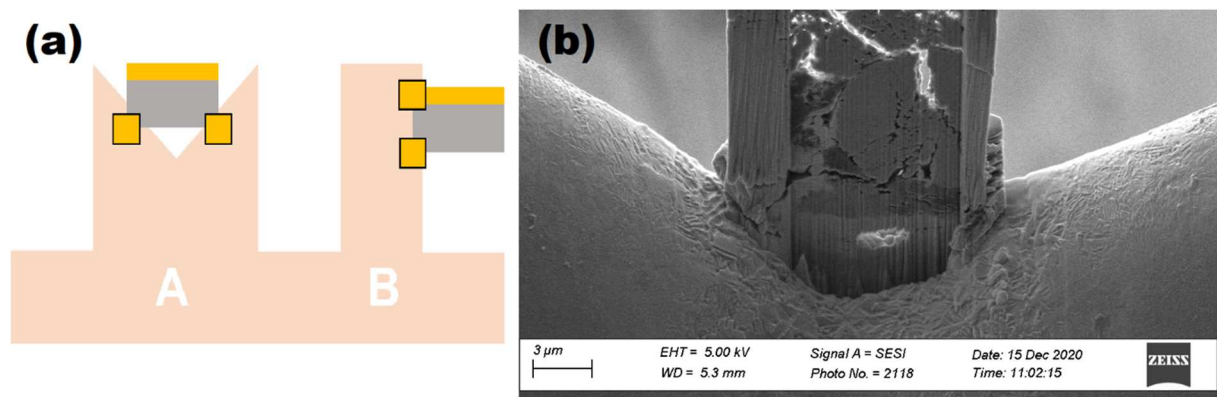


Figure 2.16. Schematic representation of the two possible approaches for the attachment of the TEM lamella on the TEM copper grid (a) and the issues given by the horizontal approach when working with porous materials (b).

Once again, it is the user responsibility to choose the best strategy based on the pros and cons of each method. In particular, the attachment on both sides can easily bring

to a structure collapse when working with porous materials, as showed in Figure 2.16b. Moreover, the proximity with the grid increases the redeposit of metallic Cu, which is eroded from the grid during the thinning step, in the porosities of the lamella. This can induce false results during EDX analysis, hindering the true surface status. For these reasons, this attachment approach was rapidly abandoned.

On the other hand, some difficulties were encountered even using the one side attachment method, which requires thence some adaptations. The lamella is in fact highly unstable in this configuration, especially during the thinning step and it can easily break during the transfer to the TEM. We will report in next section the best way to obtain the final lamella from NMC811 electrodes using this type of attachment.

2.2.3. Lamella thinning

The lamella thinning is the most delicate step of this procedure, and it becomes particularly difficult when handling hard, porous and heterogeneous materials as NMC electrodes. The bases are though simple: the thick lamella (already attached on the grid) is gradually eroded by the ionic beam on both sides until obtaining a sample that is thin enough —meaning largely inferior to 100 nm for EELS. During this operation, the sample holder is tilted by 54° to be perpendicular to the FIB, and it is repeatedly rotated by 180° to attack one side after the other.

However, since NMC is harder than the amorphous Pt deposited on the upper part of the lamella, the latter can easily be eroded before the material itself and thus not fulfil its protective purpose. It is thence essential to adapt the tilting angle during thinning in order to attack principally the material and not the Pt. By applying a tilting angle of 53° instead of the classical 54° , it was possible to make the lamella bottom thinner only, without affecting the Pt thickness too much. In this way, it is although very unlikely to obtain homogeneous thickness in the whole lamella, since the ionic beam is not perpendicular to the surface (Figure 2.17a).

The deposition of the Pt layer is also essential because of the morphology of the sample. NMC811 electrodes were found to be particularly porous (see Figures 2.14, 2.15 and 2.16), increasing the probability of curtaining effect, forming stripes extremely thick and thus that cannot be analysed by EELS. Actually, the ionic beam can be “captured” in the porosity and not erode the underlying part of the sample.

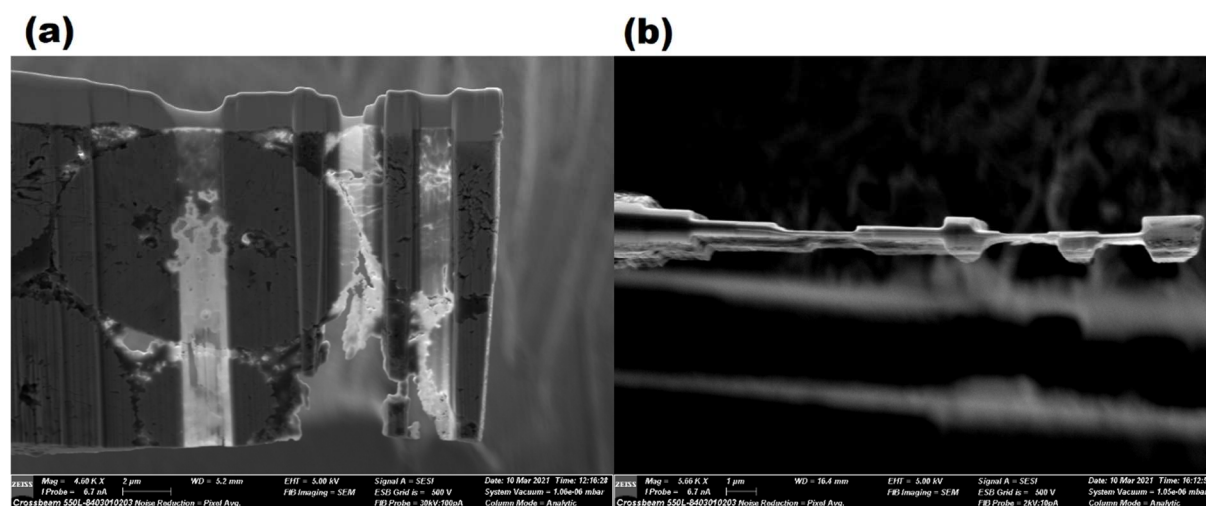


Figure 2.17. Results obtained by applying the multiple windows approach for thinning the TEM lamella. View from SEM (a) and FIB (b).

In addition to porosities situated inside NMC secondary particles, the presence of the binder and the active carbon in the electrode formulation helps to create new porosities during the thinning step. As a matter of fact, since these compounds have lower density than the active material, they are eroded more easily by the ionic beam, leaving new porosities behind them. This contributes tremendously to the instability of the lamella upon thinning. Voids are particularly dangerous not only because they can cause the detachment of material, but also because they decrease notably the conductivity of the sample. When a sample is poorly conductive, as in thinned lamellas containing a large amount of voids, it can become particularly unstable and bend on the effect of the electrostatic field. In order to avoid these issues, instead of thinning the whole area, we decided to focus on smaller thinning windows during this work. As it can be seen in Figure 2.17, several areas were thinned, letting some thicker zones between them to stabilise the sample. This method was particularly effective and it

was the only way to produce lamellas thin and stable enough to be transferred into the TEM.

2.3. Acquisition of 3D volumes

The acquisition of 3D volumes is the most efficient way to analyse the internal morphology of a solid specimen, providing reliable measurements of internal porosities.

The ionic beam is used to slice the material, while the SEM beam records images of the so-obtained cross-sections in an automatic way, as schematised in Figure 2.18. Even if acquisitions are automatic, many parameters have to be carefully chosen by the user. We will present here how to obtain a good 3D dataset on NMC811 electrodes and how to properly analyse it.

Acquisitions were performed as a part of the internship of Pierre Guihard, who was in charge of the data treatment, one of the most delicate part of 3D experiments. The aim of the internship being to successfully couple 3D and EDX acquisitions, the last Section of this part will be dedicated to exposing the progresses done in this field.

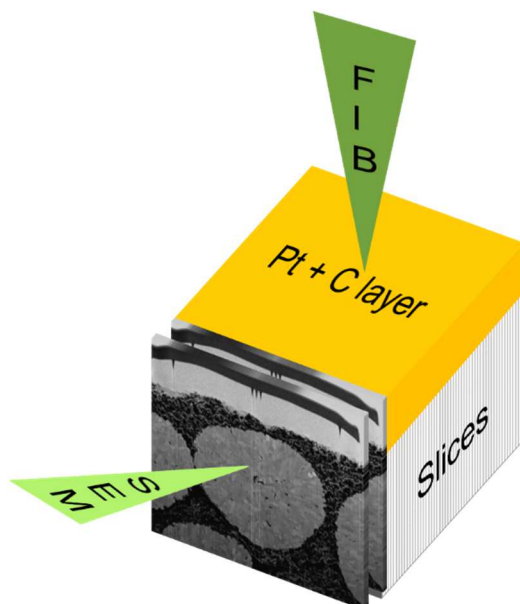


Figure 2.18. Schematic representation of the instrument configuration used for 3D-FIB acquisitions.

2.3.1. Experimental set-up and sample preparation

Even if 3D acquisitions are completely automatized, obtaining a good volume strongly depends on the sample preparation steps. As a matter of fact, only by preparing properly the sample surface, the acquisition program can successfully alternate milling and imaging processes. Since the sample is not moving during the acquisition, it is essential to readjust the focus and the astigmatism of the beam to compensate the increasing distance from the detector (z) after each milling step. The acquisition program needs to have a detail it will always be able to focus on. This is the role of the autofocus marks. Moreover, in order to calculate exactly the size of each slice, two tracking marks have to be drawn at a defined and decreasing distance one from the other (Figure 2.19). By calculating the distance between these two marks, it will be possible to know the milling progress. In order to have the best contrast, autofocus and tracking marks are done by alternating Pt and C deposition.

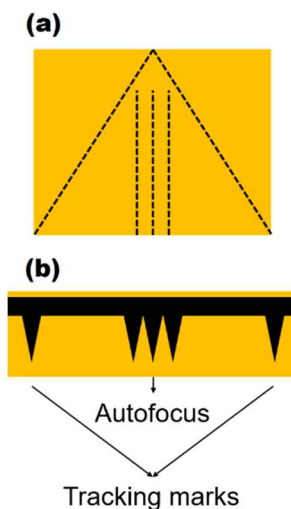


Figure 2.19. Schematic representation of autofocus and tracking marks used during 3D-FIB acquisitions. View from FIB (a) and SEM (b).

Summarizing, the sample preparation step consists in making the automatic acquisition easier and the results better and more easily interpretable. To complete the sample preparation, a rough cross-section is milled using the ionic beam at high current (30 nA) and then cleaned by applying a lower current (700 pA). Both the internal surface and the marks are now visible by SEM and the acquisition can start.

Despite the apparent feasibility of these steps, things can get rapidly complicated when working with non-flat surfaces, as in non-calendared electrodes. The auto-tracking, in particular, can easily fail, impeding the acquisition program to find the surface, re-centre it in case of image drifting and calculate the correct slice size. In order to overcome this issue, it could be conceivable to simply deposit a thicker layer of Pt to obtain a surface that is flatter and thence an easier auto-tracking, as it was done during the example represented in Figure 2.20a. However, it has to be noted that the milling depth becomes logically higher (since several μm of Pt have to be milled as well) and the milling efficiency consequently worse. This solution is thus not the best in terms of acquisition time —nor from an economic point of view. An alternative could be to focus on one single secondary particle only, as it is shown in Figure 2.20b. This allows to successfully bring the acquisition to its term without any sort of auto-tracking problems, but a huge number of acquisition has to be performed in order to have good statistic, due to the limited volume obtained using this method (less than $10\ \mu\text{m} \times 10\ \mu\text{m} \times 10\ \mu\text{m}$).

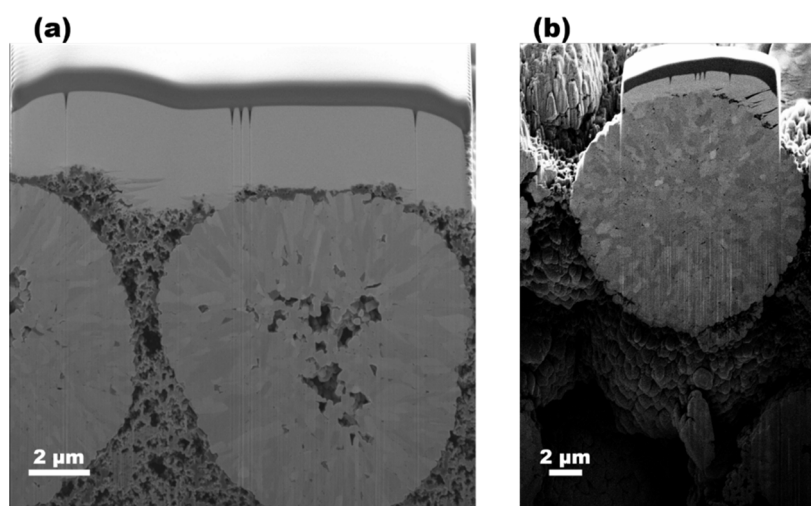


Figure 2.20. Two possible approaches to ease the analysis of non-flat surfaces: deposition of a thicker platinum layer (a) and analysis of smaller surfaces (b).

2.3.2. Data treatment

The treatment of the 2D images stacks to obtain a 3D reconstruction was performed in DragonFly. This process can be divided into three steps, namely slice alignment, artefacts correction and segmentation.

The first aims at aligning the whole dataset of images, which often drift slightly during the acquisition, ensuring a good continuity between images during the volume visualisation. The alignment is done by focusing on a precise and well-contrasted detail (e.g. the autofocus marks), through translation or rotation in the plan of the image, while any rotation out of this plan is neglected.

Once aligned, the images must be carefully corrected for artefacts. The curtaining effect particularly affects 3D volumes of NMC electrodes, due to the high material porosity. DragonFly offers a tool to automate the correction process. The amount of iteration is chosen by the user, who has to keep in mind that a higher number of iteration brings not only to a lower amount of vertical stripes, but also to a poorer image resolution. The good compromise has thence to be found. The curtaining artefact correction is essential for the following segmentation step. As a matter of fact, data segmentation groups together components of the same nature in the 2D images (porosities, NMC, Binder etc.) on the basis of their grey level. This separation allows then calculating the amount of each component and visualising its position inside the 3D volume. Since SEM images are made up of shades of grey, data segmentation is done by determining threshold values of grey for each component, which thence allows the software to sort out the nature of every pixel automatically. The presence of uncorrected curtaining effect would create false results due to the brighter and darker areas typical of this effect.

Segmentation can be done either manually or automatically. By manual segmentation, the user manually associates every pixel of every image in the stack by means of a brush tool. The segmentation will be very accurate and completely controlled, but dependent on the user. The defects on the images are not taken into account, which

can provide more reliable quantitative results. However, this method is particularly time-consuming and not repeatable on different stacks. On the other hand, the automated segmentation separates the grey scale into a chosen number of intervals, corresponding to different phases in the stack, and instantly proceeds to the segmentation of the whole dataset of images. Even if this method requires a shorter amount of time when compared to the manual segmentation, manual checking is always needed afterwards to avoid errors, e.g. pores that are not considered as such because the material in the following image is already visible due to poor contrast.

Figure 2.21a represents the final 3D volume representation obtained by manual segmentation on a pristine calendared NMC811 electrode. The three phases chosen to represent the system –namely binder and active carbon, NMC and porosities– are represented in Figure 2.21b, 2.21c and 2.21d respectively.

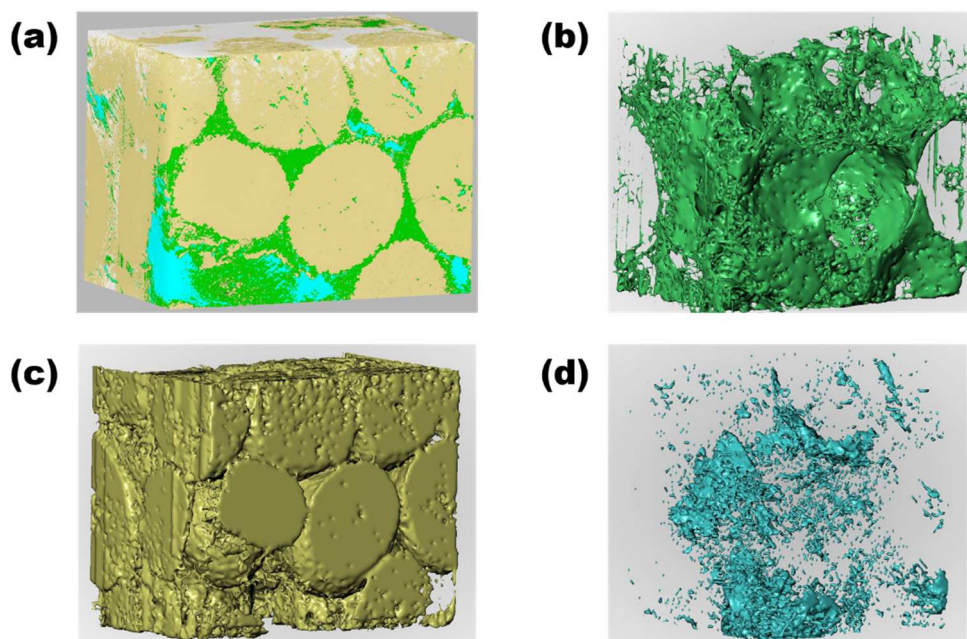


Figure 2.21. Reconstruction of a 3D volume obtained on a NMC811 electrode (a). Three contributions were used: conductive carbon and PVdF binder in green (b), NMC material in yellow (c) and porosities in light blue (d).

2.3.3. 3D-FIB-EDX coupling

EDX Spectroscopy can be extended to 3D microanalysis using a dual beam microscope equipped with an EDX detector. Indeed, it is possible to interrupt the 3D milling

process after each step in order to acquire an EDX spectrum-image of the considered slice, leading to a complete description of each slice chemical composition. The recorded 3D dataset is thence composed of a stack of SEM images and a stack of EDX Spectrum-Images. The coupling 3D-FIB-EDX is therefore a very convenient way to reconstruct a 3D volume gathering both geometrical and chemical information on the sample.

However, some considerations have to be kept in mind when deciding the parameters for this complex analysis. As for STEM-EDX, a good compromise between accelerating voltage, current and researched information is to be looked for. Since the accelerating voltage strongly affect the volume interaction of the electron beam, it has to be chosen as a function of the slice thickness. Using a too elevated accelerating voltage could in fact bring to errors in the quantification, since the obtained information would not be only about the observed slice, but they would concern the following slices as well because of the depth probed by the electron beam. Moreover, since the energy of the emitted X-rays depends on the energy of the electron beam, the choice of the accelerating voltage is also affected by the elements one wants to observe. A higher accelerating voltage could in fact be required to excite all the X-ray lines of interest. With an accelerating voltage greater than 10kV, the interaction volume is, in general, dramatically larger and typically in the micron range. The large interaction volume is therefore the main limitation during the coupling 3D FIB-SEM-EDX, but one can choose to concentrate on light elements only to preserve a better spatial resolution.

Another issue comes from the analysis of porous materials. Even if voids do not emit X-rays, the material behind them does. It is thence necessary to check and remove manually pixels corresponding to pores and containing an EDX signal, by exploiting the back-scattered electron images (BSE) used to get the 3D representation.

Moreover, as already mentioned for TEM acquisitions, it is essential to take the problem of the degradation under electron beam into great consideration. In particular, the contamination compounds contained at the surface demonstrated to be

extremely sensitive to the electron beam, especially during long EDX acquisition. The same behaviour is supposed to be typical of the contamination compounds inside the secondary particles — meaning those species that are the principal focus of 3D FIB-EDX experiments. Figure 2.22 represents the BSE image recorded after EDX acquisition of two powder secondary particles aged in ambient atmosphere for a long time. The blue arrows indicate the area on which Ga^+ ions were focused to make the cross-section, while the orange ones point towards the area analysed by EDX. Thanks to the nature of back-scattered electrons, it is possible to observe a degradation of the contamination layer during EDX acquisition, since BSE are sensitive to the molecular weight of the observed elements. Light elements — such as the ones constituting the contamination layer — are represented by darker shades of grey, while heavier ones (e.g. transition metals) appears to be brighter. The lighter grey in the area corresponding to the EDX acquisition confirms a degradation of the contamination layer upon long-term electron exposition.

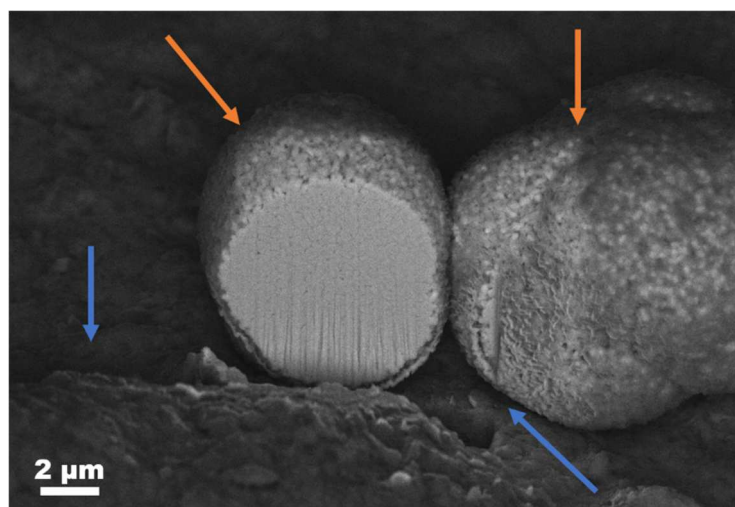


Figure 2.22. BSE image of an NMC811 cross-section after a 15 minutes EDX acquisition. Blue arrows indicate the area that was cut using the Ga^+ ionic beam and orange arrows the area analysed by EDX to highlight the degradation of the surface contamination layer by electrons.

In order to avoid such beam damages, acquisition should be performed while cooling down the whole system. We strongly believe that cryo-FIB would allow the good observation of the contamination layer at the surface of secondary particles as well as the correct identification and quantification of contamination compounds between the

primary particles. Such experiments were not performed during this work, but since the degradation under electron beam was clearly demonstrated, next works aiming at visualising and analysing the NMC surface should consider the possibility of performing acquisitions in cryo mode.

2.4. Experimental conditions

Current values for TEM lamellas preparations and the acquisition of 3D volumes are reported in Table 2.3. The FIB accelerating voltage was kept constant at 30kV for all the steps of these two procedures.

Table 2.3. Experimental conditions used for the preparation of TEM lamellas by FIB and for 3D volumes acquisitions.

Action	TEM lamellas	3D volumes
Ionic Pt deposition (pA)	Dependent on the area size	Dependent on the area size
Rough cross-section (nA)	30	30
Surface cleaning (pA)	700	700
Thinning (pA)	100-300	---
Slice milling (pA)	---	700-1500 ^c
Slice thickness (nm)	---	10-50 ^d
SEM imaging	7 nA, 5 kV	1 nA, 2 kV
EDX acquisition	---	1 nA, 7 kV

^c Depending on the slice thickness

^d 10 nm for simple 3D acquisitions, 50 nm for 3D-EDX

Part 3. Solid State Magic Angle Spinning Nuclear Magnetic Resonance

Solid State Magic Angle Spinning Nuclear Magnetic Resonance (SS MAS-NMR) is particularly useful in the quantification of battery materials thanks to the possibility to probe Li.

In this part, we will show how this technique can be used to obtain both qualitative and quantitative information about NMC materials and their surface contamination layer. The principal issues encountered during NMR experiments will be listed here as well as the precautions that were taken to overcome them.

3.1. Theoretical principles

Nuclear Magnetic Resonance (NMR) spectroscopy detects re-emitted electromagnetic radiation from magnetic nuclei placed in a magnetic field. Since the isotopes exhibiting a nonzero spin are electrically charged, they also have an intrinsic magnetic moment (μ) caused by transitions between the different nuclear spin levels that are at the origin of the NMR phenomenon. Since μ is given by the equation

$$\mu = \gamma \cdot \hbar \cdot I \quad 2.3$$

, with γ representing the gyromagnetic ratio of the investigated isotope, \hbar the reduced Planck constant, and I the spin, only isotopes having $I \neq 0$ are observable by NMR. In this case, nuclei can be treated as small magnetic dipoles, which are susceptible to interact with an applied external magnetic field.

In the absence of an external field, all nuclear spin states are degenerate, (i.e. there is no energy difference between them). Hence, the population of these states will be approximately equal at thermal equilibrium. On the contrary, when placed in an external static magnetic field B_0 the spin states suddenly split apart in energy and the nuclear spins align either with or against the magnetic field (polarisation), following the so-called Zeeman interaction. In these conditions, the nuclear spin states are not

degenerate anymore and nuclear spins are spread amongst the available energy levels according to the Boltzmann distribution; the resulting macroscopic magnetisation M_0 is thence nonzero and parallel to the external B_0 . The energy gap between these energy levels is thence proportional to the intrinsic magnetic moment and given by the just mentioned Zeeman interaction (Figure 2.23).

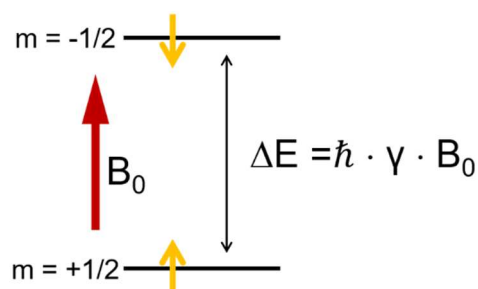


Figure 2.23. Schematic representation of the effect of the Zeeman interaction on a hydrogen nucleus.

Transitions between adjacent energy levels are thence allowed when an electromagnetic radiation having this same energy is applied. In particular,

$$\Delta E = h\nu = \hbar \cdot \gamma \cdot B_0 \quad 2.4$$

or

$$\nu = \frac{\gamma \cdot B_0}{2\pi} \quad 2.5$$

where ν is the frequency of the electromagnetic radiation. Resonant absorption by nuclear spins will thence occur when a RF pulse of the correct perturbing frequency ν is being applied to match the ΔE . The signal will be maximal when M is located in the transverse plane (the x - y plane perpendicular to B_0) for a $\pi/2$ pulse duration (Figure 2.24c).

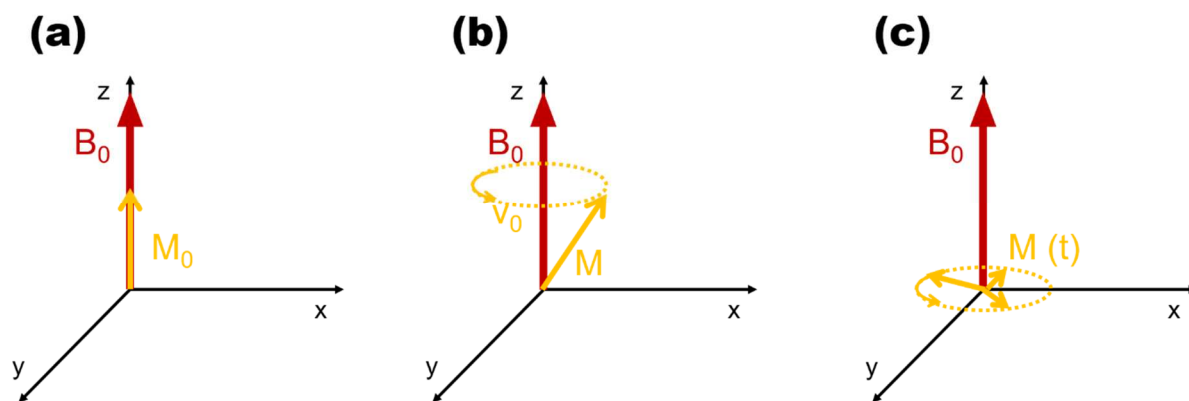


Figure 2.24. Evolution of magnetisation before (a) and during (b) the application of the radiofrequency pulse. For a $\pi/2$ pulse duration, the magnetisation is transferred in the x-y plane (c).

The time-dependant relaxations of the magnetic nuclear spins resulting from these transitions are the phenomena that are exploited in NMR spectroscopy. The relaxation phenomena can be distinguished via two distinct relaxation times:

- The longitudinal (or spin-lattice) relaxation time T_1 , which represents the lifetime of the process that returns the magnetization to the Boltzmann equilibrium along the z-axis. As a matter of fact, the distribution of the population between the energy levels is not instantaneous and it can remain equal for a certain time (T_1) before spins are enabled to flip amongst their energy levels so as to establish the Boltzmann population differences. The interval between two transients should be long enough ($D1 \approx 3-5 T_1$) to recover the M_0 magnetization. This condition is necessary to ensure an accurate quantitative integration of NMR spectra.
- The transverse (or spin-spin) relaxation time T_2 , which defines the lifetime of the signal in the transverse plane (x-y plane). The time dependant signal of the return to equilibrium in this plane is recorded in the reception/emission coil and is known as the Free Induction Decay (FID). Applying a Fourier transform to the FID, the NMR spectrum is obtained. The evolution of the FID (and thus the NMR spectrum) depends on the interactions present in the solid.

The nuclear spin probed by NMR can interact with the surrounding electronic cloud in different ways, as listed in Table 2.4.

Table 2.4. Principal characteristics of interactions in solids exploited by NMR.

Interaction	Cause	Amplitude (Hz)	Information	Field dependency
Zeeman	Interaction with B_0 magnetic field	10^7 - 10^9	Nucleus selection	$\propto B_0$
Chemical Shift	Local field modification by electrons	10 - 10^4	First neighbours, coordination	$\propto B_0$
Dipolar spin-spin coupling	Spin-spin interaction through space	10^4 - 10^5	Distances	Independent
Dipolar nuclear-electron spin coupling	Paramagnetic nuclear-spin interaction through space	10^7 - 10^8	Distances	$\propto B_0$
Indirect J coupling	Spin-spin interaction through bonds	10 - 10^3	Bonds, distances	Independent

Among the different interactions occurring in materials containing paramagnetic transition metals —as NMC811, in which Mn^{4+} has electronic configuration $[Ar] 3d^3$ and $Ni^{3+} [Ar] 3d^7$ —, the dipolar nuclear-electron spin coupling is the strongest and it determines the shape of the NMR spectra, while all the others appear as perturbations. This coupling is due to the anisotropic interaction of the probed nuclear spin with a localized unpaired electron through space; chemical bonding —and thus overlapping orbitals— is thence not necessary to have this type of interaction. Since the intensity of the dipolar nuclear electron spin coupling is directly proportional to the external magnetic field B_0 , a higher magnetic field results in a stronger interaction and thence in a faster relaxation time T_2 . Hence the resulting NMR spectrum will be broader. In

order to be able to properly detect the signal of a nucleus in very close intimacy with a paramagnetic centre it is thence essential to work with a low-field spectrometer. Actually, the dipolar nuclear electron interaction can be represented by the Hamiltonian:

$$H_{\text{en}} = \frac{\mu_0}{4\pi} \cdot \left(\frac{h}{2\pi}\right)^2 \cdot I_z^2 \cdot \mu_n \cdot \mu_e \cdot D_{ij} \cdot \frac{1}{r^3} \quad (2.6)$$

in which r represents the distance between the probed nucleus and the paramagnetic centre. Nuclear spins closer to the paramagnetic centre (as Li inside NMC materials) will thence be characterised by a stronger interaction than nuclei further from it (as Li at the surface of secondary particles of NMC). This principle has largely been exploited during acquisitions to separate these two contributions, and to focus on surface compounds only, as previously studied by our group.⁶ As a matter of fact, when increasing the magnetic field, the signal becomes so broad and spans over an extremely large frequency range (but maintaining the same overall intensity) that it cannot be detected anymore.

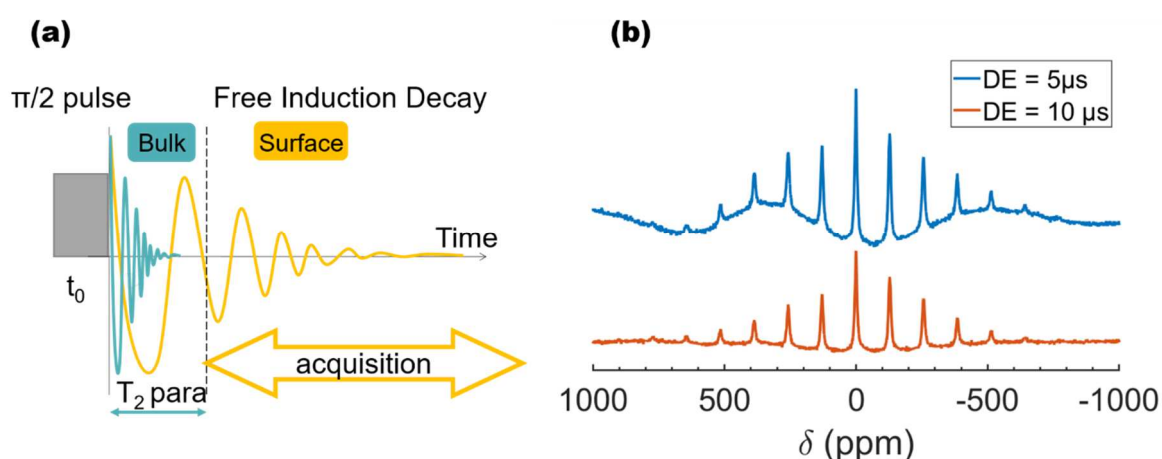


Figure 2.25. Effect of the application of a pre-scan delay (DE) during the acquisition of NMR spectra on a paramagnetic material.

By using a 500 MHz spectrometer, we can thence make the relaxation extremely fast. Applying a pre-scan delay (DE) of 10 μs before acquiring the FID, we can select the signal corresponding to the diamagnetic surface species only, since they are characterised by a slower T_2 due to their longer distance from the paramagnetic centre

(Figure 2.25a). Figure 2.25b shows the influence of the paramagnetic material signal when a too short DE is applied (blue spectrum).

Furthermore, it is worth mentioning that a nucleus in a paramagnetic material is also prone to interact with the paramagnetic centre via Knight or Fermi shift. While the first one is typical of metals, the Fermi shift is characteristic of metal oxides as NMC materials and is at the basis of the large chemical shifts (between 400 and 2000 ppm) usually observed for these compounds. Contrary to the dipolar electron nucleus interaction previously seen, this interaction occurs via the chemical bonding. In NMC materials e.g., one electron of the transition metal can couple with the Li via the oxygen bond. This results in a transfer of electronic spin density from the occupied 3d orbitals to the empty 2s orbitals of the lithium ion through the overlapping with the 2p orbitals on the oxygen. Different transition metals or transition metals with different oxidation states would thence influence differently the Li environment bringing to signals at different chemical shifts. In addition, the Fermi contact, depending on the efficiency of the orbitals overlapping, bond lengths and angles will influence strongly the value of the Fermi contact shift.

In solution, molecules reorient quickly so that anisotropic interactions are averaged and isotropic ones are only visible, in form of very sharp signals. On the other hand, when observing a polycrystalline powder, crystals are oriented in all directions and the NMR signal results to be broader due to the large number of dipolar interactions happening at different frequencies.

In solid state NMR, the magic angle spinning technique provides an efficient way to reduce or eliminate anisotropic interactions, leading to better resolution spectra. As a matter of fact, the first order anisotropic component of the dipolar coupling depends on the orientation through a factor of $3 \cos^2 \theta - 1$, which is zero when $\theta = 54.74^\circ$. When spinning the rotor with an angle of 54.74° it is thence possible to average all the anisotropic interactions to zero and obtain a sharper spectrum, easier to analyse. In order to successfully remove anisotropic interactions in a polycrystalline powder, the

spinning frequency around the magic angle has to be equal or greater than the magnitude of the interactions. Since dipolar interactions are characterised by an extremely high magnitude (Table 2.4), it is hardly possible experimentally to remove them completely. Instead of the very broad static solid-state NMR spectra exhibiting the full effect of anisotropic interactions, a manifold of spinning sidebands (separated by the MAS rate in Hz) becomes visible when spinning at the magic angle.

3.2. Quantification method

The integrated intensity of NMR signals depends on the number of nuclei present in the analysed sample; SS MAS-NMR is thus considered a semi-quantitative technique, just as Nuclear Magnetic Resonance in the liquid state. However, a direct correlation between the integrated intensity of a signal and the mass of the corresponding compound does not exist. The signal intensity varies as a function of acquisition conditions, namely number of scans, receiver gain and mass of the analysed sample. For this reason, in order to exploit NMR data to obtain absolute quantification – and comparison between various species – the use of a calibration curve is essential.⁷

For this purpose, eight samples were prepared by mixing NMC811 with different quantities of LiF in a planetary ball miller for 2 × 30 minutes to guarantee the best possible intimacy between the paramagnetic material and the LiF. By using a recycle delay (D1) of 50 s, the acquisition of quantitative spectra was assured.

⁷Li integrated intensities were determined by using spectral simulation (DMFit Software) after performing a numerical fit of each set of peaks corresponding to a chemical compound.⁸ The so obtained integrated intensities were normalised considering the mass of the sample contained in the NMR rotor, the number of scans and the received gain. Calibration curves for both ⁷Li and ¹⁹F were thence obtained by plotting the diamagnetic amount (in μmol) of lithiated or fluorinated material as a function of their normalised integrated intensities. The spinning sidebands were also taken into account. The equations obtained from the linear fitting of the experimental

data (integrated intensity vs diamagnetic amount of Li or F) were used to calculate the amount of diamagnetic species found at the surface of the NMC throughout this work.

The interest of this approach lies in the possibility of easily obtain an absolute quantification of all the lithiated species in the material, at the surface of both primary and secondary particles. While quantification by XPS is limited by the analysis depth (c.f. Part 4) and STEM-EDX by electron beam damages (c.f. Part 1), SS MAS-NMR allows having a complete description of the sample surface in its original state. Lithiated species in the porosities of secondary particles are e.g. particularly difficult to analyse by XPS, whilst they are as visible as the ones at the extreme surface by NMR. Furthermore, NMR being a non-destructive technique not presenting degradation issues, it is an effective tool for the analysis of battery materials, often particularly sensitive to analysis conditions.

Moreover, by analysing the signal distribution over the spinning sidebands, it is possible to determine which compounds are closer or further from NMC. Actually, species very close to the surface (or trapped in the porosities) suffer more of the effect of the paramagnetic material and their signal —and thus the spinning sidebands manifold— will be wider. SS MAS-NMR can thus be exploited to have qualitative information about the distribution of lithiated compounds too.

3.3. Technique limitations and possible solutions

The analysis on NMC electrodes appeared to be particularly complicated. The removal of the slurry from the aluminium collector on industrially coated electrodes is indeed tricky since the adhesion is very strong. Some metallic aluminium parts remaining stuck with the materials are likely present in the rotor during the analysis. The magnetic pulse could thence be dissipated in the aluminium as an electric current, impeding the correct excitation of the material. Moreover, the so induced current would create a local magnetic field (often in the opposite direction than the external magnetic field) resulting in the instability of the rotation spinning (Figure 2.26). In order to overcome this issue, we decided to analyse dried slurries instead, having the

same formulation as electrodes, but not being coated on Al foils nor calendered. In this way, we were able to investigate the effect of electrode formulation without having problems related to electrode removal from the current collector. XPS was then used to analyse both dried slurries and electrodes (c.f. Chapter 3) to identify possible differences between the two samples –and thence the influence of induction and calendering steps.

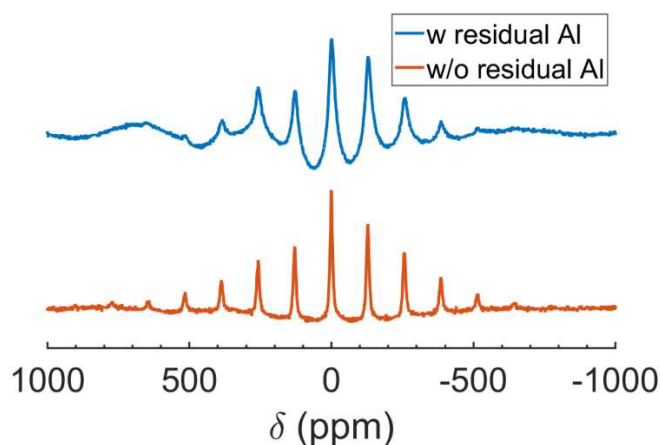


Figure 2.26. Effect of metallic aluminium residuals during the NMR analysis of electrodes.

When working with NMC materials, it is important to keep in mind that even if spinning at the magic angle, electron nucleus dipolar interactions are so strong that the signal still appears very large. Moreover, the presence of a large number of different environments makes the signal and its spinning side bands even larger. The resulting NMR spectrum recorded on a low-field spectrometer appears thence to be the sum of extremely broad signals often overlapping with the spinning sidebands of each different environment and thus extremely complicated to analyse. The identification of the isotropic bands results appears to be often impossible without having further information on the material.

One possible solution to this issue is to acquire ${}^6\text{Li}$ spectra instead of ${}^7\text{Li}$, since the former isotope has a much smaller gyromagnetic factor ($\gamma_{7\text{Li}}/\gamma_{6\text{Li}} = 2.6$), resulting in spinning sidebands with typically very low intensity. On the other hand, its low isotopic natural enrichment (7.6 %) leads to a very low signal to noise ratio even after

one week acquisition when compared to ${}^7\text{Li}$ spectra. Moreover, since the total energy given by the Zeeman interaction is proportional to intrinsic magnetic moment μ , it also depends on the gyromagnetic ratio γ in a direct way (Equation 2.4). Hence, for NMR experiment purposes, the smaller the gyromagnetic ratio, the less sensitive the nucleus.

The use of the MATPASS pulse sequence was thence decided to be the best strategy for the acquisition of low magnetic field MAS-NMR spectra. This particular experiment firstly developed by the collaboration between Z. Gan's and C. Grey's groups consists in the combination of magic-angle turning (MAT) and phase-adjusted sidebands separation (PASS) to obtain isotropic NMR spectra with apparently infinite MAS spinning rate.⁹

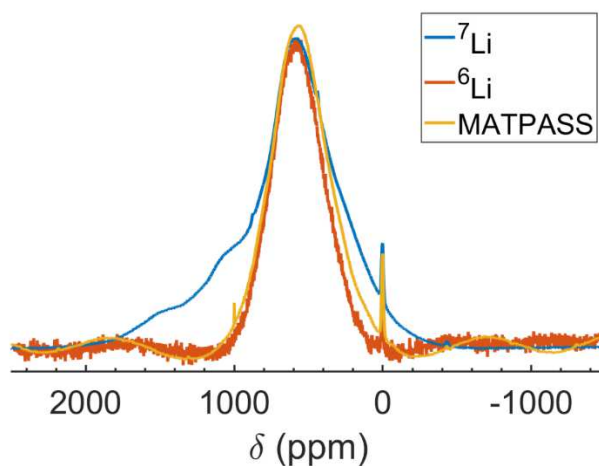


Figure 2.27. Comparison between powder NMC811 ${}^7\text{Li}$ MAS-NMR spectra (in blue), ${}^6\text{Li}$ (in orange) and ${}^7\text{Li}$ using MATPASS pulse sequence (in yellow) using a 200 MHz spectrometer.

In this way, it was then possible to acquire ${}^7\text{Li}$ spectra —thus fast acquisitions— without having to deal with the many spinning sidebands usually associated to this nucleus. Figure 2.27 represents the comparison between a ${}^7\text{Li}$ MAS-NMR spectrum, a ${}^6\text{Li}$ MAS-NMR spectrum and a ${}^7\text{Li}$ MAS-NMR spectrum using the MATPASS pulse sequence of pristine NMC811 powder. Even if the acquisition in MATPASS largely simplifies the resulting spectrum, the signal still appears to be too broad to be resolved. For this reason, the identification of the different components of 200 MHz spectra that

will be presented throughout this work will not be performed. Instead, the overall width and the chemical shift of the principal peaks will only be compared between different samples (c.f. Chapter 4).

On the other hand, the analysis of diamagnetic surface species using a high magnetic field spectrometer in the conditions explained in the previous section appears easier at a first sight, since signals are sharper. However, when zooming on the principal isotropic band, it becomes clear that the apparently well-defined peak is instead the resultant of a larger number of contributions not particularly well separated. As a matter of fact, chemical shifts of lithiated diamagnetic compounds typically found at the NMC surface are very similar and usually measured within -1.2 and 3.9 ppm. The true speciation of the diamagnetic contamination layer at the surface of NMC is thus not possible to obtain by MAS-NMR only. For this reason, MAS-NMR spectra were analysed in combination with XPS results throughout this work. Such a synergetic use of these two techniques appeared essential in the complete analysis of NMC materials and allowed us deeply exploiting all the possible information coming from both MAS-NMR and XPS spectra.

Part 4. X-rays Photoelectron Spectroscopy (XPS)

X-rays Photoelectron Spectroscopy (XPS) is one of the most commonly tools used to analyse NMC surface chemistry –and battery materials surfaces and interfaces in general– in the literature.

The aim of this part is to give the reader the theoretical principles of this technique to point then out its principal limits. XPS results are often taken as true without further investigation; we will highlight here the principal precautions that should be taken while acquiring and analysing XPS data.

On the other hand, XPS gave a precious contribution throughout this study, in particular in the interpretation of NMR quantification data. In the last section of this part, we will show how XPS data can be exploited to obtain a compound quantification that can be compared with NMR results.

4.1. Theoretical principles

When a sample is irradiated by monochromated soft X-rays (e.g. Al K_{α} or Mg K_{α} in XPS), electrons from all orbitals of an atom with binding energy (BE) lower than the X-ray energy can be excited, with creation of a photoelectron that can be brought to the surface and escape from the sample surface to the vacuum (Figure 2.28a). The photoelectron kinetic energy E_k corresponds to the difference between the initial binding energy (BE) of the excited electron and the incident beam energy ($h\nu$), following the total energy conservation relation:

$$BE = h\nu - E_k \quad (2.7)$$

By measuring the kinetic energy of the emitted photoelectron, which is at the basis of XPS analysis, and knowing the photon energy sent on the sample, it is possible to deduce the binding energy, which is characteristic of the orbital from which the electron is ejected. On a XPS spectrum, photoelectrons are counted depending on their binding energies, unique to each element.

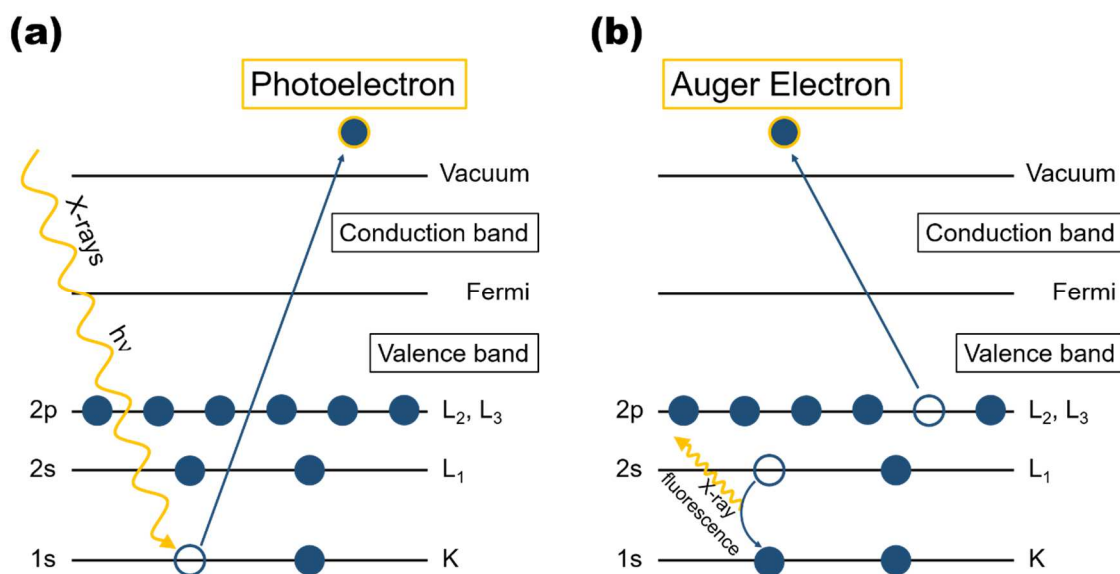


Figure 2.28. Schematic representation of photoelectron formation (a) and relaxation by formation of an Auger electron (b) in XPS.

According to the Beer law, the intensity of emitted photoelectrons as a function of the depths (z) is given by:

$$I = I_0 \exp\left(-\frac{z}{\lambda \cos\theta}\right) \quad (2.8)$$

where I_0 is the intensity of emitted photoelectron from an infinity thickness substrate, λ the inelastic mean-free-path of an electron (typically 0.4–5 nm), and θ the electron emission angle relative to the sample surface normal. By integrating XPS signals and correcting them with the so-called Relative Sensitivity Factors (RSFs), typical of each transition, it is thence possible to obtain the elemental atomic composition of the sample surface. Instead of the classical atomic quantification, XPS data was exploited throughout this work to obtain compound quantification. Details of this procedure will be given in Section 4.4.

In addition to quantitative elemental analysis, chemical information of the surface elements can be obtained by studying the variations in elemental binding energies. Indeed, chemical shifts can result from the variations of the electron density of the valence orbitals (due to different chemical environments and oxidation states) on the initial atomic energy and on the final energy resulting from the photoelectron

emission. Decomposing the core-shell elemental spectra into various components centred on specific binding energies – depending on the existing bonds –, it is thence possible to obtain information about the sample extreme surface chemical composition.

On the other hand, elemental or chemical quantification using XPS appears relatively tricky due to the rapid intensity decay with the depth probed. Chemical inhomogeneities along z can critically influence the quantification results; the obtained mean compositions are usually severely affected by the so-called screening effect of surface species, which result to be overestimated compared to those that they overlap. This and more technique drawbacks will be the focus of next sections.

4.2. Experimental conditions

XPS acquisitions were performed using a Kratos Axis Nova Instrument using a monochromatic Al K_{α} (1486.6 eV) X-rays source operating at 300 W. Samples were prepared inside an Argon filled glovebox. Adhesive conductive carbon tapes were used to fix electrodes on the XPS sample holder, while powders were inserted in designated holes to assure the analysis of the sample only, without any influence of the adhesive tape. The sample holder was positioned on the XPS transfer chamber and it was sealed before moving out of the glovebox to the XPS machine. The tube containing the samples was fixed on the XPS instrument and left under vacuum overnight to reach base pressure of 5×10^{-10} Torr.

Wide range survey spectra were acquired with a pass energy (PE) of 80 eV, leading to an overall instrumental resolution of 0.9 eV measured on Fermi edge. PE of 20 eV at $\theta = 0^\circ$, X-ray spot size of $700 \mu\text{m} \times 300 \mu\text{m}$ and 100 meV step were used instead to acquire high-resolution spectra, exploited to quantify the compounds at the surface of the materials. In this way, it was possible to achieve an instrumental resolution of 0.55 eV measured at Fermi edge.

Data processing was performed using CasaXPS software applying the U 3 Tougaard background correction. All the spectra were calibrated with respect to C 1s, which binding energy was fixed at of 284.8 eV. Fitting was performed to identify the different peaks based on their binding energies. Gaussian/Lorentzian (70/30%) line shapes were used to fit the majority of the peaks.

4.3. Technique limitations and possible solutions

4.3.1. Depth analysis and spot size

Figure 2.29 shows the schematic representation of an NMC811 secondary particle with its native surface contamination layer. As already pointed out in Chapter 1, NMC materials are in fact affected by the presence of surface species already in their pristine state. Moreover, the presence of other impurities trapped into the porosities of secondary particles was hypothesised throughout this work.

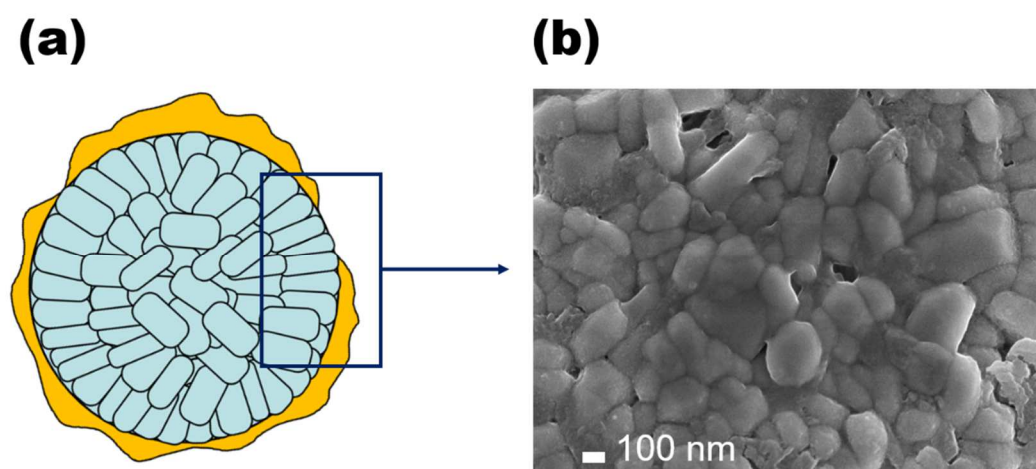


Figure 2.29. Inhomogeneity of the surface contamination layer schematised (a) and pictured by SEM (b).

The low-energy nature of the Al-monochromated sources usually employed for acquisitions at a laboratory scale does not allow probing the material deeper than 10 nm. This results in the impossibility to detect impurities inside secondary particles. In order to avoid this issue, powder samples were grinded before the analysis.

Furthermore, Figure 2.29 shows how the surface contamination layer is generally not homogeneous in thickness. Therefore, when such samples are observed by XPS, results can often depend strongly on the analysed area. It is thence essential to perform acquisitions on multiple points to average data. Concurrently, it has to be kept in mind that the X-ray spot size is quite large ($700\ \mu\text{m} \times 300\ \mu\text{m}$ in studied conditions) when compared to the particles size (10-15 μm diameter for NMC811 secondary particles). The information obtained by XPS are thence averaged over various particles and it is essential to be aware of this when analysing XPS data. E.g., the presence of a Ni 2p signal during the analysis of NMC811 powder aged in humid atmosphere for one year conducted by Jung et al. does not necessary mean that Ni is contained in the contamination layer as they suggest. Such a signal could in fact simply be due to the non-homogeneous nature of the contamination layer and to the large X-ray spot size: if the contamination layer is somewhere thinner than 10 nm, the underlying NMC811 could be seen by XPS, resulting in the consequent presence of the Ni 2p peak.

4.3.2. Degradation issues

The possible degradation of some species under X-ray beam is often not taken into consideration seriously. While it has already been demonstrated that polymers (such as the PVDF usually contained into electrode formulations) and other organic materials are sensitive to X-rays, inorganic materials have always been considered immune to degradation with such low-energy radiations (especially when compared to electrons in TEM).¹⁰ Figure 2.30 represents instead how even species like carbonates – that have always been considered particularly stable – are affected by degradation under X-rays in the studied conditions. Here, 10 scans of around 30 minutes each were performed to acquire peaks relative to Ni 2p, Co 2p, Mn 2p, O 1s, C 1s, S 2p and Li 1s in this order. Figure 2.31a shows the evolution of the $(\text{CO}_3)^{2-}$ signal (here considered as Li_2CO_3) upon exposition to X-rays. Similarly, Figure 2.31b represents the evolution of the Li 1s peak during the same amount of time, in which the contribution around 55 eV is attributed to Li_2CO_3 . In both cases, the intensity of the signal corresponding to

Li_2CO_3 decreases by 35% in the 6 hours acquisition, demonstrating how even inorganic stable species can be degraded upon long exposition to X-rays.

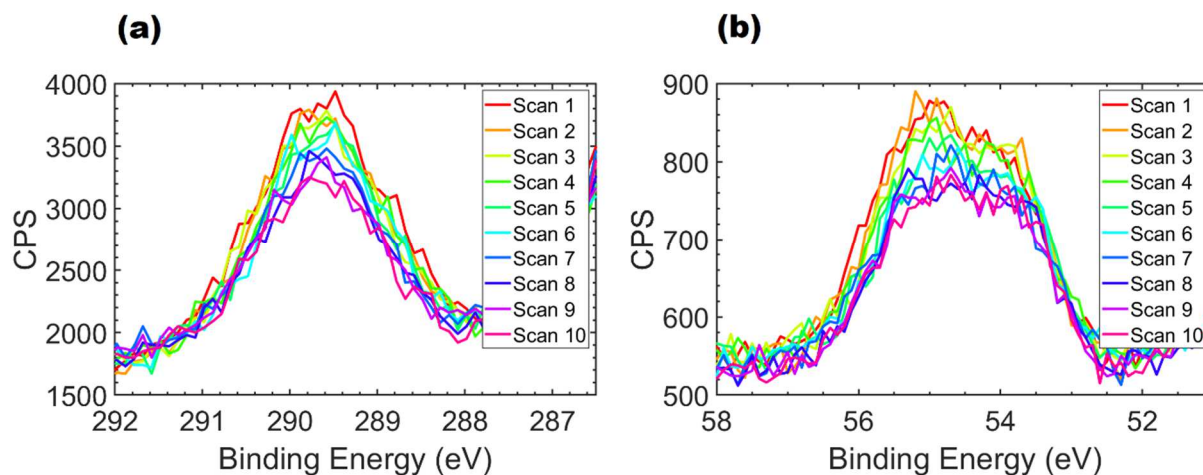


Figure 2.30. Degradation under X-Rays exposure at the C 1s peak (a) and at the Li 1s peak during the analysis of NMC811 powder.

When drawing conclusions about XPS results, such phenomenon should be taken into great account. The partial degradation of carbonates species from the NMC surface would in fact decrease the contamination layer thickness and make the signal corresponding to the active material (AM) visible on the spectra. In particular, in the already mentioned paper by Jung et al., the AM signal is not present on the O 1s spectrum, while it is visible on the Ni 2p one. If the degradation phenomenon was not taken into account during acquisitions and the Ni 2p spectrum was registered after all the other elements, the appearance of a Ni signal could be due to the decreased contamination layer thickness. Moreover, Ni 2p peak is not always well-defined and longer acquisitions are needed when compared to the O 1s (around 3 minutes for Ni 2p vs 20 seconds for O 1s in pristine materials in which Ni signal is quite strong).

The best option to avoid X-ray beam degradation would be to perform acquisitions while cooling the system down, but the difficulty in preparing the set-up for such experiments often does not allow its use for analysing a large number of samples.¹¹ In alternative, the use of shorter dwell time and the focus on a limited number of elements could improve the acquisition time and reduce the X-rays exposition. Hence, TM 2p

peaks were e.g. not registered throughout this work. Instead, TM 3p peaks were acquired together with Li 1s. Moreover, the C 1s peak was the first one to be registered in order to be able to properly quantify carbonates before any degradation could occur. Furthermore, the acquisition of wide spectra, which takes alone around 30 minutes, was generally done at the end of the HR scans.

4.3.3. Difficulties in data processing

It has to be mentioned that the choice not to acquire TM 2p peaks did not come only from the degradation issues, but also from the difficulties encountered in analysing such peaks. In particular, Figure 2.31 represents the typical electron binding energy values for elements present in NMC materials and classical electrode formulations from 600 to 900 eV.

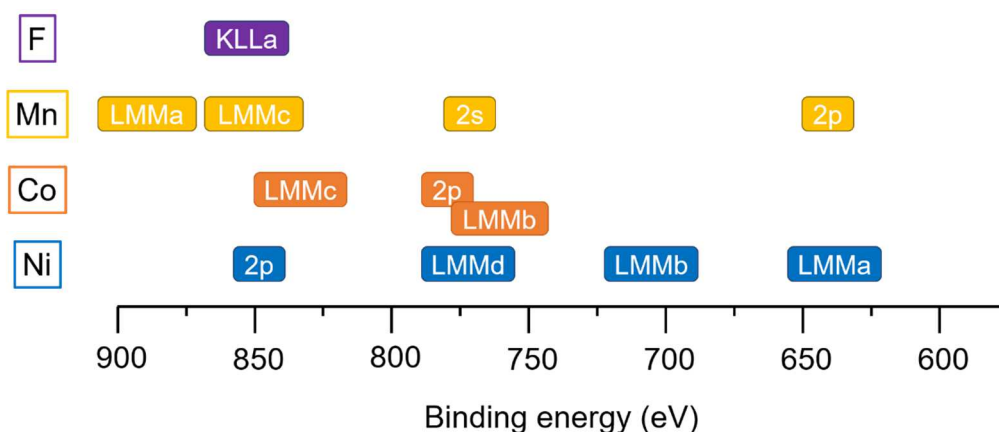


Figure 2.32. Typical binding energy (BE) values for nickel (in blue), cobalt (in orange), manganese (in yellow) and fluoride (in purple).

Let us focus now on TM 2p peaks: Ni 2p is around 853 eV, Co 2p around 778 eV and Mn 2p around 639 eV. On the other hand, when taking into account the Augers emissions of such elements it appears that they strongly overlap with the 2p peaks:

- Mn $L_3M_{45}M_{45}$ transition has a binding energy typically around 852 eV, thence overlapping with Ni 2p;
- Ni $L_3M_{45}M_{45}$ transition is on the other hand around 641 eV, overlapping with Mn 2p;

- When looking at Co 2p peak, the situation becomes even more complicated, with not only Co L₃M₂₃M₄₅ transition, but also Ni L₃M₂₃M₂₃ and Mn 2s peaks characterised by almost the same energy as Co 2p.

The analysis of TM 2p peaks to determine their oxidation state becomes thus extremely challenging already for pristine powders. When analysing electrodes, the contribution of F (very strong KLL transition around 845 eV) from PVDF binder has to be taken into consideration as well. Since information about transition metals oxidation states at a nanometric level can be obtained by STEM-EELS, we considered that trying fitting TM 2p XPS peaks was not worthy.

4.4. Compounds quantification: how to exploit XPS data to obtain speciation information

XPS was used in our study to obtain compounds quantification instead of the simple atomic percentage quantification for which XPS is commonly used. As already pointed out in Section 3.3, SS MAS-NMR ⁷Li chemical shifts of species typically found at the surface of NMC materials are very similar and an efficient deconvolution of the NMR isotropic resonance is particularly tricky. For this reason, XPS was exploited to obtain information about the speciation of surface lithiated species that would be subsequently used to properly deconvolve MAS-NMR spectra. Although lithiated compounds have very similar peak positions on the Li 1s XPS spectra too, the advantage of XPS is the possibility to probe and quantify other elements than Li. Putting together all the information it was thence possible to quantify surface lithiated compounds by both MAS-NMR and XPS and to compare the results obtained by these two techniques.

XPS fits were performed by imposing the integrated areas of peaks assigned to a same compound to be proportional to the amount of the other elements involved into the considered species based on their formula. The first step for such a process (after calibration using the contamination C–C, C–H signal at 284.8 eV) is to analyse the

XPS wide spectrum to individuate all the elements present at the NMC surface. By looking at the HR spectra of the identified elements, it is often possible to define already in which form they are thanks to the peak position.

Let us take sulphur as the easiest example. The S 2p peak is typically split into two components (S 2p 1/2 and S 2p 3/2 with an area ratio of 1:2) because of the spin orbit coupling effect. The peak position (168.9 eV for the S 2p 3/2) is typical of the sulphate (SO₄)²⁻ group. Another contribution corresponding to such a compound will thence be found on the O 1s peak (around 532 eV). Moreover, its area will have to account for four times the area of the involved S, meaning:

$$A_{O\ 1s} = \frac{A_{S\ 2p} \cdot RSF_{O\ 1s}}{RSF_{S\ 2p}} \cdot 4 \quad (2.9)$$

Relative Sensitivity Factors (RSF) normalisation is here necessary to compare the quantification of different elements. RSF are empirically derived factors generally used to normalise peak intensities to provide atomic concentrations. They take into account the Mean Free Path Length (λ), the photoionization cross-section (σ), as well as several experimental parameters specific to the used instrument.^{12,13}

Sulphates can be found in form of both Li₂SO₄ and Na₂SO₄. Since sodium is expected to only be in the form of sulphates while multiple lithiated compounds are generally found in the surface contamination layer, it is important to determine sodium quantity before deducing the Li₂SO₄ amount. The S 2p peak area corresponding to Li₂SO₄ will thence be:

$$A_{S\ 2p_{Li_2SO_4}} = A_{S\ 2p_{tot}} - A_{S\ 2p_{Na_2SO_4}} = A_{S\ 2p_{tot}} - \left(\frac{A_{Na\ 1s} \cdot RSF_{S\ 2p}}{RSF_{Na\ 1s}} \cdot \frac{1}{2} \right) \quad (2.10)$$

Subsequently, the Li 1s peak intensity related to the compound Li₂SO₄ results to be:

$$A_{Li\ 1s_{Li_2SO_4}} = \frac{A_{S\ 2p_{Li_2SO_4}} \cdot RSF_{Li\ 1s}}{RSF_{S\ 2p}} \cdot 2 \quad (2.11)$$

A component having this constrained integrated area can thence be incorporated to the complex Li 1s peak around 56 eV (typical energy binding value for Li₂SO₄).

The same process can be applied to all the other compounds. The critical point is to find a well-defined and isolated peak that can be attributed to a specific compound, as just showed for sulphates. This procedure can also be quite easy e.g. to quantify Li_2CO_3 by focusing on the C 1s peak around 290 eV corresponding to $(\text{CO}_3)^{2-}$ or LiO from the O 1s signal around 528 eV.

In the beginning, not only peak intensities were constrained, but also peak positions and Full Widths at Half Maximum (FWHMs), generally by imposing the same FWHM for similar compounds (e.g. LiOH, Li_2CO_3 and Li_2SO_4 contributions on the Li 1s peak).

Once acceptable fits were obtained, constraints on FWHMs and positions were removed and fits were proven to be stable and consistent. The phase quantification was deduced from the addition of all element percentages involved in the same compound. If we take again the previous example of Li_2SO_4 , the compound percentage amount will be given by the sum of the atomic percentage concentrations of all the contributions related to Li_2SO_4 on the peaks of Li 1s, S 2p and O 1s. This value can be thence normalised with respect to the total atomic concentration of the considered compounds only. For instance, when comparing XPS results with NMR quantification, only species that can be detected by NMR will be considered, ignoring the amount of NMC, organic species and contamination hydrocarbons.

Part 5. Conclusions

The perfect characterisation technique does not exist. It is indeed difficult –and disappointing really– to realise the truthfulness of this sentence. Each technique has its strengths and its limits, and it is essential to identify them to find alternative approaches to exploit all the information we could obtain.

We showed in the first part of this chapter how a different strategy was necessary to obtain a relative quantification of oxygen and transition metals at the surface of primary particles by EELS. However, electrons used for (S)TEM are too energetic to analyse the contamination layer at the surface of the material, composed principally of light elements. A similar degradation was surprisingly found to occur during XPS measurements, as demonstrated in the fourth part of this chapter. The acquisition conditions were therefore adapted to obtain the best and most truthful information. In the same way, parameters and procedures were readjusted to prepare TEM lamellas by FIB and analyse 3D volumes.

Moreover, the small probe depth and large spot size typically used for XPS measurements did not allow obtaining reliable quantification data. ^7Li MAS-NMR was demonstrated to be the only technique capable of providing such results. Nevertheless, in order to define the exact composition of the surface layer, it was necessary to exploit XPS results since MAS-NMR signals are too large to obtain such information on its own. By using XPS and MAS-NMR together in a synergistic way, it was thence possible to go beyond the limits of each technique and acquire new knowledge about qualification, quantification and distribution of the observed species.

Despite the imperfection of every characterisation technique, we showed here how using a combination of many of them could allow finding proper answers to our questions, exploiting the assets of each one.

References

- (1) Williams, D. B.; Carter, C. B. *Transmission Electron Microscopy: A Textbook for Materials Science*, 2. ed.; Springer: New York, **2009**.
- (2) Egerton, R. F. *Electron Energy-Loss Spectroscopy in the Electron Microscope*; Springer US: Boston, MA, **2011**. <https://doi.org/10.1007/978-1-4419-9583-4>.
- (3) Gatan Inc. <https://www.gatan.com/products/tem-imaging-spectroscopy/k3-cameras>.
- (4) Botton, G. A.; Appel, C. C.; Horsewell, A.; Stobbs, W. M. Quantification of the EELS Near-Edge Structures to Study Mn Doping in Oxides. *J. Microsc.* **1995**, *180* (3), 211–216. <https://doi.org/10.1111/j.1365-2818.1995.tb03680.x>.
- (5) Gatan Software Team. *Digital Micrograph 3.40.2804.0*; Gatan Inc., **2020**.
- (6) Dupré, N.; Martin, J.-F.; Guyomard, D.; Yamada, A.; Kanno, R. Detection of Surface Layers Using ^7Li MAS NMR. *J. Mater. Chem.* **2008**, *18* (36), 4266. <https://doi.org/10.1039/b807778a>.
- (7) Cuisinier, M.; Martin, J.-F.; Moreau, P.; Epicier, T.; Kanno, R.; Guyomard, D.; Dupré, N. Quantitative MAS NMR Characterization of the $\text{LiMn}_{1/2}\text{Ni}_{1/2}\text{O}_2$ Electrode/Electrolyte Interphase. *Solid State Nucl. Magn. Reson.* **2012**, *42*, 51–61. <https://doi.org/10.1016/j.ssnmr.2011.09.001>.
- (8) Home | dmfit - D.Massiot - NMR@CEMHTI CNRS UPR3079 Orléans France <https://nmr.cemhti.cnrs-orleans.fr/Dmfit/> (accessed 2022 -04 -02).
- (9) Hung, I.; Zhou, L.; Pourpoint, F.; Grey, C. P.; Gan, Z. Isotropic High Field NMR Spectra of Li-Ion Battery Materials with Anisotropy >1 MHz. *J. Am. Chem. Soc.* **2012**, *134* (4), 1898–1901. <https://doi.org/10.1021/ja209600m>.
- (10) Grissa, R.; Abramova, A.; Tambio, S.-J.; Lecuyer, M.; Deschamps, M.; Fernandez, V.; Greneche, J.-M.; Guyomard, D.; Lestriez, B.; Moreau, P. Thermomechanical Polymer Binder Reactivity with Positive Active Materials for Li Metal Polymer and Li-Ion Batteries: An XPS and XPS Imaging Study. *ACS Appl. Mater. Interfaces* **2019**, *11* (20), 18368–18376. <https://doi.org/10.1021/acsami.9b01761>.
- (11) Grissa, R.; Fernandez, V.; Fairley, N.; Hamon, J.; Stephant, N.; Rolland, J.; Bouchet, R.; Lecuyer, M.; Deschamps, M.; Guyomard, D.; Moreau, P. XPS and SEM-EDX Study of Electrolyte Nature Effect on Li Electrode in Lithium Metal Batteries. *ACS Appl. Energy Mater.* **2018**, *acsam.8b01256*. <https://doi.org/10.1021/acsam.8b01256>.
- (12) Spectral Interpretation. In *X-Ray Photoelectron Spectroscopy*; John Wiley & Sons, Inc.: Hoboken, NJ, USA, **2011**; pp 101–140. <https://doi.org/10.1002/9781118162897.ch5>.
- (13) Watts, J. F.; Wolstenholme, J. *An Introduction to Surface Analysis by XPS and AES*, 1st ed.; Wiley, **2019**. <https://doi.org/10.1002/9781119417651>.

Chapter 3

Characterisation of NMC811 surfaces before cycling

The literature review presented in Chapter 1 resulted in the identification of the insufficient characterisation of the pristine material in the existing literature. In order to respond to this need, we report an extensive study of a pristine NMC811 powder sample in the first part of this chapter. The sample surface, analysed by STEM-EELS, STEM-EDX, ^7Li MAS-NMR and XPS, will be described in details, following the procedures reported in Chapter 2. The same approach was used to analyse the powder after short-term storage in defined conditions of low-humidity (RH = 30%). These results were gathered in a paper that will be submitted to the ACS Applied Materials & Interfaces journal and that is reported entirely in the first part of this chapter.

Since a large part of the characterisations published in the literature is performed on electrodes instead of powders, we report in the second part of this chapter an investigation of the impact of the electrode preparation steps on NMC811 samples aged in similar conditions as in the first part. In particular, we focused on the evolution of the native surface layer, suggesting possible correlations between the pristine surface conditions and the observations resulting from the analysis of both dried slurries and calendered electrodes.

The industrial samples were always analysed following the same methods in order to allow a proper comparison between them.

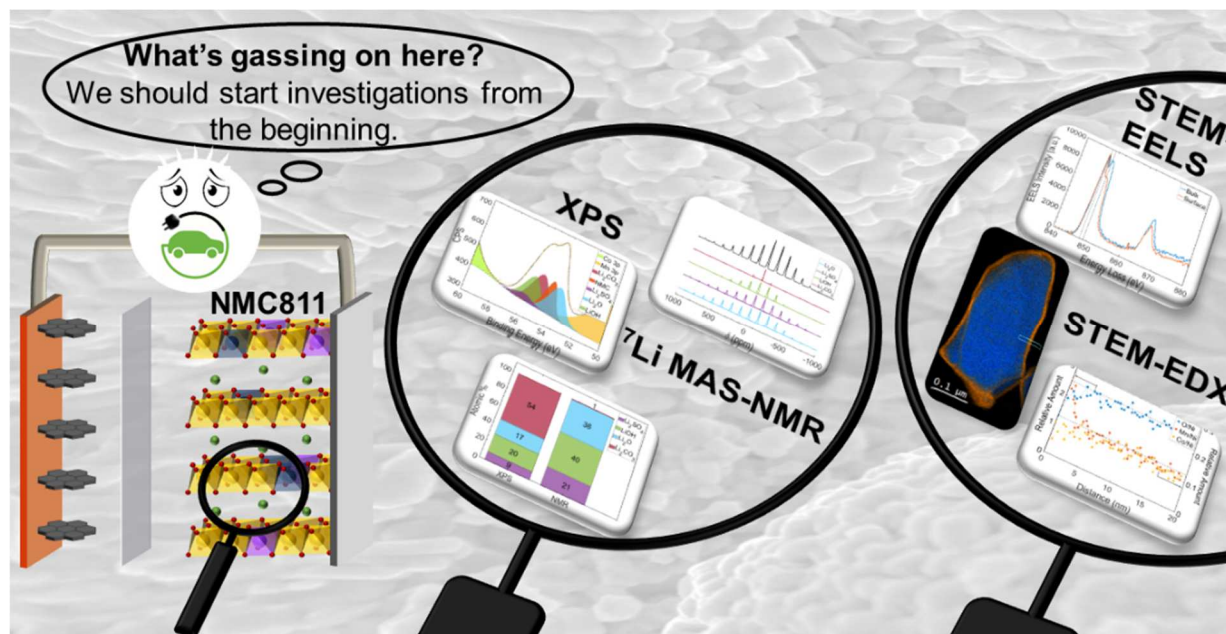
Part 1. Influence of storage conditions

Pristine surface of Ni-Rich NMC as a premise of future surface reactivity

Angelica Laurita¹, Liang Zhu², Pierre-Etienne Cabelguen², Jérémie Auvergniot², Dominique Guyomard¹, Vincent Fernandez¹, Jonathan Hamon¹, Nicolas Dupré¹, Philippe Moreau^{1,*}

¹Nantes Université, CNRS, Institut des Matériaux Jean Rouxel, IMN, F-44000 Nantes, France

²Umicore, 31 rue du marais, Brussels BE-1000, Belgium



1.1. Introduction

The fast world population growth combined to life modernization due to the rapid development of new technologies have brought, over the past years, a strong increase in the demand for primary energy, which has been initially met mainly by the combustion of fossil fuels.

Nowadays, in order to lower the contribution of fossil resources to the existing energy mix, our modern society relies increasingly on electrochemical energy storage for the electrification of vehicles. Performance of Lithium-ion batteries, currently vastly employed for this purpose, must therefore step up as fast as the technology evolution to meet the requirements of an ever more demanding market. In a world producing more than 50 million passenger cars per year (20 % of which could become hybrid electric vehicles or electric vehicles (HEV/EV) within the next 10 years), Li-ion batteries are required to provide an ever increasing energy density to guarantee a longer driving range.¹

Most positive electrode materials currently produced by the industry belong to the NMC family, described as layered oxides with general formula $\text{Li}(\text{Ni}_x\text{Mn}_y\text{Co}_{1-x-y})\text{O}_2$ with properties that depend on the relative amount of the different transition metals.²

In particular, in order to achieve a higher capacity and thence higher energy density, the research has been heading towards high Ni-content NMCs for some years now.²⁻⁵ Moreover, this approach allows lowering the Co content, reducing the cost in the material production, its toxicity and the humanitarian issues related to Co mining. Nevertheless, by increasing the Ni content, the material thermodynamic instability increases as well as the gas evolution upon electrochemical cycling, phenomenon of which the comprehension becomes an essential safety challenge at the industrial level.⁶

Many studies were conducted on Ni-rich NMCs in order to understand the gassing and instability issues during cycling and to elucidate both their origins and consequences. In fact, different gases in various amounts are released during the

electrochemical cycling depending on the battery state of charge.⁶ Together with H₂, C₂H₄ and CO released during the SEI formation in NMC-graphite full-cells at low potential, CO₂, CO and O₂, forming at the interface between active material and electrolyte at the end of the first charge, were demonstrated to be released from the cathode material. Among these gases, the quantity of released oxygen was proposed to be dependent on the material composition. In particular, theoretical calculations showed a decrease in the Ni–O energy bonding upon increase of the Ni oxidation state.⁷ The energy levels of Ni⁴⁺ are indeed closer to oxygen energy levels than Ni²⁺ ones, yielding an overall increase of the covalency of the M–O bond within the NMC active material. This trend was supported experimentally by Dixit et al. as they showed the release of O₂ together with a reduction of Ni to its more stable state (Ni²⁺).⁷ The oxygen release mechanism is thus logically exacerbated in the richest Ni-rich NMC due to the overall increase of Ni oxidation state with Ni concentration, in order to balance the total charge.

Also linked to the nature of the material surface, both high voltage reactions with the electrolyte and the degradation of surface impurities like Li₂CO₃ were proposed by several groups as a possible reason for the release of CO and CO₂.^{8–10}

From these studies, it is clear that the nature of the active material surface, which often depends on synthesis and storage conditions, lead to different reactivities towards the electrolyte. Since it is the seed for later evolution in cycling, the pristine surface of the NMC material is thus of utmost importance. However, despite the large number of publications on Ni-rich NMCs, only a few studies precisely describing the pristine material can be found in the literature.^{11,12} Surface reconstruction layers (SRL) dependent on the nature of the surface and bulk composition were observed by STEM-HAADF. It was associated with oxidation state reduction of Mn and Co at the extreme surface, although in an apparent larger extent than the SRL.¹¹ Some EDX analyses tend also to indicate an increase of Co composition at the extreme surface (first couple of nanometer), sometimes with an increase or a decrease of Mn content.¹²

It should be here mentioned that all these observations were performed on nano-powder samples prepared in air.

Such a necessary understanding of the initial state of positive electrode active materials, conducted by other groups on other similar transition metal oxides such as LiCoO_2 (LCO), $\text{Li}_{1.2}(\text{Mn}_{0.6}\text{Ni}_{0.2})\text{O}_2$ (LMNO) and Li-Mn-rich oxides, always demonstrated a different nature of the surface compared to the bulk of the material in its initial state and revealed the importance of proper and thorough surface characterizations of these materials at a nanometric scale.¹³⁻¹⁶ The segregation of Co and Ni along with the nucleation of domains with a spinel structure at the surface of Li-Mn-rich transition metal oxides (LMRTMOs) was reported by both Shukla et al. and Yan et al., at the pristine state.^{15,16} Moreover, a Li-poor and thus Co-rich surface (the electrochemically inactive Co_3O_4 layer) was observed at the surface of LiCoO_2 at the interface with the solid electrolyte and this behavior was proven to exist also in the case of NCA cathode materials.^{13,17} A surface Ni segregation was observed in the case of LMNO; the authors suggested here that this increased Ni concentration at the surface could occur during the synthesis.¹⁴

All these considerations are all the more important with the development of gradient composition Ni-Rich NMCs, where surface compositions are purposely tailored to differ from that in the bulk, with tremendous positive consequences on the cycling behavior.¹⁸ The actual state of the surface just after synthesis needs thus to be determined precisely.

Moreover, materials are usually not used straight from the furnace but are stored for a certain period of time before electrode fabrication. The effect of these storage conditions were examined in various studies and related to the surface and contamination layer evolutions and to the production of gases.^{9,19-21} Gasteiger's group investigated the evolution of the amount of surface impurities upon storage both in dry and humid air, highlighting a severe surface reactivity of NMC811 compared to NMC111.^{9,21} Basic nickel carbonate, with general formula $\text{NiCO}_3 \cdot 2\text{Ni}(\text{OH})_2 \cdot 2\text{H}_2\text{O}$, was

here identified as the major surface contaminant, affecting detrimentally both electrochemical performance and gassing (O_2 , CO, CO_2).

Since the synthesis and storage conditions were often identified as a possible cause of diversity between results obtained by different research groups, we propose to focus here on the characterization of an industrial NMC811 (UMICORE) in its initial state, as arrived from the production plant (Sample A0).²¹⁻²³ This approach permits a comprehension of the Ni-rich NMC surface reactivity and most of all to provide representative results that can be generalized at an industrial level. In order to respond to the lack of studies on the material in its initial state previously mentioned, that we consider essential for its comprehension, we present here a complete characterization of a pristine industrial grade NMC811, down to the sub-nanometer level. We also provide a possible explanation for its behavior during storage in defined conditions.

A multi-analytical approach based on on-site characterization techniques was used to give a complete picture of this complex material at different scales. MAS-NMR was used to give a correct quantification of the Li diamagnetic species at the surface of the material, while their speciation was possible thanks to the XPS. STEM-EDX and STEM-EELS were then used to monitor the composition trend within the first atomic layers of the active material through the quantification of oxygen and transition metals at a nanometric scale.

We present how surface inhomogeneity can be detected and quantified in a meaningful manner on the pristine material, relying on the coupling and crosstalk of advanced characterization techniques. We also show how storage conditions can further modify the production and the repartition of new compounds at the surface of the active material.

1.2. Experimental section

1.2.1. Pristine samples

Pristine NMC811 powder was synthesized at Umicore company by co-precipitating sulfates of TMs in presence of NaOH followed by calcination at high temperature. The nominal composition was found to be 80.2 : 9.8 : 10.0 (Ni : Mn : Co), with a Li/Metal ratio of 1.013 determined by ICP analysis.

The so prepared sample was then stored in the industrial partner's dry room before being shipped in a sealed aluminum bag under a humidity poor atmosphere; it was henceforth stored in an argon glovebox from reception. The relative humidity in an industrial dry room is usually controlled to be between about 0.7 and 1.5%. Although minimal, the particular sensitivity of NMC811 compared to other NMCs could lead to some modification of the material surface.^{4,24} These alterations are expected to occur principally at the secondary particles external surface, since this little amount of humidity is not likely to affect the primary particles inside the aggregates, due to the irrelevant porosities existing within the secondary particles.

The powder was further observed after storage in different conditions of relative humidity (RH) and exposure time and compared to the surface of pristine NMC811, as obtained from the industrial shelf. The powder constituted of secondary particles was manually grinded by using an agate mortar and pestle in the argon-filled glovebox in order to obtain primary particles with a clean pristine surface before putting them in a climatic chamber with a controlled Relative Humidity (RH) of 30% and ambient oxygen and CO₂ partial pressures. Two different samples were obtained: sample A1 was stored under the described conditions for 15 minutes and sample A2 for 2 days.

1.2.2. Electron Energy Loss Spectroscopy (EELS)

Samples prepared as previously described were deposited on a holey carbon copper grid inside the glovebox without the use of any solvent. The grid was then sealed in argon atmosphere in a vacuum transfer holder (Gatan 648). The sample surface was

cleaned by means of a Fischione Instruments plasma cleaner (model 1070) with pure Ar gas for 30 seconds at a power level of 30% and a gas flow of 30 sccm. The grid was then sealed under secondary vacuum and transferred into the microscope, without any contact of the sample with the ambient atmosphere.

STEM-EELS analyses were performed on a monochromated probe-corrected TEM/STEM Themis Z G3 (Thermo Fisher Scientific) equipped with a double camera spectrometer (Gatan Imaging Filter Quantum ERS 969). STEM-EELS data were collected at 300 kV with a current of 60 pA by using the direct detection camera (Gatan K2 Summit), which allows, together with the excited monochromator, achieving an energy resolution of ≈ 0.1 eV as given by the zero loss peak (ZLP) full width at half-maximum. Monochromated conditions were only used for detailed analysis of fine structures at Ni and O edges. The energy dispersion was chosen to be 0.25 eV/pixel in order to obtain a 927.5 eV range allowing a O-K edge to Ni L_{2,3} edge simultaneous analysis. Convergence and collection semi-angles were respectively 29.1 and 34.1 mrad and the camera length was set at 29.5 mm. Thanks to the high performance of the used spectrometer configuration, it was possible to perform very fast acquisitions, exposing each pixel for only 20 ms. The current and the exposition time were chosen in such a way as to prevent the sample from electron beam degradation.

In order to obtain representative data of all the sample, a large number of particles was analyzed as well as different facets of a same primary particle (see Figure S5 as an example).

The collected data were processed by both Multiple Linear Least Square (MLLS) fitting and Principle Components Analysis (PCA) integrated in Digital Micrograph software in order to identify any differences between the surface and the bulk of the observed primary particles. Both procedures gave the same results.²⁵

EEL spectra were used to quantify the different elements at a nanometric scale. For this purpose, the second derivative of the whole dataset was calculated in order to overcome the problem of overlapping edges, background subtraction difficulties, and to obtain more pronounced signals for Co and Mn (Figure 1), that are in very small quantity compared to Ni and O (1; 1; 8; 20, respectively). Through MLLS fitting on the whole dataset, the relative composition profile of the particle can be plotted. A detailed description of the method can be found in Supporting Information (Figures S1-S4).

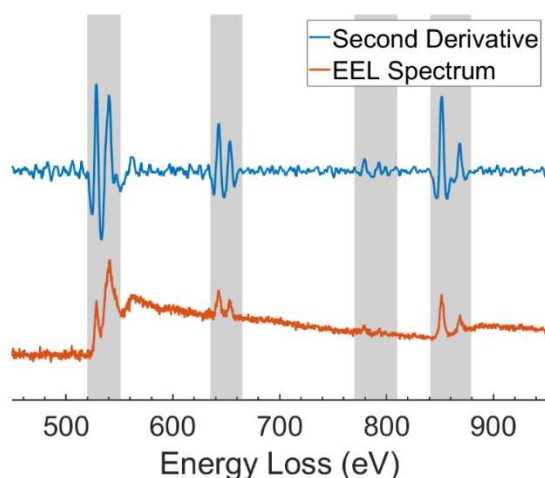


Figure 1. Typical second derivative (blue) of an EEL spectrum extracted from the very surface of a primary particle. Gray areas indicate O K-edge (around 530 eV), Mn L_{2,3}-edges (around 630 eV), Co L_{2,3}-edges (around 780 eV) and Ni L_{2,3}-edges (around 850 eV).

1.2.3. NMR spectroscopy

⁷Li MAS-NMR spectra were acquired on a Bruker Avance 500 spectrometer ($B_0 = 11.8$ T, Larmor frequencies ν_0 (⁷Li = 194 MHz) at RT. A Bruker MAS probe with a cylindrical 2.5 mm (o.d) zirconia rotor spun at a frequency of 25 kHz was used. Spectra were obtained by applying a single pulse sequence coupled with a pre-scan delay of 10 μ sec before the acquisition of the signal. In this way it was possible to select the surface diamagnetic Li signal only. The paramagnetic Li contained in the active material is indeed characterized by a much faster relaxation time T_2 .²⁶

Since NMR spectroscopy is not an absolute quantitative technique, the realization of a calibration curve was essential in order to successfully quantify surface diamagnetic

species. For this purpose, eight samples were prepared by mixing NMC811 with different quantities of LiF in a planetary ball miller for 2×30 minutes to guarantee the best possible intimacy between the paramagnetic material and the LiF. By using a recycle delay (D1) of 50 s the acquisition of quantitative spectra was assured.

^7Li integrated intensities were determined by using spectral simulation (DMFit Software²⁷) after performing a numerical fit of each set of peaks corresponding to a chemical compound. The so obtained integrated intensities were normalized considering the mass of the sample contained in the NMR rotor, the number of scans and the received gain.²⁸ For the compounds identification based on the isotropic chemical shift (δ), Li_2CO_3 was used as reference at 0.0 ppm.

1.2.4. XPS Analysis

XPS measurements were conducted on a Kratos Axis Nova Instrument, using a monochromated Al $K\alpha$ source (1486.6 eV) operating at 300 W. The instrument base pressure was 5×10^{-10} Torr and a Pass Energy (PE) of 80 eV was used during the acquisition of the wide-range survey spectra, leading to an instrumental resolution of 0.9 eV. PE of 20 eV at $\theta = 0^\circ$, X-ray spot size of $700 \mu\text{m} \times 300 \mu\text{m}$ and 100 meV steps were used instead to acquire high-resolution spectra and exploited to quantify the compounds at the surface of the materials. In this way, it was possible to achieve an instrumental resolution of 0.55 eV measured at Fermi edge. The 3p peaks of the transition metals were acquired together with the Li 1s between 35 and 85 eV to have a better quantification of the elements of NMC material. Spectra of the C 1s (277–300 eV), O 1s (523–537 eV) and S 2p (160–177 eV) were also measured and exploited in the following analysis.

All the samples were transferred from the Ar-filled glovebox into the instrument using a dedicated transfer chamber system that was then connected directly to the XPS apparatus, allowing thence the analysis without letting the materials to be in contact with air.

All data were collected using charge compensation with a low-energy electron gun and calibrated with the adventitious carbon 1s peak at 284.8 eV binding energy. After calibration, all spectra were analyzed using the CasaXPS software (version 2.3.24). The fit was performed using a Shirley type baseline for the background and a pseudo-Voigt function with Gaussian (70 %) – Lorentzian (30 %) for each component. A full-width-at-half-maximum (FWHM) of 1.4 eV and peak positions were initially fixed according to internal references of Li_2CO_3 , LiOH and pristine NMC for each component of the Li 1s peak.

XPS was used in our study to obtain compounds quantification and not as a simple atomic percentage quantification as it is commonly done. Following Grissa et al., fits were performed by imposing the integrated areas of peaks assigned to identified compounds (by means of the peak position) to be proportional to the amount of the other elements involved into the considered compounds based on their formula.²⁹ For instance, once sulfates (here considered as Li_2SO_4) were identified on the S 2p peak, a component corresponding to this compound was added to the O 1s fit around 532.2 eV) with an integrated area accounting for 4 times that of sulfur (after normalization by the relative sensibility factors). Once acceptable fits were obtained, constraints on FWHMs and positions were removed and fits were proven to be stable and consistent. The phase quantification was deduced from the addition of all element percentages involved in the same compound.

1.3. Results and discussion

Cathode materials such as NMCs are typically organized in polycrystalline micrometer-sized particles, namely secondary particles, formed by nanometric aggregated single crystals called primary particles. As it can be seen in Figure 2, the orientation of primary particles is not necessarily controlled during the synthesis. The importance of these primary particles in the diffusion of Li during cycling was largely demonstrated and their characterization at a nanometric scale has become crucial for the comprehension of the NMC Ni-rich behavior. In order to obtain and analyze NMC

single crystals it was thus important to grind the powder before each characterization. In this way, it was possible to break aggregates and look at each primary particle separately. In doing so, the surface of these primary particles could be observed, without further modification from their pristine state. Due to the grinding process, primary particles in the core of the secondary particles cannot be differentiated from those closer to the surface of the secondary particles. The question of the representativeness of analysis performed using local probes such as TEM is always raised and this is why, in this study, a large number of primary particles were observed (see Figure S5 as a small example). For best clarity, we present in the following sections STEM-EELS results obtained on representative particles.

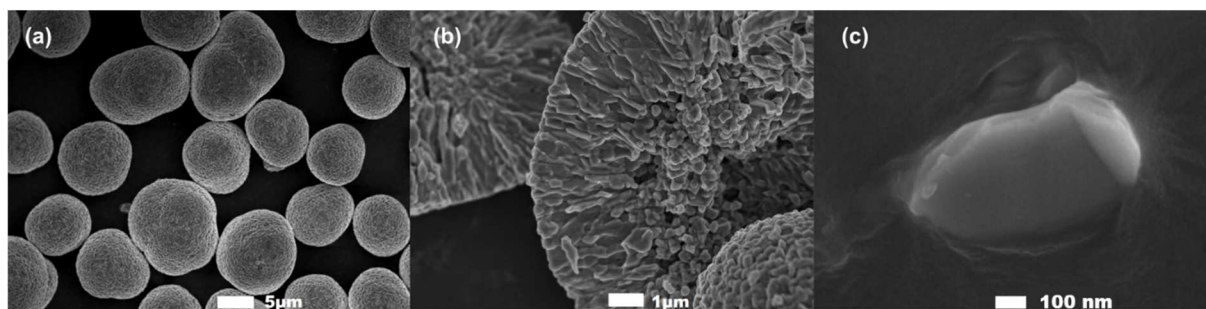


Figure 2. SEM image of the hierarchical microstructure of NMC, from micrometer agglomerates (a) composed of crystallites of few tens of nanometers (b) to primary particles (c).

1.3.1. Nanometric characterization of the pristine material

In Figure 3a is presented a typical spectrum-image dataset (1 spectrum per pixel) for the pristine powder (Sample A0). In Figure 3b are given the two Ni L-edges EELS spectra used as components to fit the Spectrum-Image. The orange spectrum appears to be predominant at the surface of the pristine primary particle. It is characterized, compared to the bulk spectrum (here in blue), by a decrease in the intensity of the high energy peak of the L₃-edge split (around 848 eV), resulting in an overall shift of the Ni L-edge maximum towards a lower energy. This indicates a reduced state of the Ni at the surface of the pristine powder, closer to a Ni²⁺ ion signal.³⁰

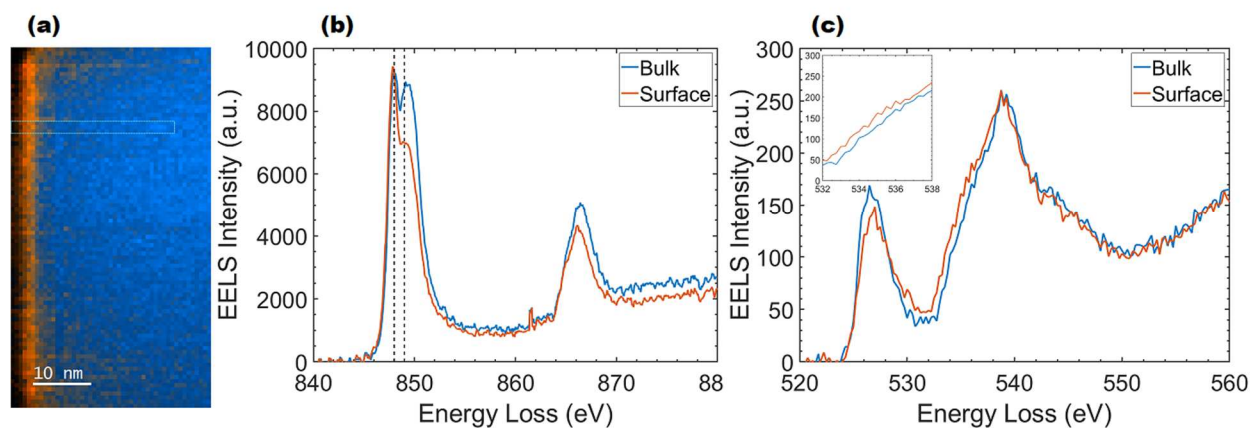


Figure 3. monochromated EELS Spectrum image of A0 sample fitted by MLLS fit (a) using Ni spectra (b) and O spectra (c) from the surface (orange) and the bulk (blue) of an internal zone of a broken secondary particle corresponding to pristine primary particles.

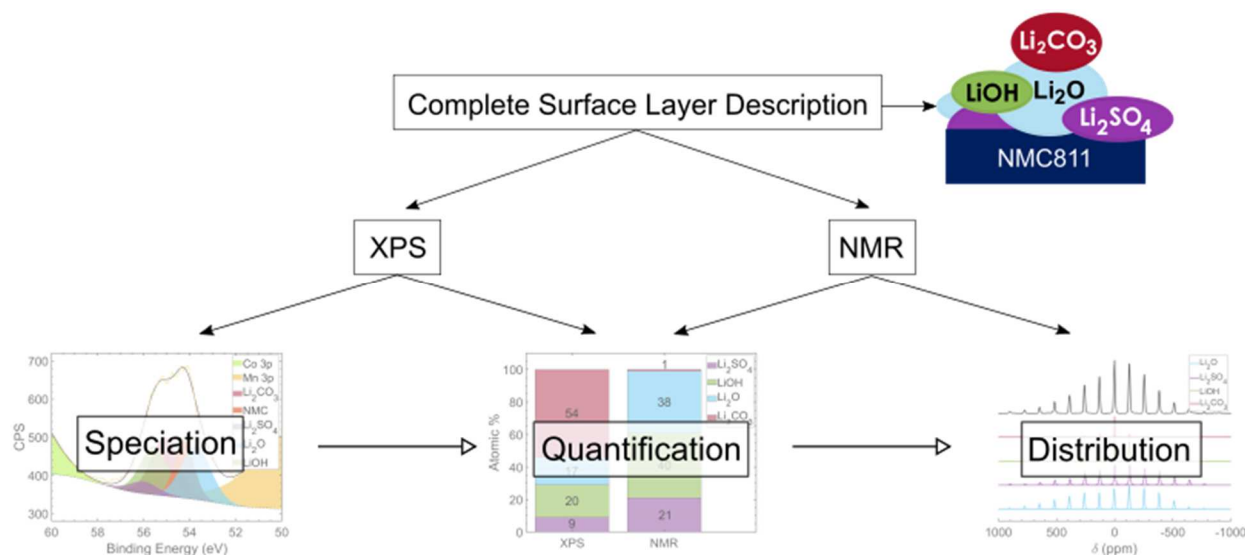
Surface and bulk spectra for the O K-edge are also slightly different (Figure 3c). The shift towards a lower energy of the edge situated at around 535 eV (at higher magnification in the inset of Figure 3(c)) indicates an increased electron density (equivalent to a reduction) for oxygen close to the surface compared to the one in the bulk. Ni^{2+} (surface) levels are destabilized compared to Ni^{3+} (bulk) levels and tend to produce more ionic interactions with oxygen surrounding atoms.⁷ The resulting increased electron density on the oxygen levels explains the edge shift to lower energy. Such interpretation is consistent with the decrease of the intensity of the pre-edge peak (at around 528 eV) for the surface spectrum compared to the bulk one. Oxygen levels are slightly more filled by electrons at the surface, hence allowing fewer transitions to empty states probed by the EELS technique. Considering the limited extend of the surface region and an incomplete transformation, it is clear in our mind that these considerations should be viewed as a qualitative trend and not as a statement of a well-defined “NiO” phase at the surface. Very similar surface differentiations on fine structures at the O K-edge as well as at the $L_{2,3}$ edge of Ni have previously been observed, although usually more pronounced, after prolonged cycling (successive lithiation/delithiation) or even after water-washing of Ni-rich layered materials.^{22,30}

The pristine material, as it arrives from the production plant, is thus already affected by a surface modification. Since this surface specificity can be associated with, or lead to, the formation of impurities, other spectroscopy techniques, namely XPS and MAS-NMR were considered to assess on an even larger scale (up to secondary particles) possible consequences. The presence of a peculiar pristine surface layer could indeed be coupled with the formation of Li-containing phases well-characterized by these techniques.

1.3.2. Analysis of the native contamination layer

Essential to the quantification of diamagnetic Li-containing species at the surface of materials, we first exploit high field ^7Li MAS-NMR. The method introduced previously and developed in our group by Dupré et al. allows separating the signal of the Li in paramagnetic local environments contained in the active material from the Li in diamagnetic local environments contained in the impurities and/or contamination layer at its surface.^{26,31}

The lithium contained in diamagnetic species at the surface of the pristine material (Sample A0) was found to account for $125 \mu\text{mol}_{\text{Li}}/\text{g}_{\text{AM}}$ (i.e. 1.2%_{mol}). However, the identification of the various species contained in the native contamination layer cannot be performed by NMR only. The NMR chemical shifts for the expected surface species, such as Li_2CO_3 and LiOH , are in fact very similar and most lithiated diamagnetic impurities are measured within -1.1 to 4.0 ppm. Consequently, XPS has been used to provide for a more exhaustive description of the speciation of surface species in order to ensure a deconvolution of the ^7Li MAS-NMR isotropic band around 0.0 ppm. The description of this powerful method coupling MAS-NMR and XPS is summarized in Scheme 1.



Scheme 1. Method used for the complete description on the surface contamination layer.

XPS spectra of the pristine Sample A0 are shown in Figure 4 and all XPS quantitative data are gathered in Table 1. The C 1s spectrum (Figure 4 (a)) shows the hydrocarbon surface contamination component (C–C, C–H) at 284.8 eV, commonly detected on sample surfaces. Other signals corresponding to species with doubly bound oxygen functionalities (at 287.2 eV) and ester functions (at 288.2 eV) in smaller quantities were also used to deconvolve the adventitious carbon signal.

An important signal at 289.7 eV was assigned to the carbonate function, here considered as Li_2CO_3 , a typical contaminant at the surface of NMC materials. A carbonate signal was detected as well on the O 1s peak (Figure 4 (b)) at 531.3 eV and on the Li 1s peak at 55.2 eV (Figure 4 (d)), confirming the presence of Li_2CO_3 .

The S 2p peak (Figure 4 (c)) is split in two components ($\text{S } 2p_{1/2}$ and $\text{S } 2p_{3/2}$ with an area ratio of 1:2) because of the spin orbit coupling effect. The peak position (168.9 eV for the $\text{S } 2p_{3/2}$) is typical of the sulfate (SO_4)²⁻ group. These sulfates are attributed to some residue from the synthesis and could correspond to lithiated species or not.

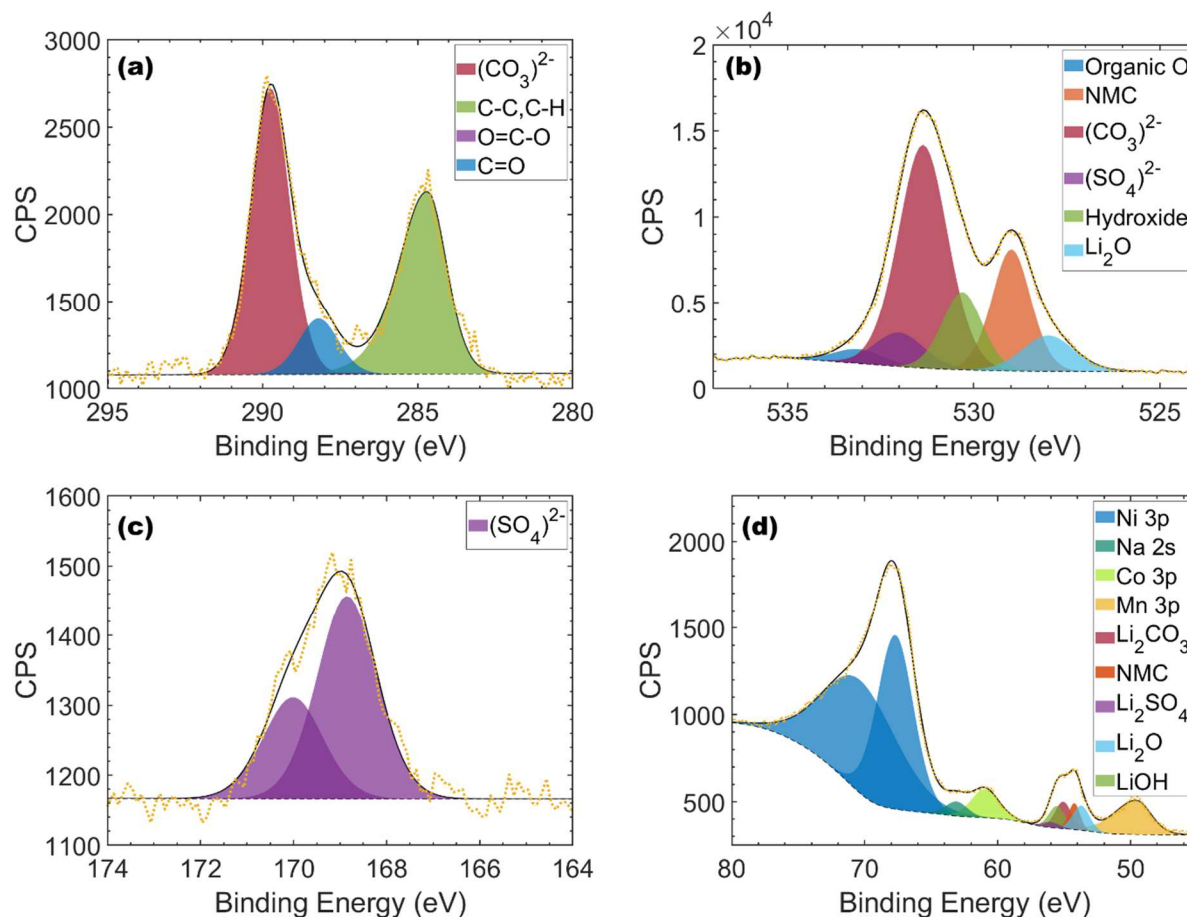


Figure 4. XPS C 1s (a), O 1s (b), S 2p (c) and Li 1s (together with Ni 3p, Mn 3p and Co 3p in (d)) spectra of A0 pristine sample. Experimental data are represented in yellow dashed line and the fit result in straight black line. 3p peaks for Ni, Co and Mn are modeled for deconvolution purposes but their intensity is not exploited.

Unlike the C 1s peak, the deconvolution of the O 1s peak (Figure 4 (b)) is more complicated since distinct components are not clearly visible, except for NMC (529.0 eV) and Li₂O at 528.0 eV. Additional contributions to the O 1s spectrum were deduced from identified oxygen containing species in the previously analyzed C 1s and S 2p high-resolution spectra and incorporated in the fit. It was thence possible to identify a component corresponding to (SO₄)²⁻ at 532.0 eV thanks to the previous fit of the S 2p peak and a component gathering all the organic compounds at 533.1 eV, together with the component corresponding to the carbonate function as explained earlier. Constraints on the integrated areas were imposed as described in the Experimental Section.

Table 1. Binding Energy (eV), FWHM, atomic percentages (%) and assignments of C, O, S and Li peaks from XPS spectra of pristine NMC811 powder.

Orbital ⁵	B.E. (eV)	FWHM (eV)	Atomic %	Peak assignment ³²
C 1s	284.7	1.5	6.7	C–C, C–H
	286.0	1.5	0.0	C–OH, C–O–C
	287.2	1.5	0.1	C=O
	288.2	1.5	1.6	O–C=O
	289.7	1.5	8.2	Li ₂ CO ₃
Total C			16.6	
O 1s	528.0	1.7	4.3	Li ₂ O
	529.0	1.2	10.9	NMC
	530.3	1.3	7.2	LiOH
	531.3	1.6	25.5	Li ₂ CO ₃
	532.0	1.6	3.9	Li ₂ SO ₄
	533.1	1.6	1.4	Organic compounds
Total O			53.2	
S 2p _{3/2}	168.9	2.4	0.6	Li ₂ SO ₄ ³³
S 2p _{1/2}	170.0	2.4	0.3	Li ₂ SO ₄
Total S			0.9	
Li 1s	53.8	1.4	8.2	Li ₂ O
	54.3	1.4	5.6	NMC
	55.2	1.5	7.1	Li ₂ CO ₃
	55.2	1.5	6.4	LiOH
	55.9	1.4	2.0	Li ₂ SO ₄
Total Li			29.3	
Total			100.0	

⁵ Ni 3p, Co 3p and Mn 3p peaks were used here only for a better deconvolution of the Li 1s signal. B.E. and FWHM for these elements are thence not physically significant and so not reported in the Table and not further discussed. Atomic percentages were recalculated and normalized after subtracting transition metal signals.

These components once fixed and incorporated in the fit could not fully explain the experimental O 1s spectrum and an additional component had to be considered at 530.3 eV. The integrated area of this contribution, corresponding to the hydroxide function, was let free to obtain the best fit.

This same method was used to decompose the Li 1s core peak (Figure 4 (d)) into 5 contributions. This approach permitted to distinguish five different components. Li₂O (deduced from the O 1s peak) can be found at 53.8 eV, slightly superimposed with the component at 54.2 eV corresponding to Li ions intercalated in the NMC. For simplification purpose, all the sulfates were hypothesized to be Li₂SO₄ and a peak was thence fixed at 55.9 eV to represent this compound. On the other hand, it was trickier to make the difference between lithium carbonate and hydroxide. Some references were analyzed by XPS evidencing a very similar peak position for the two compounds (Figure S6). For this reason, two different components at 55.2 eV were used to represent Li₂CO₃ and LiOH. The fit was here performed by constraining the LiOH Li 1s peak integrated area in relation to the corresponding LiOH signal in the O 1s spectrum, while Li₂CO₃ integrated area was let free from any constraints, since the carbonate amount was the only one not consistent with the ⁷Li MAS-NMR as it will be detailed later.

Once Li₂CO₃, LiOH, Li₂O and Li₂SO₄ were identified by XPS as the principal surface lithiated species, this information was incorporated into the fit of the ⁷Li MAS-NMR spectrum displaying the contributions of Li nuclei in various diamagnetic environments. The deconvolution of the isotropic resonance corresponding to the pristine powder is shown in Figure 5 and the experimental isotropic chemical shifts (δ) and FWHM corresponding to each diamagnetic compound are summarized in Table 2. δ values of the four identified compounds are given as a difference with respect to Li₂CO₃ used here as a reference. These values were set by taking into account the ones calculated by Kösher et al.³⁴ A good fit was obtained by using a component at 4.0 ppm (Li₂O), one at 1.8 ppm (LiOH), one at 0.0 ppm (Li₂CO₃) and a last one at -1.1 ppm for

Li_2SO_4 . Once these chemical shifts were identified and used for the deconvolution and the fit of the pristine spectrum, they were fixed for all the other analyzed spectra (e.g. in spectra corresponding to aged samples) and letting FWHM and the intensity free to change.

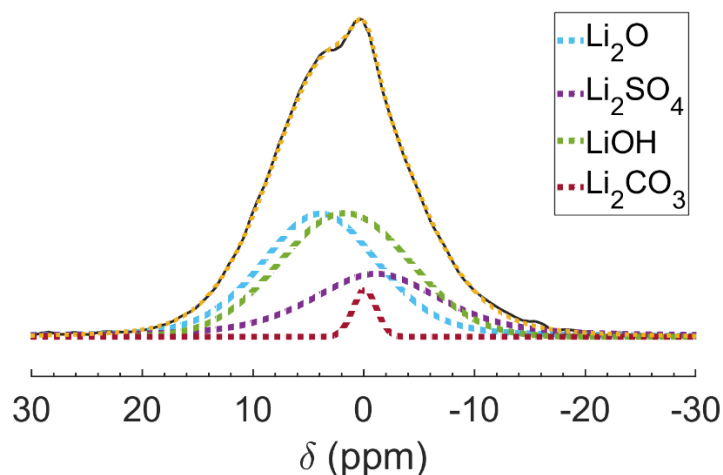


Figure 5. ^7Li MAS-NMR spectrum of pristine A0 powder (black) fitted using four contributions: Li_2O (light blue), Li_2SO_4 (purple), LiOH (green) and Li_2CO_3 (red). The sum of the different contributions is represented by the yellow line.

As it can be seen in Figure 5, while the peak corresponding to Li_2CO_3 , at 0.0 ppm, is very sharp (FWHM = 2.4 ppm), all the other contributions are much broader (Table 2). This sharp signal suggests the formation of a well-defined Li environment in Li_2CO_3 (narrow distribution of environments) as well as further distance from the surface of the paramagnetic material (weaker Li nucleus-electron dipolar interaction) with respect to the other detected lithiated species. A more disordered environment as well as a close intimacy with the active material would be expected in the case of the formation of Li_2CO_3 from the direct reaction of the surface of the active material with the surrounding atmosphere (although controlled). The formation of well-defined and separated Li_2CO_3 as a secondary product hence further away from the surface, is in better agreement with the observed sharper NMR signal.

Table 2. Isotropic Chemical Shift δ (ppm) and FWHM of the contributions used for the deconvolution of ^7Li spectrum of pristine NMC811 powder.

Compound	δ (ppm)	FWHM (ppm)
Li_2SO_4	-1.1	13.9
Li_2CO_3	0.0	2.4
LiOH	1.8	13.9
Li_2O	4.0	12.3

The larger FWHM of Li_2O , Li_2SO_4 and LiOH signals compared that of Li_2CO_3 reported in Table 2, could be due both to a higher disorder in the Li environment and to a higher proximity to the paramagnetic surface of the NMC material. This proximity indeed leads to a faster T_2^* relaxation time and thus a broader line width. Analyzing the intensity distribution of these four contributions over the spinning side bands helped us confirming the second explanation. Larger sideband manifolds, like those shown in Figure 6 (c, d and e) for Li_2O , Li_2SO_4 and LiOH are in fact typical of a stronger electron-nucleus dipolar interaction between the observed Li nuclei and the paramagnetic centers of the NMC. Li_2CO_3 with a small 155 ppm FWHM for the sideband manifold (Figure 6 (b)), is therefore submitted to a much weaker dipolar interaction. Such an interaction typically decreases quickly with distance (typically as $1/r^3$ where r is the distance between the observed nucleus and the paramagnetic center), and suggests that Li_2CO_3 is the further away from the bulk material, then LiOH seems to be present at an intermediate distance while Li_2SO_4 and Li_2O are the closest to the bulk material.²⁸

Li_2SO_4 and Li_2O are expected to be “native” impurities, straight from the synthesis. Li_2SO_4 is the expected form of sulfur, which is often detected by ICP on the pristine powder because of the sulfate based precursors. Li_2O has often been considered as the form of residual lithium after calcination.^{9,35}

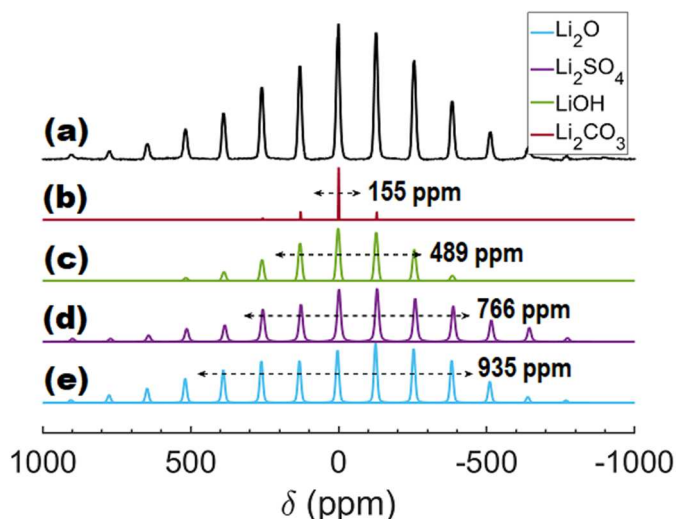


Figure 6. ${}^7\text{Li}$ MAS-NMR spectrum of pristine powder (black) and distribution of the intensity of each contribution (Li_2CO_3 in red, LiOH in green, Li_2SO_4 in purple and Li_2O in light blue) over the spinning side bands (b-e). Spectra b-e are normalized with respect to the intensity of the isotropic resonances and indications of the FWHM of the sidebands manifold are given for each contribution.

The results for the quantification of the native contamination layer performed by both XPS and NMR are shown in Figure 7. For the XPS data here presented, the components of NMC and residual hydrocarbon and adventitious carbon contaminations were disregarded in order to solely compare the distribution of species that are measurable by both techniques. MAS-NMR based on ${}^7\text{Li}$ nucleus obviously detects only surface diamagnetic lithiated species (a complete XPS quantification can be found in Table 1). Clear differences can be seen between the two quantification measurements. Li_2O , LiOH and Li_2SO_4 quantities seem to be underestimated when calculated by XPS, while the amount of Li_2CO_3 is largely overestimated. These two techniques are in fact sensitive to different parts of the sample. While the NMR analyses the whole sample, XPS is limited by the spot size ($700 \times 300 \mu\text{m}$) and especially by the sampling depth, typically around 5 nm. XPS is thence not representative of the complete sample, but only of the extreme surface of the analyzed area. Moreover, one has to keep in mind that the composition and thickness of the native contamination layer are expected to vary significantly from one place to another over the spot size. The coupling with NMR

is therefore a major asset in this study considering XPS is one of the most common tools used to analyze NMCs surface chemistry in the literature.

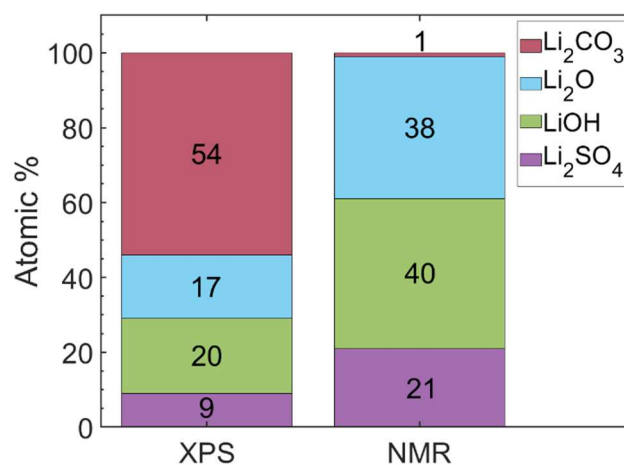


Figure 7. Quantification of the native contamination layer on pristine grinded powder determined by both XPS and NMR. Phase percentages for Li₂CO₃ (red), Li₂O (light blue), LiOH (green) and Li₂SO₄ (purple) are indicated.

The difference in the Li₂CO₃ quantification, representing only 1% in the NMR quantification (that is 0.4 μmol/g_{AM}) *versus* 54% from XPS, can be explained considering that this compound is mostly formed at the very surface of the sample (as demonstrated by the dipolar interaction study in the MAS-NMR signal, Figure 6) and is situated on the external part of the pristine interphase. XPS quantification thus largely overestimates the Li₂CO₃ percentage.

It is however quite interesting that the respective proportions of Li₂O, LiOH and Li₂SO₄ are found as very similar in both techniques. Ratios LiOH/Li₂O and Li₂SO₄/Li₂O are indeed close to 2 and 0.5, respectively. From the good agreement between both analysis techniques it can be deduced that even if Li₂O, Li₂SO₄ and LiOH are staged (in that order) from the NMC surface, this average evolution seen by NMR should not be seen as well-defined successive layers. For example, some areas are surely having a direct succession Li₂O followed by LiOH, others might be missing Li₂O as proximity layer. XPS results thus help us tempering an oversimplified vision of an ideal layered surface suggested by NMR.

The reasoning above is based on the fact that all surface species detected by XPS are also detected by NMR. Considering solely ${}^7\text{Li}$ MAS-NMR was used, surface species not containing lithium will be missed by MAS-NMR. A deeper examination of XPS results concerning the carbonate (reported in Table 1) yield a ratio $\text{Li}_{(\text{Li}_2\text{CO}_3)} / \text{C}_{(\text{Li}_2\text{CO}_3)}$ of 0.9/1 instead of the expected 2/1, if all carbonates were fully lithiated. Other carbonate sources may thus be present at the material surface such as LiHCO_3 and $(\text{TM})\text{CO}_3$. Fits, detection limits and specificity of XPS and NMR techniques did not allow us to go deeper in this determination.

The possible existence of transition metal carbonate is a very valuable piece of information considering that this hypothesis was already proposed by Jung et al., who suggested the extraction of Ni from the NMC811 surface to form part of the contamination layer upon storage in ambient conditions.²¹ However, in our pristine powder (not an electrode as opposed to their work), the quantity of such transition metal carbonates appears to be quite small when XPS and NMR results are combined. As a matter of fact, if we make the hypothesis that the composition found by XPS is representative of the average composition of the surface lithiated layer, approximately the 50% of the carbonates would be under the form of $\text{TM}(\text{CO}_3)$. This would mean that Li_2CO_3 and $\text{TM}(\text{CO}_3)$ would be in the same amount of around $0.6 \mu\text{mol/g}_{\text{AM}}$, i.e. 0.007%_{wt.} This represents roughly 10 times less than that deduced from gas chromatography of their fresh electrode.

1.3.3. Nanometric quantification at the primary particle surface

Despite our measurement of a limited upper value for the transition metal carbonates, these transition metal impurities could significantly modify the NMC811 extreme surface composition (over a few atomic layers). In order to determine whether TM compositional variation could be evidenced at the surface, the pristine powder was analyzed by both STEM-EDX and STEM-EELS, the sole techniques with sufficient spatial resolution. This is a quite challenging task since any sample preparation that would be too harsh on the material chemistry would prevent any sensible conclusion.

This is the reason why we chose to simply crush in a mortar the pristine secondary particles. The following results thus reflect both surfaces of primary particles in the core of the secondary particles and surfaces of primary particles at the periphery thus more exposed to the environment. The latter case is however in large minority with respect to the former one.

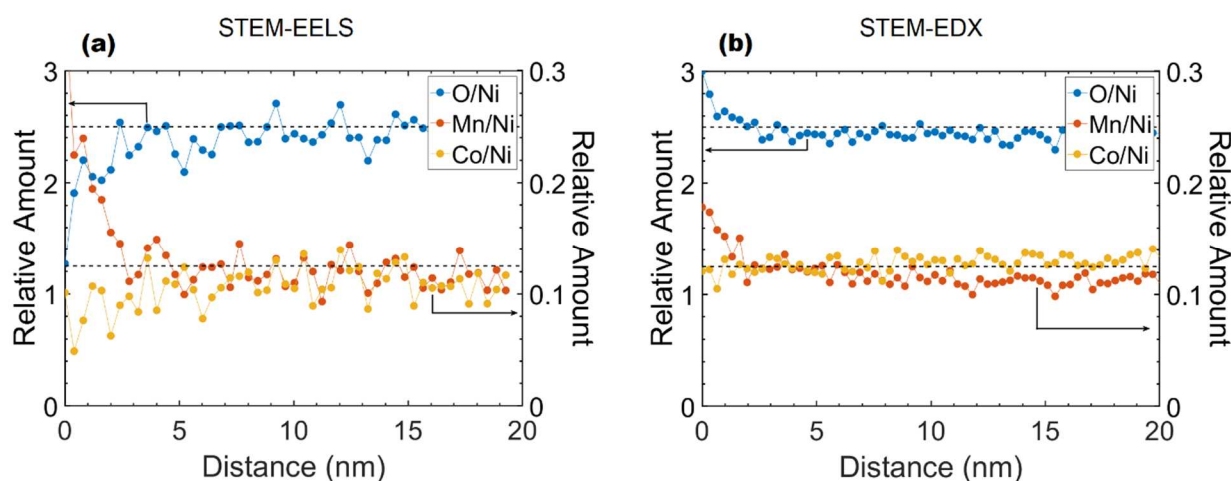


Figure 8. Calculated ratios for A0 pristine sample: O/Ni (blue), Mn/Ni (orange) and Co/Ni (yellow) from (a) STEM-EELS and (b) STEM-EDX data. Theoretical bulk values are indicated by the dashed black line and are 2.5 and 0.125 for O/Ni and TM/Ni, respectively.

The ratios Mn/Ni, Co/Ni and O/Ni calculated from the STEM-EELS spectra of the pristine powder are represented in Figure 8a as a function of the distance from the beginning of the surface of the observed primary particle (0 nm). A detailed description of the method can be found in the Supporting Information file. This same analysis was performed on many particles of different shapes and with different crystalline orientations, always obtaining similar results. Our method does not rely on a lengthy and possibly biased crystal orientation procedure and thus allows measurements on dozens of surfaces (Figure S5). Figure 8a is thus quite representative of the pristine sample surface state. Since these analyses were obtained after binning all the pixels at the observed surface, they each represent an average over hundreds of nanometers. The EELS method necessitates the use of a reference element and Ni was chosen as the less prone to low signal to noise. Surface composition in Figure 8 (a) is thus given with respect to Ni. The composition is measured to be quite stable within

the bulk of the primary particles (~5 nm onwards). Closer to the surface, variations are identified. Considering that Mn/Ni, Co/Ni and O/Ni ratios behave quite differently when approaching the surface, the variations cannot be interpreted as due to solely a Ni depletion (or increase). Thanks to the high spatial resolution, compositional changes in the first 3 nm near the surface of the active material are identified. Firstly, the surface appears to be oxygen deficient with respect to nickel. Even if only a trend could be here asserted, the ratio tends towards 1 and is coherent with an extreme surface (<1 nm) approaching a NiO phase. This analysis is consistent with our previous result on the surface reduction of the oxidation number of Ni to Ni²⁺ thanks to the Ni-L_{2,3} fine structure measurement. It is also in line with affirmation found in literature.^{36,37} The decrease of oxygen content is however not in line with a NiCO₃ contamination layer.²¹ Secondly, a Mn enrichment is clearly visible at the extreme surface. Such a result was unexpected and has never been reported before to our knowledge. One could argue that a nickel depletion with respect to Mn would be consistent with a Ni departure to form new compounds outside the primary particle, but this would be inconsistent with the rather stable Co/Ni ratio. The slight argument here mentioned due to the use of EELS ratios is overcome by STEM-EDX measurements on the transition metal analysis at the surface. In this case, percentages of the 4 elements (oxygen + TMs) can be obtained without necessitating a reference element. For the sake of comparison with EELS, ratios are also presented in Figure 8b. The same increasing trend in the Mn quantity is measured (Co quantity being roughly constant until the extreme surface). In spite of the different detection methods (inelastically transmitted electrons or emitted X-rays), results are, on numerous occasions, consistent. It should however be mentioned that the oxygen content is not seen most of the time decreasing at the surface with STEM-EDX. Since the oxygen K_α emission energy (0.5 keV) is much lower than that for transition metals (from 5.9 keV to 7.5 keV), absorption corrections impact the oxygen percentage determination. Despite the use of the four EDX detectors, the variable orientations of the crystal surfaces with respect to them cannot be totally compensated. Furthermore, the presence of high oxygen content compound

such as LiOH and/or carbonates cannot be excluded from time to time. Nevertheless, such limitation has little effect on high energy transition metal peaks and we can thus be affirmative on the Mn enrichment of the surface (50 to 100% increase vs. bulk composition, Figure 8). A last comment on these results should be that no variability could be evidenced as a function of the surface crystallographic planes, suggesting that the natural extreme surface of pristine primary particles present this divergence from the nominal bulk composition.

Following the work of Jung et al. showing the formation of nickel based carbonates after storage, a strong nickel deficient surface would be more logical.²¹ Other authors have instead found Co increase at the extreme surface.¹⁶ We may suggest that this Mn enrichment is unrelated to storage but rather consecutive of differential stability of phases at the surface during the synthesis. Thermodynamic data were gathered by Shurtz et al. for LiMnO₂, LiCoO₂ and LiNiO₂.³⁸ Even if a certain lack of thermodynamic data for these compounds exists, we can roughly assume that oxide stabilities are correlated with their formation enthalpy (enthalpies of mixing should here be neglected).³⁹ At 298 K, formation enthalpies for LiNiO₂, LiCoO₂ and LiMnO₂ have experimental values of -593.0, -679.6 and -839.5 kJ mol⁻¹, respectively. There is a large difference between Ni, Co based oxides and the Mn one. Since a high temperature step is necessary for the formation of the desired NMC811 phase, the observed Mn enrichment could be an expression of the higher stability of a Mn-rich surface in NMC layered materials. The Mn need not to be compensated by a departure of Ni and Co from the material but could be provided by a negligible (and unmeasurable) gradient of Mn composition from the core of the primary particles. We have not found a detailed theoretical study that would infirm nor validate this proposition.

The above extreme surface analyses revealed a reduced oxidation state for nickel and a Mn enrichment. They might in fact not be correlated and submitting the material to an accelerated aging could help us determine what are the conditions governing their advent.

1.3.4. Influence of storage conditions

The pristine NMC powder studied till now was then stored in specific conditions to obtain samples A1 and A2, after 15 minutes and 2 days in RH = 30%, respectively, as detailed in Experimental Section. The aim is here to exacerbate reactions occurring at the NMC surface in order to determine whether small amounts of water vapour could initiate the transformation seen previously. Specific RH storage conditions have already been shown to result in the formation of various species, such as Li_2CO_3 .^{21,40} Based on our previous detailed study, we used ^7Li MAS-NMR and XPS to characterize and quantify the lithiated species at the NMC surface after storage. Moreover, since the extraction of lithium from the material is expected to occur together with a change in the TM oxidation state, STEM-EELS experiments were carried out to confirm this hypothesis and determine its extend.

Equally to the A0 pristine powder, two components were used to fit the Ni $L_{2,3}$ -edges Spectrum-Image (Figure 9), in which each pixel can be described as a combination of both a surface spectrum (Ni in a more reduced state) and a bulk spectrum (mainly Ni^{3+}). Coefficients are normalized so that their evolution from the surface can be compared, but their absolute values are much smaller at the surface, due to much smaller thicknesses.

In the case of the pristine sample, the surface component (orange full line) becomes negligible around 7 nm from the surface, then, the bulk component is predominant. In the case of the sample kept for two days in RH 30% (orange dotted line), the thickness of this reduced Ni layer increases up to 15-20 nm. The phase change is thus clearly extended further inside the material compared to the pristine material. Such a change appears to be very similar in nature to that observed on the pristine material. No particular dissimilarities of the fine structures at the edges were identified between A0 and A2. This phase change is associated with a lithium extraction from the active material, as proven by the examination of the ^7Li MAS-NMR spectra. The total lithium contained in the diamagnetic species at the surface of the NMC indeed increases

markedly from $117 \mu\text{mol}_{\text{Li}}/\text{g}_{\text{AM}}$ to $148 \mu\text{mol}_{\text{Li}}/\text{g}_{\text{AM}}$ then to $176 \mu\text{mol}/\text{g}_{\text{AM}}$ when going from A0 to A1 and A2, respectively.

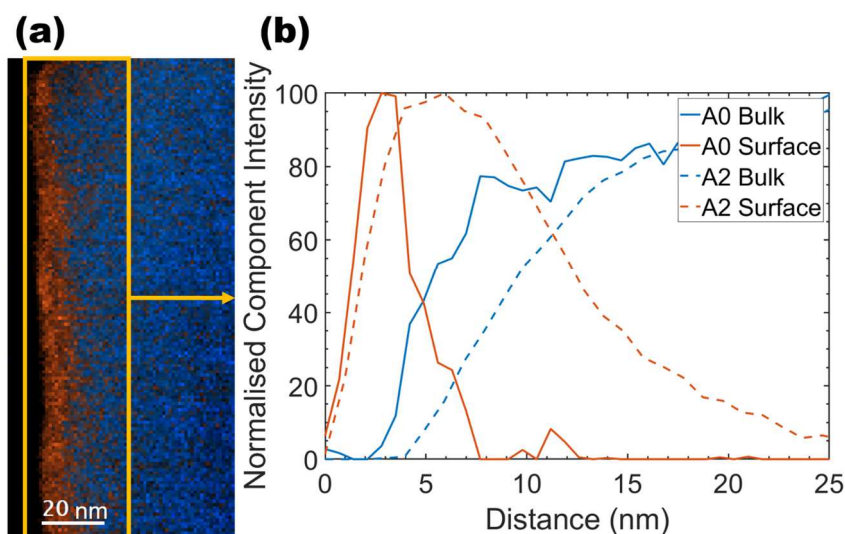
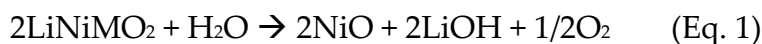


Figure 9. (a) EEL Spectrum-image of A2 sample after MLLS fit and (b) comparison for A0 (straight line) and A2 (dashed line) samples of surface (orange) and bulk (blue) contributions as a function of the distance from the beginning of the particle surface.

In order to be more precise, in Figure 10 are presented the evolutions upon storage of the measured quantities ($\mu\text{mol}/\text{g}_{\text{AM}}$) of each diamagnetic compound (Li_2SO_4 , LiOH , Li_2O , Li_2CO_3) at the surface. Our deconvolution method allows for showing that the quantities of Li_2SO_4 and Li_2O remain nearly constant, while a large increase is measured for Li_2CO_3 and LiOH . The first two compounds appear to be not affected by the storage conditions, and thus could well be interpreted as stemming from initial residues of the synthesis. Although not unexpected, this result further validates our analytical strategy and points at LiOH and Li_2CO_3 as the essential coupled products of surface reactivity. It should be stressed that after only 15 minutes of exposure (sample A1), NMR-MAS quantities are multiplied by ~ 2 and ~ 30 for LiOH and Li_2CO_3 , respectively. This result first suggests a very fast reaction time. Even if the relative humidity used here is much higher than that typically found in storage conditions in industrial dry room, it indicates a hypersensitivity of the NMC811 bare surface to the $\text{H}_2\text{O}/\text{CO}_2$ atmosphere. The much greater increase in carbonate than in hydroxide could also be indicative of the carbonate being the end product of the surface change. The

reaction $2\text{LiOH} + \text{CO}_2 \rightarrow \text{Li}_2\text{CO}_3 + \text{H}_2\text{O}$ is thus instrumental to the observed change. The LiOH could be –at least partially– formed according to the proposed reaction:



This reaction would also justify the measurement of a reduced Ni at the surface of the NMC811.

The hydroxide quantity roughly doubles again (from 68 to 112 $\mu\text{mol/g}_{\text{AM}}$) only after 2 days. Quite understandably, the carbonate after its huge initial increase also only doubles after 2 days, the formation paths being linked between the two. At the beginning of exposure, the surfaces are relatively fresh and the new phase identified on the pristine material is not thick enough to prevent a fast reaction with atmosphere to form new LiOH and Li_2CO_3 . A further progression of the reaction front is then more difficult and would necessitate similar kinetics even in the presence of the 10 nm layer measured in Figure 9b. A strong decrease in the production rate of Li_2CO_3 and LiOH is thus consistent with the new interphase observed.

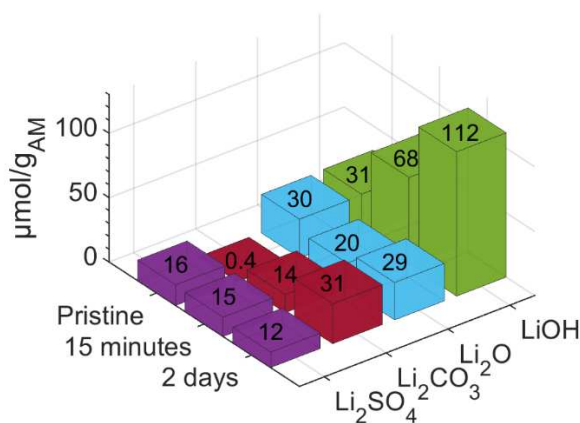


Figure 10. Quantity of lithiated species detected by ^7Li MAS-NMR at the AM surface for the pristine (A0), A1 (15 minutes) and A2 samples (2 days in RH = 30%). Li_2SO_4 (purple), Li_2CO_3 (red), Li_2O (blue) and LiOH (green).

The ^7Li MAS-NMR signal of Li_2CO_3 gives further information on its localization. The broadening of the signal (Table 3) implies that the formation of the new carbonate species is situated closer to the active material surface than that measured on A0. The

distribution of the intensity on the spinning side bands indeed increases upon aging. It could be interpreted as a consequence of the relatively fresh production of this Li_2CO_3 compared to the initial one, that could somehow have detached from the surface with time. Since the evolution from A1 to A2 of the ^7Li MAS-NMR linewidth and intensity distribution between isotropic resonance and sidebands is very limited for both Li_2CO_3 and LiOH species, we can assume that the reaction path stays the same along aging. In the case of Li_2O , linewidth and distribution of intensity between isotropic resonance and sidebands remain nearly constant, indicating that the Li_2O present in the pristine sample is unaffected by the large surface modifications described above.

Table 3. Parameters from ^7Li MAS-NMR signal features for A0, A1 and A2 samples.

	δ (ppm)	FWHM (ppm)	I isotropic resonance %
A0			
Li_2SO_4	-1.1	14	15
Li_2CO_3	0.0	2	74
LiOH	1.8	14	25
Li_2O	4.0	12	13
A1			
Li_2SO_4	-1.0	12	15
Li_2CO_3	0.0	5	25
LiOH	1.7	12	17
Li_2O	4.0	13	13
A2			
Li_2SO_4	-1.1	13	19
Li_2CO_3	0.0	7	18
LiOH	1.7	14	15
Li_2O	4.0	12	15

XPS experiments confirm these conclusions. The Li_2CO_3 signal represents 95% of the phases in sample A2 (Figure S7). Other species become extremely difficult to quantify. The newly created Li_2CO_3 is thus most probably present in the form of an extended layer ~ 10 nm thick masking the underlying LiOH. The sequence NMC/LiOH/ Li_2CO_3 is further confirmed with the measurement of a larger FWHM for the LiOH ^7Li MAS-NMR spectrum compared to that of Li_2CO_3 , again indicative of a LiOH higher proximity with the active material.

Moreover, as for the A0 pristine sample, XPS fits on samples A1 and A2 were performed in order to evaluate the possible quantity of carbonates that would be different from Li_2CO_3 . It appears that for these two samples the quantity of lithium is very close to that expected to get a phase Li_2CO_3 from the carbonate signal (C 1s and O 1s peaks, Figure S8). This would mean that species like LiHCO_3 or transition metal carbonates have become highly minority phases after aging in humid air. Such finding is consistent with the idea that the newly created and thicker lithium carbonate is formed on an increasingly thick LiOH layer and could not interact anymore (if any) with transition metals of the surface.

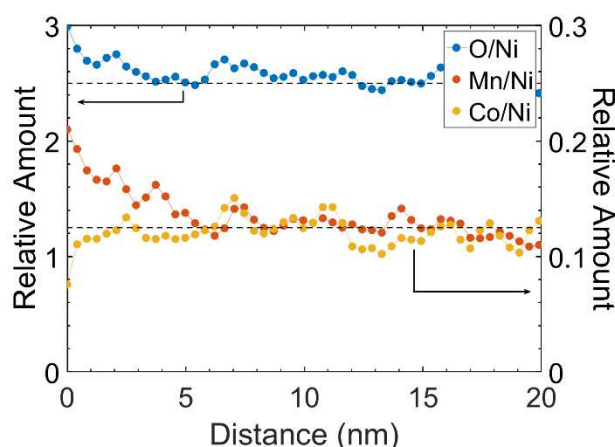


Figure 11. Calculated ratios for A2 sample: Co/Ni (blue), Mn/Ni (green) and O/Ni (red) as measured by STEM-EELS. Theoretical bulk values are indicated by the dashed black line and are 2.5 and 0.125 for O/Ni and TM/Ni, respectively.

Finally, the determination of the surface composition performed on A1 and A2 by STEM-EELS was carried out to check on the effect of storage on element quantification at the surface. Concerning the transition metals, very similar results as those seen in the case of the pristine materials were found (Figure 11). A small (~5 nm) surface Mn enrichment is consistently measured. It should be stressed that these samples have a markedly different history from the A0 one since they were subject to a higher RH atmosphere, have largely reacted producing LiOH and show an increased reduced Ni surface layer, as demonstrated above. These sizeable changes are however realized without major relative TM compositional modifications and are thus not strong enough to promote a selective diffusion of transition metals. From Figure 11 it can also be noticed that the oxygen composition at the surface is not measured as reduced as in the case of the pristine material. In fact, in many instances, the oxygen content can be found above the nominal value for bulk. This result is due to the contamination (mainly oxygen-carbon based) that considerably occurs on these exposed to humid air samples. Surface contamination is a well-known consequence of such treatment.

1.4. Conclusion

We presented in this study a complete characterization of a pristine industrial grade NMC811 powder, down to the sub-nanometer level, providing a possible explanation for its behavior during storage in defined short-term and low-humidity conditions. A multi-analytical approach based on on-site characterization techniques was used to give a complete picture of the material at different scales.

The lithium contained in diamagnetic species at the surface of the pristine material (Sample A0) was found to account for 1.2%_{mol} by MAS-NMR and to account up to 1.5%_{mol} and 1.7%_{mol} upon storage in the studied conditions (Samples A1 and A2 respectively). Such species were identified to be Li₂O, Li₂SO₄, LiOH and Li₂CO₃ (from the closest to the furthest from the surface of the active material). Li₂CO₃ is found in minor proportion but its amount increases faster after exposure to humid air. By combining both MAS-NMR and XPS, it was possible to quantify the evolution of the

lithiated species and their distribution from the surface. This allowed us to propose a succession of reactions taking place at this surface and to stress its hyper reactivity even towards minute amounts of H₂O.

The lithium extraction from the material to the surface layer was demonstrated to be accompanied by a progressive reduction of the surface nickel, tending to form NiO, as evidenced by the STEM-EELS data acquired in monochromated mode. STEM-EDX and STEM-EELS were then used to monitor the composition trend within the first atomic layers of the active material through the quantification of oxygen and transition metals at a nanometric scale, showing a Mn enrichment at the surface, not dependent on the storage conditions and therefore probably coming from the synthesis.

References

- (1) United Nations. Paris Declaration Electro-Mobility and Climate Change & Call to Action. 2015.
- (2) Myung, S.-T.; Maglia, F.; Park, K.-J.; Yoon, C. S.; Lamp, P.; Kim, S.-J.; Sun, Y.-K. Nickel-Rich Layered Cathode Materials for Automotive Lithium-Ion Batteries: Achievements and Perspectives. *ACS Energy Lett.* **2017**, *2* (1), 196–223. <https://doi.org/10.1021/acsenergylett.6b00594>.
- (3) Assat, G.; Tarascon, J.-M. Fundamental Understanding and Practical Challenges of Anionic Redox Activity in Li-Ion Batteries. *Nat. Energy* **2018**, *3* (5), 373. <https://doi.org/10.1038/s41560-018-0097-0>.
- (4) Noh, H.-J.; Youn, S.; Yoon, C. S.; Sun, Y.-K. Comparison of the Structural and Electrochemical Properties of Layered $\text{Li}[\text{Ni}_x\text{Co}_y\text{Mn}_z]\text{O}_2$ ($x = 1/3, 0.5, 0.6, 0.7, 0.8$ and 0.85) Cathode Material for Lithium-Ion Batteries. *J. Power Sources* **2013**, *233*, 121–130. <https://doi.org/10.1016/j.jpowsour.2013.01.063>.
- (5) Zhang, S.; Ma, J.; Hu, Z.; Cui, G.; Chen, L. Identifying and Addressing Critical Challenges of High-Voltage Layered Ternary Oxide Cathode Materials. *Chem. Mater.* **2019**, *33*.
- (6) Jung, R.; Metzger, M.; Maglia, F.; Stinner, C.; Gasteiger, H. A. Oxygen Release and Its Effect on the Cycling Stability of $\text{LiNi}_x\text{Mn}_y\text{Co}_z\text{O}_2$ (NMC) Cathode Materials for Li-Ion Batteries. *J. Electrochem. Soc.* **2017**, *164* (7), A1361–A1377. <https://doi.org/10.1149/2.0021707jes>.
- (7) Dixit, M.; Markovsky, B.; Schipper, F.; Aurbach, D.; Major, D. T. Origin of Structural Degradation During Cycling and Low Thermal Stability of Ni-Rich Layered Transition Metal-Based Electrode Materials. *J. Phys. Chem. C* **2017**, *121* (41), 22628–22636. <https://doi.org/10.1021/acs.jpcc.7b06122>.
- (8) Gao, H.; Cai, J.; Xu, G.-L.; Li, L.; Ren, Y.; Meng, X.; Amine, K.; Chen, Z. Surface Modification for Suppressing Interfacial Parasitic Reactions of a Nickel-Rich Lithium-Ion Cathode. *Chem. Mater.* **2019**, *31* (8), 2723–2730. <https://doi.org/10.1021/acs.chemmater.8b04200>.
- (9) Sicklinger, J.; Metzger, M.; Beyer, H.; Pritzl, D.; Gasteiger, H. A. Ambient Storage Derived Surface Contamination of NCM811 and NCM111: Performance Implications and Mitigation Strategies. *J. Electrochem. Soc.* **2019**, *166* (12), A2322–A2335. <https://doi.org/10.1149/2.0011912jes>.
- (10) Renfrew, S. E.; McCloskey, B. D. Residual Lithium Carbonate Predominantly Accounts for First Cycle CO_2 and CO Outgassing of Li-Stoichiometric and Li-Rich Layered Transition-Metal Oxides. *J. Am. Chem. Soc.* **2017**, *139* (49), 17853–17860. <https://doi.org/10.1021/jacs.7b08461>.
- (11) Zhu, J.; Sharifi-Asl, S.; Garcia, J. C.; Iddir, H. H.; Croy, J. R.; Shahbazian-Yassar, R.; Chen, G. Atomic-Level Understanding of Surface Reconstruction Based on $\text{Li}[\text{Ni}_x\text{Mn}_y\text{Co}_{1-x-y}]\text{O}_2$ Single-Crystal Studies. *ACS Appl. Energy Mater.* **2020**, *3* (5), 4799–4811. <https://doi.org/10.1021/acsaem.0c00411>.

- (12) Han, B.; Key, B.; Lapidus, S. H.; Garcia, J. C.; Iddir, H.; Vaughey, J. T.; Dogan, F. From Coating to Dopant: How the Transition Metal Composition Affects Alumina Coatings on Ni-Rich Cathodes. *ACS Appl. Mater. Interfaces* **2017**, *9* (47), 41291–41302. <https://doi.org/10.1021/acsami.7b13597>.
- (13) Nomura, Y.; Yamamoto, K.; Hirayama, T.; Ohkawa, M.; Igaki, E.; Hojo, N.; Saitoh, K. Quantitative *Operando* Visualization of Electrochemical Reactions and Li Ions in All-Solid-State Batteries by STEM-EELS with Hyperspectral Image Analyses. *Nano Lett.* **2018**, *18* (9), 5892–5898. <https://doi.org/10.1021/acs.nanolett.8b02587>.
- (14) Gu, M.; Belharouak, I.; Genc, A.; Wang, Z.; Wang, D.; Amine, K.; Gao, F.; Zhou, G.; Thevuthasan, S.; Baer, D. R.; Zhang, J.-G.; Browning, N. D.; Liu, J.; Wang, C. Conflicting Roles of Nickel in Controlling Cathode Performance in Lithium Ion Batteries. *Nano Lett.* **2012**, *6*.
- (15) Shukla, A. K.; Ramasse, Q. M.; Ophus, C.; Duncan, H.; Hage, F.; Chen, G. Unravelling Structural Ambiguities in Lithium- and Manganese-Rich Transition Metal Oxides. *Nat. Commun.* **2015**, *6* (1), 8711. <https://doi.org/10.1038/ncomms9711>.
- (16) Yan, P.; Zheng, J.; Zheng, J.; Wang, Z.; Teng, G.; Kuppan, S.; Xiao, J.; Chen, G.; Pan, F.; Zhang, J.-G.; Wang, C.-M. Ni and Co Segregations on Selective Surface Facets and Rational Design of Layered Lithium Transition-Metal Oxide Cathodes. *Adv. Energy Mater.* **2016**, *6* (9), 1502455. <https://doi.org/10.1002/aenm.201502455>.
- (17) Nomura, Y.; Yamamoto, K.; Hirayama, T.; Igaki, E.; Saitoh, K. Visualization of Lithium Transfer Resistance in Secondary Particle Cathodes of Bulk-Type Solid-State Batteries. *ACS Energy Lett.* **2020**, *5* (6), 2098–2105. <https://doi.org/10.1021/acsenergylett.0c00942>.
- (18) Sun, Y.-K.; Myung, S.-T.; Park, B.-C.; Prakash, J.; Belharouak, I.; Amine, K. High-Energy Cathode Material for Long-Life and Safe Lithium Batteries. *Nature Mater.* **2009**, *8* (4), 320–324. <https://doi.org/10.1038/nmat2418>.
- (19) Ramakrishnan, Srinivasan; Park, Byungchun; Wu, Jue; Yang, Wanli; McCloskey, Bryan D. (2019): Extended Interfacial Stability Through Simple Acid Rinsing in a Li-Rich Oxide Cathode Material. *ChemRxiv. Preprint*.
- (20) Doo, S. W.; Lee, S.; Kim, H.; Choi, J. H.; Lee, K. T. Hydrophobic Ni-Rich Layered Oxides as Cathode Materials for Lithium-Ion Batteries. *ACS Appl. Energy Mater.* **2019**, *acsam.9b00786*. <https://doi.org/10.1021/acsam.9b00786>.
- (21) Jung, R.; Morasch, R.; Karayaylali, P.; Phillips, K.; Maglia, F.; Stinner, C.; Shao-Horn, Y.; Gasteiger, H. A. Effect of Ambient Storage on the Degradation of Ni-Rich Positive Electrode Materials (NMC811) for Li-Ion Batteries. *J. Electrochem. Soc.* **2018**, *165* (2), A132–A141. <https://doi.org/10.1149/2.0401802jes>.
- (22) Lee, W.; Lee, S.; Lee, E.; Choi, M.; Thangavel, R.; Lee, Y.; Yoon, W.-S. Destabilization of the Surface Structure of Ni-Rich Layered Materials by Water-Washing Process. *Energy Storage Mater.* **2022**, *44*, 441–451. <https://doi.org/10.1016/j.ensm.2021.11.006>.

- (23) Busà, C.; Belekoukia, M.; Loveridge, M. J. The Effects of Ambient Storage Conditions on the Structural and Electrochemical Properties of NMC-811 Cathodes for Li-Ion Batteries. *Electrochim. Acta* **2021**, *366*, 137358. <https://doi.org/10.1016/j.electacta.2020.137358>.
- (24) Wood, M.; Li, J.; Ruther, R. E.; Du, Z.; Self, E. C.; Meyer, H. M.; Daniel, C.; Belharouak, I.; Wood, D. L. Chemical Stability and Long-Term Cell Performance of Low-Cobalt, Ni-Rich Cathodes Prepared by Aqueous Processing for High-Energy Li-Ion Batteries. *Energy Storage Mater.* **2020**, *24*, 188–197. <https://doi.org/10.1016/j.ensm.2019.08.020>.
- (25) Lucas, G.; Burdet, P.; Cantoni, M.; Hébert, C. Multivariate Statistical Analysis as a Tool for the Segmentation of 3D Spectral Data. *Micron* **2013**, *52–53*, 49–56. <https://doi.org/10.1016/j.micron.2013.08.005>.
- (26) Dupré, N.; Martin, J.-F.; Guyomard, D.; Yamada, A.; Kanno, R. Detection of Surface Layers Using ^7Li MAS NMR. *J. Mater. Chem.* **2008**, *18* (36), 4266. <https://doi.org/10.1039/b807778a>.
- (27) Massiot, D. DMFit <https://nmr.cemhti.cnrs-orleans.fr/dmfit/>.
- (28) Cuisinier, M.; Martin, J.-F.; Moreau, P.; Epicier, T.; Kanno, R.; Guyomard, D.; Dupré, N. Quantitative MAS NMR Characterization of the $\text{LiMn}_{1/2}\text{Ni}_{1/2}\text{O}_2$ Electrode/Electrolyte Interphase. *Solid State Nucl. Magn. Res.* **2012**, *42*, 51–61. <https://doi.org/10.1016/j.ssnmr.2011.09.001>.
- (29) Grissa, R.; Fernandez, V.; Fairley, N.; Hamon, J.; Stephant, N.; Rolland, J.; Bouchet, R.; Lecuyer, M.; Deschamps, M.; Guyomard, D.; Moreau, P. XPS and SEM-EDX Study of Electrolyte Nature Effect on Li Electrode in Lithium Metal Batteries. *ACS Appl. Energy Mater.* **2018**, *1* (10), 5694–5702. <https://doi.org/10.1021/acsaem.8b01256>.
- (30) Liu, H.; Bugnet, M.; Tessaro, M. Z.; Harris, K. J.; Dunham, M. J. R.; Jiang, M.; Goward, G. R.; Botton, G. A. Spatially Resolved Surface Valence Gradient and Structural Transformation of Lithium Transition Metal Oxides in Lithium-Ion Batteries. *Phys. Chem. Chem. Phys.* **2016**, *18* (42), 29064–29075. <https://doi.org/10.1039/C6CP05262B>.
- (31) Ménétrier, M.; Vaysse, C.; Croguennec, L.; Delmas, C.; Jordy, C.; Bonhomme, F.; Biensan, P. ^7Li and ^1H MAS NMR Observation of Interphase Layers on Lithium Nickel Oxide Based Positive Electrodes of Lithium-Ion Batteries. *Electrochem. Solid-State Lett.* **2004**, *7* (6), A140. <https://doi.org/10.1149/1.1697905>.
- (32) Grissa, R.; Fernandez, V.; Fairley, N.; Hamon, J.; Stephant, N.; Rolland, J.; Bouchet, R.; Lecuyer, M.; Deschamps, M.; Guyomard, D.; Moreau, P. XPS and SEM-EDX Study of Electrolyte Nature Effect on Li Electrode in Lithium Metal Batteries. *ACS Appl. Energy Mater.* **2018**, *1* (10), 5694–5702. <https://doi.org/10.1021/acsaem.8b01256>.
- (33) C.D. Wagner; A.V. Naumkin; A. Kraut-Vass; J.W. Allison; C.J. Powell; J.R.Jr. Rumble. NIST Standard Reference Database 20, Version 3.4.
- (34) Köcher, S. S.; Schleker, P. P. M.; Graf, M. F.; Eichel, R.-A.; Reuter, K.; Granwehr, J.; Scheurer, Ch. Chemical Shift Reference Scale for Li Solid State NMR Derived

- by First-Principles DFT Calculations. *J. Magn. Reson.* **2018**, 297, 33–41. <https://doi.org/10.1016/j.jmr.2018.10.003>.
- (35) Cho, D.-H.; Jo, C.-H.; Cho, W.; Kim, Y.-J.; Yashiro, H.; Sun, Y.-K.; Myung, S.-T. Effect of Residual Lithium Compounds on Layer Ni-Rich Li[Ni_{0.7}Mn_{0.3}]O₂. *J. Electrochem. Soc.* **2014**, 161 (6), A920. <https://doi.org/10.1149/2.042406jes>.
- (36) Shizuka, K.; Kiyohara, C.; Shima, K.; Takeda, Y. Effect of CO₂ on Layered Li_{1+z}Ni_{1-x-y}Co_xMyO₂ (M=Al, Mn) Cathode Materials for Lithium Ion Batteries. *J. Power Sources* **2007**, 166 (1), 233–238. <https://doi.org/10.1016/j.jpowsour.2007.01.013>.
- (37) Liu, W.; Oh, P.; Liu, X.; Lee, M.-J.; Cho, W.; Chae, S.; Kim, Y.; Cho, J. Nickel-Rich Layered Lithium Transition-Metal Oxide for High-Energy Lithium-Ion Batteries. *Angew. Chem. Int. Ed.* **2015**, 54 (15), 4440–4457. <https://doi.org/10.1002/anie.201409262>.
- (38) Shurtz, R. C.; Hewson, J. C. Review—Materials Science Predictions of Thermal Runaway in Layered Metal-Oxide Cathodes: A Review of Thermodynamics. *J. Electrochem. Soc.* **2020**, 167 (9), 090543. <https://doi.org/10.1149/1945-7111/ab8fd9>.
- (39) Wang, M.; Navrotsky, A. LiMO₂ (M=Mn, Fe, and Co): Energetics, Polymorphism and Phase Transformation. *J. Solid State Chem.* **2005**, 178 (4), 1230–1240. <https://doi.org/10.1016/j.jssc.2005.01.028>.
- (40) Busà, C.; Belekoukia, M.; Loveridge, M. J. The Effects of Ambient Storage Conditions on the Structural and Electrochemical Properties of NMC-811 Cathodes for Li-Ion Batteries. *Electrochim. Acta* **2021**, 366, 137358. <https://doi.org/10.1016/j.electacta.2020.137358>.

Supporting information

Pristine surface of Ni-Rich NMC as a premise of future surface reactivity

Angelica Laurita, Liang Zhu, Pierre-Etienne Cabelguen, Jérémie Auvergniot, Dominique Guyomard, Vincent Fernandez, Jonathan Hamon, Nicolas Dupré, Philippe Moreau*

A. Second Derivative Method for elemental quantification of transition metals

Considering the proximity of transition metal edges, especially those of Co and Ni, the extraction of their characteristic signal is difficult and unreliable. The background extraction is indeed highly dependent on the model, the local thickness and the statistics achieved for data acquisition. The method of the second derivatives exploits the fact that such background removal is unnecessary.¹

Acquisition of Spectrum Images (SI) were performed with the surface aligned with the y vertical axis (easy in STEM-HAADF mode). Only surfaces with sufficient rectilinear lengths in this direction were chosen (at least roughly 50 nm corresponding to about 170 pixels). The first step consists in binning data along the y direction to obtain a sufficient S/N ratio even at the surface, where the signal for Co and Mn elements can be really low due to their small amount (Figure S1).

The second derivative can then be calculated for all spectra in the SI. Two reference spectra for each edge (one taken in the bulk, far from the surface, and one corresponding to noise only) can then be extracted directly from the SI and be implemented in the Multiple Linear Least Square fitting routine of DM.² The fit ranges for all edges (O-K edge, L_{2,3} edges of TMs) were chosen by taking into account both the extend of EEL signal and the noise appearing in the second derivatives. Since the pre-

peak at the oxygen K edge is known to be very sensitive to the oxidation state and site environment, it was not included in the fit. Likewise, the ratio of L₃/L₂ edges of TM are known to be sensitive to oxidation states, so fits were only performed based on their L₃ edge. Slight energy shifts at the L₃ edges have in fact no effect considering the energy resolution we used for the quantification. The method showed a remarkable robustness whatever the analyzed particles.

The fit coefficients obtained for the four MLLS fits (one for each edge) represent the relative contributions of the two reference spectra within each binned pixel. The relative amount of each element can thus be calculated as a function of the distance from the surface. We decided to take Ni as reference since its signal is less prone to be influenced by noise. Ratio values in the bulk (far from the surface) are set to the expected nominal values (1/8 for Co and Mn and 2.5 for O).

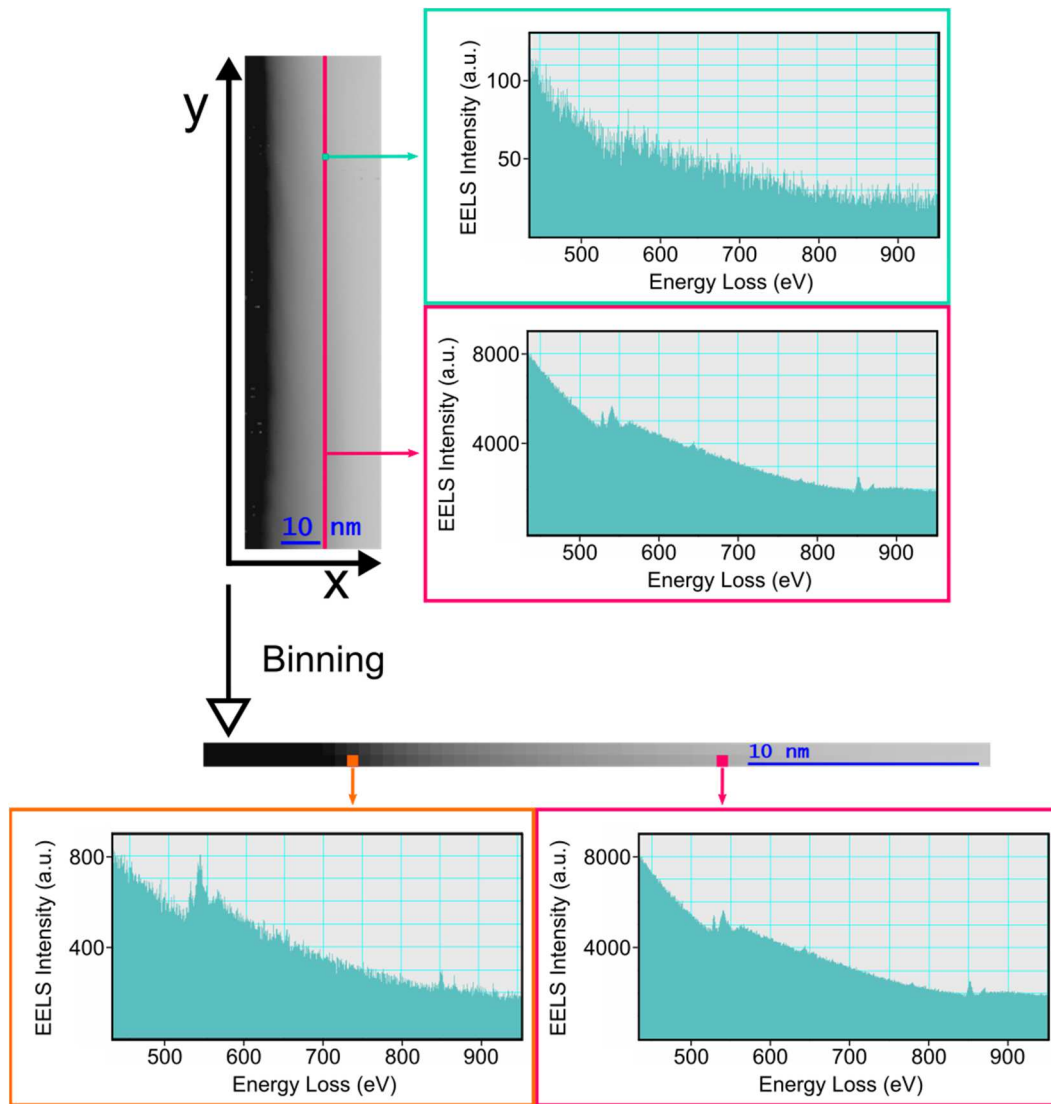


Figure S1. Example of the effect of the binning step on the S/N ratio. The spectra corresponding to a single bulk pixel of the original SI (green line) and of the binned SI (pink line) are compared. The spectrum in the orange box represents the spectrum of one pixel at the surface after binning.

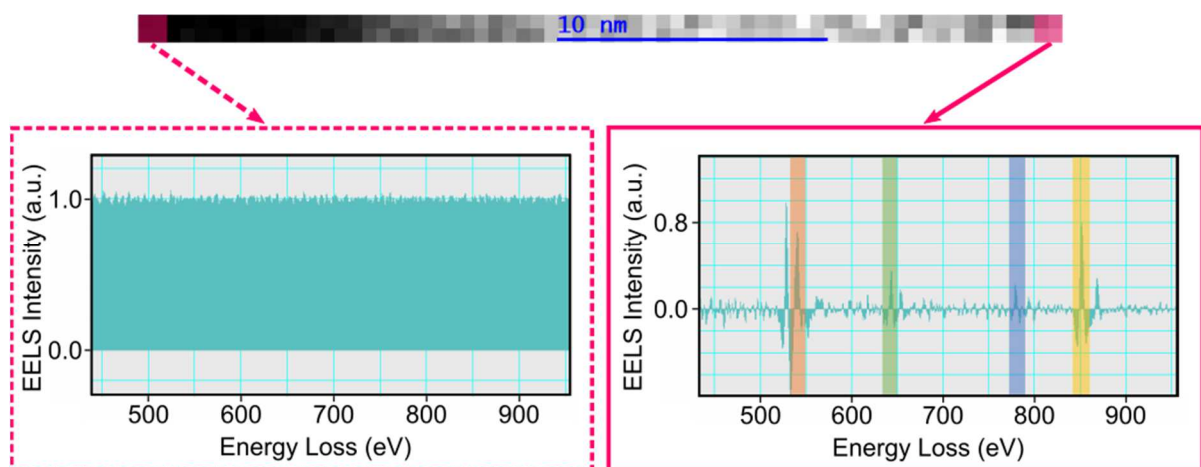


Figure S2. Reference spectra used for the MLLS fitting. The noise only reference is represented in the pink dotted box, while the bulk one in the full pink line.

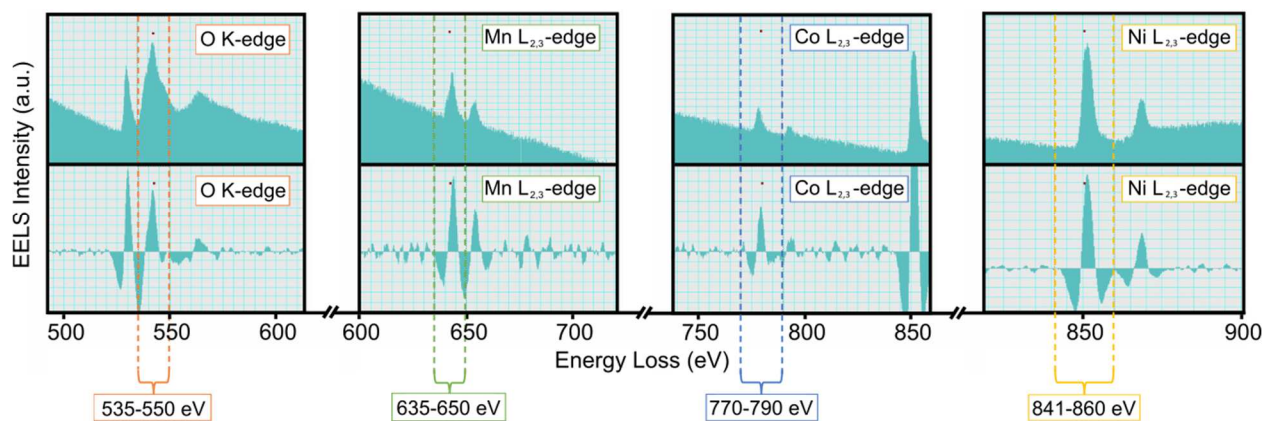


Figure S3. Chosen MLLS fitting ranges for each edge.

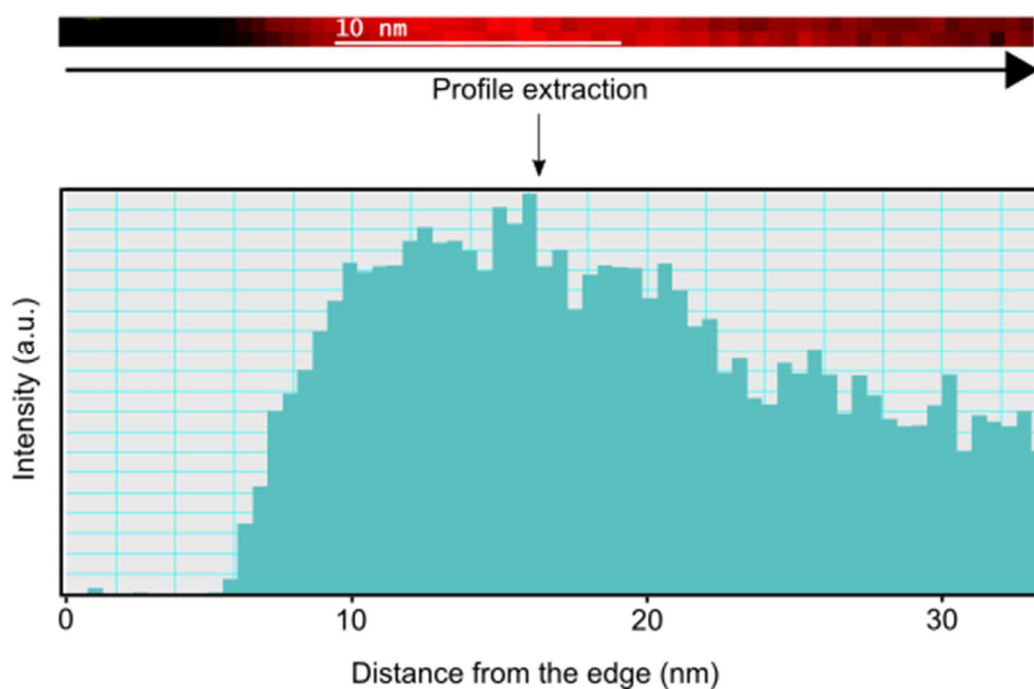


Figure S4. Fit coefficient map obtained for the MLLS fitting of the O K-edge on one of the analyzed particles and its extracted profile. The same map was obtained for each element and the fit coefficient values extracted the same way. The decrease of the coefficient for distances superior to 15 nm in this example is a consequence of the thickness increase. Performing ratios compensate for this effect.

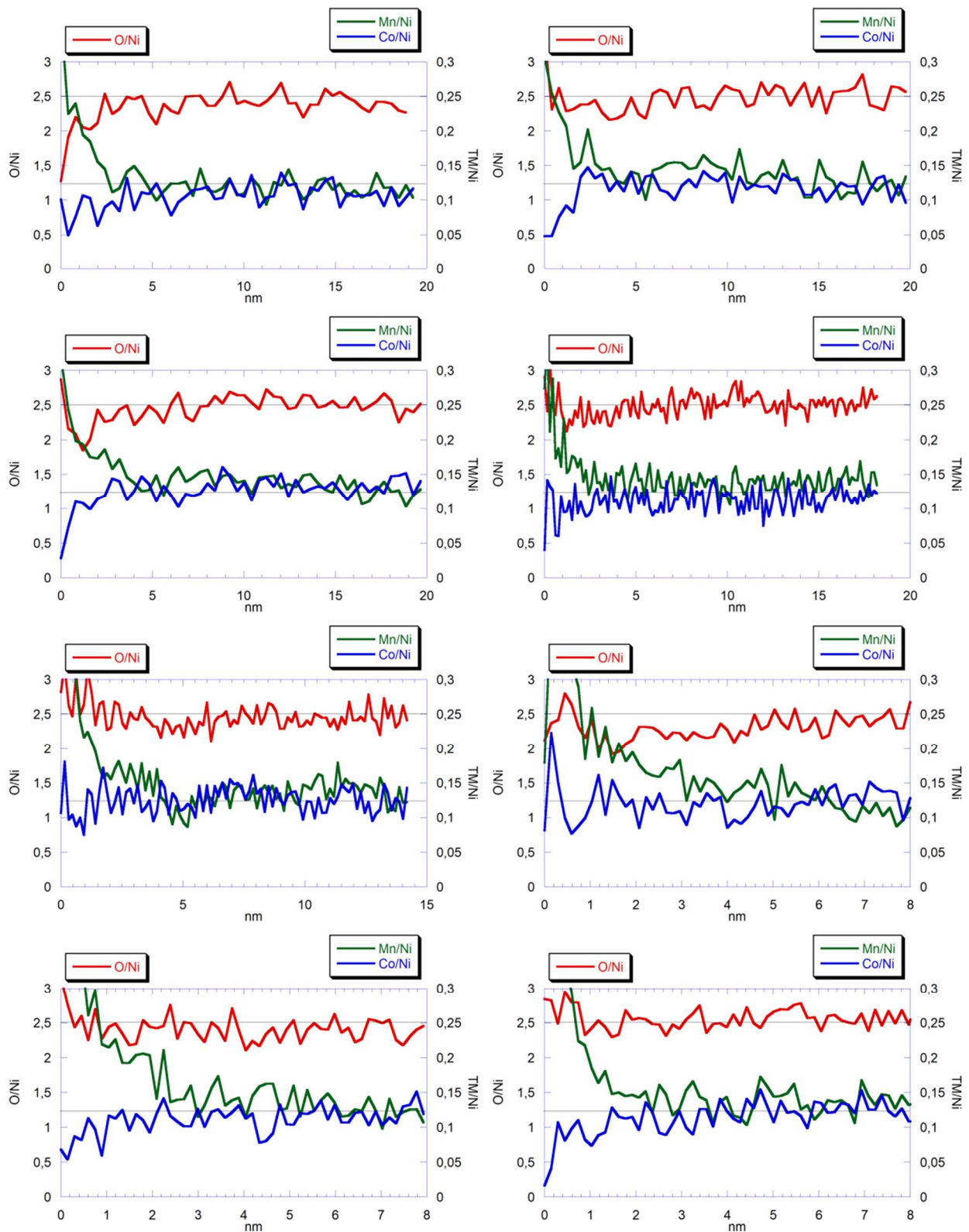


Figure S5. Quantification results obtained by STEM-EELS on various primary particles. Ratios O/Ni (in red), Mn/Ni (in green) and Co/Ni (in blue) are presented. A Mn enrichment is proven to occur over the first ~3 nm from the surface. Different pixel sizes were used and can explain the different amount of noise in the data.

B. XPS reference spectra and data fit

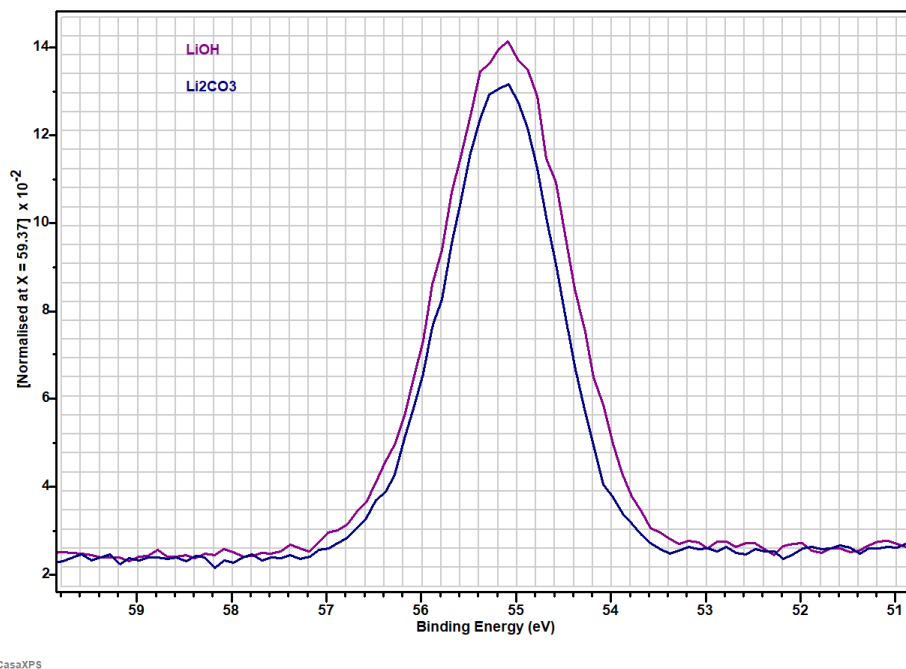


Figure S6. Experimental Li 1s XPS reference spectra for LiOH (in purple) and Li₂CO₃ (in blue) showing that the two compounds have similar peak positions. Spectra were acquired in the same conditions as the samples in the main text.

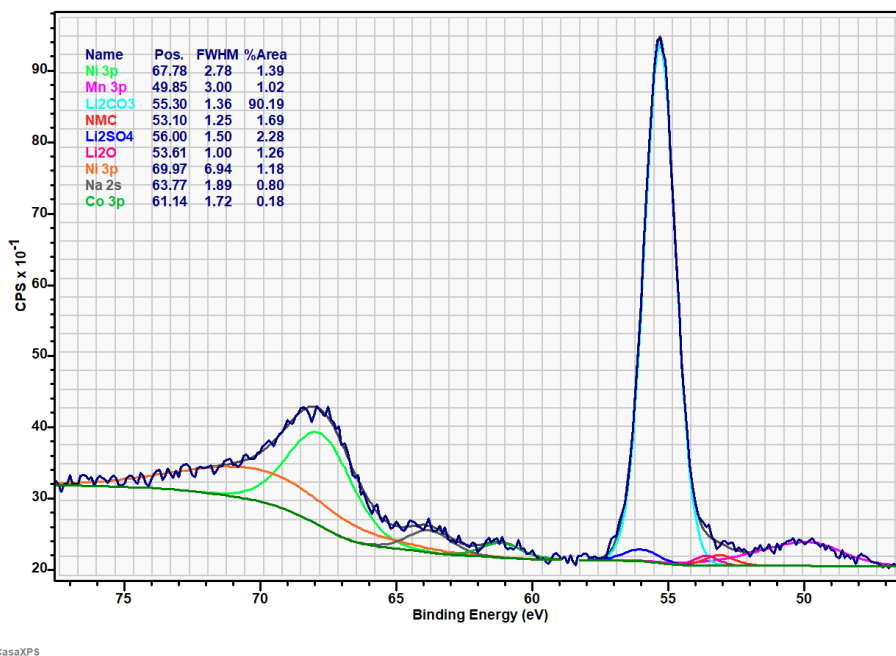


Figure S7. Li 1s XPS spectrum obtained for sample A2 (after 2 days in RH = 30%) showing that almost only Li₂CO₃ can be detected as a lithiated species after aging in these conditions.

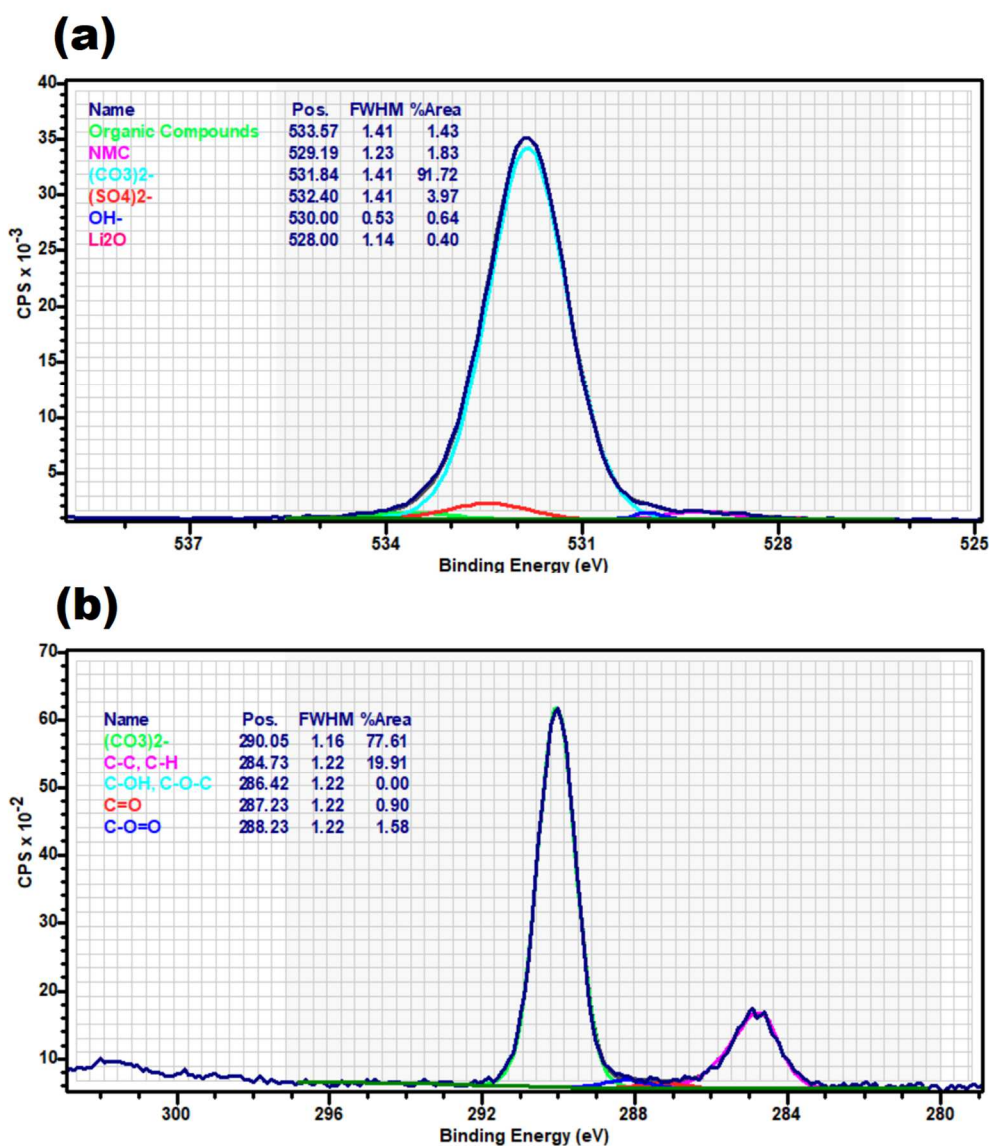


Figure S8. O 1s (a) and C 1s (b) XPS spectra obtained for sample A2 (after 2 days in RH = 30%)

References

- (1) Botton, G. A.; Appel, C. C.; Horsewell, A.; Stobbs, W. M. Quantification of the EELS Near-Edge Structures to Study Mn Doping in Oxides. *J. Microsc.* **1995**, *180* (3), 211–216. <https://doi.org/10.1111/j.1365-2818.1995.tb03680.x>.
- (2) Gatan Software Team. *Digital Micrograph 3.40.2804.0*; Gatan Inc., 2020.

Part 2. Influence of the electrode preparation steps

The impact of the electrode preparation steps will be investigated in this second part, focusing on the evolution of the native surface layer and looking for possible correlations between the pristine and the corresponding electrode surface conditions.

In this way, we hope to allow an easier comparison with data in the literature, often acquired on electrodes instead of powders.

The samples aged in short-term low-humidity conditions were analysed here following the same methods as in the first part (and explained in Chapter 2), to allow a proper comparison between them.

2.1. Contamination layer

Once a good method for the analysis of the contamination layer at the surface of the pristine powder was determined, we applied this same approach in the study of electrodes. Actually, instead of investigating electrodes after coating on the current collector, we decided to focus first on dried slurries in order to ease their analysis by MAS-NMR, as already mentioned in Chapter 2 (c.f. Section 3.3).

The first step of the analysis of the surface contamination layer being the determination of the species contained in it, we recorded XPS spectra of the dried slurries obtained after simple mixing of the active material (AM), polyvinylidene fluoride (PVDF) as a binder, and carbon black (CB) to improve conductivity, in *N*-Methyl-2-pyrrolidone (NMP). The same experimental conditions as for the powder –therefore taking into account the degradation issues (c.f. Section 4.2.2 in Chapter 3)– were used here; however, the results were unsatisfactory. Figure 3.1 shows the XPS signals obtained for the C 1s (a), O 1s (b), S 2p (c) and Li 1s (d) peaks in both a powder and a slurry sample. It appears that recorded counts for O, S and Li of slurries spectra are extremely low when compared to the powder sample. This is due to the low probing depth of soft X-rays already mentioned in

Chapter 2 (c.f. Section 4.2.1). The AM signal is very likely hidden by the layer containing CB and PVDF, which appears instead to be very intense in the C 1s peak (Figure 3.1a). This seems to imply the impossibility to properly identify the species contained in the contamination layer.

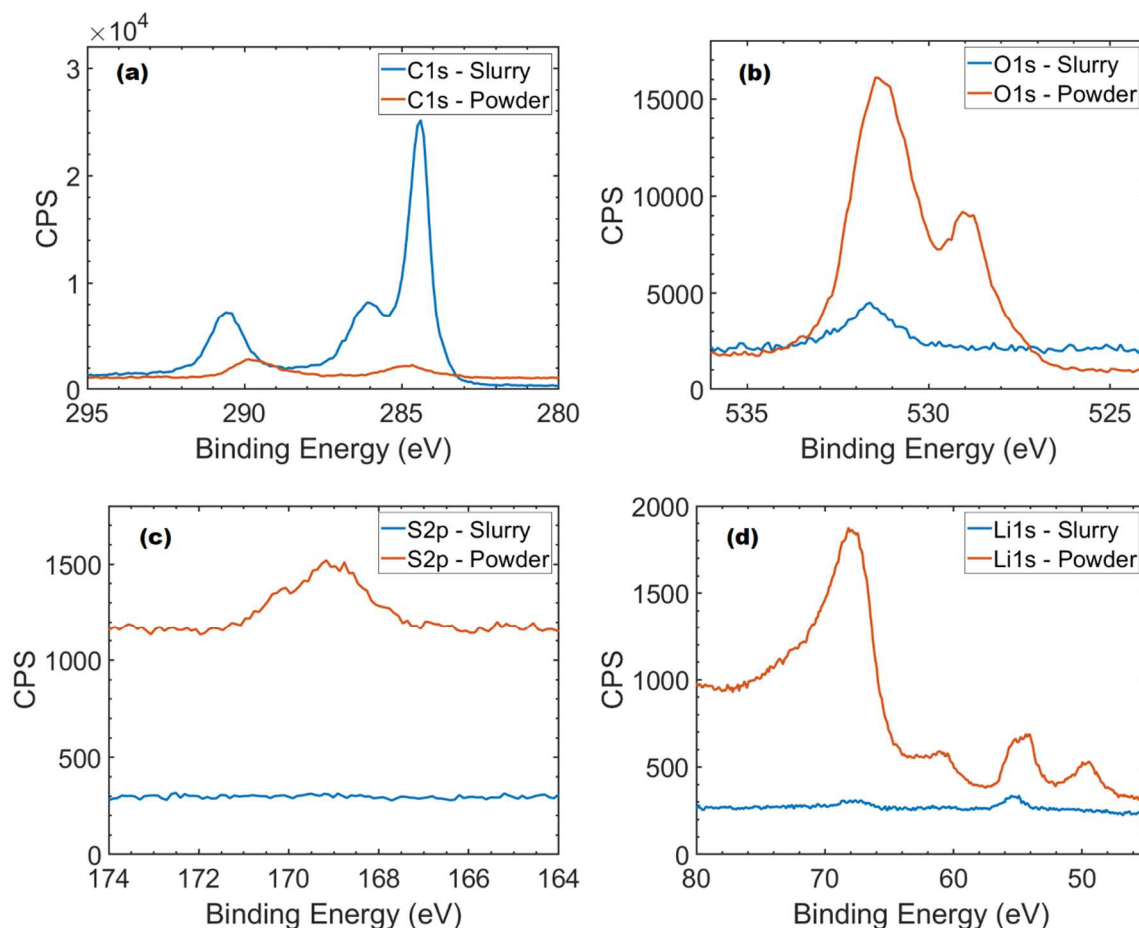


Figure 3.1. Comparison between XPS signals from slurry (blue line) and powder (orange line) analysis. Peaks relative to C 1s (a), O 1s (b), S 2p (c) and Li 1s (d) are reported.

In order to unveil the AM and increase its XPS signal, slurries were manually grinded by using an agate mortar and pestle inside the argon-filled glovebox. The so obtained powder was inserted into designated holes on the XPS sample holder, following the considerations already made for the pristine powder and reported in Section 4.2 of Chapter 2. Nevertheless, the resulting XPS spectra quality was still insufficient to draw any conclusion. A stable neutralisation of the sample appeared indeed unattainable, most likely because of the inhomogeneity of the sample due to the manual grinding. Figure 3.2 depicts the C 1s spectrum obtained during the first scan of a non-grinded

slurry (dashed black line) to be used as a comparison with the five acquisitions made on the grinded sample. The spectra corresponding to the grinded slurry appear to be broader and shifted —especially when considering the peak around 290 eV—, which is consistent with an inefficient neutralisation. This is also confirmed by the small bump around 282 eV reported in the inset of Figure 3.2, which appears during the two first scans and disappears afterwards. Accordingly, data corresponding to the grinded slurry will not be considered hereafter.

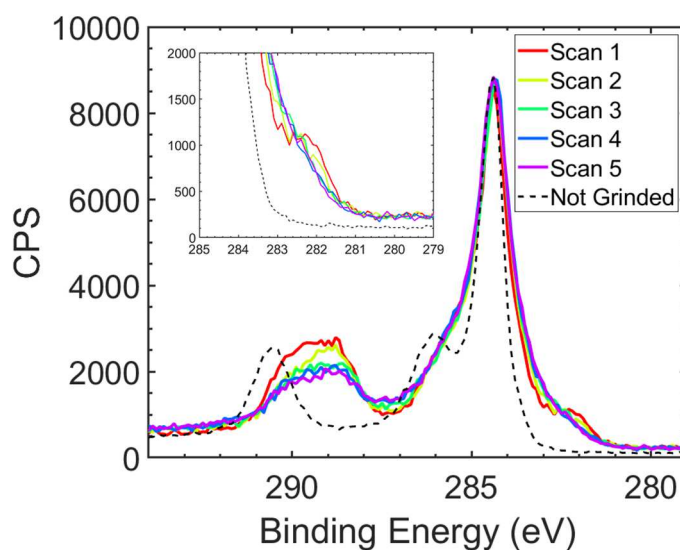


Figure 3.2. Effect of the bad neutralisation of a grinded slurry on the evolution of the C 1s peak during the five scans of the acquisition (lines in colours). The first scan of a non-grinded slurry is reported as a comparison in black dashed line.

Despite the inconclusive information about lithiated compounds given by XPS acquisitions on these samples, it was possible to quantify the totality of surface diamagnetic lithium by MAS-NMR to investigate the influence of the electrode preparation step on the extraction of lithium from the AM.

In this context, the ^7Li MAS-NMR spectra of three powder samples and the corresponding slurries were recorded. The three powders were obtained by letting the pristine powder A0 secondary particles aging under a controlled atmosphere for different amounts of time without formerly grinding them (contrary to samples A1 and A2 of the first part of this Chapter). The aging conditions used to obtain the

samples A3, A4 and A5 are reported in the scheme of Figure 3.3. It has to be mentioned here that the relative humidity in the tube furnace (sample A5) was particularly tricky to control, varying between 53 and 70%, while the absence of CO₂ was successfully assured.

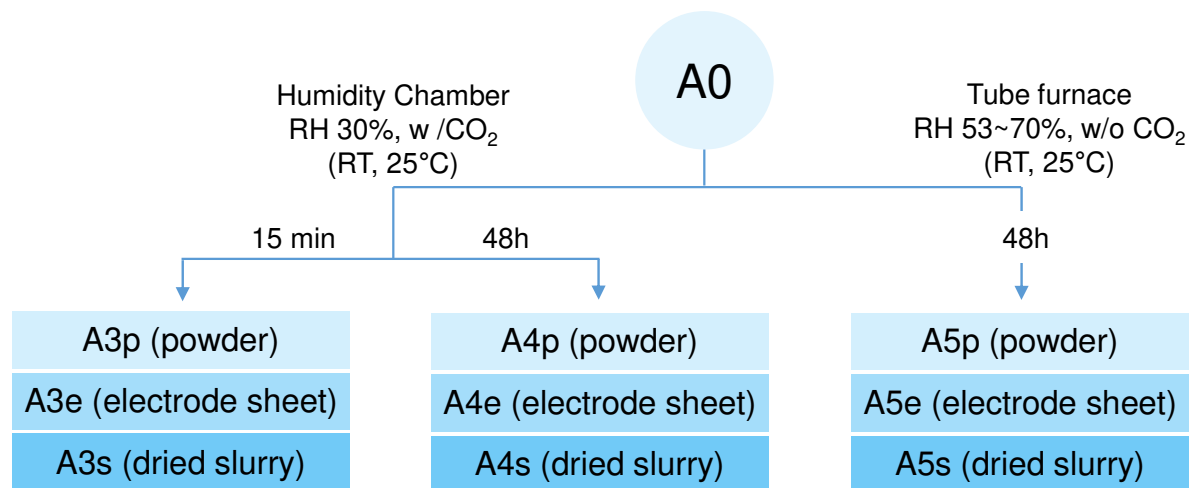


Figure 3.3. Aging conditions used to obtain samples A3, A4 and A5 from the pristine powder A0.

Given the similarity of these samples with the previously characterised A1 and A2, the fit of the ⁷Li MAS-NMR spectra corresponding to A3p, A4p and A5p were performed by considering the presence of the same species (Li₂O, Li₂CO₃, LiOH and Li₂SO₄) and thence using the same contributions reported earlier. While the chemical shift of each peak was fixed, the FWHM were sensibly reduced to respect the higher distance of the surface species from the AM. Actually, by not grinding powders, the new contamination species due to aging are necessarily forming upon the already existing ones and thence further from the material when compared to the ones developing on a brand new surface emerging after grinding. Therefore, the corresponding MAS-NMR signals are expected to be narrower due to the lower influence of the paramagnetic material (c.f. Part 3 of Chapter 2). This hypothesis was actually confirmed by the fit.

The fits of samples A3s, A4s and A5s were instead obtained by adding a new contribution at 0.25 ppm corresponding to LiF, which presence will be the focus of Section 2.2.

The quantification of the surface diamagnetic lithiated species was thence performed following the method described in Chapter 2 (c.f. Section 3.2). The total amount of diamagnetic lithium (in $\mu\text{mol}/\text{g}_{\text{AM}}$) found in the six samples is reported in Figure 3.4. The extraction of lithium from the AM to form the considered surface species increases in all the samples during the electrode preparation step, demonstrating that additional changes affect the NMC811 surface upon this procedure.

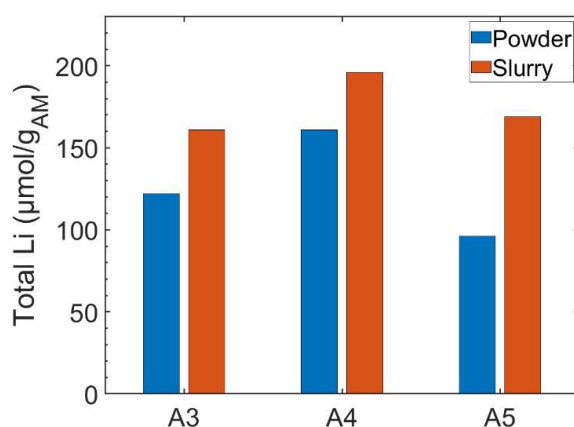


Figure 3.4. Total surface diamagnetic lithium amount evolution during the slurry preparation (in orange) in dry room from powder samples (in blue) aged for 15 minutes in 30% relative humidity in presence of CO_2 (A3), two days in 30% relative humidity in presence of CO_2 (A4) and two days in 53-70% relative humidity in absence of CO_2 (A5).

Moreover, it is interesting to notice here how the increase in the amount of surface lithium after the electrode preparation step strongly depends on the initial status of the surface. In particular, sample A4 — meaning the one with the higher initial amount of surface lithium — is affected by a 22% increase only (from 161 to 196 $\mu\text{mol}/\text{g}_{\text{AM}}$) upon electrode preparation. On the other hand, this quantity rises by 32% in sample A3 (from 122 to 161 $\mu\text{mol}/\text{g}_{\text{AM}}$). Sample A5 is a special case: despite the more humid atmosphere (more than twice the humidity applied on samples A3 and A4), the absence of CO_2 during aging hinders the formation of new surface lithiated compounds and thus the extraction of lithium from the AM. During the subsequent electrode preparation in the dry room — meaning in relatively low humidity, but atmospheric CO_2 level —, sample A5 surface reacts extremely rapidly to form new lithiated compounds accounting for 76% of the initial value. These considerations lead

to two conclusions: i) the lithium extraction occurs when both H₂O and CO₂ are present in the atmosphere; ii) the surface contamination layer protects the NMC surface from further reacting during the electrode preparation in presence of carbon dioxide.

2.2. A focus on LiF

As briefly mentioned in the previous section, a contribution corresponding to LiF was used to fit the ⁷Li MAS-NMR isotropic resonance of the analysed slurries. The addition of such a line was suggested by XPS at first. As a matter of fact, the XPS F 1s signal was well defined, contrarily to the others (Figure 3.1) and LiF was easily identified in both electrodes and dried slurries.

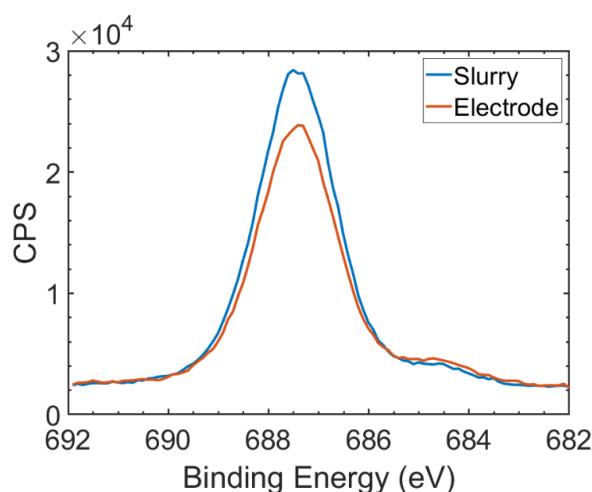


Figure 3.5. XPS F 1s spectra corresponding to a dried slurry (blue line) and the corresponding electrode.

It has to be mentioned that LiF is known to be present at the surface of NMC electrodes as a consequence of the high energy and high temperature calendering process.¹ Grissa et al. showed indeed how LiF/PVdF ratio at the surface of NMC532 electrodes increases from 0.1 to 0.3 when a mild or a heavy calendering is performed, respectively. Since the polymer is the only possible source for the fluoride contained in the LiF, these observations indicate that a PVdF degradation occurs when this compound is submitted to energetic treatments. The presence of such a species was therefore unexpected for both the analysed electrodes (not calendered) and the dried slurries (not coated on the current collector).

In particular, when comparing samples A4s and A4e e.g., the LiF/PVdF ratio decreases from 0.06 to 0.04 when the coating on the current collector is not performed (Figure 3.5). These quantities are sensibly lower than the ones found by Grissa et al., in line with previous considerations on the calendaring effect. Moreover, the higher LiF amount on the electrode suggests a similar influence of the step corresponding to the coating on the current collector. However, new hypotheses to explain the PVdF degradation in the dried slurries still have to be suggested since the polymer was not exposed to any energetic treatment to prepare these samples.

The LiF contribution was thence attributed at first to a degradation of the PVdF binder under X-Rays exposure. Figure 3.6 shows how the C-F₂ signal around 687 eV decreases upon X-rays exposure, while the one around 684.5 eV corresponding to LiF increases, demonstrating the occurrence of the above mentioned degradation.

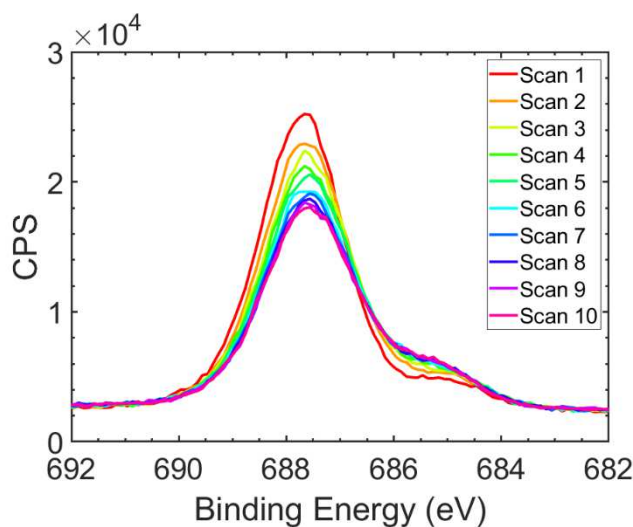


Figure 3.6. X-rays exposure effect on the XPS F 1s signal of a dried slurry.

In order to confirm the presence of LiF on the dried slurries independently of the X-Rays exposure, ¹⁹F MAS-NMR was performed. Figure 3.7 represents the obtained spectrum for Sample A4s, showing a peak around -205 ppm corresponding to the LiF contribution (clearly visible in the zoomed spectrum in the inset of Figure 3.7 and indicated by straight orange arrows) with its relative spinning sidebands (dashed orange arrows in Figure 3.7). Since the slurry is not exposed to any energetic source

during MAS-NMR analysis, the hypothesis of a PVdF degradation coming from X-rays exposure can now be excluded.

Once the PVdF degradation was confirmed to happen during the slurry preparation, we shifted our focus on the understanding of its origin in order to suggest a possible mechanism for the formation of LiF. A reaction between surface basic LiOH and PVdF was often proposed in the literature as a possible cause of the widely observed slurry gelification.¹⁻⁶ Such a phenomenon was indeed found to occur more likely for high-Ni compositions —more affected by the formation of lithiated surface species— than during the preparation of low-Ni NMC electrodes. Following this explanation, the PVdF would undergo dehydrofluorination following the simplified reaction proposed by G.J. Ross et al.:⁷

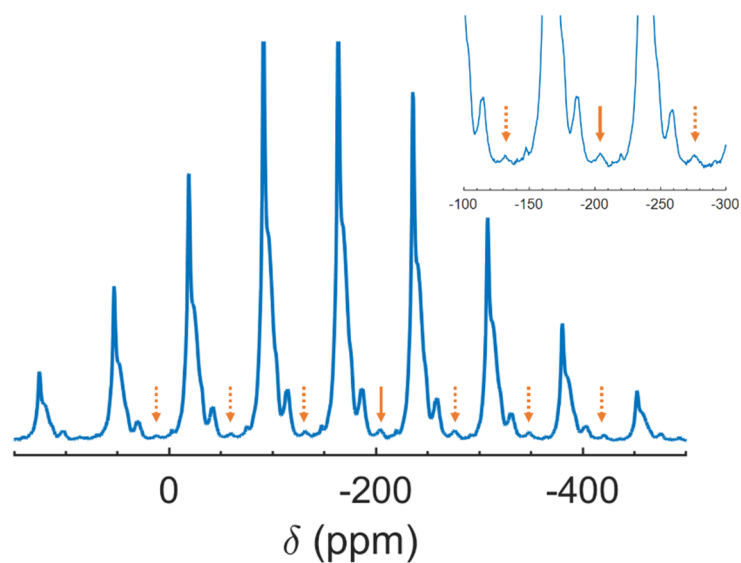


Figure 3.7. ^{19}F MAS-NMR spectrum of a NMC811 dried slurry.

To confirm such a mechanism, slurries were dissolved in deuterated DMF (known to effectively solubilise PVdF) and ^{13}C liquid NMR was performed on the so obtained solution after filtration of the AM and conductive carbon. The low sensitivity of this technique together with the low amount of degraded PVdF —and thence C=C bonds— expected in our samples did not allow the detection the double bonded carbons that

could have been a proof of the occurrence of the reaction proposed by Ross et al. However, we strongly believe that this approach applied to calendered electrodes — meaning with a higher amount of degraded PVdF— could help clarifying the occurring reactions and their final products.

On the other hand, ^7Li SS MAS-NMR was exploited here to follow the amount of the surface diamagnetic lithiated species in the samples described in Section 2.1. If reaction 3.1 were really happening, a higher amount of LiOH at the initial powder surface would imply a higher quantity of LiF in the corresponding slurry, with a concurrent decrease in LiOH.

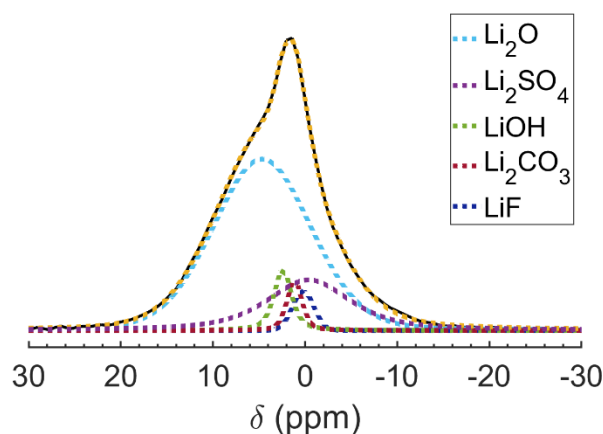


Figure 3.8. Isotropic band fit of the ^7Li MAS-NMR spectrum of A4s sample. The total fit is represented by the yellow dotted line, while original data are in black straight line.

By combining the new information about the presence of LiF and the knowledge about the surface lithiated species acquired during the analysis of the pristine powder (c.f. Part 1 of this chapter), we were able to successfully fit MAS-NMR spectra with contributions corresponding to the five expected species: Li_2O , Li_2SO_4 , LiOH, Li_2CO_3 and LiF —the latter for slurry samples only. The same chemical shifts used for the A0 sample (c.f. Part 1 of this chapter), but narrower lines due to the different aging method, as already elucidated in Section 2.1, were used here to fit the isotropic resonance and the ssb of samples A3, A4 and A5 (p and s). The fit refinement conducted using DMFit Software validated the use of narrower lines to represent the

spectra corresponding to samples A3, A4 and A5.⁸ The so-obtained fit of the isotropic resonance for Sample A4s is showed in Figure 3.8 as an example and the main characteristics of each contribution (chemical shift and FWHM) as well as their quantification (in $\mu\text{mol/g}_{\text{AM}}$) are reported in Table 3.1 for all the samples. All the spectra were calibrated with respect to LiCl and the quantification was performed as detailed in Chapter 2 (Section 3.2) taking into account the integrated intensities of both the isotropic resonance and the spinning sidebands.

Before proceeding to the interpretation of these results, some preliminary observations are needed:

- i- Electrodes are prepared in an industrial dry room. The relative humidity of this environment (typically controlled to be between 0.7 and 1.5%) is sensibly lower than the one of the climatic chamber samples were aged in. Reactions with H_2O (if there are any occurring) will be therefore ignored when analysing the effect of the electrode preparation step. On the other hand, the presence of elevated amounts of CO_2 in the dry room suggests that reactions with the carbon dioxide continue occurring during electrode preparation. This is particularly true for Sample A5, as already mentioned in Section 2.1.
- ii- Li_2SO_4 coming from the synthesis is considered to be inhomogeneous in the analysed samples. Any increase or decrease in its quantity will thence not be taken into account.
- iii- Since both the total Li and Li_2O amounts always increase when passing from the powder to the electrode, we can hypothesise that the Li extraction from the AM surface brings to the formation of Li_2O and is faster than the reactions consuming this compound. This reaction will not be made explicit during the following discussion, since it is out of scope here.
- iv- The LiF FWHM is always larger than the LiOH and Li_2CO_3 ones (with exception of Sample A3 in which $\text{FWHM}_{\text{LiF}} = \text{FWHM}_{\text{LiOH}}$), suggesting that the formation

of this species happens at the interface between Li_2O (very close to the AM) and LiOH (closer to the material than Li_2CO_3).

Table 3.1. Parameters from ^7Li MAS-NMR signal features for A3, A4 and A5 samples and corresponding quantification.

	δ (ppm)		FWHM (ppm)		Amount ($\mu\text{mol}/\text{g}_{\text{AM}}$)	
	p	s	p	s	p	s
A3						
Li_2O	4.6	4.6	13	13	46	59
Li_2SO_4	-0.6	-0.6	16	13	10	19
LiOH	2.4	2.6	3	4	3	2
Li_2CO_3	1.0	1.0	3	3	0.3	1
LiF	---	0.2	---	3	---	2
Total Li					115.6	162
A4						
Li_2O	4.7	4.7	12	12	63	76
Li_2SO_4	-0.8	-0.4	14	11	15	18
LiOH	2.4	2.4	2	2	2	3
Li_2CO_3	1.0	1.1	2	2	1	2
LiF	---	0.2	---	3	---	3
Total Li					160	198
A5						
Li_2O	4.7	4.6	14	13	43	46
Li_2SO_4	-0.6	-0.9	15	11	6	22
LiOH	2.4	2.4	2	4	0.3	6
Li_2CO_3	1.2	1.1	1	3	0.1	4
LiF	---	0.2	---	5	---	13
Total Li					98.5	163

Taking into account these considerations and the quantities reported in Table 3.1, we suggest that the degradation of the PVdF binder to form the observed LiF is induced by Li₂O, and not LiOH as previously proposed in the literature, according to the reaction:



As a matter of fact, LiOH quantity increases in both Sample A4 and A5, suggesting that this species is unlikely the one reacting with the PVdF to give LiF. Moreover, Li₂O (or lithia) is an extremely basic species, which could thence react with the PVdF more easily than LiOH, due to its higher basicity. In addition, comparing the F 1s XPS spectra acquired by Im et al. on lithia pristine electrodes and the ones presented by Grissa et al. for NMC532 PVdF based electrodes, the contribution of Li₂O in the polymer degradation appears clearly.^{1,5} These two spectra are represented in Figure 3.9a and 3.9b respectively, showing how NMC electrodes are significantly less affected by PVdF degradation than lithia ones even after heavy calendaring.

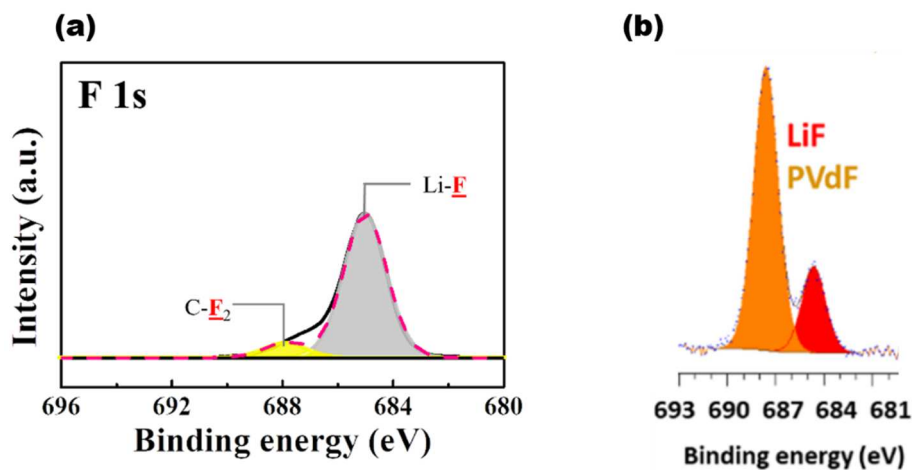


Figure 3.9. Comparison between LiF amount at the surface of a Li₂O electrode (a) and an NMC532 heavily calendared one (b).^{1,5}

Concurrently, it has to be kept in mind that LiOH is consumed to form Li₂CO₃ in presence of carbon dioxide according to the already suggested reaction:



To demonstrate the truthfulness of our hypothesis, we can now follow the evolution of the amount (in $\mu\text{mol}/\text{g}_{\text{AM}}$) of the species that take part in the proposed reaction, as found by ^7Li MAS-NMR and reported in Table 3.1. Let us take Sample A4 as an example. During the electrode preparation, $3 \mu\text{mol}/\text{g}_{\text{AM}}$ of LiF are formed at the NMC811 surface. According to Reaction 3.2, this should be accompanied by the formation of the same quantity of LiOH. Similarly, $1 \mu\text{mol}/\text{g}_{\text{AM}}$ of Li_2CO_3 was formed during the process as indicated in Table 3.1, meaning that $2 \mu\text{mol}$ of LiOH were consumed, in agreement with Reaction 3.3. It results that the amount of LiOH should increase by $1 \mu\text{mol}/\text{g}_{\text{AM}}$ ($3 \mu\text{mol}/\text{g}_{\text{AM}}$ formed $- 2 \mu\text{mol}/\text{g}_{\text{AM}}$ consumed), which is in line with the quantities found by ^7Li MAS-NMR. By using the same process, we were able to explain the LiOH evolution upon electrode preparation on Sample A5 as well, confirming our hypothesis.

On the other hand, Sample A3 seems quite different from the others and the evolution of lithiated species amounts is not completely in line with observations on Sample A4 and A5. Actually, following the above explained process, we found that $0.4 \mu\text{mol}$ of LiOH should have been consumed during the slurry preparation step, whilst $1 \mu\text{mol}$ are actually consumed according to results reported in Table 3.1. Since Sample A3 was aged 15 minutes only in the climatic chamber, the NMC811 surface had most likely not completely reacted with the humid atmosphere, making the assumption (i) above mentioned untrue for this sample. If the AM surface were not in equilibrium with water contained in the atmosphere, multiple reactions could still occur during the slurry preparation. Therefore, the identification of reactions taking place at the Sample A3 surface turns out to be more complicated than for Samples A4 and A5, and new reactions should be added to the two we proposed to entirely explain the observed changes.

2.3. Calendering step

The detrimental effect of the calendering step on the surface LiF evolution was demonstrated by Grissa et al. as just mentioned in the previous section. However, such

a calendering process is commonly known to increase electrodes performance by decreasing porosity and improving the conductivity. 3D-FIB experiments can be used to verify the effect of calendering by visualising the evolution of the porosities in calendered (or not) electrodes. After segmentation of the stack of data as described in Chapter 2, it is indeed possible to determine the amount of each phase in the analysed 3D volume.

Figure 3.10 represents the typical cross-section of a calendered electrode (Figure 3.10a) and a non-calendered one (Figure 3.10b) obtained during 3D-FIB analysis. The non-calendered electrode is characterised by huge porosities and AM secondary particles well dispersed over the whole volume. The calculated porosity amount results therefore to be around 13% of the entire volume, meaning more than the double of the one found for a volume of the same size on a calendered electrode (around 6%), in line with the generally accepted hypothesis of a beneficial effect of the calendering step on porosity.

On the other hand, calendered electrodes secondary particles appear to be strongly affected by the applied pressure, resulting in multiple cracks even before cycling (highlighted by the orange arrows in Figure 3.10a). This is most likely accompanied by a loss of connectivity between the primary particles, known to be one of the principal causes of a scarce diffusivity of lithium ions. While the calendering step seems to be essential to increase conductivity, the applied pressure has to be carefully chosen in order to limit particles damage. As a matter of fact, by selecting one secondary particle only of each dataset and performing the same data treatment as on the entire volume, it is possible to notice that while non-calendered particles show around 2% of porosity, this amount increases to 5-10% in the bottom or top of calendered particles, meaning almost the totality of the porosity found for the whole volume is contained inside the secondary particles.

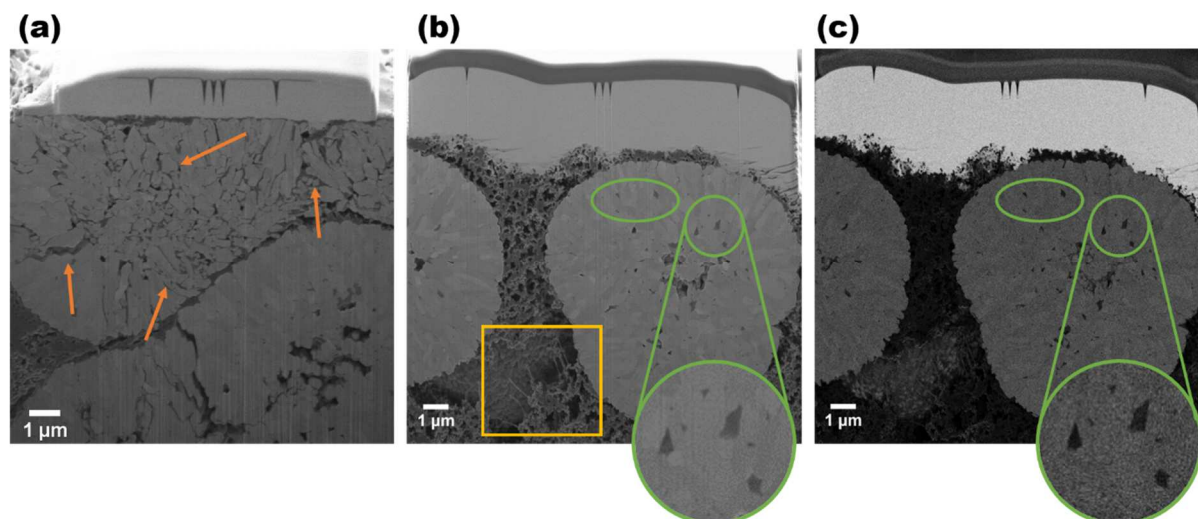


Figure 3.10. Cross-sections of a calendared electrode (a) and a non-calendared one (b,c). (a) and (b) were acquired with the SESI detector during 3D analysis. (c) is the BSE image corresponding to (b).

It is interesting to notice how the largest porosities are typically situated in the core of the secondary particles and at the origin of the deep cracking observed in Figure 3.10a. By carefully examining the slice of Figure 3.10b and the corresponding back-scattered electron image in Figure 3.10c, it is possible to notice how porosities (as the ones indicated by green circles) are often characterised by a darker shade of grey than the AM, but lighter than the black colour of voids in the BSE image. This indicates that porosities are often not completely empty, but filled by species with a lower molecular weight than the AM. If we take into consideration the quantification and distribution of lithiated species found by MAS-NMR and XPS, we could suppose that impurities trapped in the porosities of the secondary particles are most likely lithium oxide or sulphates.

Moreover, the filaments visible on the bottom of Figure 3.10b and highlighted by the yellow area are generally attributed to the degraded PVdF chains bringing to the slurry gelification mentioned earlier.⁵ Following this explanation, some LiF formed during this reaction should be found nearby.

In order to verify these hypotheses, we coupled the 3D acquisitions with EDX spectroscopy. The principal goal was to be able to reconstruct a 3D volume containing

composition information in it, thence providing additional knowledge on the distribution of impurities. The presence of sulphur in some of the porosities would indicate that sulphates remain trapped inside the material during synthesis and are possibly the source of the cracking behaviour of secondary particles upon cycling or calendaring. On the other hand, the existence of fluoride-rich domains without carbon associated to it —ideally close to the filaments observed during the 3D analysis— would be an additional proof of the formation of LiF. Figure 3.11 shows the cartography of four slices analysed by EDX during the 3D acquisition. It is possible to follow here the disappearance of the top particle (very large in Figure 3.11a) together with the appearance of bottom particles (not visible in Figure 3.11a and increasing in size in Figures 3.11b, 3.11c and 3.11d) upon the progress of the ionic beam. From a composition point of view, Ni (in red) is used to indicate the presence of the active material together with the oxygen (in yellow), while fluoride (in blue) and carbon (in green) represent the binder and the active carbon. Although a proper 3D reconstruction is not reported here, it is indeed already possible to observe some inhomogeneity principally in the binder and conductive carbon, as in the bluer zones of Figures 3.11a and 3.11b.

However, due to the complexity of both 3D-FIB acquisitions and its coupling with EDX, a complete volume reconstruction combining both morphology and composition information has not been obtained yet for all the samples. Actually, even when 3D-FIB acquisitions were successful —which is often tricky, as showed in Chapter 2— the image could easily drift during EDX acquisition due to the high duration of this analysis, making data interpretation impossible. Moreover, due to the higher voltage and current used for EDX —necessary to have enough signal for high-energy emitting elements (c.f. Chapter 2)—, the spatial resolution ends up to be lower in cartographies with respect to images, and small-size porosities are therefore not visible in these conditions.

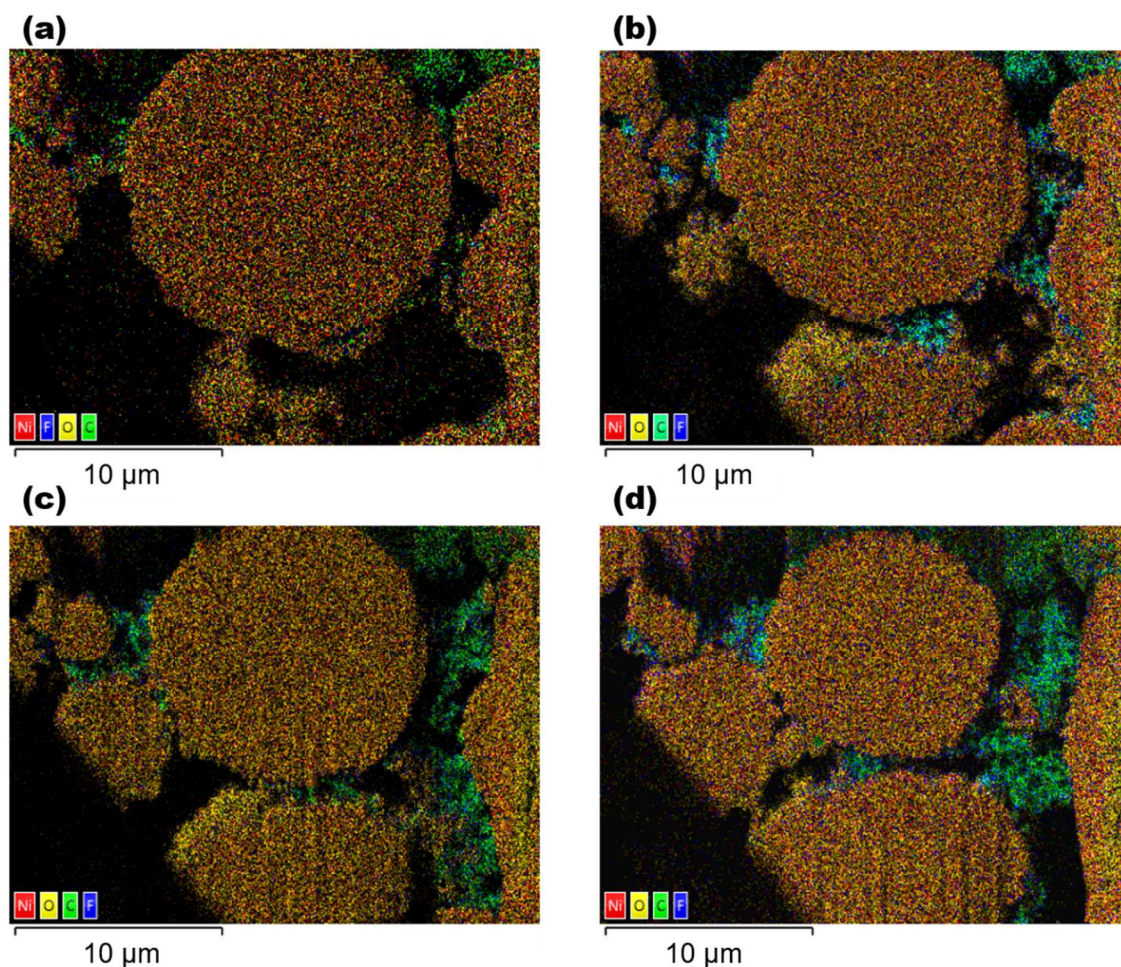


Figure 3.11. EDX cartography at 0 μm (a), 1 μm (b), 2 μm (c) and 3 μm (d) from the starting cross-section of the 3D-FIB acquisition.

Information about the composition of the species contained in the porosities were instead obtained by performing simple cross-sections on powder samples. A porosity with similar characteristics to that already observed in Figure 3.11c —meaning in a darker grey than the AM, but lighter than voids— is clearly visible in the middle of the secondary particle represented in Figure 3.12a. The intensity of the sulphur peak reported in the cartography of Figure 3.12b confirms the presence of such an element in the considered porosity as well as at the surface of the particle, as previously suggested. The analysis of the EDX spectra extracted from the so-identified areas (Figure 3.12c) confirms the presence of sulphates, with both oxygen and sulphur emission peaks well defined. Moreover, lower signals corresponding to both sodium and potassium also appear in these spectra, in line with XPS observations. Sulphate

impurities coming from synthesis appear thence to have an influence on the material porosities and most likely on its subsequent cracking behaviour.

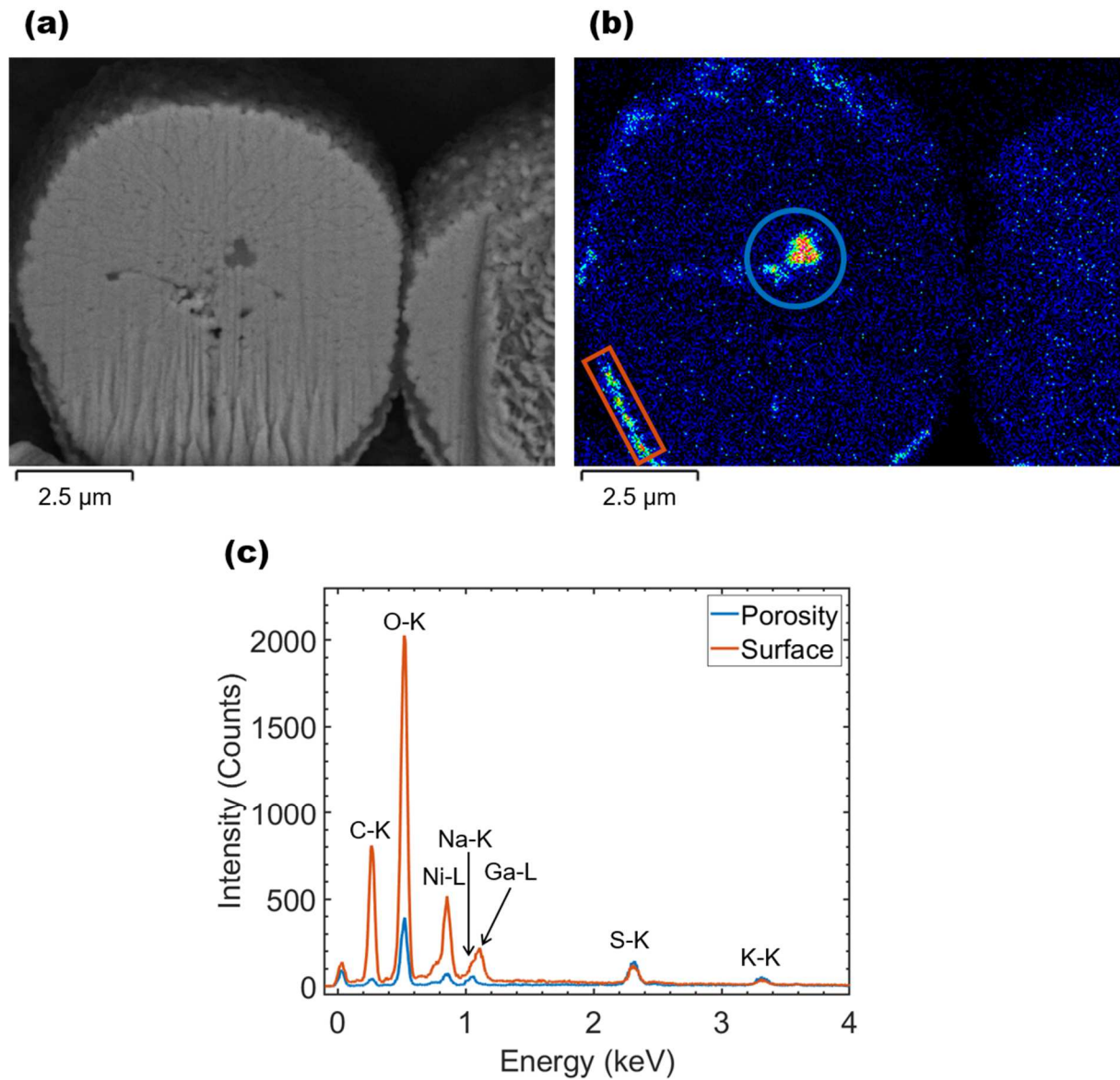


Figure 3.12. BSE image of a secondary particle (a) with indication of the intensity distribution of the EDX sulphur peak (b). The EDX spectra corresponding to the high sulphur intensity areas are reported in (c): the spectrum corresponding to the porosity indicated by the blue circle in (b) is in blue, and the one corresponding to the area highlighted by the orange rectangle in (b) is in orange.

Part 3. Conclusions

The first part of this chapter was dedicated to the study of the surface of a powder sample in its initial state (Sample A0) and after short-term storage in defined conditions of relative humidity (Samples A1 and A2). The powders analysed in this part were grinded before aging in order to allow their analysis by STEM-EELS.

The principal findings of this part can be resumed as follows:

- A reduced Ni layer was observed at the surface of the primary particles in Sample A0. Both the layer thickness and the relative amount of Ni in its reduced state increase upon storage in the studied conditions.
- Similarly, diamagnetic lithiated species were found at Sample A0 surface under the form of Li_2CO_3 , LiOH, Li_2O and Li_2SO_4 (from the further to the closer to the surface) by means of both ^7Li MAS-NMR and XPS that were here exploited in a synergic way. The amount of Li_2CO_3 and LiOH grow significantly in Samples A1 and A2.
- The evolution of the Mn/Ni ratio at the surface of the primary particles was followed thanks to the second derivative method applied on our STEM-EELS results. A Mn-enriched surface accounting for around 3 nm was observed in both Sample A0 and the powders after aging (A1 and A2), showing that storage conditions have no influence on such a feature.

The aim of the second part was instead to verify the impact of the electrode preparation steps on the surface of the material. Indeed, in order to compare our studies to those reported in the literature — principally focusing on the analysis of electrodes — as well as to give an interpretation of cycling and/or gassing behaviour, it is essential to identify a possible relation between the state of the powder surfaces and the obtained electrodes. To this scope, we analysed both dried slurries and real electrodes, prepared using powders aged in similar conditions as Samples A1 and A2.

The reaction between surface Li_2O and the PVdF binder was proposed here as a possible explanation for the presence of LiF on the dried slurries. Similarly, it was confirmed how this reaction is promoted when energy is provided from an external source (X-rays during XPS analysis or electrode calendaring), as already suggested in the literature.

A preliminary study of electrodes at larger scale by means of SEM-FIB 3D reconstructions was presented in the last section of this chapter, highlighting the interest of coupling this technique with EDX acquisitions. The localisation of sulphur containing species (most probably sulphates) was identified, confirming that, being contained inside closed porosity, their amount should not be subjected to variation with air exposure, as measured previously by MAS-NMR.

References

- (1) Grissa, R.; Abramova, A.; Tambio, S.-J.; Lecuyer, M.; Deschamps, M.; Fernandez, V.; Greneche, J.-M.; Guyomard, D.; Lestriez, B.; Moreau, P. Thermomechanical Polymer Binder Reactivity with Positive Active Materials for Li Metal Polymer and Li-Ion Batteries: An XPS and XPS Imaging Study. *ACS Appl. Mater. Interfaces* **2019**, *11* (20), 18368–18376. <https://doi.org/10.1021/acsami.9b01761>.
- (2) Papp, J. K.; Forster, J. D.; Burke, C. M.; Kim, H. W.; Luntz, A. C.; Shelby, R. M.; Urban, J. J.; McCloskey, B. D. Poly(Vinylidene Fluoride) (PVDF) Binder Degradation in Li–O₂ Batteries: A Consideration for the Characterization of Lithium Superoxide. *J. Phys. Chem. Lett.* **2017**, *8* (6), 1169–1174. <https://doi.org/10.1021/acs.jpcclett.7b00040>.
- (3) Seong, W. M.; Kim, Y.; Manthiram, A. Impact of Residual Lithium on the Adoption of High-Nickel Layered Oxide Cathodes for Lithium-Ion Batteries. *Chem. Mater.* **2020**, *32* (22), 9479–9489. <https://doi.org/10.1021/acs.chemmater.0c02808>.
- (4) Zhang, S. S. Problems and Their Origins of Ni-Rich Layered Oxide Cathode Materials. *Energy Storage Mater.* **2020**, *24*, 247–254. <https://doi.org/10.1016/j.ensm.2019.08.013>.
- (5) Im, H. J.; Park, Y. J. Interfacial Reactions in Lithia-Based Cathodes Depending on the Binder in the Electrode and Salt in the Electrolyte. *Sci. Rep.* **2022**, *12* (1), 527. <https://doi.org/10.1038/s41598-021-04439-6>.
- (6) Rehwoldt, M. C.; Wang, Y.; Xu, F.; Ghildiyal, P.; Zachariah, M. R. High-Temperature Interactions of Metal Oxides and a PVDF Binder. *ACS Appl. Mater. Interfaces* **2022**, *14* (7), 8938–8946. <https://doi.org/10.1021/acsami.1c20938>.
- (7) Ross, G. J.; Watts, J. F.; Hill, M. P.; Morrissey, P. Surface Modification of Poly(Vinylidene Fluoride) by Alkaline Treatment1. The Degradation Mechanism. *Polymer* **2000**, *41* (5), 1685–1696. [https://doi.org/10.1016/S0032-3861\(99\)00343-2](https://doi.org/10.1016/S0032-3861(99)00343-2).
- (8) Home | dmfit - D.Massiot - NMR@CEMHTI CNRS UPR3079 Orléans France <https://nmr.cemhti.cnrs-orleans.fr/Dmfit/> (accessed 2022 -04 -02).

Chapter 4

Influence of synthesis conditions on NMC811 surface

After having been focused on the study of one single material to investigate how storage conditions and electrode preparation steps affect the surface of NMC811, this last chapter will bring synthesis parameters into focus.

We will describe here two new series of samples, obtained by varying slightly one or more synthesis conditions. The samples surface and bulk characterisations will be presented and possible correlations between synthesis methods and the observed differences will be discussed.

This chapter, significantly shorter than the previous ones, aims to highlight the importance of working with industrial samples when conducting systematic investigations, assuming that synthesis conditions cannot be implemented in an industrially relevant manner at the laboratory scale.

In the first part, the sintering temperature will be let varying to obtain samples belonging to the “B” series. These samples were cycled in full cells and the gassing evaluated by measuring the cell expansion percentage. The diamagnetic lithiated species at their surface were evaluated by ^7Li MAS-NMR prior to electrochemical cycling and related to both the sintering temperature and the gassing phenomenon.

The second part of the chapter will instead focus on samples synthesised using different Li/TM blends and sintering atmospheres to evaluate the impact of these parameters on the Mn enrichment recorded for Sample A0 and reported in Chapter 3.

Part 1. Influence of the firing temperature

In Chapter 1, it was discussed how gassing is a typical issue for Ni-rich NMC materials and how scarcely it was related to the pristine surface of the material according to the literature. The principal goal of this part is to exploit the procedures described in Chapter 2 and in Chapter 3 to study the influence of the firing temperature on the surface of industrial NMC811 materials, investigating the possible relation between surface lithiated species and gassing.

1.1. Samples description

Three new samples were prepared in Umicore to conduct this study: Sample B1, Sample B2 and Sample B3. In order to focus exclusively on one synthesis parameter at a time, the same precursor and Li/TM blend were used during the synthesis of this series of materials. The sintering was realised in a tube furnace under pure oxygen at three increasing temperatures: T1, T2 and T3, to obtain Samples B1, B2 and B3 respectively (Figure 4.1).

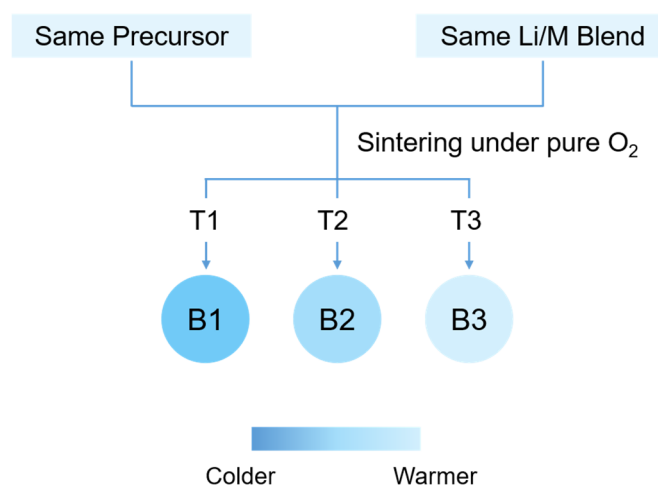


Figure 4.1. Synthesis conditions used to obtain samples B1, B2 and B3.

From a macroscopic point of view, Samples B1 and B2 present similar morphologies, with monodispersed secondary particles having the typical diameter of between 9.1 and 17.0 μm (Figure 4.2). Sample B3 — meaning the one synthesised at the highest

temperature— shows a different bi-dispersed particle size distribution instead, gathering both secondary particles with a diameter between 10.9 and 18.7 μm and smaller ones of around 2.4 μm diameter, as confirmed by the PSD (Particle Size Distribution) analysis.

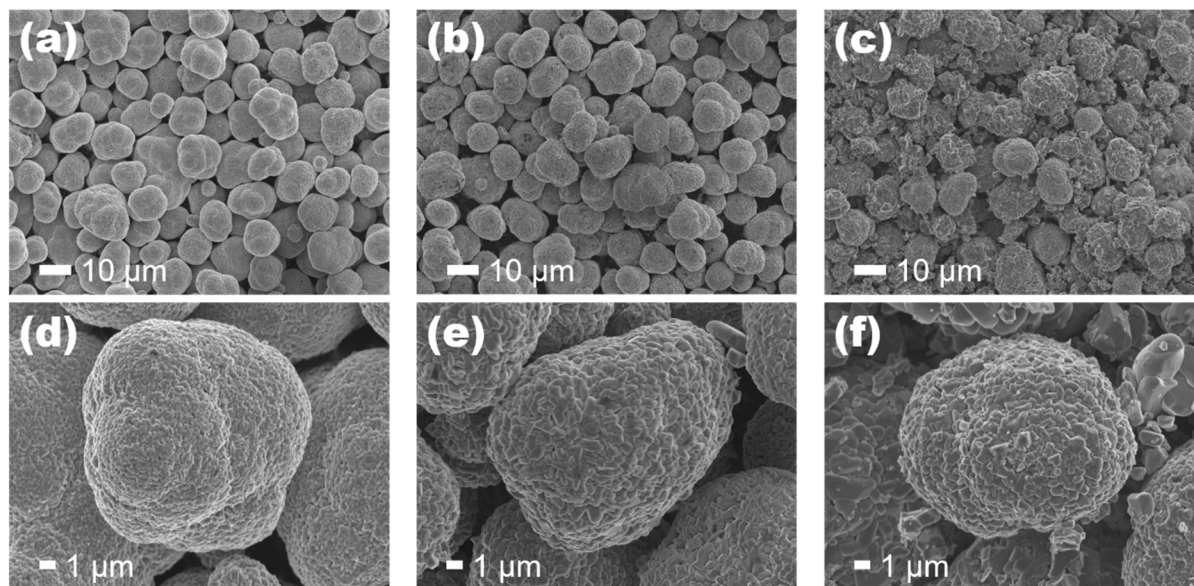


Figure 4.2. SEM images at low (a, c, b) and higher (d, e, f) magnifications showing the morphology of secondary particles of sample B1 (a and d), sample B2 (b and e) and sample B3 (c and f).

The surface lithium compounds were quantified by ^7Li MAS-NMR on the three powders, applying the quantification procedure already explained in details in Section 3.2 of Chapter 2. The parameters used for the fit of the isotropic resonance of the ^7Li spectra are listed in Table 4.1 together with the amounts (in $\mu\text{mol}_{\text{compound}}/\text{g}_{\text{AM}}$), of each identified lithiated compound. The compounds percentage amounts are instead reported in Figure 4.3. Spectra were calibrated with respect to Li_2CO_3 .

Comparing the features of the contributions reported in Table 4.1 and those used to fit the ^7Li MAS-NMR spectrum of Sample A0 (c.f. Table 2, Chapter 3), a significant difference in the FWHM of the LiOH —significantly wider in Sample A0— can be observed. As a matter of fact, despite the attempts, the isotropic resonance intensities of spectra belonging to the B series could not be explained using a wider LiOH contribution. A combination of both a wide —as the one used for Sample A0— and a

narrow LiOH signals did not give better results neither. This discrepancy could be due to the different storage periods; Sample A0 has been indeed stored for long time in the industrial dry room before shipping, while samples belonging to the “B” series were synthesised more recently and shipped to Nantes in a shorter time. Since the history before shipping is not the same, we therefore decided to compare exclusively samples belonging to the same sample series.

Table 4.1. Parameters from ^7Li MAS-NMR signal features for B1, B2 and B3 samples and corresponding quantification.

	δ (ppm)	FWHM (ppm)	Amount ($\mu\text{mol/g}_{\text{AM}}$)
B1			
Li ₂ O	3.6	13	45
Li ₂ SO ₄	-1.7	12	22
LiOH	---	---	0
Li ₂ CO ₃	0	2	2
Total Li			140
B2			
Li ₂ O	3.6	12	39
Li ₂ SO ₄	-1.7	13	27
LiOH	1.6	2	1
Li ₂ CO ₃	0.1	2	1
Total Li			136
B3			
Li ₂ O	3.4	11	34
Li ₂ SO ₄	-1.6	9	26
LiOH	1.5	1	0.5
Li ₂ CO ₃	-0.2	3	6
Total Li			132

When comparing Samples B1, B2 and B3, the compounds FWHMs do not present significant differences from one sample to another, meaning that the overall distribution of the lithiated species at the surface is similar in all the samples and thus not influenced by the sintering temperature.

From a quantification point of view, a trend can be observed in the total diamagnetic lithium amount. Despite the relatively small differences between the three samples ($140 \mu\text{mol}_{\text{Li}}/\text{g}_{\text{AM}}$ in Sample B1, $136 \mu\text{mol}_{\text{Li}}/\text{g}_{\text{AM}}$ in Sample B2, and $132 \mu\text{mol}_{\text{Li}}/\text{g}_{\text{AM}}$ in Sample B3), higher firing temperatures seem to partially hinder the formation of surface lithiated species. Actually, Sample B3 secondary particles appear to be more creased than the ones belonging to Sample B1 and Sample B2 in the SEM images reported in Figure 4.2. Surface impurities seem therefore to smoothen the secondary particle surfaces.

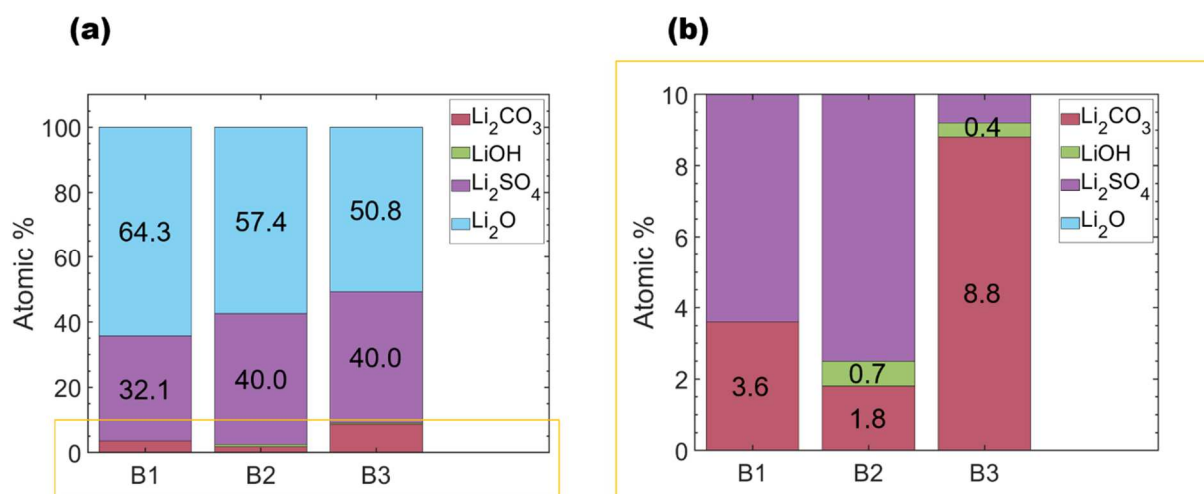


Figure 4.3. Percentage amounts of diamagnetic lithiated species found at the surface of Samples B1, B2 and B3 by ^7Li MAS-NMR. (b) represents the enlargement of the yellow rectangle of (a), to better show the amounts of Li_2CO_3 (in red) and LiOH (in green), significantly lower than Li_2SO_4 (in purple) and Li_2O (in light blue).

Moreover, the speciation of the extracted lithium over the different compounds results to be influenced as well (Figure 4.3). In particular, the amount of Li_2O decreases gradually with increasing firing temperatures, from 64% in B1, to 57% in B2 and 51% in B3. Concurrently, significant differences in the amount of LiOH and Li_2CO_3 were observed, even if a correlation with the sintering temperature was not found. LiOH

appears to be absent in Sample B1, where the quantity of Li_2O is the highest, while the highest LiOH amount was found in Sample B2 synthesised at the intermediate temperature. On the other hand, the formation of Li_2CO_3 results to be promoted by high firing temperatures and its quantity appears particularly elevated at the surface of Sample B3 (almost 9% vs 4 and 2% in Sample B1 and B2 respectively). The high surface specific area measured on Sample B3 by BET (almost three times higher than in Samples B1 and B2), could also be at the base of the higher Li_2CO_3 amount, being a larger surface available for further reactions.

All these observations will be used in the next Section to attempt giving an explanation to the observed gassing phenomena.

1.2. Gassing evaluation

In order to evaluate gassing, the three materials were cycled in full cells against graphite between 2.7 and 4.2 V at a cycling rate of 1C. The cell expansion was then measured at the end of life –meaning when the battery attains 80% of the initial capacity. Cycling was performed at 25°C, 45°C and 55°C following the typical industrial protocol. These analyses were conducted at Umicore facility and the measured cell expansion percentages for the Sample B1 (in black), Sample B2 (in blue) and Sample B3 (in red) at the three cycling temperatures are reported in Figure 4.4.

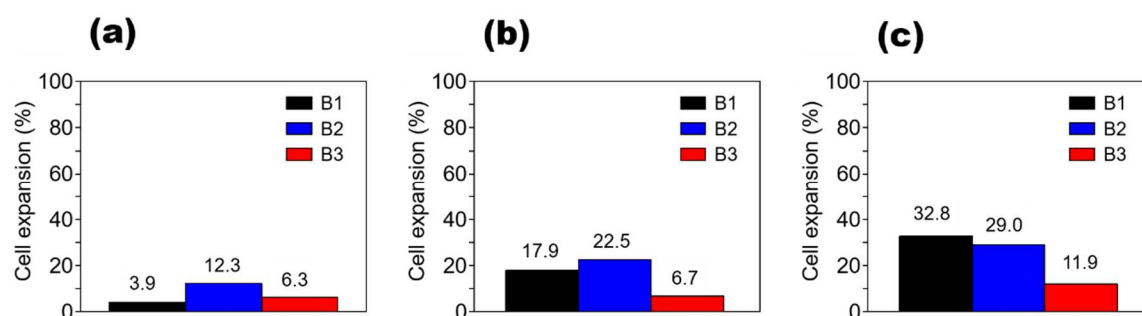


Figure 4.4. Percentage cell expansion measured on full cells containing Sample B1 (black), Sample B2 (blue) and Sample B3 (red), cycled at 25°C (a), 45°C (b) and 55°C (c). Cycling were performed between 2.7 and 4.2 V until end of life of the battery (80% on the initial capacity).

It is interesting to observe how Sample B3 presents a very small cell expansion independently from the cycling temperature, despite the highest amount of Li_2CO_3 found by ^7Li MAS-NMR on the pristine material. The existence of relatively high amounts of Li_2CO_3 after the synthesis therefore does not seem to affect gassing significantly in full cells.

Gassing in Samples B1 and B2 seems instead to be strongly influenced by the cycling temperature. In particular, Sample B1 has the lowest cell expansion at 25°C and the highest at 55°C .

Before proceeding with the interpretation of these results by suggesting possible reactions giving rise to the observed gassing phenomena, some remarks have to be noted:

- i- Slurries and electrodes prepared with the powders belonging to the “B” series were not analysed. It is important to keep in mind that the electrode preparations steps can induce changes at the surface of the AM, as already pointed out in Part 2 of Chapter 3. Observations and conclusions drawn for Samples A3, A4 and A5 in Chapter 3 can be exploited to predict the surface state of electrodes evaluated in full cells, but we believe that a more systematic characterisation of these samples would have given a better support for discussion and interpretation of the results.
- ii- Many processes are going on during cycling and discriminating the effects of each one can be particularly tricky. Specifically, it is worth mentioning that other battery components could have an influence on gassing. Some electrolyte solvents, e.g., are known to be unstable at high temperature and could thence affect the gassing behaviour. Moreover, the exact composition of the electrolyte is unknown; therefore, our hypotheses are proposed by considering electrolyte salts and solvents are —or are similar to— those commonly used in the literature (e.g. LiPF_6 in a mixture of carbonates).

- iii- It is necessary mentioning that the quantities of surface lithiated species found by ^7Li MAS-NMR are associated with a certain error (typically around 5-10%), which could be very close to the nominal value when dealing with small quantities, as for LiOH in samples B2 and B3. Nevertheless, we believe an interpretation of gassing results exploiting these quantification data is still possible whether they are used warily.
- iv- Since cycling was performed up to a cut-off voltage of 4.2 V, we can assume that the measured cell expansion percentage is due solely to the presence of species as CO and CO₂. The production of O₂ from the AM surface was indeed largely demonstrated to occur at higher potential in the literature and it will not be taken into account during the interpretation of our data.¹⁻⁴

Since gassing seems to be highly affected by the cycling temperature (Figure 4.4), we will discuss data recorded at 25°C separately (Section 1.2.1), before evaluating the possible correlation between surface lithiated species and cell expansion at higher temperature (45°C and 55°C) in Section 1.2.2.

1.2.1. Room temperature cycling

Cell expansion at 25°C is the highest in Sample B2 (12.3%) and the lowest in Sample B1 (3.9%). Sample B3 is situated in the middle, with a cell expansion of 6.3%, as evidenced in Figure 4.4. Similarly, the amount of LiOH is the highest at the surface of Sample B2 (1 $\mu\text{mol/g}_{\text{AM}}$) followed by Sample B3 (0.5 $\mu\text{mol/g}_{\text{AM}}$), according to data reported in Table 4.1. LiOH was instead not found at the surface of Sample B1. The measured cell expansion is reported in Figure 4.5 as a function of this quantity and those related to the other lithiated surface compounds that could be involved in gassing —meaning Li₂O and Li₂CO₃— to evidence a possible correlation between surface lithiated species and gassing. A quasi-linear relation can therefore be outlined between the quantity of surface LiOH (in green in Figure 4.5a) and the cell expansion percentage upon cycling at 25°C. Indeed, the cell expansion increases significantly at increasing amount of LiOH. On the other hand, as already mentioned, the amounts of

Li_2CO_3 and Li_2O (in red and light blue in respectively in Figure 4.5) cannot be correlated with the measured percentage expansion after cycling.

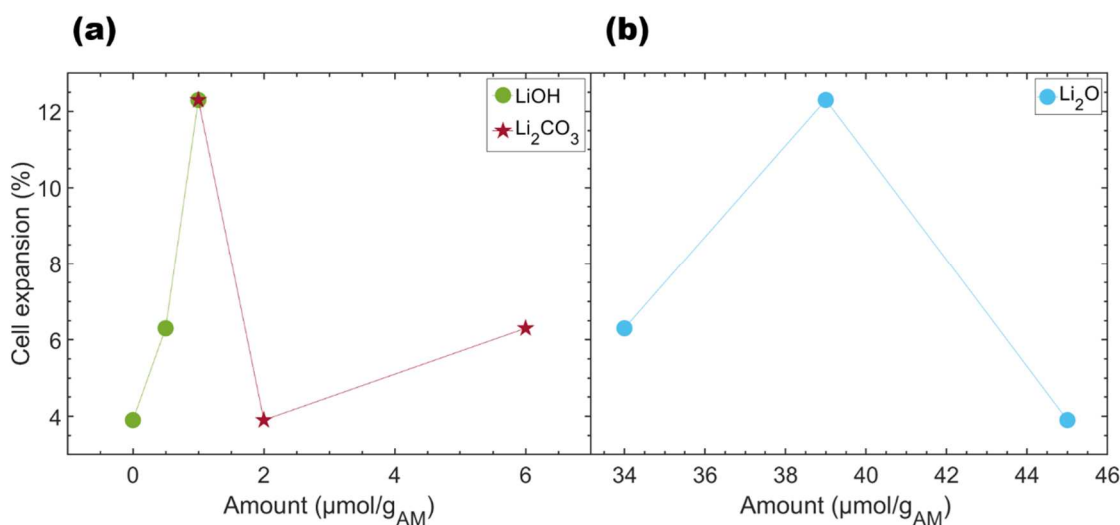
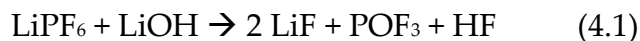
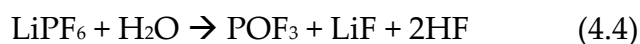
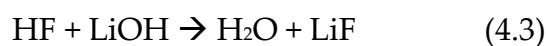


Figure 4.5. Correlation between the amount of surface lithiated species found by ^7Li MAS-NMR (LiOH in green and Li_2CO_3 in red in (a) and Li_2O in light blue in (b)) and the measured cell expansion percentage after cycling in full battery at 25°C .

Accordingly with these observations, we believe that LiOH is likely reacting (directly or indirectly) with the electrolyte salt —here supposed to be LiPF_6 — to form fluorophosphates such as POF_3 already observed in the Solid Electrolyte Interface (SEI) in the literature.⁵ The compound POF_3 would then react with the electrolyte solvent to form the CO_2 responsible for the recorded cell expansion.⁶ Whether Ethylene Carbonate (EC) is used as electrolyte solvent, e.g., the proposed mechanism could be summarised by the following reactions:



Alternatively, LiOH could react with the traces of HF that are usually present in the electrolyte to form water, which would then react with the salt electrolyte LiPF_6 forming the fluorophosphates, with the production of 2 molecules of HF :



POF_3 could subsequently react with the electrolyte solvents as suggested in Reaction 4.2. The resulting total reaction obtained summing Reaction 4.3 and Reaction 4.4 would still be the same as Reaction 4.1.

It is interesting noticing here that Sample B1 is also affected by slight gassing upon cycling (3.9%), despite the absence of LiOH at its surface. This phenomenon could be explained by taking into account the results reported by S. Renfrew and B. McCloskey.¹ In their paper, residual lithium carbonate at the surface of NMC622 was demonstrated to be the principal cause for CO and CO₂ production during the first electrochemical cycle, according to the presented in situ gas analysis and isotopic labelling results. The minor cell expansion recorded for Sample B1, could therefore be due to the surface Li₂CO₃, the presence of which was confirmed by our ⁷Li MAS-NMR measurements.

1.2.2. High temperature cycling

Gassing during cycling at higher temperature (45°C and 55°C in this study) results to be more important than at 25°C, with cell expansions up to more than 30% at 55°C vs 12% at 25°C, as reported in Figure 4.4. Similarly, the gassing behaviour of each sample changes significantly. If Sample B1 is the one presenting the smallest cell expansion at 25°C (3.9%), it becomes the one affected by the largest cell expansion at 55°C (32.8%). Therefore, we believe new reactions are occurring at higher temperature and/or others are kinetically favoured. As already mentioned, carbonate electrolyte solvents are known to be unstable at high temperature, and the increasing gassing phenomenon is thence expected. On the other hand, if LiOH was the principal responsible for the degradation of the carbonate electrolyte solvents and the resulting formation of CO and CO₂ during cycling, as suggested by Reaction 4.1, the gassing behaviour of the analysed samples should not resent the effect of the temperature. In other words, Sample B1 should be affected by very low gassing even at 55°C since no LiOH was found at its surface.

One possible explanation for the gassing behaviour at both 25°C and 55°C, is that new LiOH is forming during cycling at high temperature. In Section 2.2 of Chapter 3 we already discussed the possible reaction between Li₂O and the polymeric binder PVdF to form the LiF observed at the surface of the slurries, and we showed how this reaction could be amplified with increasing temperature (as during XPS measurements). Actually, one molecule of LiOH was formed together with the LiF in the suggested reaction that we remind here:



We can then expect this reaction occurring during cycling at high temperature as well. In alternative, the Li₂O present at the surface of NMC811 could react directly with the traces of HF often present in the electrolyte according to the reaction:



Reaction 4.5 could already occur during the electrode preparation and calendaring, as already shown in Section 2.2 of Chapter 3, while Reaction 4.6 needs the presence of the electrolyte. The analysis of the slurry and/or the electrode before and after cycling would be the only way to know if the new LiOH that we presume to be at the origin of gassing during cycling is formed during Reaction 4.5, Reaction 4.6 or a combination of both.

In both cases, the so formed LiOH would then react with the electrolyte salt LiPF₆ as suggested in Reaction 4.1, giving rise to the sequence of reactions responsible for the electrolyte solvent degradation and the resulting gassing. In these conditions, the limiting factor would though be the amount of Li₂O at the surface of the AM, instead of the initial quantity of surface LiOH.

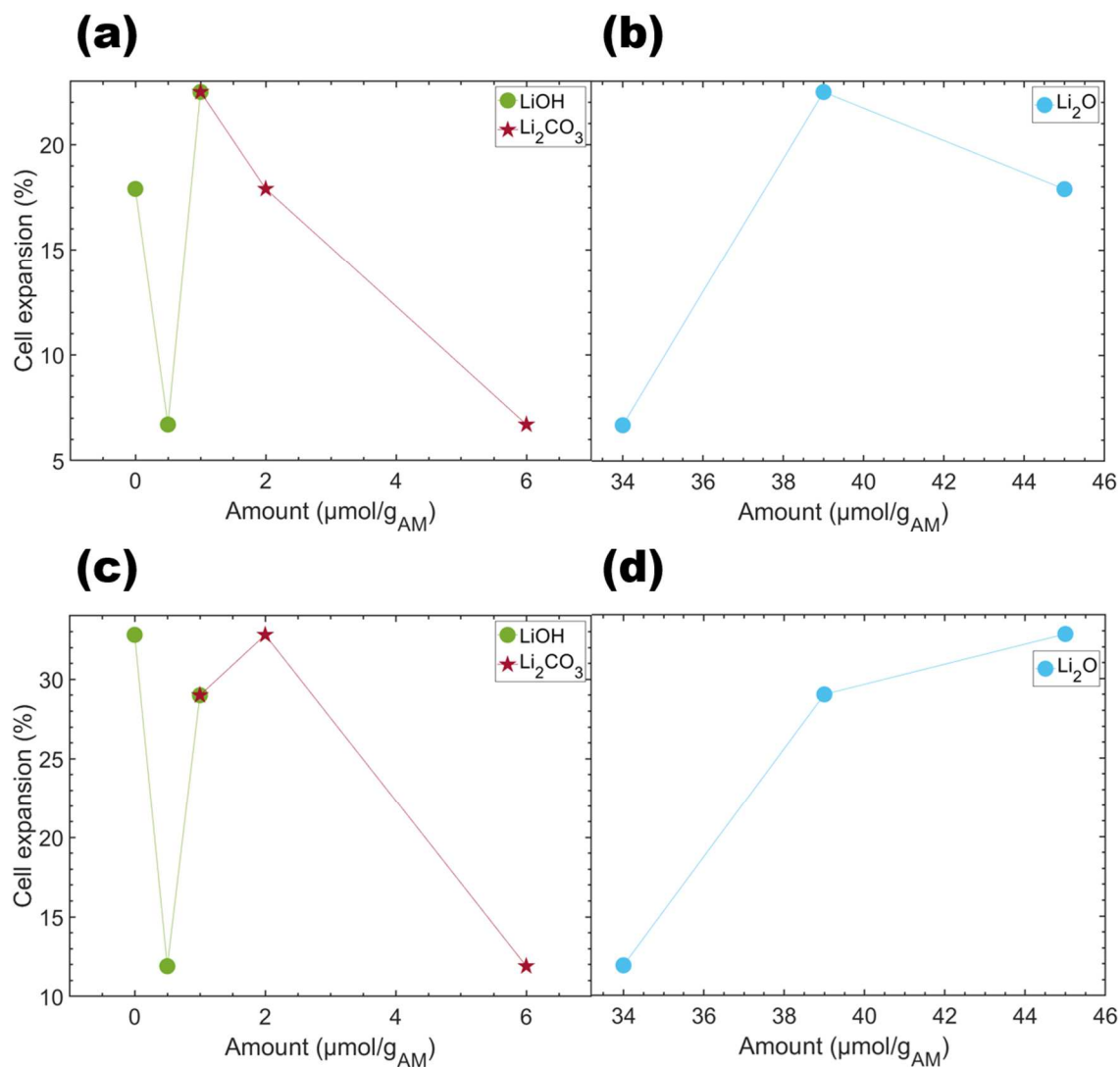


Figure 4.6. Correlation between the amount of LiOH, Li₂CO₃ (a and c) and Li₂O (b and d) and the measured cell expansion after cycling at 45°C (a and b) and at 55°C (c and d).

As a matter of fact, when analysing the evolution of the cell expansion percentage after cycling at 55°C as a function of the amount of surface lithiated species represented in Figure 4.6c and Figure 4.6d, it is possible to observe a correlation with the Li₂O amount. At increasing Li₂O quantity, the percentage cell expansion increases indeed, confirming our hypothesis (Figure 4.6d). At 45°C, a direct correlation explaining the highest cell expansion in Sample B2 was instead not found for any compound (Figure 4.6a and Figure 4.6b), indicating that multiple processes are probably occurring at the same time, making the interpretation of these results more difficult. On the other hand, it is interesting noticing that gassing decreases considerably when

a higher amount of surface Li_2CO_3 is present on the pristine powder. Similarly, we showed in Section 2.1 of Chapter 3 how a high amount of lithiated species at the surface of Sample A4 is hindering the extraction of new lithium from the material during the slurry preparation step. The possible protection role of surface Li_2CO_3 is therefore suggested here again. The surface Li_2O in Sample B3 could indeed be covered by the large amount of Li_2CO_3 —demonstrated to be further from the material according to ^7Li MAS-NMR measurements— that would prevent (or at least hinder) its decomposition into LiOH and LiF . Alternatively, the surface Li_2CO_3 could immediately react with the traces of HF contained in the electrolyte, decreasing in this way the amount of HF that would be liable to react with the Li_2O , according to the reaction suggested by Park et al. and reported in Chapter 1:⁷



As already mentioned, these are solely suggestions, made with the scarce data in our possession. This represents purely the first step of a work that would demand a larger number of information, experiments and samples to draw any reliable conclusion. The complexity of a full cell working system implies the need for analysis of each component in a first moment —not exclusively of the AM— and of different combinations of more components afterwards, to be able to discriminate the contribution of every single part.

Part 2. Influence of Li/TM blend and firing atmosphere

In the attempt to exacerbate the Mn enrichment observed on Sample A0, different conditions were used to synthesise new samples, namely Samples C1, C2, C3, D1, D2 and D3. Both the Li/TM blend and the firing atmosphere were modified, while the firing temperature was kept constant. Samples C1, C2 and C3 were obtained performing the firing step in synthetic air and using increasing Li/TM blends – the lowest in C1 and the highest in C3. These same Li/TM blends were used for the synthesis of Samples D1, D2 and D3, but the firing step was performed in pure oxygen instead. The heating rate and dwell time of firing were chosen to be as similar as possible to the conditions used during the synthesis of Sample A0, where the surface Mn enrichment was firstly observed.

2.1. Bulk characterisation

Powder X-Ray Diffraction (XRD) was performed in Umicore, proving that all the samples were obtained in their lamellar crystalline structure, typical of NMC811. In this context, a superstructure characterised by peaks at a 2θ angle of 22.2° (highlighted by the black arrow in Figure 4.7a) and 19.7° , typically attributed to Li_2MnO_3 domains in the literature, was identified.^{8,9} Following the previous studies, these peaks are supposed to indicate a higher Li/TM ordering in the bulk structure here as well.

The so-obtained diffraction patterns were fitted using the Fundamental Parameters (FP) approach and the sum of the peaks areas was calculated. The area ratios between the superstructure and the 104 peak is reported in Figure 4.7b as a function of the Li/TM blend used for the synthesis of each sample.

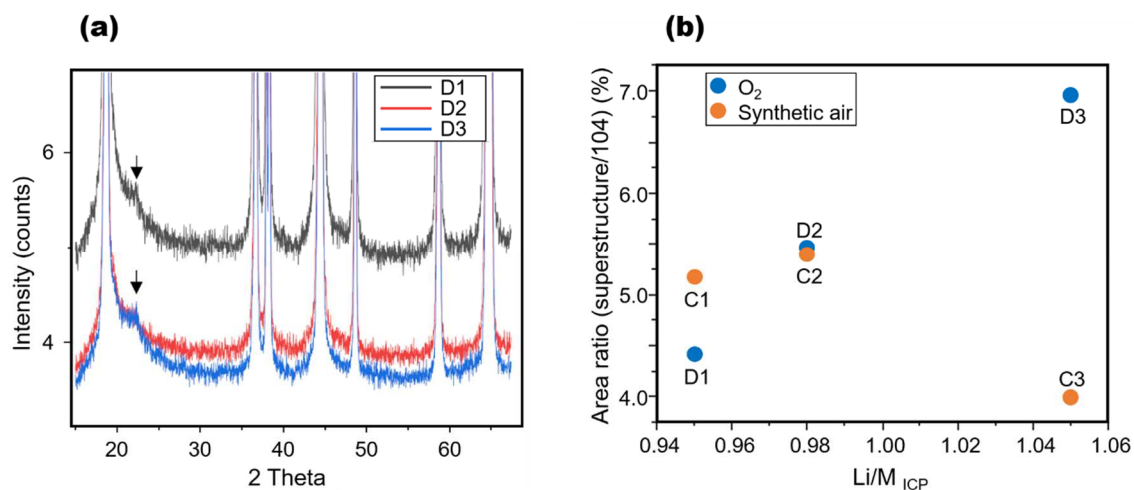


Figure 4.7. XRD patterns of samples belonging to the “D” series to highlight the identified superstructure, indicated by the black arrow (a), and relation between the area ratio of the superstructure and the 104 peak with the Li/TM blend used for the synthesis in samples of the “C” and “D” series (b).

In order to confirm the different ordering level in the bulk of these samples, ^7Li MAS-NMR MATPASS was performed on a 200 MHz spectrometer allowing the observation of Li environments in the paramagnetic material. Only three samples were observed by ^7Li MAS-NMR MATPASS, namely C1, C3 and D3, due to lack of time and instrument availability. The obtained ^7Li MAS-NMR MATPASS spectra are reported in Figure 4.8a together with the one corresponding to Sample A0, used here as reference, and show similar features for the four analysed samples.

Actually, while the overall chemical shift of the principal peak (resulting from the sum of all the contributions of the different Li environments) is the same for Sample C1, C3 and D3 (indicated by the green dotted line), the overall envelope width changes slightly from a sample to the other. This difference is more clearly visible in the inset of Figure 4.8a, representing a higher magnification of the right side of the spectra (with all the lines superimposed on the left side). Sample C3 results to be the one having the largest overall signal width, followed by Sample C1 and Sample D3, as also evidenced in Figure 4.8b.

Since the ^7Li MAS-NMR signal is the sum of the contributions corresponding to all the Li environments present in the bulk of the material, as previously mentioned, a lower

total width could imply a lower number of different Li local environments. Consequently, its value is related to the level of ordering and/or lithium/TM distribution. As a matter of fact, Sample D3 is characterised by both the smallest envelope width and the highest area ratio calculated from the XRD pattern (Figure 4.8b). Similarly, Sample C3 present the smallest superstructure diffraction peak and the largest ^7Li MAS-NMR signal. The concordance between XRD and ^7Li MAS-NMR data supports therefore a different cationic ordering level in the analysed samples.

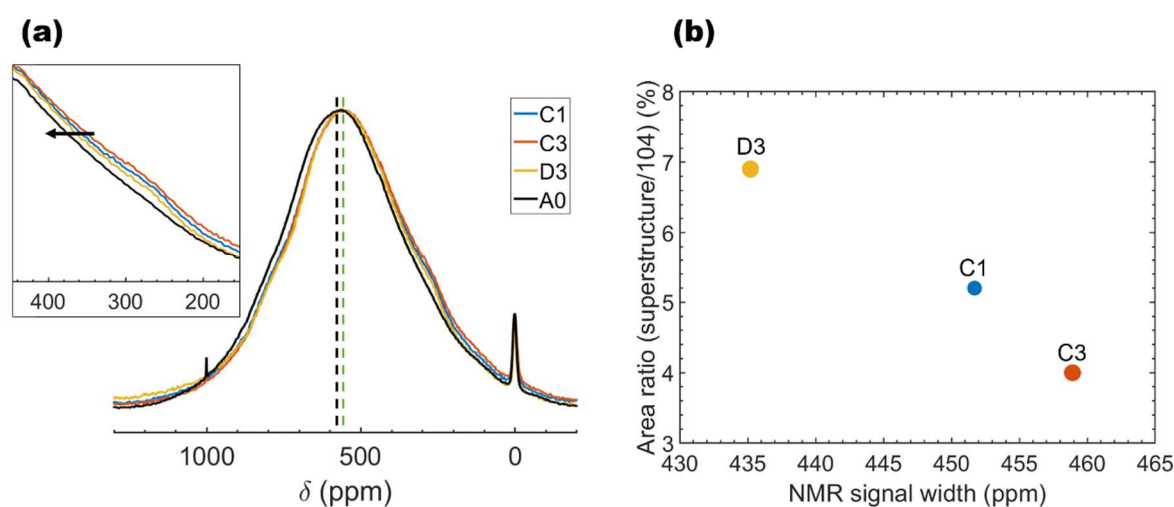


Figure 4.8. ^7Li MAS-NMR MATPASS spectra acquired on a 200 MHz spectrometer for Sample C1 (in blue), C3 (in orange), D3 (in yellow) and Sample A0 (in black) used here as a reference (a). The principal peak chemical shift of Sample A0 is represented by the black dotted line, while the chemical shift of Samples C1, C3 and D3 is in green dotted line. The correlation between the NMR overall signal width (in ppm) and the area ratio of the superstructure and the 104 peak is represented in (b).

Moreover, ^7Li MAS-NMR MATPASS spectra show an overall shift of the principal peak around 500 ppm towards lower chemical shifts for all the samples when compared to Sample A0. This could indicate a slightly different mean oxidation state for the transition metals in the bulk. In particular, since the Fermi contact shift from 0 ppm is a typical effect of the nucleus-electron dipolar interaction between Li nuclei and paramagnetic TM, we could suppose that the lower shift recorded for Samples C1, C3 and D3 is due to a slightly weaker paramagnetism of the Li local environment.

In order to confirm this hypothesis, STEM-EELS was performed on Sample C3 and Sample D3. The analysis of Ni oxidation state was possible thanks to the use of an excited monochromator, as explained in Section 1.2.2.1 of Chapter 2. The Ni L-edge EEL Spectrum of the bulk of Sample C3 is compared to that of Sample A0 in Figure 4.9a.

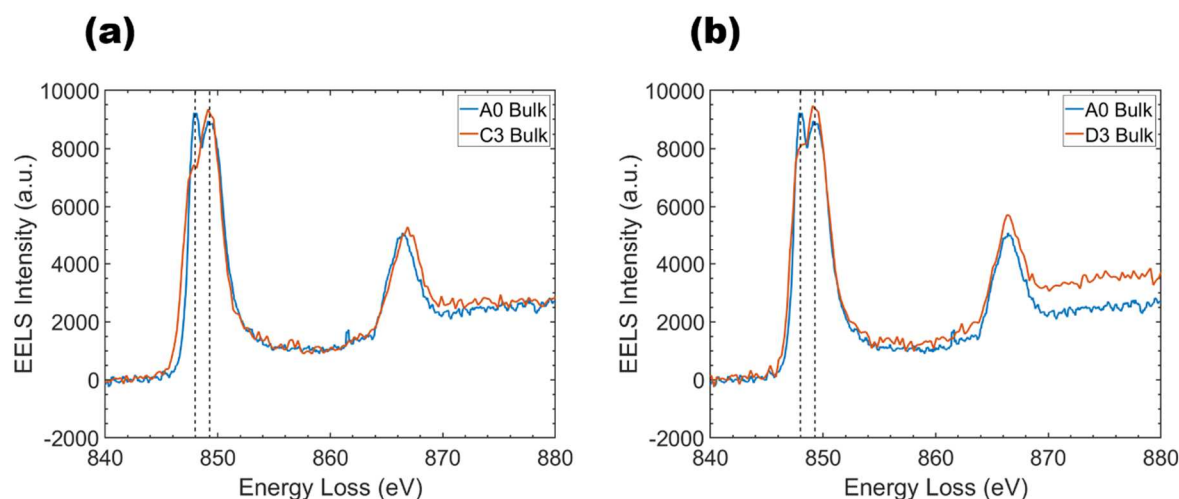


Figure 4.9. Comparison between Ni L-edge bulk EEL Spectra of Sample A0 (in blue) and Sample C3 (in orange) in (a) and Sample D3 in (b).

The principal difference between the Ni L-edge of these two samples is at the level of the higher energy peak of the L_3 -edge (around 848 eV). The ratio between the high-energy and the low-energy peak of the L_3 split is indeed higher in Sample C3 than in Sample A0. A similar spectrum was also acquired for Sample D3 (Figure 4.9b). As already mentioned in Chapter 3, the high energy peak of the Ni L_3 split can be attributed to Ni in a +3 oxidation state. The higher intensity of this feature with respect to the low-energy one in the bulk of Samples C3 and D3 indicates therefore that Ni is in a higher oxidation state — meaning that there are more Ni in a +3 oxidation state when compared to Sample A0. While Ni^{2+} in NMC materials displays typically a high spin $t_{2g}^6e_g^2$ electronic configuration, Lee et al. showed that Ni^{3+} undergoes a Jahn-Teller distortion leading to a low spin $t_{2g}^6e_g^1$, with only one unpaired electron, thence reducing the bulk paramagnetism in the vicinity of the Li nuclei.¹⁰ STEM-EELS results appear therefore in agreement with 7Li MAS-NMR observations.

2.2. Surface characterisation

The principal goal of this part of our research work is to investigate how different synthesis conditions can influence the surface of NMC811 and in particular the surface enrichment in some elements. We already showed in Chapter 3 how the surface of Sample A0 is enriched in manganese and how this feature is not influenced by the storage conditions – Samples A1 and A2 showed the same 3 nm Mn enrichment. The Mn segregation at the surface is thence expected to occur during the synthesis of the material.

STEM-EELS spectra were therefore acquired with a 0.25 eV/ch. energy dispersion for all the samples and the second derivative method was applied to obtain relative quantification information on the surface of the primary particles, as explained in details in the Supporting Information of the paper reported in Chapter 3.

In order to provide relevant information, multiple surfaces were analysed for each sample, and data were averaged over thousands of nanometres. In particular, each Spectrum Image (SI) was firstly analysed individually, binning data in the y-direction and obtaining a Mn/Ni tendency for each acquisition, as the one reported in Figure 4.10a, following the same procedure described in Chapter 3. A weighted average between the so-obtained results was then performed for each pixel (px_i), over all the SI corresponding to a same sample ($SI_a, SI_b, SI_c, \dots, SI_z$), using the following formula:

$$\left(\frac{Mn}{Ni}\right)_{av,px_i} = \frac{\sum_a^z \left[\left(\frac{Mn}{Ni}\right)_{px_i,a} \cdot h_a \right]}{\sum_a^z h_a} \quad (4.8)$$

, where h_a is the height of SI_a in pixel and $(Mn/Ni)_{px_i,a}$ is the Mn/Ni value obtained for the px_i in the SI_a . In this way, it was possible to obtain results averaged over the entire dataset of acquired SI, taking into account the statistical weight of each one of them. As a matter of fact, some analysed surfaces were relatively small (around 50 pixels) compared to others (up to 600 pixels). The so-obtained averaged Mn/Ni ratios for

Sample D3 are reported in Figure 4.10b, showing a significantly lower dispersion of data when compared to those resulting from the analysis of a single surface (Figure 4.10a).

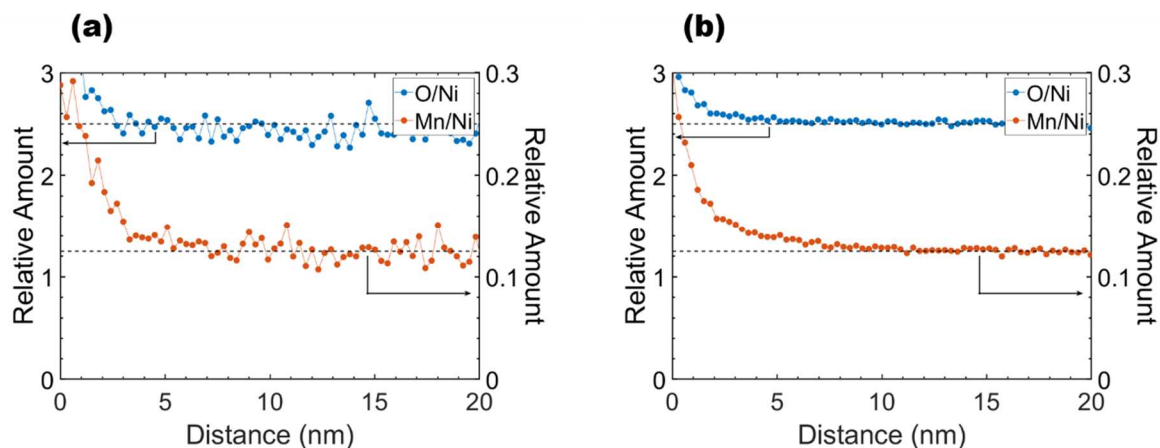


Figure 4.10. Comparison between data acquired on one surface of Sample D3 (a) and those resulting from the weighted average over all the particles analysed for Sample D3.

This method was used to analyse between 15 and 40 particles per sample and to obtain averaged results over 5000 to 10000 pixels; since the pixel size used for the acquisitions was 0.3 nm, the averaged data reported in Figure 4.11 corresponds to 1500 to 3000 nm of surface depending on the sample.

By analysing these results, a proper correlation between firing atmosphere and surface Mn enrichment or between Li/TM ratio and surface Mn enrichment is not immediately visible. As a matter of fact, all the samples presented a similar composition at the surface, with the Mn/Ni ratio increasing in the first 3 to 9 nm. The only sample having a different Mn/Ni trend is Sample C3 (Figure 4.11e), where the Mn/Ni ratio decreases for about 10 nm before increasing slightly again at the extreme surface. Both a high Li/TM blend composition and synthetic air firing atmosphere were therefore necessary to change significantly the surface composition of NMC811.

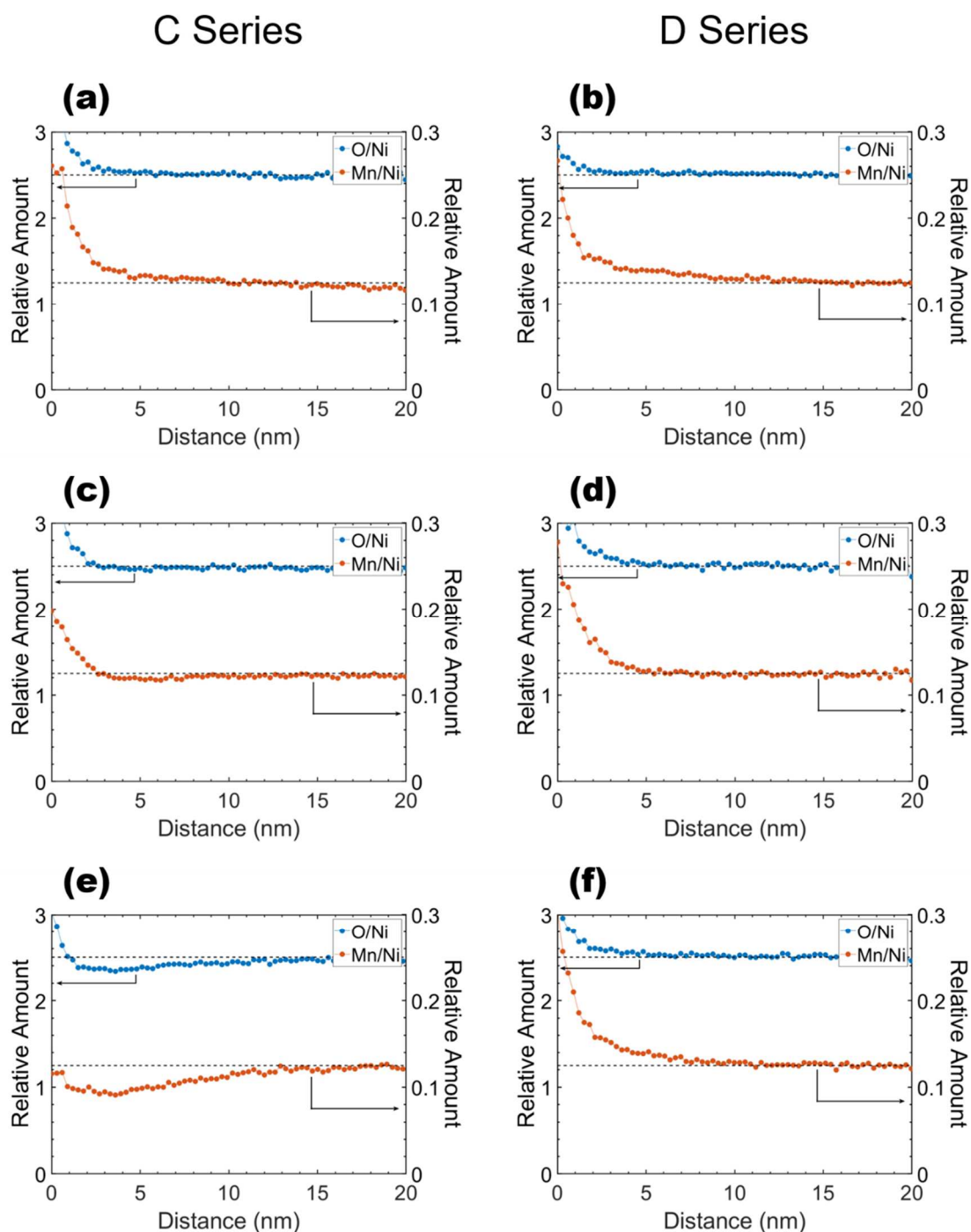


Figure 4.11. Relative amount of O (in blue) and Mn (in orange) in Sample C1 (a), C2 (c), C3 (e), D1 (b), D2 (d) and D3 (f).

If we consider now samples synthesised with a synthetic air firing only — meaning samples belonging to the “C” series — (Figure 4.11a, 4.11c and 4.11e), letting one single parameter varying — the Li/TM ratio in the synthesis blend — a trend in the Mn enrichment becomes visible. Actually, the Mn enriched surface — considered to begin

where values for Mn/Ni ratio start to be higher than the mean bulk value of 0.125—accounts for more than 5 nm in Sample C1. The Mn enriched surface thickness becomes less than 3 nm when the Li/TM ratio in the synthesis blend is increased (Sample C2) and a Mn depletion is found at the surface of Sample C3, when an even higher Li/TM ratio is used for the synthesis.

On the other hand, this same correlation was not found for samples synthesised with a firing in pure oxygen. The Mn/Ni ratio increases similarly in Samples D1 and D3, while the Mn enriched surface thickness is slightly lower in Sample D2.

Since Mn is known to have a beneficial effect on NMC (it is actually used to stabilise its surface when a concentration gradient engineering of the secondary particles is proposed, as reported in Chapter 1), we decided to quantify the lithiated diamagnetic species at the surface of the samples by ^7Li MAS-NMR, to investigate its possible beneficial effect on the lithium extraction from the material. Only three samples were analysed due to lack of time and instrument availability, namely Sample C1, Sample C3 and Sample D3 —meaning the same already analysed with the 200 MHz NMR spectrometer and described in Section 2.1. The total surface Li amounts found using the 500 MHz NMR spectrometer are $145 \mu\text{mol/g}_{\text{AM}}$, $149 \mu\text{mol/g}_{\text{AM}}$ and $131 \mu\text{mol/g}_{\text{AM}}$ respectively. Even if these data are subjected to a certain error (5-10%), they seem to respect the surface Mn enrichment: when the Mn/Ni ratio is lower (Sample C3, Figure 4.11e), the extracted lithium amount from the surface AM is higher, while for a highly Mn enriched surface (Sample D3, Figure 4.11f), the amount of surface diamagnetic lithium is significantly reduced.

To go further with the analysis, we can try to correlate these values to the bulk cation ordering previously observed and described in Section 2.1. As a matter of fact, when lithium ions are extracted from the NMC811 structure, they can be replaced easily by Ni^{2+} ions, which move thence from the TM layer to the Li layer, having a similar ionic radius as mentioned in Chapter 1. In this way, new environments are created, increasing the cationic disorder. A higher amount of surface diamagnetic lithium (as

in Sample C3) would therefore imply a higher cationic disorder and thence a wider ^7Li MAS-NMR bulk signal (200 MHz spectrometer) and a lower XRD superstructure peak. Comparing the amount of surface diamagnetic lithium found by ^7Li MAS-NMR with both the superstructure area reported in Figure 4.7 and the ^7Li MAS-NMR bulk signal total width visible in Figure 4.8, it is possible to confirm this hypothesis. Sample D3 displays the most intense XRD superstructure, the lower bulk signal overall width and the lower diamagnetic surface lithium amount.

Similarly, we could extrapolate the amount of surface lithium in the samples that were not analysed by MAS-NMR using the information we have on the superstructure observed by XRD. Even if these considerations would undermine the previously proposed correlation between surface lithium and Mn enrichment, a new correlation for the “D” series can now be proposed between Li/TM ratio blend and the surface lithium amount.

In order to propose a significant interdependence between all the observed phenomena –cationic ordering, Mn enrichment and lithium extraction– and the synthesis conditions –Li/TM blend and firing atmosphere–, a complete characterisation of all the samples seems therefore to be essential.

Moreover, the analysis of the surface lithiated species in the analysed samples seems to suggest that both the firing atmosphere and the Li/TM blend have an influence on the species forming at the surface of the AM. When comparing Sample C3 and Sample D3 –synthesised with the same Li/TM blend–, the use of synthetic air for firing seems to promote the formation of LiOH (Figure 4.12), which is instead absent from the surface of Sample D3.

On the other hand, the comparison between Sample C1 and Sample C3 –both obtained with a firing in synthetic air– suggests that lithium hydroxide is formed preferably when a high Li/TM blend.

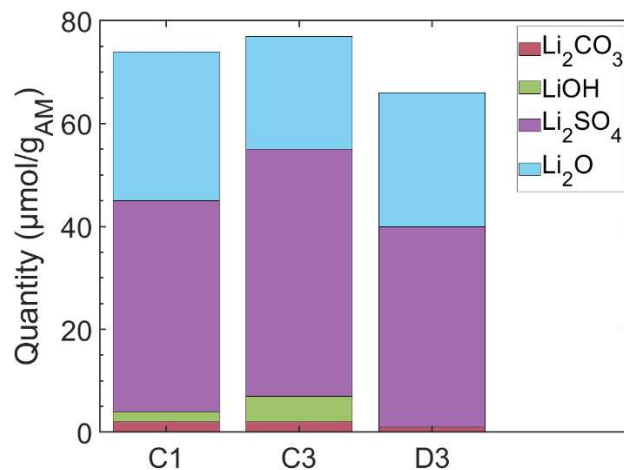


Figure 4.12. Amount of surface lithiated species found by ^7Li MAS-NMR on Samples C1, C3 and D3.

In conclusion, both the firing atmosphere and the Li/TM blend used for synthesis appear to have an influence on both the cationic ordering in the bulk and the surface lithiated species speciation and quantification. A definitive correlation between these parameters and the Mn enrichment previously observed on Sample A0 has to be confirmed, but we strongly believe that a complete characterisation of the entire group of samples could help us suggesting a more complete mechanism for the formation of different NMC811 surfaces originated in various synthesis conditions.

Part 3. Conclusions

A study on the effect of synthesis conditions on the surface of NMC811 was presented in this last chapter in line with the complex chemistry demonstrated in previous chapters.

We showed here how multiple synthesis parameters can affect the NMC811 surface state before cycling, namely the firing temperature, the atmosphere and the Li/TM blend composition.

In line with the rest of the manuscript, we evidenced here the importance of a complete and deep characterisation of samples, in which a multi-analytical approach plays an essential role for the observation of complex surfaces.

In particular, a possible interdependence between surface lithiated species and gassing upon cycling was suggested, highlighting the important role of Li_2O in this context. Actually, it is interesting noticing that even particularly small quantities of impurities ($1 \mu\text{mol/g}_{\text{AM}}$ of LiOH , which is around 25 ppm) seem having a significant impact on long-term cycling. It appears therefore relevant to take any little variation (of the surface or the bulk) into consideration.

Moreover, we demonstrated in the second part of the chapter how bulk and surface characterisation can be deeply connected. Slight changes in the bulk structure and/or ordering —due to variations in the synthesis conditions in our case— seem indeed to have an influence on the surface of the material.

To conclude, the aim of this chapter was to insist on the importance of collaborating with industrial partners when working with materials having surfaces particularly sensible to synthesis conditions, as NMC811 samples do.

References

- (1) Renfrew, S. E.; McCloskey, B. D. Residual Lithium Carbonate Predominantly Accounts for First Cycle CO₂ and CO Outgassing of Li-Stoichiometric and Li-Rich Layered Transition-Metal Oxides. *J. Am. Chem. Soc.* **2017**, *139* (49), 17853–17860. <https://doi.org/10.1021/jacs.7b08461>.
- (2) Renfrew, S. E.; McCloskey, B. D. Quantification of Surface Oxygen Depletion and Solid Carbonate Evolution on the First Cycle of LiNi_{0.6}Mn_{0.2}Co_{0.2}O₂ Electrodes. *ACS Appl. Energy Mater.* **2019**, *2* (5), 3762–3772. <https://doi.org/10.1021/acsaem.9b00459>.
- (3) Jung, R.; Metzger, M.; Maglia, F.; Stinner, C.; Gasteiger, H. A. Oxygen Release and Its Effect on the Cycling Stability of LiNi_xMn_yCo_zO₂ (NMC) Cathode Materials for Li-Ion Batteries. *J. Electrochem. Soc.* **2017**, *164* (7), A1361–A1377. <https://doi.org/10.1149/2.0021707jes>.
- (4) Strehle, B.; Kleiner, K.; Jung, R.; Chesneau, F.; Mendez, M.; Gasteiger, H. A.; Piana, M. The Role of Oxygen Release from Li- and Mn-Rich Layered Oxides during the First Cycles Investigated by On-Line Electrochemical Mass Spectrometry. *Journal of The Electrochemical Society* **2017**, *164* (2), A400–A406. <https://doi.org/10.1149/2.1001702jes>.
- (5) Confronting the Challenges of Next-Generation Silicon Anode-Based Lithium-Ion Batteries: Role of Designer Electrolyte Additives and Polymeric Binders <http://chemistry.europe.onlinelibrary.wiley.com/doi/epdf/10.1002/cssc.201900209> 9 (accessed 2022 -04 -14). <https://doi.org/10.1002/cssc.201900209>.
- (6) Champion, C. L.; Li, W.; Lucht, B. L. Thermal Decomposition of LiPF₆-Based Electrolytes for Lithium-Ion Batteries. *J. Electrochem. Soc.* **2005**, *152* (12) A2327–A2334.
- (7) Park, K.-J.; Choi, M.-J.; Maglia, F.; Kim, S.-J.; Kim, K.-H.; Yoon, C. S.; Sun, Y.-K. High-Capacity Concentration Gradient Li[Ni_{0.865}Co_{0.120}Al_{0.015}]O₂ Cathode for Lithium-Ion Batteries. *Adv. Energy Mater.* **2018**, *8* (19), 1703612. <https://doi.org/10.1002/aenm.201703612>.
- (8) Armstrong, A. R.; Holzapfel, M.; Novák, P.; Johnson, C. S.; Kang, S.-H.; Thackeray, M. M.; Bruce, P. G. Demonstrating Oxygen Loss and Associated Structural Reorganization in the Lithium Battery Cathode Li[Ni_{0.2}Li_{0.2}Mn_{0.6}]O₂. *J. Am. Chem. Soc.* **2006**, *128* (26), 8694–8698. <https://doi.org/10.1021/ja062027+>.
- (9) Lu, Z.; MacNeil, D. D.; Dahn, J. R. Layered Cathode Materials Li[Ni_xLi_(1/3-2x/3)Mn_(2/3-x/3)]O₂ for Lithium-Ion Batteries. *Electrochem. Solid-State Lett.* **2001**, *4* (11), A191. <https://doi.org/10.1149/1.1407994>.
- (10) Lee, W.; Muhammad, S.; Kim, T.; Kim, H.; Lee, E.; Jeong, M.; Son, S.; Ryou, J.-H.; Yoon, W.-S. New Insight into Ni-Rich Layered Structure for Next-Generation Li Rechargeable Batteries. *Adv. Energy Mater.* **2018**, *8* (4), 1701788. <https://doi.org/10.1002/aenm.201701788>.

General Conclusion and Future Work

The principal key findings of this work will be summarised in this last part, followed by some recommendations and perspectives for future works in the characterisation of Li-ion battery positive electrode materials.

The aim of this thesis being to provide an extensive and detailed picture of the pristine surface state of industrial NMC811 samples, we were able to identify three principal parameters affecting the quality of their surfaces, namely the storage atmosphere, the electrode preparation steps and the synthesis conditions (Figure 4.1). All these steps, occurring before any electrochemical cycling, have been shown to influence strongly and correlatively the surface layers of the active material itself and the presence of lithiated surface impurities, which, are in turn expected to influence reactions with the electrolyte and gas production upon cycling.

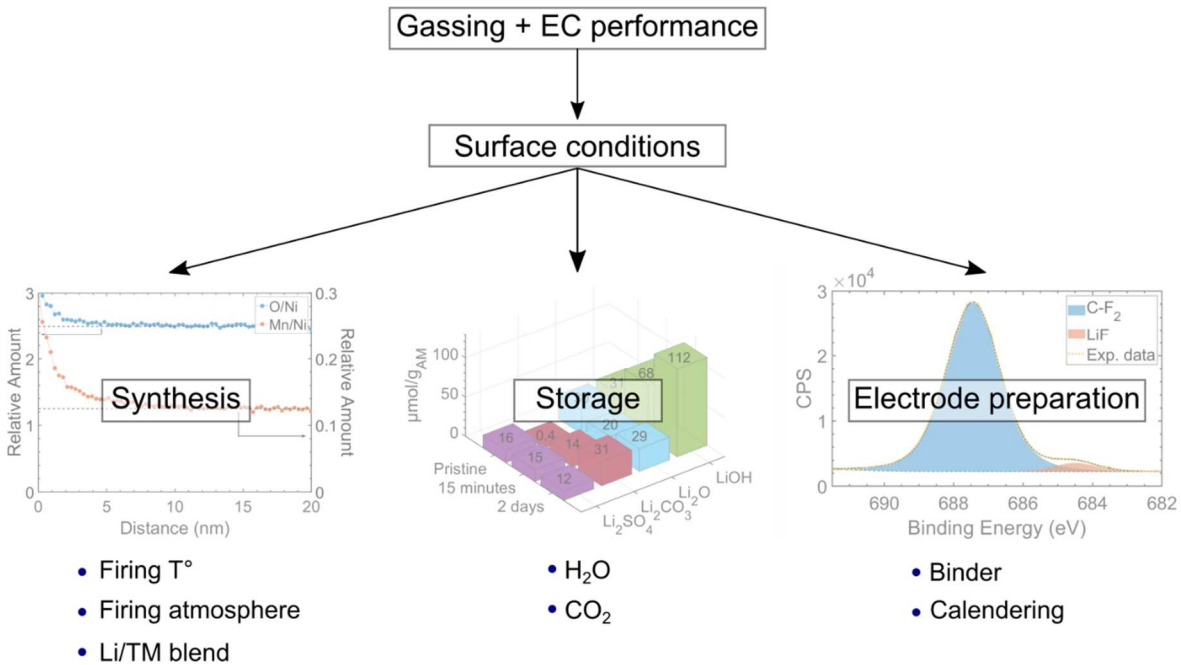


Figure 5.1. Schematic representation of the identified parameters having an influence on the state of NMC811 surface.

In the first part of this manuscript results, we showed indeed how the powder surface is different from the bulk directly after shipping, and we attributed the observed changes to the very elevated reactivity of the material towards the extremely low humidity of the industrial dry rooms that are considered as standard for reliable production and storage. In particular, a manganese excess as well as nickel in a more reduced state were found at the surface of the primary particles of the AM. Concomitantly, diamagnetic lithiated species such as Li_2O , Li_2SO_4 , LiOH and Li_2CO_3 contained in the native contamination layer were identified and quantified. Both active material surface and native contamination surface layer characteristics were demonstrated to be exacerbated and even alimeted on short-term storage in the studied low-humidity conditions whether in presence of CO_2 or not.

The importance of these lithiated species is even more evident when analysing dried slurries and electrodes. As a matter of fact, an additional extraction of lithium, supplying the surface layer, was demonstrated to occur during the slurry preparation. In this context, the amount of Li_2O was suggested to be correlated to the formation of LiF during the slurry preparation, bringing to the degradation of the PVdF binder. Similarly, this same reaction was suggested to occur during cycling, producing the LiOH that we suggest being responsible for the observed gassing. Contrarily to what it is often hypothesised in the literature, we showed here that Li_2CO_3 does not have a significant influence on gassing.

Studies of syntheses at different firing temperatures evidenced how this parameter can bias the formation of surface lithiated species. Even if a direct correlation with the formed LiOH quantity was not identified, we showed how a higher firing temperature results in the extraction of smaller amount of lithium and in the formation of lower quantities of Li_2O .

Moreover, both the firing atmosphere and the Li/TM blend used for synthesis exert a synergetic influence on both the cationic ordering in the bulk and the surface lithiated species speciation and quantification. A clear correlation between these synthesis

parameters and the Mn enrichment previously observed was however not found during the pilot study concluding this thesis even if the combination of high Li/TM blend and firing in synthetic air leads to a drastic change in surface characteristics.

These results were obtained by combining wisely multiple characterisation techniques, allowing the observation of the material at different scales, down to the sub-nanometric level. We showed throughout this entire work how the synergic use of STEM-EELS, STEM-EDX, MAS-NMR and XPS can give reliable results and help going beyond the limits of each single technique alone. In addition, acquisitions exploiting the coupling of SEM-FIB 3D reconstruction and EDX mapping were reported here, suggesting this approach as a possible way to confirm the reaction path of LiF formation.

In the future, we believe that a similar approach could provide improved characterisation of battery materials, since one of the biggest challenges concerning these materials is their description at different scales, from the nano to the micrometer. The combination of different characterisation techniques, local and at a larger scale at the same time, is therefore essential to draw any conclusion when their behaviour in batteries must be correlated to their nanometric features.

In particular, a further investigation of the possible reaction between Li_2O and PVdF should bring a new light on both the analysis of degradation products after cycling and the conception of the emerging Ni-rich NMC electrode preparation dry processes, often using high temperatures for the activation of polymers. In doing so, the analysis must be conducted gradually, taking into account the material at each step.

Finally, we strongly believe that the use of our method for the quantification of surface lithiated species could provide a new insight into the NMC gassing issue. A larger number of samples should be analysed with this combination of techniques in order to propose definitive conclusions. Similarly, we have found particularly relevant working with industrial samples when investigating the impact of synthesis

conditions and we expect significant advances of future studies following this same path, always paying attention to vary one single synthesis parameter at the time.

Titre : Caractérisation de la réactivité de surface de matériaux d'électrode positive riches en nickel pour batteries Li-ion

Mots clés : Batteries Lithium-ion, NMC riche en nickel, Caractérisation

Résumé : L'électrification des véhicules se base aujourd'hui sur l'utilisation de batteries Lithium-ion utilisant des oxydes lamellaires de nickel, manganèse et cobalt (NMC) comme matériaux d'électrode positive. Au niveau industriel, la production de matériaux riches en nickel est désormais privilégiée pour satisfaire la demande de meilleures autonomies de la batterie de la part des consommateurs. Cependant, ces matériaux sont affectés par un fort dégagement gazeux pendant le cyclage en batterie. Plusieurs études ont été conduites pour définir les principales causes de ce dégazage et trouver les meilleures solutions pour le réduire. En revanche, la plus grande partie de ces recherches se concentre exclusivement sur une observation des matériaux pendant le cyclage. Pour répondre au besoin d'une caractérisation systématique du NMC riche en Ni dans son état

initial, les surfaces de plusieurs échantillons industriels ont été observées à l'aide de différentes techniques d'analyse.

⁷Li MAS-NMR, XPS, STEM-EELS et SEM-FIB ont été combinées pour obtenir une description complète des matériaux et de leurs surfaces. Les limites et complémentarités de chaque technique sont discutées et les résultats obtenus comparés et exploités de façon synergique. Il a donc été possible de décrire en détail la surface du matériau dans son état initial à l'échelle nanométrique et d'évaluer ensuite l'influence des conditions de stockage, ainsi que des étapes de mise en forme en électrode. Le mode opératoire ainsi défini a pu être utilisé par la suite pour analyser la surface de matériaux issus de différentes méthodes de synthèse.

Title: Characterisation of the surface reactivity of Ni-rich positive electrode materials for Li-ion batteries

Keywords: Lithium-ion batteries, Ni-rich NMC, Characterisation

Abstract: The electrification of vehicles is currently based on the use of Lithium-ion batteries using lamellar oxides of nickel, manganese and cobalt (NMC) as positive electrode materials. At the industrial level, the production of nickel-rich materials is now the main focus in order to satisfy the need for longer range battery performances demanded by consumers. However, these materials are affected by strong outgassing during battery cycling. Several studies have been conducted to define the main factors contributing to this outgassing and to find the best solutions to reduce it. The majority of this research, though, focuses exclusively on observing the materials during cycling. To address the necessity of a systematic characterisation of Ni rich NMC in its

initial state, the surfaces of several industrial samples were observed using different analytical techniques.

⁷Li MAS-NMR, XPS, STEM-EELS and SEM-FIB were used to obtain a thorough description of the materials and their surfaces. The limitations and complementarities of each technique are discussed and the results obtained compared and exploited in a synergistic way. It was thus possible to describe in detail the surface of the material in its initial state at the nanometric scale and to evaluate the influence of the storage conditions, as well as the electrode preparation steps. The procedure thus defined could then be used to analyse the surface of materials from different synthesis methods.